Image Processing Methods for Multi-Nuclear Magnetic Resonance Imaging of the Lungs

By:

Paul John Clifford Hughes, MEng

A thesis submitted in partial fulfilment of the requirements for the degree of
Doctor of Philosophy

The University of Sheffield
Faculty of Medicine, Dentistry and Health
Department of infection, Immunity and Cardiovascular Disease
Unit of Academic Radiology
Royal Hallamshire Hospital
S10 2JF, Sheffield
United Kingdom

Supervisors: Professor Jim Wild, Dr. Helen Marshall and Dr. Alberto Biancardi
Industrial sponsor: Fred Wilson

Examiners: Dr. Paul Armitage, Professor Jens Vogel-Claussen

Final submission date: April 2018

ACKNOWLEDGMENTS

It would not have been possible to complete this thesis without the support of my friends, family, university colleagues and of course my supervisors.

Firstly, I thank my supervisor Professor Jim Wild for his patient support and guidance as well as offering me the opportunity to work in this field. I also thank him for the opportunity to develop my own ideas and for allowing me the opportunities to attend scientific training courses and conferences. Secondly I thank Dr Helen Marshall for the time spent training me on the technical aspects of MRI and overall supervision over the course of this PhD. I thank Dr Alberto Biancardi for his technical guidance and time spent helping me to develop better experimental validation methods. I thank my industrial sponsor Fred Wilson of GSK who gave helpful insight and feedback on my work over the last three years.

I also thank all of my colleagues in the POLARIS group and Academic Unit of Radiology at Sheffield, without whom this work would not have been possible. I thank Neil Stewart and Fung Chan for aiding me with scanning. I also thank Laurie Smith for his help in understanding lung physiology and PFTs. I thank Bilal Tahir for his help in understanding image registration and for the useful discussions and his enthusiasm on this subject. Finally, thanks to all of my other colleagues for the helpful discussions and support over the course of this project.

I also extend thanks to my parents, Nigel and Shan for their constant support and help over my time in Sheffield. I also thank my siblings Jordan and Shelby for their support, my uncle Carl for his help in moving and his family for visiting. Finally, I would like to thank my fiancée Anya for her constant support and understanding throughout my PhD.

Declaration of funding: The University of Sheffield and GlaxoSmithKline (agreement number STU100037614) funded this thesis.

ABSTRACT

This thesis is concerned with image processing methods for multi-nuclear magnetic resonance lung images. Specifically, analysis of hyperpolarised gas (^{3}He and ^{129}Xe) and dynamic contrast-enhanced proton images is presented. This work is separated into four distinct themes:

1. A semi-automated method of segmenting ventilation-weighted (hyperpolarised gas) and proton (anatomical) images is presented. This method is shown to improve agreement between observers compared to the current method of manual segmentation.

2. The coefficient of variation is investigated as a marker of ventilation heterogeneity for separating healthy volunteers from patients with a range of obstructive disease. The effect of image signal-to-noise ratio, kernel size and kernel dimensionality on the measures are all investigated, along with the effect of the type of sequence used. Furthermore, the difference in metrics acquired from ^{3}He and ^{129}Xe datasets is assessed.

3. The effect of inflation level on quantitative metrics of lung function and the repeatability of these measures is investigated in healthy volunteers. Additionally, data from a small cohort of patients with asthma and cystic fibrosis, acquired at functional residual capacity plus 1 litre and total lung capacity, are analysed to show the effect of inflation level on metrics in patients. It is shown that lung ventilated volume percentage is highly reproducible in healthy volunteers.

4. An analysis pipeline is developed to investigate ventilation and perfusion matching using a combination of hyperpolarised gas and dynamic contrast-enhanced MRI. This methodology is validated on healthy volunteers and then applied to a small cohort of patients with asthma pre and post administration of a bronchodilator, and a small cohort of patients with chronic obstructive pulmonary disease.

LIST OF ABBRVIATIONS

Abbreviation	Definition
2D	Two-dimensional
3D	Three-dimensional
4D	Four-dimensional
^{1}H	Proton
^{3}He	Helium-3
^{129}Xe	Xenon-129
AIF	Arterial input function
ASL	Arterial Spin Labelling
AUC	Area under the curve
BD	Bronchodilator
BH	Breath hold
BPleth	Body plethysmography
bSSFP	Balanced steady state free precession
CA	Contrast agent
CF	Cystic fibrosis
CNN	Cellular neural network
COPD	Chronic obstructive pulmonary disease
CoV	Coefficient of Variation
CT	Computed tomography
CTEPH	Chronic thromboembolic pulmonary hypertension
CV	Coefficient of variation of signal intensity
CVH	Coefficient of variation of signal intensity histogram
DCE-^{1}H	Dynamic contrast enhanced proton
D_{LCO}	Diffusing capacity of the lungs for carbon monoxide
DSC	Dice similarity coefficient
ERV	Expiratory reserve volume
FA	Flip angle
FB	Free breathing
FCM	Fuzzy c-means
FD	Fourier decomposition
FEV_1	Forced expiratory volume in 1 second

FID	Free induction decay
FOV	Field of view
FRC	Functional residual capacity
FRC+1L	Functional residual capacity plus one litre
FVC	Forced vital capacity
FV	Fractional ventilation
Gd	Gadolinium
GUI	Graphical user interface
HASTE	Half-Fourier Acquisition Single-shot Turbo spin Echo imaging
HA	Healthy adults
HC	Healthy children
HP	Hyperpolarised
HPV	Hypoxic pulmonary vasoconstriciton
HU	Hounsfield units
IC	Inspiratory capacity
ICC	Intraclass correlation
ILD	Interstitial lung disease
IPF	Idiopathic pulmonary fibrosis
IQR	Interquartile range
IRV	Inspiratory reserve volume
LCI	Lung clearance index
LOA	Bland-Altman Limits of agreement
MALF	Multi-atlas label fusion
MBW	Multiple breath washout
MIGET	Multiple inert gas elimination technique
$\boldsymbol{M_0}$	Baseline (equilibrium) magnetisation
MRI	Magnetic resonance imaging
MR	Magnetic resonance
MTT	Mean transit time
MI	Mutual information
NC	Noise corrupted
NMR	Nuclear magnetic resonance
NSCLC	Non-small cell lung carcinoma
$\mathbf{N_{slices}}$	Number of slices

NN	Neural network
N_2	Nitrogen
OE	Oxygen enhanced
PaO_2/PO_2	Partial pressure of oxygen
$PaCO_2$/PCO_2	Partial pressure of carbon dioxide
PBF	Pulmonary blood flow
PBV	Pulmonary blood volume
PE	Pulmonary embolism
PET	Positron emission tomography
PFT	Pulmonary function test
Q	Perfusion
Q_{vol}	Perfused volume
RF	Radio frequency
ROI	Region of interest
R	Pearson/Spearman correlation coefficient
RV	Residual volume
S1/S2	Session 1 or Session 2
S_{acin}	Measure of ventilation heterogeneity in the acinar airway zone
S_{cond}	Measure of ventilation heterogeneity in the conductive airway zone
SD	Standard deviation
SENSE	Sensitivity encoding
SFCM	Spatial Fuzzy c-means
Sh_{vol}	Shunt volume
SNR	Signal to noise ratio
SPGR	Spoiled gradient echo
SPECT	Single photon emission computed tomography
SSFP	Steady state free precession
SV	Specific ventilation
SVD	Singular value decomposition
$\boldsymbol{T_1}$	Spin-lattice relaxation time
$\boldsymbol{T_{1,0}}$	Baseline (equilibrium) spin-lattice relaxation
$\boldsymbol{T_2}$	Spin-spin relaxation time
$\boldsymbol{T_2^*}$	Actual observed spin-spin relaxation time
TE	Echo time

TLC	Total lung capacity
TLV	Total lung volume
T/R	Transmit-Receive
TRICKS	Time resolved imaging of contrast kinetics
TR	Repetition time
TV	Tidal volume
%VV	Lung ventilated volume percentage
VDP	Ventilated defect percentage
V	Ventilation
V/Q	Ventilation-Perfusion ratio
V∩Q	Ventilated and perfused (intersection)
VV	Ventilated volume
V_{vol}	Ventilated volume
WV_{vol}	Wasted ventilation volume

TABLE OF CONTENTS

CHAPTER 5. Assessment of the influence of lung inflation state on the quantitative parameters derived from HP gas lung ventilation MRI 107

CHAPTER 6. Quantitative measurement of the Ventilation-Perfusion ratio using HP gas and DCE-^{1}H lung MRI 144

LIST OF TABLES

LIST OF FIGURES

CHAPTER 1. INTRODUCTION

1.1 Motivation

Respiratory diseases affect a large portion of the world's population [1-4] and affect the lung in different ways through functional impairment. Many of these diseases are progressive (e.g. cystic fibrosis, idiopathic pulmonary fibrosis and cancer) and require longitudinal monitoring to evaluate response to treatment. Pulmonary function tests such as spirometry [5] and multiple breath washout [6, 7] are the clinical standards for analysing lung function, however these methods give only a global overview of the lung as does the gold standard of ventilation and perfusion analysis, the multiple inert gas elimination technique [8]. Clinical imaging to assess these diseases' effect on ventilation and/or perfusion usually makes use of ionizing radiation (nuclear scintigraphy [9-15], computed tomography [16-26] or single photon emission computed tomography [27-32]) and is not desirable for these longitudinal assessments due to the radiation doses. Additionally, early detection and sensitivity to disease is important in a number of conditions, such as cystic fibrosis [33], and any technique developed for assessing the respiratory system needs to have this capability.

Magnetic Resonance Imaging (MRI) is a non-ionizing imaging modality that is able to assess structure [34] and has been used in the clinic to analyse the brain [35] and abdomen [36] for many years. The main attraction is the excellent soft tissue contrast, ability to weight images differently and also for being able to detect the flow of blood or acquire diffusion-weighted images in a single protocol [37-42]. Lung function can also be measured using proton MRI, with the addition of a contrast agent, such as oxygen to generate ventilation images [43-45] or gadolinium-based contrast agents to assess perfusion [46-55].

Lung function can also be assessed by using hyperpolarised gas MRI [56-71, 33] with numerous analysis techniques existing to derive different measures. With improvements in both sequences [72-74] and hardware [75, 76] for imaging with hyperpolarised gases this technique has recently been adopted into the clinic in Sheffield. The common method of analysing these images is by analysing lung ventilation volume percent; the ratio of ventilated volume (from hyperpolarised gas images) to total lung volume (from proton anatomical images) or its counterpart ventilation defect percent. These metrics have previously been used to detect early obstructive changes in the lungs of smokers [77], detect sub-clinical cystic fibrosis [33], compare ventilation acquisitions pre and post treatment in asthmatics [63], assess exercise-induced bronchoconstriction [78] and assess treatment efficiency in cystic fibrosis patients [79]. Respiratory diseases may also affect the pulmonary vasculature leading to decreased perfusion and poor gas exchange [80, 81]. Using Dynamic contrast-enhanced proton MRI the distribution of blood volume and flow may be probed using quantitative modelling [82, 83] adding to the analysis of respiratory disease using MRI.

1.2 Thesis outline

The development and evaluation of image processing techniques for analysis of the lung is the focus of this thesis with the main modalities being anatomical proton imaging, hyperpolarised gas (Helium-3 and Xenon-129) ventilation imaging and dynamic contrast-enhanced proton imaging. This thesis will focus on the application of image registration [84], segmentation and development of novel image processing pipelines. The tools developed are evaluated with lung imaging data from healthy volunteers and patients and are also used to investigate physiological hypotheses.

Chapter 2 introduces an overview of the basics of imaging using magnetic resonance and the underlying principles of nuclear magnetic resonance. A brief description of lung physiology and pulmonary function tests are presented.

Chapter 3 presents the method developed for semi-automated lung ventilated volume percentage analysis during this PhD. The main focus of this chapter is the comparison of the developed method to manual segmentation and also to a well-known K-means method [62].

Chapter 4 investigates the use of the coefficient of variation of ventilation images as a possible biomarker in differentiating ventilation heterogeneity in healthy volunteers from patients. Additionally, markers from the coefficient of variation histograms usefulness in separating health from disease were investigated. Differences between two and three-dimensional analysis are reported as well as differences caused by the kernel size, gas properties of Helium-3 and Xenon-129 and image signal to noise ratio.

Chapter 5 investigates the reproducibility of quantitative metrics of lung function at different inflation levels in healthy volunteers using both Helium-3 and Xenon-129. Additionally, the effect of the inflation level on quantitative regional metrics of lung function is investigated in diseased lungs.

Chapter 6 introduces a method to analyse the ventilation-perfusion ratio using a combination and fusion of hyperpolarised gas and dynamic contrast-enhanced proton MRI. An image-processing pipeline was developed to spatially register all images and allow for a voxel-by-voxel comparison of ventilation and perfusion. Healthy volunteers, patients with asthma and patients with chronic obstructive pulmonary disease were then analysed using this methodology.

CHAPTER 2. BACKGROUND THEORY

2.1 Introduction

This chapter of the thesis provides a basic introduction into the fundamental principles underpinning this work. The basics of lung physiology, with some specific details on the diseases of patients analysed in this work, and pulmonary function tests (PFTs) are presented. A basic overview of nuclear magnetic resonance (NMR) and magnetic resonance imaging (MRI) theory is discussed along with the specific acquisition strategies used in this work for hyperpolarised (HP) gas ventilation and Dynamic contrast enhanced proton (DCE-^{1}H) perfusion MRI. Methods of image registration are also discussed.

2.2 Lung physiology and pulmonary function testing

2.2.1 Lung physiology

The lungs are located in the thoracic cavity. Each lung has its own pleural space and is protected by two pleurae (serous membranes; the parietal pleura, which covers the chest wall and mediastinum and the visceral pleura, which covers the lungs). In between the pleurae is a fluid that allows smooth movement when breathing [85, 86]. Generally the right lung will be larger than the left due to the fact that the heart is on the left side and occupies some of the space that would otherwise be taken up by the lung [86]. The lungs are supplied blood by the pulmonary and bronchial arteries, however it should be noted that gas exchange is only affected by the pulmonary arteries as the bronchial arteries generally do not take part in gas exchange [87, 88].

Figure 2.1a shows how the trachea splits into bronchi, the bronchi into lobar bronchi and so on all the way down to the alveoli. The full respiratory tract can be considered as having two sections, the upper (conductive) and lower (transit and respiratory) section [89]. Figure 2.1b shows the terminal bronchioles (TB, the final section of the non-respiratory zone), 3 generations of respiratory bronchioles (RB, bronchioles connecting TB to alveoli (Alv small air sacs)), a single alveolar duct (AD, small intralobular ducts), atrium (Atr, the end of an alveolar duct) and alveoli [90].

Copyright material – see reference

Figure 2.1 Basic illustrations of airway structure (a) Airway generations (known as Weibels tree) and (b) an illustration of the respiratory zone. Reprinted with permission from [89] http://www.lww.co.uk/respiratory-physiology and (b) reprinted with permission from [90] TB = terminal bronchiole, RB = respiratory bronchiole, Alv = alveoli, AD = alveolar duct and Atr = ending of alveolar duct.

The primary function of the lung is to facilitate gas exchange [89] which, in basic terms, allows oxygen (O_2) from the air to move into the blood whilst carbon dioxide (CO_2) is transferred to the exhaled air [89]. Gas exchange is controlled by the diffusion of the O_2 and CO_2 from an area of high pressure to an area of lower pressure [89]. The lungs' anatomy allows for good gas exchange due to the extremely thin blood-gas barrier [89]. The matching of ventilation (V) and perfusion (Q) in the lungs is essential for good gas exchange in the lung.

In the healthy lung, due to gravitational effects and the vascular and airway tree geometry it is reported that the ventilation-perfusion ratio (V/Q) will be in the range of 0.3-2.0 [81], in the upright position. In a healthy lung, the airways, pulmonary vasculature and membranes allow efficient gas exchange whereas pulmonary diseases will affect the lung in different ways. For example cystic fibrosis (CF) and asthma will increase the airway resistance resulting in obstructed airflow, whilst other diseases may affect the vasculature, reducing perfusion [91] and some diseases may have an effect on both the vasculature and airways, which in turn, means the ability to maintain efficient gas exchange is affected [92-94, 90, 68, 64, 95, 96, 81]. The reason behind this is that gas exchange relies on ventilation and perfusion, and having a ventilation and perfusion that is matched at the alveolar level (ideally V/Q = 1)[97]. Any detrimental change to V or Q therefore causes a mismatch in V/Q.

Figure 2.2 shows the well-known three-compartment model used to represent the lung, describing perfusion shunt (left), a compartment where ventilation and perfusion take place (middle) and a compartment where there is no perfusion but ventilation.

Copyright material – see reference

Figure 2.2 Three-compartment model of perfusion shunt, gas exchange and wasted ventilation. (Reproduced with permission of the European Respiratory Society © Eur Respir J October 2014 44:1023-1041; published ahead of print July 25, 2014, doi:10.1183/09031936.00037014 (dx.doi.org/10.1183/09031936.00037014))

Where: V'_E – minute ventilation; V'_A – alveolar ventilation; Q'_T– total blood flow; Q'_S– blood flow in shunt; V'_D – dead space; $\frac{V'_A}{Q'}$– regional ratio of alveolar ventilation to perfusion

One form of impaired gas exchange can be characterised by perfusion shunt and low V/Q, meaning that there is no ventilation reaching the alveoli but venous admixture is passing through. Low V/Q can lead to hypoxemia, a low arterial oxygen tension (PaO_2<80mmHg) [98], but it must also be noted that diffusion limitation or hypoventilation can also cause hypoxemia [81]. Another form of V/Q mismatch is wasted ventilation or increased dead-space, this is where there is no blood reaching the alveoli but there is fresh gas, one result of this is that minute ventilation, the volume of air passed into the lung per minute, increases causing an increase in the work of breathing [81].

2.2.2 Introduction to lung diseases focused on in this work

Data from patients with a wide variety of diseases were analysed during the course of this PhD and therefore only a basic introduction to each of the lung diseases is given here. The diseases focused on in this work were asthma, chronic obstructive pulmonary disease (COPD), CF and non-small cell lung carcinoma (NSCLC). Asthma is an obstructive airways disease characterized by reversibility of bronchoconstriction following administration of a bronchodilator [99-102] and airway remodelling may take place if asthma is not detected early. COPD on the other hand is characterized by irreversible airflow caused by chronic bronchitis (narrowing of airways due to constant inflammation) and emphysematous elements (permanent airspace enlargement as a result of airway wall destruction leading to loss of elastic recoil and collapse on expiration) of the disease [103, 101]. CF is a genetic disorder that affects numerous organs including the lungs [104-109]. The disease affects how mucus and sweat are produced leading to mucus plugging and inflammation within the lung. Lung cancer is a disease which has numerous causes [110, 111] which result in uncontrolled growth of cells resulting in tumours. The lung cancer patients imaged in this work had non-small cell lung cancer which is usually grouped in to three main types; squamous cell carcinoma, large cell carcinoma and adenocarcinoma [110, 111].

2.2.3 Introduction to pulmonary function tests

A basic introduction of the standard non-imaging methods used in clinic for assessing respiratory disease is presented here. For details of the methods please see the ERS-ATS standards given in [5, 112].

Pulmonary function testing is an important method in assessing pulmonary disease and is the most common non-imaging method of clinical classification of disease [113]. Spirometry is the most common method used in clinic with forced expiratory volume in 1 second (FEV_1), forced vital capacity (FVC) and the ratio of the two (FEV_1/FVC) being the most commonly used measures [113]. By comparing these values to standard normal values, disease severity may be assessed whilst also differentiating obstructive and restrictive diseases based on whether FEV_1 is greater or smaller than FVC. Although spirometry has been used in the clinic for decades its main pitfall is the lack of regional information and the fact that it mainly represents the change in larger airways rather than the small airways, where some changes may occur first in certain diseases. Although the aforementioned values are still considered the gold standard for monitoring patients in clinic the method has been shown to be insensitive to early-stage disease in the lung [114, 115] and also has some insensitivity to disease progression [116, 117]. Body plethysmography is another method in which lung function can be analysed. Participants are placed in an airtight box, with a small leak that stabilizes the internal pressure [118], and a pneumotachograph to record the respiratory flow rate. Two pressure transducers are used, one to measure the pressure within the box and another to measure the pressure at the mouth and it is the changes in pressure, caused by inspiratory/expiratory efforts which the participant carries out following instruction from the attending physiologist, that allow for the calculation of lung volumes and other metrics using this technique [118] (Figure 2.3).

Copyright material – see reference

Figure 2.3 Example normal spirogram demonstrating the lung volume subdivisions. FRC = functional residual capacity, IC = inspiratory capacity, IRV = inspiratory reserve volume, ERV = expiratory reserve volume, TV = tidal volume, RV = residual volume, FVC = forced vital capacity and TLC = total lung capacity. Reprinted by permission from Macmillan Publishers Ltd: Bone marrow Transplantation, (2005) 35, 429–435, © 2005

Measuring lung volumes using inert gases has been used by pulmonary physiologists for many decades and has recently been used to assess ventilation heterogeneity within the lung using the multiple breath washout (MBW) technique [119] by deriving parameters such as the lung clearance index (LCI) [120, 6, 121]. By measuring the gas concentration washout over multiple exhalations and analysing the gas washout curves, LCI has been used successfully in detecting disease in patients [120, 6] (Figure 2.4).

Copyright material – see reference

Figure 2.4 Example result of a multiple breath washout test in a child with cystic fibrosis.(a) and a healthy child (b). The black line represents the flow and the green line is the concentration of the tracer gas. The red and blue lines indicate the section used to calculate LCI and the dotted red line indicates the time point used to determine LCI. Reprinted from The Lancet Journal, Respiratory medicine, 1(2), Hartmut Grasemann and Felix Ratjen, Early lung disease in cystic fibrosis, 148-157, Copyright (2013), with permission from Elsevier

This technique has been shown to be sensitive to early changes in the lung and to disease progression [114, 115, 120, 6, 122, 33]. However, these measures are global values of heterogeneity measured at the mouth and lack the regional information that is useful in assessing lung disease. This technique has the ability to assess the heterogeneity in the conducting and transitional zones of the airways (Figure 2.1) by analysing the phase 3 slope of the data (Figure 2.5).

The expirogram shown in Figure 2.5 is derived from the curve generated by plotting the decay of the gas shown in Figure 2.4. S_{cond} is then calculated by analysing the phase 3 slope of the decay of the tracer gas plotted as a function of lung turnover and this metric represents ventilation misplacement in the conductive respiratory zone. S_{acin} can then be calculated by subtracting S_{cond} multiplied by the lung turnover in the first breath from the normalised slope of the first breath [121, 123].

Copyright material – see reference

Figure 2.5 Basic illustration of expirogram acquired during a multiple breath washout test. To assess the heterogeneity in the conducting and transitional the phase 3 area of the expirogram is used. Reprinted with permission from reference [124] © 2012 the American Physiological Society

The multiple inert gas elimination technique (MIGET) developed by Wagner in the 1970s [8] is another pulmonary function test used in the clinic to assess the lung. This test is used as a way to measure the ventilation-perfusion ratio, shunt, physiological dead space and diffusion limitation. More detail is given in Chapter 6, section 6.1. Another test often used in the clinic when considering pulmonary diseases is one in which the diffusing capacity of the lungs for carbon monoxide (D_{LCO}) is measured. To measure this the participant inhales gas with a small amount of carbon monoxide mixed in, and, following a breath hold, the gas is expired and the difference in partial pressures between inhaled and expired carbon monoxide is used to calculate D_{LCO} [125, 126].

2.3 Nuclear magnetic resonance and magnetic resonance imaging

Nuclear magnetic resonance was first observed in the early 1930s [127, 128] following which Bloch and Purcell [129, 130] quantified the effect of spin precession in a magnetic field. Following the observation of NMR numerous advances were made, including the discovery of the spin-echo phenomenon [131], the application of the Fourier Transform to NMR [132] and utilizing imaging gradients to spatially encode signal and form images, allowing the differentiation of soft tissues [133, 134].

NMR utilizes the interaction of nuclear magnetic moment arising from spin with external magnetic fields, and unlike angular momentum, spin is an intrinsic property of the nuclei being examined. The nuclei have a dipolar magnetic moment ($\vec{\mu}$) associated with their nuclear spin ($\boldsymbol{I}$) and spin angular momentum ($\boldsymbol{S}$) [135, 136] governed by equation 2.1:

$$\vec{\mu} = \gamma \boldsymbol{S} = \gamma \hbar m_s \tag{2.1}$$

Where the gyromagnetic ratio γ is a property of the nuclei (determined by a ratio of energy and mass), ħ is the reduced Planck constant, defined as $h/2\pi$, and m_s is the spin quantum number which has a fixed number of values $(2\boldsymbol{I}+1)$ ranging from $-\boldsymbol{I}$ **to** $+\boldsymbol{I}$. Table 2.1 shows the properties of the nuclei used in this work (proton – ^{1}H, Helium-3 – ^{3}He and Xenon-129 – ^{129}Xe). As can be seen the net spin of these nuclei is non-zero (a requirement for NMR) and is a half-integer value, although other nuclei suitable for NMR may have integer values.

Table 2.1 Properties of nuclei used in this work [137-140, 39, 141]

	^{1}H	**^{129}Xe**	**^{3}He**
Gyromagnetic ratio (γ) (MHz T^{-1})	42.58	11.78	32.43
Magnetic Moment ($\vec{\mu}$)	+2.79	-0.78	-2.13
Larmor Frequency at 1.5T (MHz)	63.9	17.7	48.6
Natural abundance	-	26.4%	<<0.1%
Net spin ($\boldsymbol{I}$)	½	½	½

The interaction between an external magnetic field (B_0) and the nuclear magnetic moment results in the nuclear energy levels being split (the Zeeman splitting effect) [136], according to equation 2.2:

$$E = -\vec{\mu}\boldsymbol{B_0} = -\gamma m_s \hbar \boldsymbol{B_0} \tag{2.2}$$

For a spin-½ nucleus, this results in two energy states; one where the magnetic moment is parallel to the external field (low energy state) and one where it is anti-parallel (high energy state) (Figure 2.6). The energy difference between states is given by equation 2.3:

$$\Delta E = \gamma \hbar |\boldsymbol{B_0}| = \hbar \omega_0 \tag{2.3}$$

Where the Larmor angular frequency ω_0 is given by $\gamma|\boldsymbol{B_0}|$.

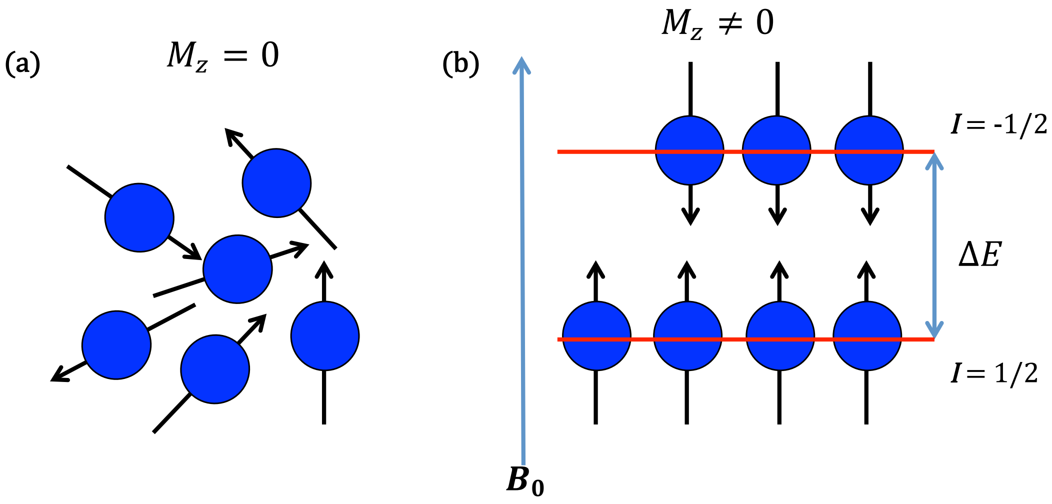

Figure 2.6 Graphical representation of the Zeeman splitting effect. (a) the alignment of nuclei without an external magnetic field and (b) the Zeeman splitting effect and alignment due to an external magnetic field $\boldsymbol{B_0}$

The polarization P is defined by equation 2.4, which represents the ratio of the difference between the number of nuclei on the lower ($N_\uparrow$) and higher ($N_\downarrow$) energy states in a spin-½ system to the total number of nuclei.

$$P = \frac{|N_\uparrow - N_\downarrow|}{N_\uparrow + N_\downarrow} \tag{2.4}$$

Where $N_\uparrow$ (parallel to $\boldsymbol{B_0}$) and $N_\downarrow$ (antiparallel) represent the number of spins per state as defined by the Boltzmann distribution (equation 2.5):

$$\frac{N_\downarrow}{N_\uparrow} = e^{-\frac{\Delta E}{k_b T}} = e^{-\frac{\gamma \hbar \boldsymbol{B_0}}{k_b T}} \tag{2.5}$$

Where k_b is the Boltzmann constant and T is the temperature. Spin excess (SE), defined as the number of spins parallel to the magnetic field exceeding the number anti-parallel, is given by equation 2.6 [139]:

$$SE \approx N \frac{\hbar \omega_0}{2 k_b T} \tag{2.6}$$

where N is the total number of spins in the sample. Therefore, the polarization can then be written as:

$$P_0 \cong \frac{|\gamma| \hbar \boldsymbol{B_0}}{2 k_b T} \tag{2.7}$$

And the magnetization is denoted as (assuming $\boldsymbol{B_0}$ acts along the z axis):

$$M_z = \rho.P.\mu_z \tag{2.8}$$

Or

$$M_0 = \frac{\rho\gamma^2\hbar^2\boldsymbol{B_0}}{4k_bT} \tag{2.9}$$

Where ρ is the spin density and μ_z is the magnetic moment. It should be noted that ρ in the lungs is low (~0.1 g/cm^3)[41] making ^{1}H imaging of the lungs challenging as discussed in section 2.4.

At body temperature the thermal energy is much greater than the energy difference between states caused by $\boldsymbol{B_0}$ [140]. The thermal polarization of a spin system at body temperature and $\boldsymbol{B_0}$ = 1.5T (standard clinical scanner strength) (T = Tesla) is 10^{-5}, due to the small number of excess spin (equation 2.6) however in many structures, e.g. the brain, proton spin density is high which counteracts this small thermal polarization leading to a magnetization (equation 2.7) sufficient for imaging.

In order to detect a magnetic signal one must first tip the magnetization vector (excite) from the axis that the $\boldsymbol{B_0}$ field is applied to in order to initiate precession. This precession produced by the aggregate proton spins causes a changing of flux, which is detected by the receiver coil(s). Excitation is accomplished via application of a radiofrequency (RF) pulse at the nuclear resonance frequency $\boldsymbol{f_0}$ for a set transmission time $\boldsymbol{t}$, which creates a small rotating magnetic field $\boldsymbol{B_1}$, perpendicular to the field $\boldsymbol{B_0}$ resulting in the tilting of the magnetization vector. The magnetization vector is tilted at angle α (equation 2.10), the flip angle, from its alignment with the $\boldsymbol{B_0}$ field into the transverse (x, y) plane.

$$\alpha = \int_0^{\boldsymbol{t}} \gamma\boldsymbol{B_1}\,(\boldsymbol{t}).dt \tag{2.10}$$

This tipping results in what is commonly referred to as transverse magnetization (M_{xy}) (equation 2.11) and this is the magnetization (signal) detected during NMR experiments:

$$M_{xy} = \boldsymbol{M_0}\sin{(\alpha)} \tag{2.1§}$$

Where $\boldsymbol{M_0}$ is the equilibrium magnetization.

Figure 2.7 is a simple graphical representation of the excitation process where a magnetization vector is at equilibrium (a) and the same system after excitation at the Larmor frequency (b).

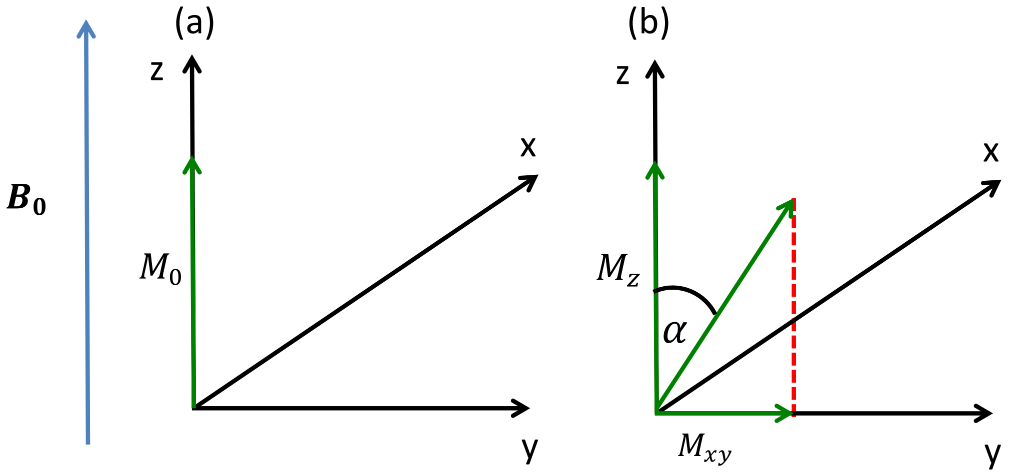

Figure 2.7 Simple graphical representation of RF excitation in the rotating frame of reference. (a) magnetisation vector at equilibrium, (b) magnetisation vector after application of RF pulse with flip angle α resulting in a reduced M_z and transverse magnetisation M_{xy}

As the magnetisation vector tips away from the z-axis it also precesses around the axis, which in the presence of a receiver coil tuned to the Larmor frequency, and with its area perpendicular to the transverse plane, induces an electrical current due to the variation of the transverse magnetization. This is the signal that is amplified and then detected in the NMR experiment and this phenomenon is known as free induction decay (FID) [139, 40].

Once the RF excitation pulse is stopped the magnetization vector will begin to tip back towards the z-axis whilst re-emitting the energy absorbed during the RF pulse as signal and via relaxation. This relaxation can be split into two different mechanisms: the longitudinal (also known as spin-lattice) relaxation of the M_z component and transverse (also known as spin-spin) relaxation of the M_{xy} component. Longitudinal decay time constant is denoted T_1 whilst transverse relaxation decay constant is denoted T_2. Longitudinal magnetization will recover according to equation 2.12 and transverse magnetization will decay according to equation 2.13 [139, 40]:

$$M_z(\boldsymbol{t}) = M_0\left(1 - e^{-t/T_1}\right) + M_z(\boldsymbol{0}) \cdot e^{-t/T_1} \tag{2.12}$$

$$M_{xy}(\boldsymbol{t}) = M_{xy}(\boldsymbol{0})\left(e^{-t/T_2}\right) \tag{2.13}$$

T_1 is the mechanism by which signal is lost to the surrounding molecular environment/lattice and T_2 is the mechanism by which the signal is broadened, and more specifically is caused by the loss of phase coherence between spins. Additionally, magnetic field inhomogeneity will cause dephasing and the combination of the effect of field inhomogeneity and T_2 decay is denoted T_2^* in MRI [139, 40]. T_2^* of the lung is very short (<2ms) [142, 143, 41] and combined with the low ρ makes ^{1}H imaging of the lung even more difficult.

To be able to create images from the signal generated due to these phenomena spatial information must be encoded. Spatial encoding is accomplished via gradient magnets $G(x, y, z)$ that vary linearly in strength with position in the directions (x, y, z). By superimposing the field from G with the external magnetic field $\boldsymbol{B_0}$ a modulation of the Larmor resonant frequency occurs as a function of the position within the field [139, 40].

By switching on a gradient for a time T the spins accumulate phase, dependent on the position along the static gradient field, and this signal is then related to the spatial frequency (k) by equation 2.14 [139, 40]:

$$s(k) = \int \rho(r) \cdot e^{-i \cdot 2\pi \cdot k \cdot r} dr \tag{2.14}$$

Where k is defined as $\frac{\gamma}{2\pi} \int_0^T G(t) \cdot dt$. What this means is that k varies as a function of the amount of time the gradient is applied, and that using these gradients, sampling of the spatial frequency domain (k-space) is possible. k-space is the inverse Fourier transform of the image domain. The central locations of k-space (low frequency components) denote contrast and brightness of the image and the edges of k-space (high spatial frequency components) denote the details such as edges of the object being imaged. For 2D sequences a specific slice selection gradient is applied to only excite a specified area within the imaging sample, whereas for 3D images the whole sample is excited [139].

As can be seen from the definitions of k-space and NMR signal these are continuous functions, however they are discretely sampled during the digital acquisition process with the sampling period Δk. To avoid aliasing the sampling frequency must be at least twice the maximum frequency of the object being imaged based on the Nyquist theorem (i.e. the field of view must be larger than the object being imaged). Image contrast can be manipulated by changing the flip angle, echo time (TE) and repetition time (TR). The ideal signal equation from a steady-state gradient echo experiment is defined by equation 2.15:

$$\boldsymbol{s_{SPGR}} = M_0 \frac{\left(1 - e^{-TR/T_1}\right) \cdot \sin(\alpha)}{\left(1 - \cos(\alpha) \cdot e^{-TR/T_1}\right)} \cdot e^{-TE/T_2^*} \tag{2.15}$$

Where TR is defined as the repetition time between two RF pulses (middle of pulse is used as the measurement point) and TE is the echo time (the time from the middle of the RF pulse to the acquisition of the centre of k-space). In most cases the e^{-TE/T_2^*} component is ignored due to negligible effects on the signal [144], however this effect is not negligible when imaging the lung because the T_2^* of ^{1}H in the lung is short (<2ms at 1.5T [142, 145]) due to large susceptibility gradients. SSFP sequences differ from SPGR by recycling magnetisation through balancing gradients along all three axes leading to improved signal to noise ratio (SNR) over SPGR sequences [146].

These two pulse sequences form the basis of the MRI methods used in this thesis. Figure 2.8a shows an example of SPGR (a(i)) and SSFP (a(ii)) hyperpolarised ^{3}He ventilation images acquired from a healthy adult.

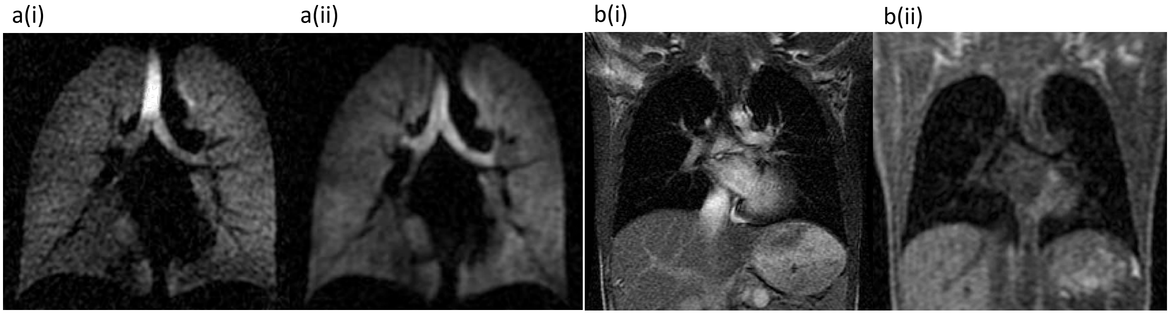

Figure 2.8 (a) Example HP ^{3}He ventilation slices from a healthy adults' dataset and (b) example ^{1}H slices from a patient with early stage cystic fibrosis datasets. a(i) SPGR, a(ii) SSFP, b(i) SSFP and b(ii) SPGR

As can be seen the SNR is improved using the SSFP sequence compared to the SPGR sequence. Note that the HP gas images were acquired with the same dose of ^{3}He (150ml) and the SPGR acquisition is 2D whilst the SSFP is 3D. Figure 2.8b shows an example slice from an SSFP (b(i)) and SPGR (b(ii)) ^{1}H structural acquisition from a patient with early stage cystic fibrosis. As can be seen in Figure 2.8b the vessels appear less bright in the SPGR image compared to the SSFP image due to the different image contrasts between the two sequences. In addition to these factors spatial resolution also has an effect on the SNR, where decreasing the voxel size, by modification of the acquisition matrix and field of view, results in decreased SNR, due to less signals per pixel being received, and increasing the spatial resolution will result in improved image SNR.

2.4 Lung imaging methods

This section of the thesis discusses the clinical gold standard for lung imaging, computed tomography (CT), before moving on to the focus of this thesis, lung imaging using MRI.

2.4.1 Computed tomography

CT has been used in the clinic for decades and has been used to detect emphysema [147-149], scoring and diagnoses of idiopathic pulmonary fibrosis (IPF) [150], scoring and diagnoses of CF [151] and detection of pulmonary nodules [152]. With the high resolution achievable with CT (in some cases <1mm isotropic resolution) it is possible to determine tissue, air and blood volumes [153]. A threshold usually defines emphysema, in most cases any voxels less than -950 Hounsfield units (HU) is used in addition to visual scoring of the percentage of lung parenchyma affected by emphysema [154, 155]. These low attenuation areas are caused by the destruction of the tissue allowing for the photons produced by the CT scanner to pass freely through that area in contrast to the absorption of the photon in normal areas.

IPF is usually characterised on CT by assessing the presence of reticulation, honeycombing and traction bronchiectasis (Figure 2.9a), although there are sometimes other issues seen on these high resolution scans [156]. Patients with CF scans usually contain a degree of mucus plugging, bronchiectasis, consolidation and bronchial wall thickening [157]. Figure 2.9b shows an example CT scan from a patient with CF where the white circle highlights airway obstruction (tree-in-bud phenomena), the white arrow shows bronchial wall thickening and the dashed white circle shows an area of bronchiectasis.

Copyright material – see references

Figure 2.9 Example CT images showing the high resolution capability and structural abnormalities in (a) a patient with IPF and (b) a patient with CF. (a) reproduced with permission from [158] and (b) reproduced with permission from [157]

Functional imaging has also been carried out with CT, specifically focusing on ventilation and perfusion measurements obtained using numerous methods [17, 21, 159, 160, 24, 31]. Ventilation can be assessed using non-contrast CT methods such as those developed by Guererro et al. and Castillo et al. [17, 18, 22]. The idea behind these methods is that high-resolution images are acquired at either fixed points in the respiratory cycle, most commonly inspiration and expiration, or during free-breathing using 4DCT. One image is then selected as the target image to which all other images are registered using a non-rigid registration method. Finally, a metric representing ventilation is calculated using either change based on volume or HU in the voxels [17, 18, 22, 161]. Figure 2.10 shows an example inspiration (a) and expiration (b) CT image whilst Figure 2.10c shows the resulting ventilation metric map generated using the HU method overlaid on the inspiration CT image.

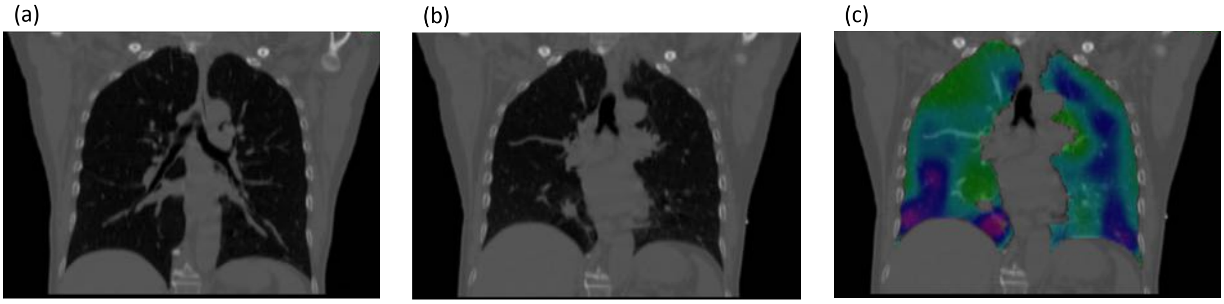

Figure 2.10 Example of CT images used to generate ventilation metrics. (a) inspiration image, (b) expiration image and (c) ventilation metric map overlaid on the inspiration image. Courtesy of Dr Bilal Tahir

The standard imaging method for assessing V and Q in the clinic is single photon emission computed tomography (SPECT) [27, 28, 162] or nuclear scintigraphy [9-15] as previously mentioned in chapter 1. These methods are generally low resolution, as shown in the SPECT example given in Figure 2.11, but provide clear information on defects.

Copyright material – see reference

Figure 2.11 Example V, Q and V/Q quotient images from a SPECT image. Modified with permission from [162]. (a) ventilation images, (b) perfusion images and (c) ventilation/perfusion images

Additionally, perfusion may be assessed using iodine CT, either by using dual-energy CT [163-165] or by acquiring a data set pre and post contrast and using a subtraction technique to generate maps of iodine concentration [166].

The main limitation of CT, SPECT and nuclear scintigraphy methods is the ionising radiation dose, however the international standards on analysing CT images and how to acquire them is an advantage which allows for more reproducible results than those obtained with MRI. CT also has the advantage of increased spatial resolution over MRI allowing for the assessment of smaller lung nodules for instance. MRI may have improved soft tissue contrast over CT, however both methods are susceptible to motion artifact.

Although this is not a comprehensive review of the analyses possible with CT, it is important to note that both structure and function can be analysed using CT, with CT being considered the gold standard for structural imaging.

2.4.2 Proton (^{1}H) imaging

As discussed in section 2.3 the proton spin density of the lung is low (0.1-0.2 g/cm^3) and there are additional issues such as tissue-air interfaces causing field inhomogeneity that make imaging of the lungs challenging [167, 41]. These interfaces between tissues with different magnetic susceptibility cause local field gradients [168] and main field inhomogeneity over the lung. Due to this magnetic field inhomogeneity, the MR signal of the lung is dephased and therefore the lung has extremely short T_2^* [169, 168, 142] meaning that unless sequences with short echo time (TE) are used most of the signal will not be seen as it will have already decayed.

Standard anatomical proton MRI results in images where the lung appears dark with vessels and most pathology, such as fibrosis, mucus, atelectasis and bronchiectasis appearing brighter (Figure 2.12). Three basic sequences are typically used for proton lung imaging; SPGR, SSFP and single-shot fast spin echo (HASTE), which all have short TEs and short acquisition times [170, 171, 41]. Ultra-short echo time (UTE) [172] imaging allows the signal to be acquired before it has decayed substantially due to T_2^* effects and shows great promise for anatomical lung imaging, but is challenging to implement and requires longer acquisition times for full lung coverage [173].

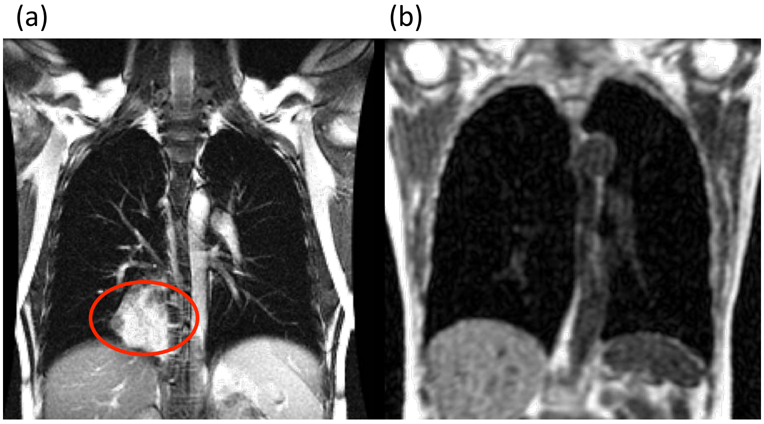

Figure 2.12 Different examples of ^{1}H images from patients (a) CF patient anatomical image (bSSFP) with a collapsed lower lobe (circled) acquired using an 8-channel cardiac coil and (b) SPGR image from an asthmatic patient acquired using the system body coil

Although proton MRI cannot match the spatial resolution of CT, MR images have been used previously to detect structural changes within the lung in patients with CF, emphysema and interstitial lung disease (ILD) [174-178, 33]. Recent advances with time resolved ^{1}H techniques e.g. Fourier decomposition (FD) imaging [179-185], have allowed for functional ^{1}H imaging of the lung with no contrast agent required. Briefly, a set of balanced steady-state free precession images are acquired during free-breathing and analysed via signal separation to distinguish changes in intensity caused by respiration and the cardiac cycle [179-181, 185] and produce ventilation and perfusion weighted images. Associated methods have been developed including those proposed by Voskrebenzev et al. [186, 187] that make use of frequency-based filtering in the image analysis step and are modifications of the standard FD method.

Arterial spin labelling (ASL) is another proton based imaging modality used in pulmonary MRI to measure perfusion with application in both pulmonary [188-191] and brain [192] MRI. Unlike contrast-enhanced techniques ASL ‘labels’ the inflowing arterial blood using a specialized preparatory RF pulse following which ‘labelled’ images are acquired. Control images without the magnetic labelling pulse are also acquired. During post-processing these control and labelled images are subtracted to remove background noise and produce an image proportional to the amount of arterial blood delivered to each voxel.

Another proton-based imaging method used to assess function in the lung is oxygen-enhanced MRI (OE-MRI) [193-195, 43, 196-198]. This method makes use of the fact that the T_1 of the blood, plasma and lung tissue will decrease with inhalation of 100% pure oxygen, leading to a signal enhancement allowing for ventilation, perfusion and even partial pressure of oxygen measurements to be made with this technique [193-195, 43, 196, 41, 197, 198].

2.4.3 Dynamic contrast enhanced ^{1}H perfusion imaging

As mentioned in section 2.4.1 ^{1}H imaging of the lungs is challenging and contrast agents can be used to add functional information. In this work a paramagnetic Gadolinium (Gd) based agent was used as a contrast agent (CA) in order to assess pulmonary perfusion using dynamic contrast enhanced ^{1}H MRI [199-201, 191, 202-206, 68, 53, 207, 198, 208, 209] (DCE^{1}H-MRI). The dosage used in this work was 0.05ml/kg body weight, injected at a rate of 4ml/s with a 20ml saline flush. Using this dose of CA should result in a change in relaxivity of around 5.7 L mmol^{-1} s^{-1} [210]. DCE^{1}H-MRI has been shown to be able to detect pulmonary embolism (PE) [56, 211, 10] and altered perfusion in COPD [191]. Gd based contrast agents reduce the T_1 of the tissue hence increasing the signal observed (equation 2.16) [212]:

$$\frac{1}{T_1(t)} = \frac{1}{T_{1,0}} + r_1[\mathrm{CA}](\mathrm{t}) \tag{2.16}$$

Where $T_{1,0}$ is the baseline longitudinal relaxation time measured prior to CA administration, $T_1(t)$ is the longitudinal relaxation time at time t in the dynamic acquisition and r_1 is the longitudinal relaxivity of the CA and $[\mathrm{CA}](\mathrm{t})$ is the contrast agent concentration at time t. The signal intensity observed in a voxel of a T_1-weighted image therefore will be proportional to the amount of CA in that area (e.g. Gd mixed with blood for pulmonary perfusion imaging) [212] and the process of quantifying this as a concentration is discussed later in chapter 6.

To image lung perfusion a DCE^{1}H-MRI acquisition is often used where a number of image acquisitions (full lung volume) are acquired equispaced over time (usually ~25s). During DCE^{1}H-MRI the contrast agent is administered as a bolus, whilst the patient holds their breath or breathes freely [213, 144, 203, 207, 206], and the first pass of the contrast agent through the lungs is monitored using a suitable fast gradient echo imaging sequence. Figure 2.13 is a simple representation of the acquisition, where at each time point a volumetric dataset is acquired.

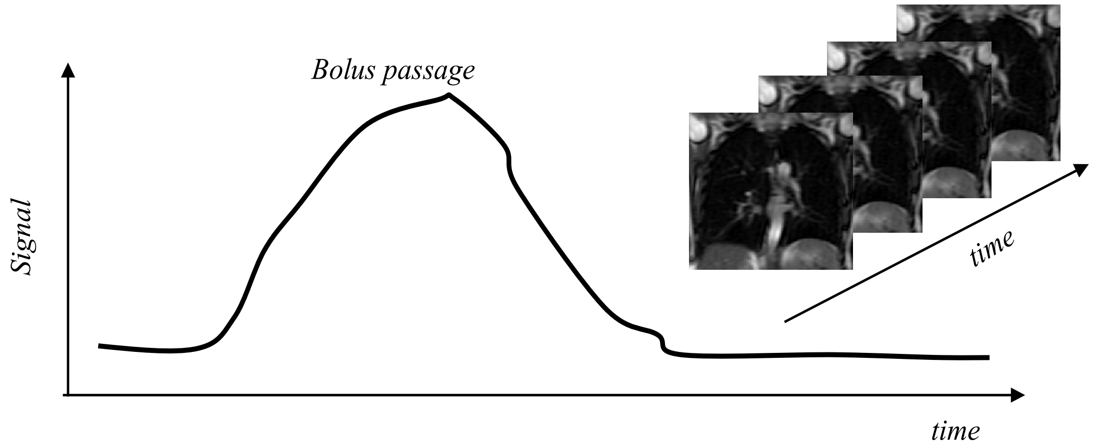

Figure 2.13 Basic illustration of a bolus passage of contrast agent in a single voxel and the image acquisition over time

Parallel imaging [214, 215] and other image acceleration techniques such as TRICKS (Time Resolved Imaging of Contrast KineticS) [216] are used in most cases as they provide high temporal resolution. As the sequences used usually employ parallel imaging, the SNR is affected not only by the regular contributors of noise in MRI but also by the acceleration and geometry factors [214]. Regular image denoising techniques will not provide satisfactory results as many assume non-spatially varying noise. Images acquired using parallel techniques have spatially varying noise [217] and therefore require specialized denoising techniques.

An important factor to consider is that the level of inspiration will affect the perfusion of the lung [199], this is one reason why free-breathing (FB) DCE^{1}H-MRI has recently been gaining more interest over the conventional breath-hold (BH) DCE^{1}H-MRI. Another reason is patient compliance, which should be improved with FB DCE^{1}H-MRI. A further consideration is the analysis of FB DCE^{1}H-MRI, as the current studies have not corrected for breathing-related motion by registration, which would be a challenging post processing step due to the signal changes caused by vessel movement through voxels during the breathing cycle [203, 206].

Perfusion is the extent to which blood travels through the capillaries which surround the alveoli [81] and Tracer-Kinetic theory is a method of quantifying the data acquired from DCE^{1}H-MRI to obtain the primary hemodynamic parameters of pulmonary blood flow (PBF), pulmonary blood volume (PBV) and mean transit time (MTT). Qualitative assessment is also possible using metrics such as time to peak signal, area under the curve and relative signal enhancement [37, 207, 218, 219]. Figure 2.14 shows an example slice from a 4D perfusion dataset (a) with corresponding signal-time curves from the pulmonary artery (b) and the lung parenchyma (c). As can be seen the signal intensity in the pulmonary artery is higher than the parenchyma, a factor of 10 in this instance. The signal-time curve from the pulmonary artery is referred to as the arterial input function and used to quantify pulmonary perfusion (discussed in detail in chapter 6, section 6.2).

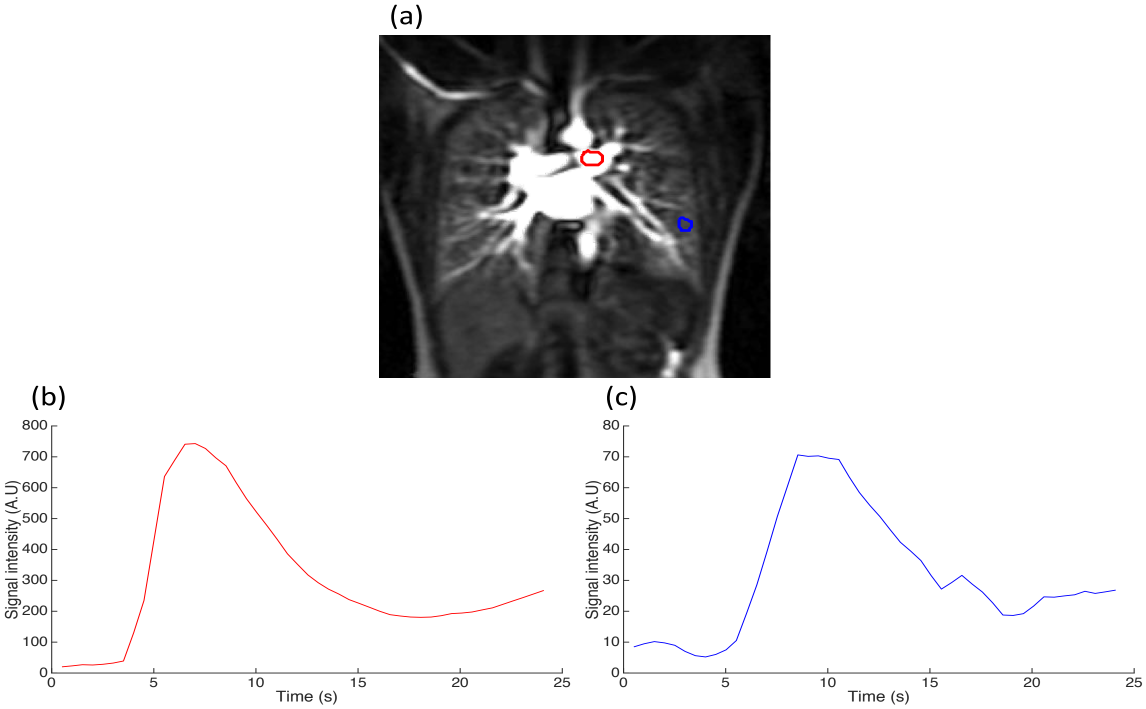

Figure 2.14 Example slice and signal time course plots. (a) slice from a 4D perfusion data set showing the region of interest for the pulmonary artery (red) and parenchyma (blue), (b) the arterial signal-time curve and (c) the parenchyma signal-time curve

2.4.4 Hyperpolarised gas imaging

Through the use of inhaled hyperpolarised (HP) noble gases, in this work Helium-3 (^{3}He) and Xenon-129 (^{129}Xe), functional imaging of the lung has been shown to be possible [220, 77, 221]. In addition to breath-hold ventilation-weighted imaging numerous other methods have been developed to assess lung function including diffusion-weighted imaging using both ^{3}He and ^{129}Xe [222, 223, 50, 224, 225] to assess the microstructure of the lung, multiple breath washout and dynamic imaging to assess fractional ventilation and the flow of gas within the lung respectively [37, 226-228, 67, 69, 70] and partial pressure of oxygen imaging [229-231] to regionally assess the partial pressure of oxygen in the lungs. Additionally, ^{129}Xe imaging methods have been developed to estimate pulmonary gas exchange and also to calculate ratios of tissue blood and plasma to red blood cells [232-236, 80, 237-242], where Figure 2.15 shows diagrammatically the type of exchange during this imaging.

Copyright material – see reference

Figure 2.15 Diagrammatic illustration of xenon solubility in tissue. Reproduced with permission from reference Mugler and Altes Copyright © 2013 by John Wiley Sons, Inc. Reprinted by permission of John Wiley & Sons, Inc.

In order to provide suitable polarisation (signal) for imaging, these gases are first hyperpolarised to increase the nuclear polarization up to 5 orders of magnitude and are inhaled acting as a gaseous contrast agent allowing the ventilated airspaces of the lung to be visualised. Details of the spin exchange optical pumping method used to polarize the gases in this work are not given here but can be found in references [243, 244, 76, 245]. In Sheffield commercial polarizers are used to hyperpolarize ^{3}He (MITI, Durham, NC, USA and GE Healthcare, Amersham, UK) and a home-built polarizer is used for ^{129}Xe [246] and were used in the projects presented here. For all imaging gases are collected in a Tedlar bag (Jensen Inert Products, Coral Springs, FL, USA) and mixed with N_2 prior to inhalation by subjects.

Figure 2.16 shows the homebuilt ^{129}Xe polarizer (a), a Tedlar bag used to collect and administer gas (b), an RF coil for HP gas imaging (c) and the 1.5T scanner used for this work (d).

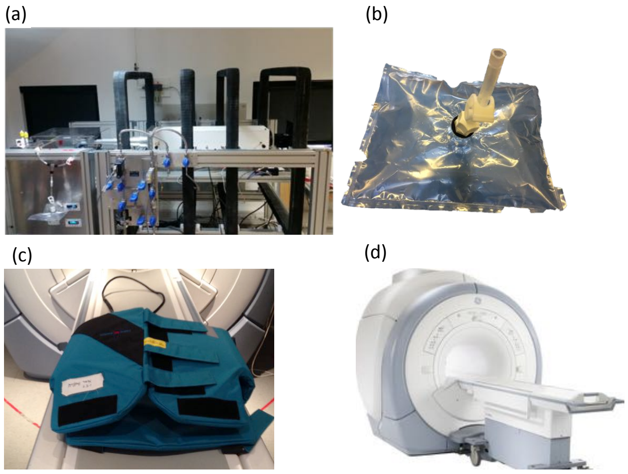

Figure 2.16 Example of the equipment used in this work. (a) Home-built ^{129}Xe polariser, (b) a Tedlar bag, (c) ^{3}He RF coil tuned to 48.67 MHz and (d) 1.5T scanner

When imaging with HP gases it is important to remember the differences between HP gas and ^{1}H imaging. One key point is that once a gas is hyperpolarised the magnetization will begin to decay due to the spins relaxing to thermal equilibrium [245]. Furthermore RF pulses destroy magnetization and in contrast to ^{1}H imaging this magnetization is not recoverable [247]. The decay means that the acquisition order of k-space affects the image appearance [248].The level of hyperpolarization achieved will affect the signal strength [140], as will the amount of gas inhaled into the lungs, whereas with ^{1}H imaging signal strength is controlled by the external magnetic field [140]. Calibration of the flip angle must also be considered and this should be calculated for the coil and loading being used, as any miscalculation will cause a reduction in SNR. Specific receiver coils tuned to the Larmor frequency of the gas of interest and a broadband RF amplifier are also required and in Sheffield there are coils available for adults and children tuned to the resonant frequencies of both ^{3}He and ^{129}Xe.

This work focuses on breath-hold ventilation-weighted images where the signal intensity is proportional to the HP gas volume within the voxel, but the effects of T_1 and T_2^* decay also contribute to the ventilation-weighted image signal intensity as well as the coil sensitivity. It is possible to acquire 2D or 3D images and these images are most commonly acquired using SPGR or bSSFP sequences. One drawback of 3D sequences is that any motion will affect all slices acquired, and cardiac motion is more likely to cause some artifact in the image, although 3D sequences do provide higher SNR than 2D sequences [220]. bSSFP sequences differ from SPGR sequences by recycling magnetisation through balancing gradients along all three axes leading to improved signal to noise ratio (SNR) over SPGR sequences [146]. The signal decay of an SPGR sequence, with a constant flip angle and TR<<T_1, can be defined by equation 2.17:

$$M_{xy}(n) = M_0 \sin(\alpha) \cos^{n-1}(\alpha) \tag{2.17}$$

Where n is the RF pulse number and α is the RF excitation flip angle. Figure 2.17 shows an example 2D SPGR image and a 3D bSSFP image from the same CF patient, where the cardiac motion artifact is circled. Even with the smaller voxel volume (~12.2mm^{3}) and ^{3}He gas dose (100ml) of the bSSFP images compared to the SPGR image (~15.6mm^{3}, 200ml) the SNR advantage of the 3D bSSFP sequence over the 2D SPGR sequence is evident.

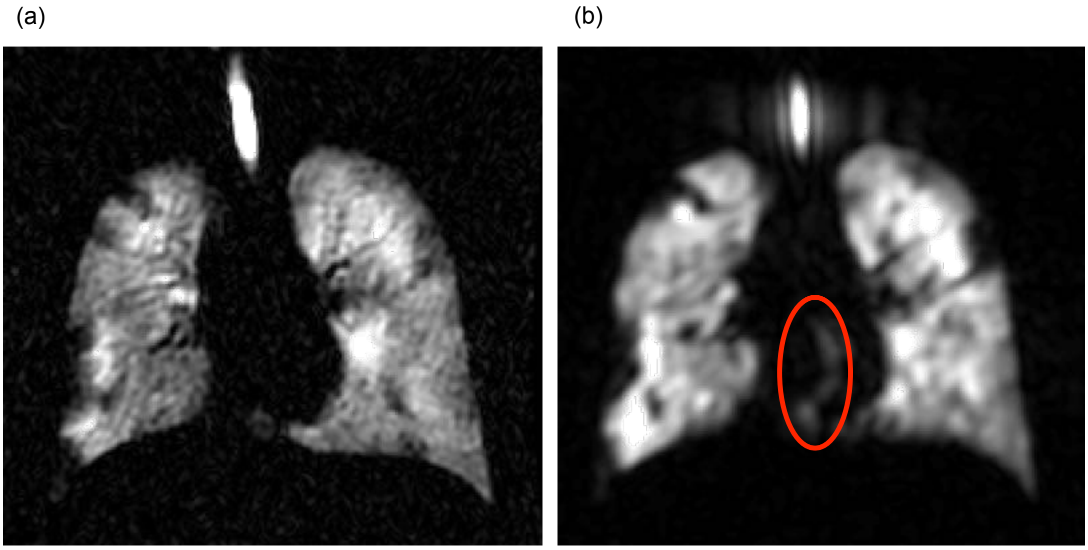

Figure 2.17 Example ventilation images from a patient with CF. (a) a 2D SPGR image (200ml HP ^{3}He, voxel size=1.25x1.25x10mm) and (b) a 3D bSSFP image (100ml HP ^{3}He, voxel size=1.56x1.56x5mm) with the red circle marking an area of cardiac motion artifact. Note that the FOV for the SPGR image was 32cm and the FOV for the bSSFP image was 40cm

2.5 Image registration

Image registration is well established in the medical imaging community with numerous reviews having taken place [249-252] for example. Image registration is used throughout this thesis to register images acquired using the same modality and to co-register images acquired using different modalities. Registration of lung MR images is difficult due to the fact that the lung is a large deformable organ. Further there are fewer features compared to other anatomical structures where registration is used, for example the brain. Furthermore, images with large contrast differences can be extremely difficult to register particularly when using intensity-based metrics.

One use of image registration in the lung MR community to date is for lung ventilation volume percent (%VV) calculation where ^{1}H anatomical images are registered to HP gas ventilation-weighted images. The registration technique used in [62] relied on landmark registration which was dependent on user selection of landmarks, although this is a proven method it introduces user-bias and can be time-consuming depending on the resolution of the images acquired. A more elegant solution would be to obtain ^{3}He and ^{1}H images in the same breath-hold [73] or to apply a registration algorithm based purely on similarity metrics or segmented images, rather than using landmarks, such as that used in [253-255, 66, 256, 257]. Horn et al. [66] compared same-breath %VV to registered separate breath %VV and found that these matched reasonably well, although the registration of ^{3}He and ^{1}H images is still a difficult process and using same-breath data is still the best option.

There are numerous ways in which to describe image registration, however this literature review will be concerned only with the transformation types as listed in [249]:

1 – Rigid
2 – Affine
3 – Projective
4 – Curved (also known as non-rigid and **deformable**)

Where a **rigid** transformation is only capable of rotation and translation of the image [252], an affine transformation is able to rotate, translate, scale and shear. This means that when registering a 3D image using a rigid transformation the model will be described by 3 rotations and 3 translations and can be described by a transformation matrix consisting of 3 parameters representing the rotations and a further 3 representing the translations. **Affine** transformations make use of all 9 parameters in the transformation matrix to carry out the operations mentioned previously whilst also maintaining the overall geometric relationships between points.

Projective transformations will map any lines onto lines and curved transformations will map lines to curves [249]. **Deformable** image registration is an important technique for medical image registration as it is able to conserve topology and provides plausible solutions to the problems of multiple acquisitions over time or multiple modality acquisitions that would need registration [258, 259]. Deformable image registration can be carried out using a number of transformations [249, 260-265, 258, 259, 252], however the method used in this work was the Greedy Symmetric Normalisation algorithm (SyN) provided as part of the ANTs registration suite [84, 266] as this method was the best performing in the EMPIRE10 CT challenge [267]. The main aspect of the deformable registration method is that it makes use of a specific type of transformation known as a diffeomorphic transform [268, 266, 259], the mathematics of which are beyond the scope of this thesis. Briefly a dense transformation field (per voxel in the image) is calculated using the desired transformation and similarity metrics and the transformation to map one point to another point is calculated and constrained so that it is invertible [269, 84, 266, 259].

Projective registration is not commonly seen in the medical imaging community with many papers using **rigid, affine, deformable** or some combination of these three methods, with many publications using either elastix [270, 271] or ANTs [84, 266] due to the possibility of applying any combination of rigid, affine and deformable registrations with the use of a single bash script. Rigid transformations are mainly used in the presence of rigid structures [272] or as the initial registration method prior to applying the more complex affine or deformable transformations [273].

When registering two images, one image will be the reference image (or fixed image) to which the target image (or moving image) will be warped. The software from [84] is based on the well-known Insight tool kit [274] which uses intensity-based registration and has options for different optimisation strategies including mutual information (MI) and normalised cross correlation (NCC). That is a geometric transformation, to be applied to the moving image, will be found which will maximise the similarity measure based on the voxel intensity [252], and more generally will attempt to minimise/maximise an energy of the form shown in equation 2.18 [258] depending on the matching method chosen.

$$\mathcal{E}(\mathcal{F}, \mathcal{M} \circ \mathcal{W}) + \mathcal{R}(\mathcal{W}) \tag{2.18}$$

Where the images are defined in the image domain Ω and: $\mathcal{E}$ is the matching of the alignment of images; $\mathcal{F}$ is the target image; $\mathcal{M}$ is the moving image; $\mathcal{W}$ is the transformation; $\mathcal{R}$ is the regularisation term; $\mathcal{M} \circ \mathcal{W}$ is applying the transform $\mathcal{W}$ to $\mathcal{M}$. The alignment is governed by the transformation term $\mathcal{W}$, and this transformation is a mapping in the image domain. The mapping of points x is determined by the addition of an identity transformation and the displacement u and is in the general form of equation 2.19 [258].

$$\mathcal{W}(x) = x + u(x) \tag{2.19}$$

The regularisation term will favour particular features depending on which type of regularisation is used. Image registration in the medical image community is still an interesting area of research and numerous algorithms and methodologies exist [249, 260-263, 275, 250, 276, 255, 270, 266, 265, 258] to list but a few, and typically vary with the anatomical structures involved.

CHAPTER 3. DEVELOPMENT OF AN IMAGE PROCESSING PIPELINE FOR HP GAS AND ^{1}H LUNG VENTILATION ANALYSIS[1]

3.1 Introduction

Previously quantitative indices of lung function have been obtained from hyperpolarised (HP) gas ventilation-weighted and proton anatomical (^{1}H) lung MRI that detect early obstructive changes in the lung [277]. The common method of analysing these images is by calculating lung ventilation volume percent (%VV) the ratio of ventilated volume (VV - from hyperpolarised gas images) to total lung volume (TLV - from proton anatomical images) or its counterpart ventilation defect percent (VDP – defined as 100-%VV). The index focused on here was %VV, however the methods can equally be used to generate VDP.

Manual segmentation has been commonly used to obtain the values of VV and TLV [277], however this can take over one hour depending on the image resolution and number of slices. Analysis of HP gas ventilation images is less challenging than the analysis of anatomical images in part due to the clearer contrast of HP gas images lending themselves to segmentation techniques. With the low proton density of the lung, partial volume effects and motion artifacts from the heart [73, 278] segmentation of the lung cavity is a challenging aspect of ^{1}H image segmentation.

The next sections of this chapter present an introduction to some related methods for lung MRI segmentation with a discussion of advantages and disadvantages that led to the motivation for this work.

3.1.1 ^{1}H image segmentation

The most basic method of segmenting ^{1}H images is manual outlining of the lung [277]. However, this method is very dependent on the experience and interpretation of images of the user. Additionally, with the advances made in 3D imaging of the lung [34, 66, 221] a data set

---

[1] This chapter is based on an article published in the Journal of Magnetic Resonance Imaging: Spatial fuzzy c-means thresholding for semiautomated calculation of percentage lung ventilated volume from hyperpolarised gas and 1 H MRI.
Hughes PJC[1], Horn FC[1], Collier GJ[1], Biancardi A[1,2], Marshall H[1], Wild JM[1,2];JMRI, 2017; doi:10.1002/jmri.25804

can consist of 40+ slices meaning manual outlining of the lung would take a considerable amount of time that is not acceptable in the clinic.

Kirby and Imelinska proposed well-developed workflows [167, 62] for the segmentation of lung MR images. The semi-automatic method proposed by Kirby et al. [62] automates the segmentation of the lung shape from ^{1}H anatomical images by using a low-pass Gaussian filter to pre-process the ^{1}H anatomical image and then applying a region-growing algorithm. This filtering reduces the chance of the region-growing algorithm leaking into areas of similar contrast [62]. One drawback of this method is the fact that finer detail is lost and that TLV may be underestimated due to the heavy Gaussian filtering of the images leading to the edge bleeding into the lung cavity. Region growing is commonly used in lung MR image segmentation [279, 62] as it is fairly straightforward to implement.

Other methods have been suggested to segment ^{1}H images including using active contours within a closed homogeneous region [279]. Although the results look promising in the publication, this method may not work well on all images. The main reason being some regions within the lung may be homogeneous while others may not and this will provide a poor segmentation, possibly including only certain parts of the total lung. Furthermore the active contours method implemented in [279] is limited to operating in a two-dimensional space, meaning that each slice of a data set must be processed individually. Applying active contours has also been used in other implementations including that of Tavares et al. [280], where they applied a modified Hough transform to identify a point cloud within the lung, which was then transformed to a contour via gravitational vector fields and Greedy contour creation [280]. One important consideration when reviewing that work was that the aim was not to evaluate the lung volume but to identify respiratory patterns from temporal acquisitions.

Recent work by Tustison et al. [281] modified the multi-atlas label fusion (MALF) algorithm described in [282] by adding to the optimization. This was achieved by considering the error of the consensus voting between atlases and not only between the atlases and target image [281], resulting in lower correlative atlas error and improved segmentations. The atlas-based method described here used a large pool of data with patients at different inflation levels and a mix of healthy and diseased patients. This mix of inflation levels is advantageous as not all patients may be able to inhale to the same level meaning this atlas can be used across patient cohorts. Further the development of the registration algorithms on an open source software platform [84] means this method is able to be applied relatively simply. Processing time is also reasonable with the authors commenting that for a single dataset processing time was approximately 36 minutes, which in the experience of this author, is around 50% of the time taken to manually segment low-quality anatomical images.

Kohlmann et al. [53] also developed a ^{1}H image segmentation strategy as part of their perfusion analysis workflow. They combined numerous low-level image-processing tasks to obtain seed points for a three-dimensional region growing algorithm to be applied. This method provided high quality results and as such were used as a comparison by Tustison et al. [281] to their method. One drawback of this method is the need to acquire coronal and axial images and then carry out an alignment for the airway segmentation presented. Although this would not greatly increase scan or processing time it may introduce errors into the final segmentation if registrations were not to a high standard.

3.1.2 HP gas image segmentation

Previous methods for HP gas ventilation image segmentation have been based on manual intensity thresholding [277], K-means clustering [62], multiple atlas labelling [283] and globally optimal graph cuts [284]. He et al. recently improved the K-means method of segmentation by characterizing the distribution of ventilation [285], whilst Zha et al. improved the K-means method by adding an adaptive aspect of the algorithm [78]. Most of these HP gas ventilation segmentation techniques [283, 62, 284, 285, 78] require little to no manual input, and the methods developed in [62] and [285] also grade ventilation. However, the K-means segmentation method [62, 285, 78] can fail with low SNR images due to its binary clustering nature and inability to differentiate noise from lung tissue.

Prior to these more complex algorithms, thresholding, as used in [277] and as part of the ^{1}H processing in [62] and [53], is a method which was popular, although this is time-consuming and user-biased. Basic thresholding, that selects a maximum or minimum value from the image that is known to be in the ROI and setting all values above or below this to 0 will vary between users, also thresholding values will vary between patients due to variations in image SNR between scans. A semi-automatic SNR-based method such as $mean(sig) - 3*std(noise)$ [277] alleviates both of these problems but can still exclude regions of poor ventilation in some cases. Using ITK-SNAP, thresholding can be combined with active contour segmentation. The user first employs thresholding to define the regions where the contour may and may not grow and then places seed points. The contour's parameters are modifiable and this is a good semi-automated approach to the problem. However due to the fact the user selects the thresholding levels there is again an issue of time and user-bias. Furthermore, in most cases the contour will require manual removal of some of the larger blood vessels.

Tustison et al. [283] created a workflow to segment ^{3}He ventilation images which not only automates aspects of segmentation it also removes pulmonary vasculature as a source of error from the ventilation defect area. With the creation of a principal component analysis model of lung shape Tustison et al. overcome one of the major issues in segmenting ^{3}He images, which is ventilation defects not being considered as part of the lung due to showing little or no signal. Principal component analysis is where a datasets dimensionality is reduced, that is a new set of variables is found which retains almost all of the information from the original dataset [94, 286-288]. This is done by successively removing the variance in a dataset and converting the set of possibly correlated data to a set of linearly uncorrelated data. This methodology is clearly very useful and provides consistent data analysis [283]. The atlas-based methods are growing increasingly popular not only in lung MRI but also in other areas of MRI analysis [289], and although these methods are well established in MRI of the brain it has not yet been well developed in MRI of the lung. This method has many advantages but the main disadvantage is the amount of time necessary to create the atlas and registration algorithms. Further were a fully ventilated atlas registered to a patient with severely reduced ventilated volume then the technique may not be able to match the heterogeneous ventilation pattern.

Recent improvements by He et al. and Virgincar et al. [290, 291] have allowed for not only ventilation defect percent calculation but also to demonstrate areas of different signal intensity within a ^{129}Xe ventilation image. He et al. improved on the method presented by Virgincar et al. by scaling and classifying voxels into 4 clusters (void, low, medium and high) automatically. This does require extra pre-processing including removal of the blood vessels via a vesselness filter [292] and B_1 correction [293] but the results can provide more information than a simple ventilated/non-ventilated comparison. Removal of the vessels via the ^{1}H image may also introduce issues particularly if the registrations are not to a high standard, and as noted by the authors may remove far too much ventilated area if the vesselness filter is not properly applied.

3.1.3 Neural networks and clustering methods

Neural networks (NN) are a useful tool in signal processing and have been adapted in some publications to aid image segmentation [294-297]. Specifically a cellular neural network (CNN) was created using a specific network design template [296] for lung MR image segmentation. This method also requires image filtering; however even with the smoothing of the Gaussian filter the method reportedly had improved accuracy over other common clustering techniques. CNN methods for image processing have been well reported [298] but remain heavily dependent on pre-processing steps, if the pre-processing steps do not improve image quality enough the final segmentation will be poor. A further drawback of this method is the complexity of designing a CNN and ensuring it is suitable for the particular task.

K-means clustering attempts to find k data points, given the integer k, in an n-dimensional space (R^n) given m data points. These k data points are known as centres/centroids and the aim is to minimise the distance from each data point (m) to its centre/centroid [299].

K-means clustering was used in [62] to segment the ^{3}He images and provide information about signal intensity rather than a binary decision of signal or no signal, this method of segmentation has been used in biomedical images before [300], but as implemented in this work attempts to emulate an expert radiologists to segment the signal intensity histogram [62] leading to improved segmentations. The k-means method employed by [62] also required extra computation due to the fact that one cluster contained both ventilation defects (signal =0) and background information, causing the need to again apply the same k-means algorithm to the first cluster, increasing computation time slightly, although this is still much shorter than manual analysis.

Another clustering method available is that of Fuzzy c-means (FCM) clustering, first introduced by Bezdek [301], building on the introduction of Fuzzy logic by Zadeh [302], and it has also been adapted for image segmentation as shown in [303]. Fuzzy clustering allows pixels to belong to more than one class with varying degrees of membership [303], that is the membership value to a class will vary and the higher the membership the more likely that it belongs to that class [303]. This is in contrast to the hard clustering of k-means or the alternative hard clustering c-means [304] where a pixel belongs only in one class or another. This fuzzy membership can be advantageous as some pixels may not be clearly identifiable as hard clusters, but using Fuzzy clustering even pixels which may have a low membership (0.2 for example) can be included into the segmentation if they are within the lung.

In the work presented here the Spatial Fuzzy C-means (SFCM) method [305] was adapted for the segmentation of HP gas ventilation and ^{1}H anatomical images of the lung, to create an image processing workflow that has high resilience to noise. The workflow was developed within a graphical user interface (GUI) for semi-automatic %VV calculation. We hypothesised that the semi-automated method would reduce inter-observer variability when compared to the current approach of fully manual image segmentation (basic method described in section 3.3.4) and improve on the segmentation achieved using the K-means method developed in [62]. The performance of the different techniques was tested on patient data sets with a range of obstructive lung diseases and disease severity, with both ^{3}He and ^{129}Xe HP gas ventilation images.

3.2 Image processing algorithm development

This section of the thesis describes the experiments carried out to develop the pipeline proposed for semi-automatic %VV calculation including the choice of filter and filter values and membership threshold for the creation of TLV/VV masks.

3.2.1 Filter choice

Hyperpolarised gas images of the lung can suffer from poor signal to noise ratio, as does any other image, due to coil uniformity or insufficient gas dose, particularly if a patient has trouble inhaling the gas dose provided. Whilst noise is normally not an issue for diagnostic images, in some cases it can corrupt an image to a point such that standard methods of processing are unable to differentiate lung tissue from noise. In order to develop a pipeline resilient to noise it was decided to incorporate filtering of the image to ensure even images with low SNR could be analysed.

Standard filters used in image processing include the Gaussian [306], mean and median filters. One assumption made whilst using these filters is that the image being processed shall vary slowly in the spatial domain, which, in pulmonary MRI and more specifically at the edges of the ventilated lung, is not always true. Mean filtering is an example of simple linear filtering; a pixel in an image is replaced by an average of its neighbours (including itself) within a window of $n \times n$ pixels. Median filtering is a nonlinear filter approach that preserves edges to a higher level than mean filtering but is executed in the same way. Gaussian filtering is a more complex filtering approach which weights pixels spatially close to the centre of the window higher than those far away.

Another filter considered to be added to the pipeline was Bias field correction (N4 correction) as described in [293]. This methodology corrects signal intensity based on the low spatial frequencies of the image information only. However, it does not remove noise, and hence can be useful in normalising for any signal inhomogeneity introduced by the transmit and receive sensitivity profiles of the RF coil, but would make no difference to a low SNR image.

One filtering method which does not rely on the assumption of slow variation in the spatial domain is the bilateral filter [307, 308]. This filter is a combination of range and domain filtering, that is the way in which a Gaussian filter weights pixels by distance the bilateral filter also weights pixels by photometric similarity, resulting in a nonlinear filter which removes noise and preserves edges well [307]. This combination will maintain edges and ventilation defects within pulmonary images, as there is high photometric dissimilarity between, for example, a defect and ventilated lung. Therefore, bilateral filtering was chosen for the image-processing pipeline.

3.2.2 Spatial Fuzzy C-means methodology

Spatial Fuzzy C-means (SFCM) was chosen for segmentation in the proposed pipeline. As previously mentioned rather than a hard clustering of data this approach applies membership to each data point [305]. The standard FCM algorithm assigns N pixels to C clusters via Fuzzy memberships. The key assumption of the Spatial Fuzzy C-means is that pixels spatially close will have high correlation and hence have similarly high membership to the same cluster. This spatial information will modify the membership value only if, for example, the pixel is noisy and would have been incorrectly classified. For the standard FCM method the cost function to be minimized is given in equation 3.1 [309]:

$$\mathrm{J} = \sum_{n=1}^{N} \sum_{m=1}^{C} \mu_{mn}^{l} \, ||i_n - v_m||^2 \tag{3.1}$$

Where the fuzziness modifier l (>1) controls the fuzziness of the data. This transforms the scalar data to fuzzy data via the membership function;

μ indicates the membership of the n-th object (N = number of objects = number of voxels in an image) to the m-th cluster;

C indicates the cluster number;

$||x||$ is any norm metric representing similarity between the measured data and the cluster centre; and i_n and v_m are the pixel and centroid of the m-th cluster respectively.

Equations 3.2 and 3.3 then describe how the membership and centroids are updated in the standard FCM method:

$$\mu_{mn} = \frac{||i_n - v_m||^{-2/(l-1)}}{\sum_{k=1}^{C}||i_n - v_k||^{-2/(l-1)}} \tag{3.2}$$

$$v_i = \frac{\sum_{n=1}^{N} \mu_{mn}^{l} i_n}{\sum_{n=1}^{N} \mu_{mn}^{l}} \tag{3.3}$$

Equations 3.2 and 3.3 are updated in an iterative manner in the FCM algorithm. The cost function is minimized when convergence to a saddle point of v_i is found. MR images can be subject to noise and artifact that can lead to erroneous classification using standard FCM techniques, hence the need for spatial information. The modified SFCM methods membership function is described by equation 3.4:

$$\mu'_{mn} = \frac{\mu_{mn}^{p} h_{mn}^{q}}{\sum_{k=1}^{C} \mu_{kn}^{p} h_{kn}^{q}} \tag{3.4}$$

$$h_{mn} = \sum\nolimits_{k \in N_n} \mu_{nk} \tag{3.5}$$

This modifies the membership function by adding the spatial function h (defined in equation 3.5) and assigning importance to the contribution by the weighting variables p and q. The standard FCM approach corresponds to $q = 0$ and $p = 1$, when $q > 0$ the spatial information will be used to modify the cluster membership. N_n is a window centred on the pixel n and for this work a window of size 5x5 was used. The user can modify the number of clusters used in the Fuzzy clustering, in order to ensure high quality segmentations are achieved. Spatial importance (q) varies with SNR and for images with SNR>20 is 1 and for all others is 2.

3.2.3 FCM or SFCM?

Previously FCM segmentation has been used in HP gas images [310] and was reported to be a successful method for segmenting ventilated airspaces in this type of image. To decide whether to use the SFCM algorithm or FCM algorithm 6 HP gas datasets acquired with ^{3}He and 6 acquired with ^{129}Xe were segmented using both techniques. The initial ventilated volume mask, (the mask output by the Fuzzy clustering including airways) were compared visually and by volume. The same filter and binary mask threshold values were used in both FCM and SFCM segmentation.

Table 3.1 shows the volumes of the ^{3}He data and ^{129}Xe data. As can be seen the FCM volumes were higher than the SFCM volumes for all patients. By carrying out Wilcoxon matched-pairs signed-rank test to compare FCM to SFCM it was found that the FCM volumes were significantly (p=0.0312, for both ^{3}He and ^{129}Xe) larger than SFCM volumes.

Table 3.1 Ventilated volume values obtained in ^{3}He and ^{129}Xe data using FCM and SFCM methods

Patient	VV FCM (L)	VV SFCM (L)	Δ%
^{3}He data			
P1	4.08	3.722	-8.78
P2	4.80	4.285	-10.41
P3	4.89	4.259	-12.86
P4	5.14	4.474	-12.97
P5	4.63	4.090	-11.74
P6	4.95	3.764	-23.98
^{129}Xe data			
P1	4.721	4.616	-2.23
P2	6.168	5.817	-5.68
P3	6.220	4.846	-22.09
P4	4.363	4.129	-5.38
P5	4.017	3.633	-9.55
P6	5.534	4.611	-16.69

Figure 3.1 shows an example slice from a ^{3}He dataset segmented using the FCM and SFCM approach. As can be seen the FCM method included areas that visually appear to be defects, this figure is representative of the pattern seen in all datasets analysed. Because of this the SFCM method was chosen.

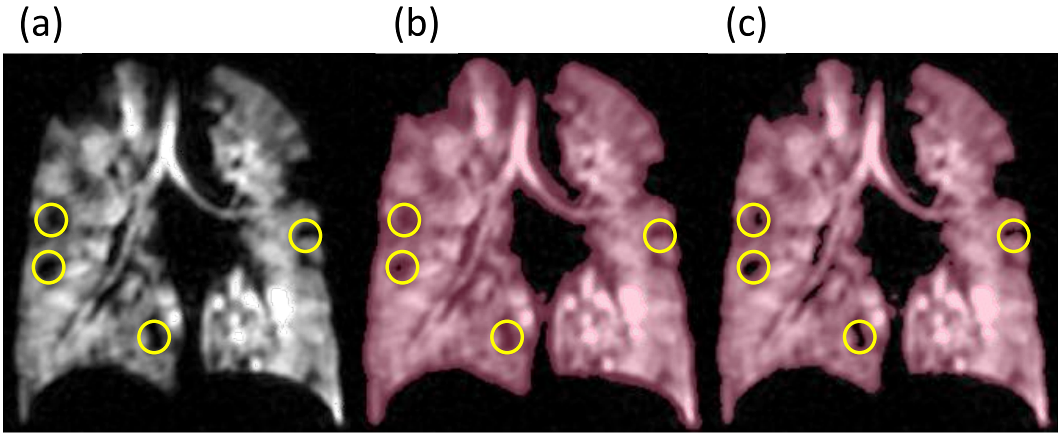

Figure 3.1 Example segmentation output from FCM and SFCM methods. (a) original image (^{3}He), (b) FCM output and (c) SFCM output. The yellow circles highlight some of the areas where differences are seen between FCM and SFCM outputs. Reproduced with permission from [311]

3.2.4 Noise resilience

To ensure the combination of bilateral filtering and increase of the weight of the spatial function would function would provide segmentations of a high quality from poor SNR images six ventilation image image datasets were selected from a clinical database. White Gaussian noise was added to the original original images using the *imnoise* function in Matlab and the SNR values of the original and noise noise corrupted images are given in Table 3.2. The initial outputs (of the original and noise corrupted images) of the segmentation pipeline, the FCM method and a K-means method were compared (

Table 3.3) by volume and the Dice similarity coefficient (DSC) [312] equation 3.6 where A and B are the two images being compared.

$$\mathrm{DSC} = \frac{2|A \cap B|}{|A| + |B|} \tag{3.6}$$

The DSC gives a measure between 0 (no overlap) to 1 (complete overlap). For this work A and B were defined as the masks of each method.

Table 3.2 Comparison of original and noise corrupted (NC) ^{3}He image SNR

Patient	Original SNR	NC image SNR
P1	47.77	8.4
P2	63.14	5.35
P3	50.79	5.44
P4	53.17	7.06
P5	70.52	3.48
P6	72.64	7.72
Mean	**59.67**	**6.24**

Table 3.3 Comparison of original and noise corrupted (NC) ^{3}He image masks using SFCM, FCM and K-means methods. Note that for K-means the window, intensity and standard deviation of the bilateral filter were increased to 5, 3 and 0.5 respectively

Patient	Original volume (L)	NC volume (L)	%Error	DSC
		SFCM data		
P1	3.8	3.68	-3.07	0.98
P2	4.44	4.21	-5.35	0.97
P3	4.04	3.31	-17.94	0.9
P4	4.73	4.47	-5.51	0.97
P5	4.28	4.04	-5.55	0.97
P6	3.84	3.15	-17.91	0.9
Mean	**4.19**	**3.81**	**9.22**	**0.95**
		FCM data		
P1	4.08	3.92	-4.03	0.97
P2	4.78	4.6	-3.74	0.96
P3	4.89	4.43	-9.44	0.9
P4	5.14	4.9	-4.75	0.96
P5	4.63	4.39	-5.14	0.96
P6	4.95	5.24	5.82	0.83
Mean	**4.75**	**4.58**	**5.49**	**0.93**
		K-means data		
P1	4.52	7.94	75.8	0.68
P2	4.7	8.59	82.81	0.68
P3	4.72	9.05	91.72	0.63
P4	5.17	9.99	93.32	0.66
P5	4.67	7.71	64.99	0.72
P6	4.86	19.85	308.75	0.37
Mean	**4.77**	**10.52**	**119.57**	**0.62**

The noise-corrupted images are an extreme case and, in reality diagnostic images would not likely have an SNR this poor, however as a test of the pipeline's ability to handle data corrupted by noise extremely low simulated SNR values were chosen. The volumes produced from the noise-corrupted images were lower than those from the original images (Table 3.2). Mean Dice similarity increases using the SFCM method compared to the FCM and K-means based methods. One reason for the loss of volume using the SFCM method is that low signal areas of the lung (e.g. Figure 3.2) are excluded using the higher spatial weighting and filtering required. However as seen in Figure 3.2c the output mask from the noise-corrupted image is very similar to that of the original image and shows the pipeline's resilience to noise.

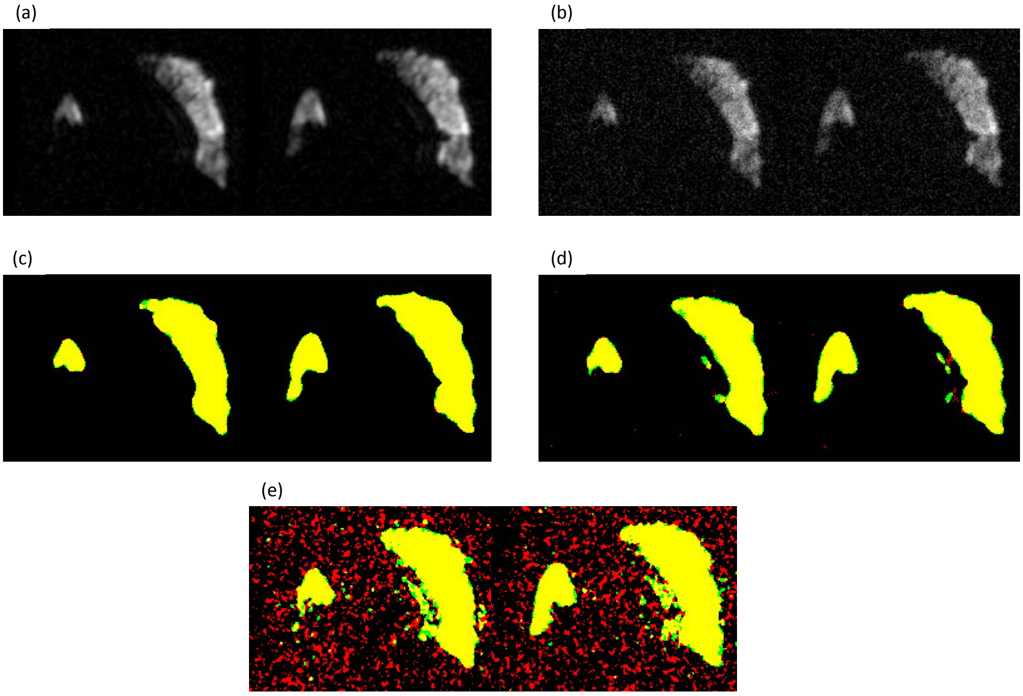

Figure 3.2 Example slices from a HP ^{3}He ventilation image with and without noise corruption and the overlap of their respective masks. (a) original image, (b) noise corrupted image, (c) overlap of the SFCM masks (green = original, red = noise corrupted), (d) overlap of the FCM masks (green = original, red = noise corrupted) and (e) overlap of the K-means masks (green = original, red = noise corrupted). Yellow indicates matching of the masks.

3.2.5 Resilience to HP gas acquisition parameters

To ensure that the SFCM method used was resilient to the effect of imaging parameters, field of view (FOV), echo time (TE) and repetition time (TR) three datasets (2 cystic fibrosis (CF) patients and one healthy volunteer (HV)) were analysed where an SPGR and bSSFP ^{3}He scan were acquired in the same session. The SFCM method was then run using the same filter and threshold values for both sequence types. Imaging parameters are given in Table 3.4.

Table 3.4 Imaging parameters for the data used to compare sequence type effect on the SFCM output

Patient	SPGR TR/TE/FOV	SSFP TR/TE/FOV
HV	3.6ms/1.06ms/35cm	3.05ms/0.86ms/35cm
CF1	3.6ms/1.06ms/35cm	3.05ms/0.86ms/35cm
CF2	3.6ms/1.06ms/35cm	3.0ms/0.84ms/35cm

TR = repetition time, TE = echo time, FOV = field of view.

Table 3.5 shows the results from this experiment, whilst Figure 3.3 shows an example slice from an SPGR and SSFP dataset with the corresponding segmentation output overlaid in pink.

Table 3.5 Ventilated volume (L) values obtained from SPGR and SSFP sequences

Patient	VV SPGR (L)	VV SSFP (L)	Δ%
HV	2.539	2.515	-0.93%
CF1	2.179	2.191	0.57%
CF2	2.449	2.538	3.64%

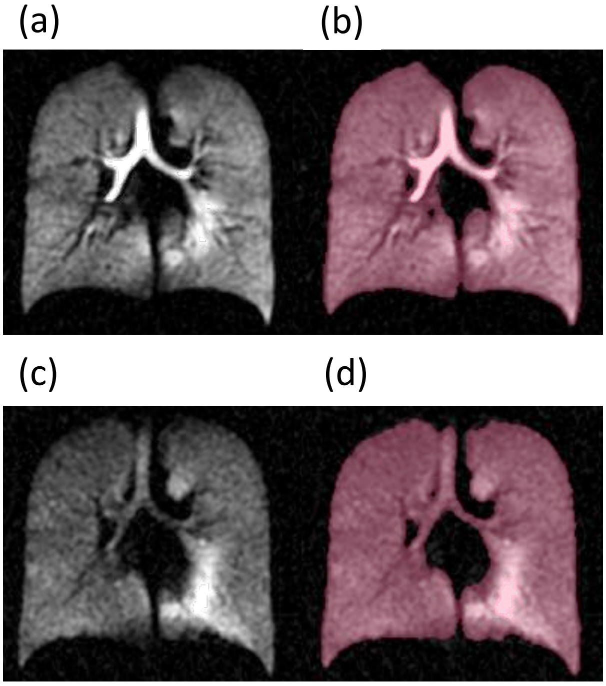

Figure 3.3 Example SPGR and SSFP images from a healthy volunteer. (a) original SPGR image, (b) SFCM mask overlaid on SPGR image, (c) original SSFP image and (d) SFCM mask overlaid on SSFP image

As can be seen from Table 3.5 and Figure 3.3 there was very little difference in the output even with the different sequence, suggesting that the SFCM method has good resilience to TR, TE and FOV.

3.2.6 Filter and binary mask threshold values

Weighting values for spatial and photometric similarity (Table 3.6) were determined empirically through experimentation on 12 data sets acquired using same-breath HP ^{3}He ventilation and ^{1}H anatomical imaging [66] from healthy volunteers and patients with COPD and 6 data sets acquired using separate-breath HP ^{129}Xe and ^{1}H anatomical imaging. ^{1}H image filter values were determined that maintained edges of the lung, evaluated qualitatively by visual inspection, and ensured TLV was within an acceptable error margin (±5%) of manual segmentation. Additionally, filter values that maintained defect integrity, smoothed artifact and noise and maintained edges were determined for hyperpolarised gas images and were again compared quantitatively by volume and qualitatively by visual inspection. Values for intensity and spatial weighting within the SFCM segmentation (Table 3.7) were determined from the same data by evaluating the segmentations visually and comparing with the output obtained from manual segmentation.

Table 3.6 Filter values determined through experimentation

Image type	Window size	Spatial SD*	Intensity SD*
^{1}H	5	3	0.1
^{3}He	3	3	0.15
^{129}Xe	3	3	0.2

**SD = standard deviation*

Table 3.7 Values used in the SFCM segmentation algorithm

Image type	Intensity weight	Spatial weight	Binary mask threshold
^{1}H	1	1*	0.15
^{3}He	1	1*	0.1
^{129}Xe	1	1*	0.05

**Spatial weight is increased when image SNR<20*

The number of clusters to be used was empirically determined from this data with 6 clusters providing TLV masks most similar to those produced manually and 3-4 clusters being the most suitable for HP gas images. Following these experiments the final pipeline (Figure 3.4) was created. The cluster selected for segmentation was the cluster with the minimum centroid, e.g. representing the noise. For calculation of VV, this cluster was transformed to the mask using the Matlab function *imcomplement*, following thresholding by the aforementioned values which removes those pixels with low membership values.

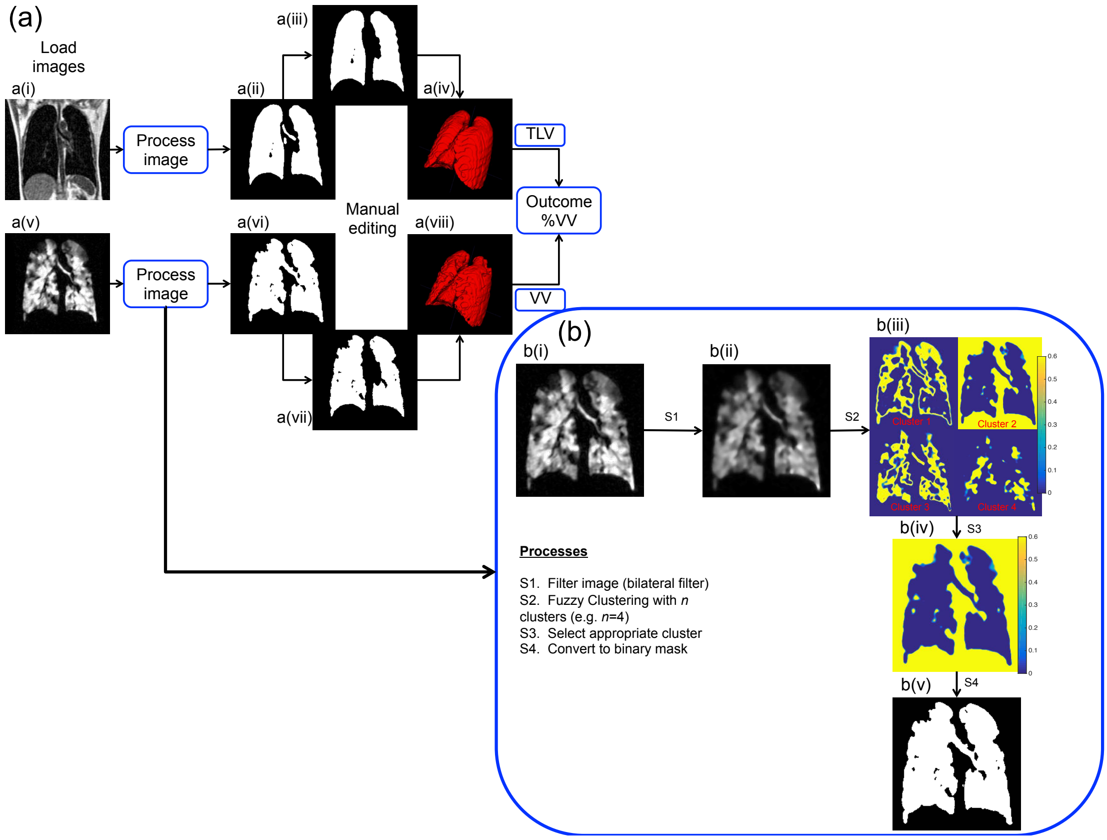

Figure 3.4 (a) Workflow for SFCM image segmentation; a(i) ^{1}H anatomical image, single slice from 3D SPGR sequence, a(ii) ^{1}H mask single slice including airways, a(iii) ^{1}H mask single slice following removal of airways, a(iv) three dimensional representation of the ^{1}H mask, a(v) HP gas ventilation image single slice from 3D bSSFP sequence, a(vi) HP gas ventilation mask single slice clustering output, a(vii) HP gas ventilation mask single slice following removal of airways and a(viii) 3D representation of the ^{3}He mask. VV = (viii) and TLV = (iv). (b) Segmentation method overview; b(i) original image, b(ii) image following application of bilateral filter, b(iii) cluster images, b(iv) selected cluster and b(v) initial binary mask including airways. Reproduced with permission from [311]

Section (a) of Figure 3.4 describes the outline of the workflow. Note that for both ^{3}He and ^{1}H images the same processing steps were used with differences only in values of the filter used and the final membership threshold. Section (b) describes the novel processing pipeline developed for this work. Areas of hypoventilation were included in the ventilation mask based on the interpretation of images by members of the multi-disciplinary research group, and by comparison with the results of the methodology of Kirby et al. [62], where areas of hypointense signal were included in the final ventilated volume reported. Additionally, in practice a threshold between ventilated and non-ventilated lung is a clearer definition than exists between hypoventilation and ‘normal’ ventilation, particularly in severe disease where ‘normal’ ventilation is very difficult to determine.

3.2.7 Registration method for breath-to-breath registration

This section of the thesis discusses a registration methodology developed for use when patients are unable to maintain a breath hold long enough to acquire a ^{1}H image in the same breath and for registration of HP ^{129}Xe images to the corresponding anatomical separate breath image. In many cases when a patient loses their breath during imaging the hyperpolarised gas image is larger than the corresponding anatomical image acquired subsequently. This is an issue for calculation of %VV as peripheral defects may be ignored providing false information on the lung volume.

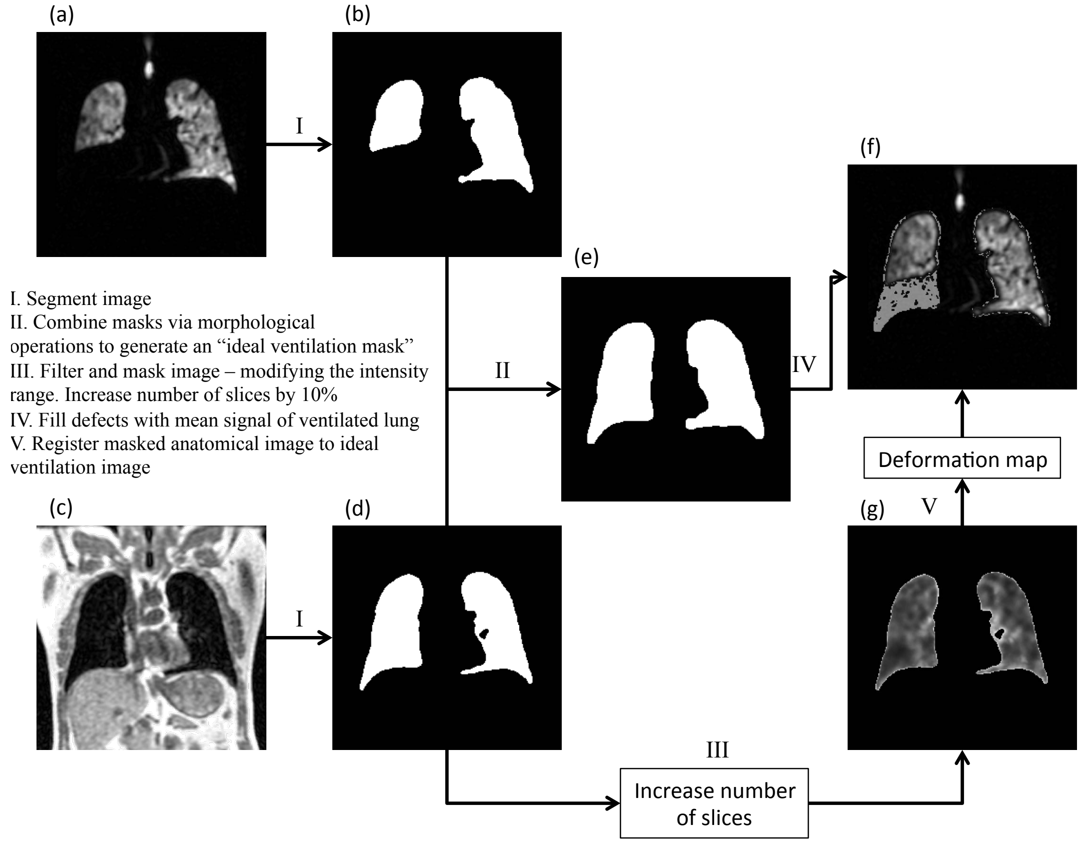

Figure 3.5 Registration workflow developed for breath-to-breath registration. (a) single slice of a 3D HP ^{3}He data set, (b) corresponding mask slice, (c) single slice of a 3D ^{1}H data set, (d) corresponding mask slice, (e) ideal ventilation mask, (f) ideal ventilation image and (g) filtered, inverted and masked ^{1}H image

The workflow presented in Figure 3.5 was developed to automate creation of images that have similar intensity. The masks are combined by a logical AND operation followed by the *imclose* and *imdilate* functions within Matlab, this is the case when the HP gas image is larger than the ^{1}H image to ensure all ventilated lung is included within the ^{1}H segmentation. These functions remove any small defects within the masks and also are adjustable should there be a significant difference between lung inflation state of the HP gas and ^{1}H images. In most cases the error at the edges of the lungs, particularly the diaphragm, are only 3-5 pixels. Following the creation of this mask areas of defect within the HP gas image that correspond to an area of the mask that is 1 are replaced by an artificial voxel with an intensity equal to the mean of the image to create an image of ideal ventilation – that is an image with no defects. The ^{1}H image is then masked and filtered via the bilateral filter and the lung parenchyma intensity inverted. The number of slices is then increased by 5-20% depending on the difference in lung inflation state.

Effective registration was required to overcome the aforementioned issues. To achieve this the workflow seen in Figure 3.5 was integrated into the aforementioned segmentation pipeline. Typically, ^{1}H images were registered to the HP gas images, as these are the images that are generally considered the ground truth of lung ventilation and size, however it is also capable of registering a hyperpolarised gas image to an anatomical image if desired. Registrations are carried out using the ANTs registration software [84].

3.3 Comparison with other methods

To quantify the algorithm's performance the outputs of this novel semi-automated approach was compared to that of the current basic segmentation and a K-means based method for %VV calculation.

3.3.1 Materials and methods

All studies were performed with local research ethics committee approval and informed consent given for ^{129}Xe scans.

3.3.1.1 *Observers*

Three observers (O1, O2 and O3) with previous experience in lung image analysis were selected. O1 had 6 years' experience in lung image segmentation whilst O2 and O3 had 1 and 5 years' experience respectively. O1, O2 and O3 analysed ^{3}He scans and O2 and O3 analysed ^{129}Xe scans, with manual segmentation (basic method), and the semi-automated method developed here. Observers analysed all images independently. All observers were physicists.

3.3.1.2 *Participants*

Scans were selected by O1 and O2 from a database of clinical lung imaging data of patients with respiratory conditions of various severities. The work was performed with research governance approval from the local NHS trust for retrospective research using clinical lung imaging data. The inclusion criterion for the scans was that the patients had held their breath for the duration of the back-to-back HP gas and ^{1}H imaging sequence. One patient suffered from horseshoe lung, one patient had asthma and four patients had COPD. In addition, images from six patients with lung cancer were analysed to test the applicability of the method to ventilation images acquired with HP ^{129}Xe. Patients' forced expiratory volume in 1 second (% predicted) ranged from 24% to 94% and age ranged from 23 to 68 years (6 male, 6 female).

3.3.1.3 *Imaging*

All imaging was carried out on a GE HDx 1.5T MR scanner (GE Healthcare, Milwaukee, IL, USA) and images were acquired at functional residual capacity + 1L. Patients were coached on the breath hold manoeuvres. Imaging parameters can be seen in Table 3.8.

Table 3.8 Imaging parameters for the scans used in this work. TR = Repetition time, TE = echo time, FA = flip angle

Acquisition	TR (ms)	TE (ms)	FA (°)	Matrix size (frequency x phase)	Voxel size (mm)	Slice thickness (mm)	Slices
^{1}H (3D SPGR)	1.5	0.6	5	100x100	3.6x3.6-4x4	5	40-48
^{3}He (3D bSSFP)	1.9	0.6	10	100x80	3.6x3.6-4x4	5	40-48
^{1}H (3D SPGR)	1.9	0.6	5	100x100	3.4x3.4-4.2x4.2	10	20-24
^{129}Xe (3D bSSFP)	6.7	2.2	10	100x80	3.4x3.4-4.2x4.2	10	20-24

Note that slice number and field of view was adjusted per patient to ensure full lung coverage

3.3.1.3.1 ^{3}He imaging

Three-dimensional ^{1}H anatomical (SPGR) and HP gas ventilation-weighted (bSSFP) images were acquired during the same breath hold following the methods in [73, 66]. HP gas ventilation-weighted images were acquired using HP ^{3}He polarized on site to approximately 25% using a rubidium spin exchange polarizer (GE Healthcare, Amersham, UK). Images were acquired using a ^{3}He transmit-receive flexible vest coil tuned to 48.62 MHz (Clinical MR Solutions, Brookfield, WI, USA) and the ^{1}H system body coil. HP gas ventilation-weighted images were acquired followed immediately by ^{1}H anatomical images. Patients inhaled 200mL HP ^{3}He mixed with 800mL N_2 from a Tedlar bag (Jensen Inert Products, Coral Springs, FL, USA) prior to the scan.

3.3.1.3.2 ^{129}Xe imaging

HP gas ventilation-weighted images were acquired using HP ^{129}Xe polarized on site [313]. Images were acquired using a ^{129}Xe transmit-receive flexible vest coil (Clinical MR Solutions, Brookfield, WI, USA) and the ^{1}H system body coil [221]. ^{1}H anatomical images were acquired in a separate breath prior to the HP gas ventilation images. Patients inhaled 550mL HP ^{129}Xe mixed with 450mL N_2 from a Tedlar bag (Jensen Inert Products, Coral Springs, FL, USA) prior to the ventilation scan.

3.3.2 Image analysis

The main outcome measure was %VV defined as ventilated volume (VV, from HP gas ventilation images) divided by total lung volume (TLV, from ^{1}H anatomical images) [277] (equation 3.7).

$$\%VV = \frac{VV}{TLV} \times 100 \tag{3.7}$$

The total lung volume masked the ventilated volume so that only voxels included in the TLV contributed to the calculated VV.

3.3.2.1 Basic method

Basic method segmentations were carried out using software written in MATLAB (The MathWorks, Inc., Natick, MA, United States). To segment ventilation images a threshold approach was used, the user chose a threshold that separated ventilated lung from background. For ^{1}H anatomical images the ventilation image was overlaid on the anatomical image with opacity of 30% and the user delineated the total lung volume for each slice, using the ventilation-weighted image as ground truth and the anatomical image as a guide on the shape of the lung.

3.3.2.2 K-means method

For a comparison to a well-known automated method the k-means segmentation presented by Kirby et al. [62] was implemented and modified for the images used in this study. The size of the window used in the Gaussian filter for ^{1}H anatomical image segmentation was reduced from 15x15 to 3x3 and the standard deviation reduced to 0.01, the radius of the closing structuring element was reduced from 15 to 7, and data outside the lung region was removed by a border clearing algorithm. No filtering of HP gas images was applied as per [62].

3.3.2.2.1 Ventilation image segmentation

As previously discussed this method uses a hierarchical k-means segmentation to classify the ventilation image into five clusters (C1 – background to C5 – hyperintense signal). To achieve this the image is normalized in the range 0-255. From this range four cluster ranges are defined (0–63, 64–127, 128–191 and 192–255) with the initial centroids being the centre of the ranges [62]. Following initial clustering all data in C1 is reanalysed to separate background and hypointense (C2) signal, this leads to a final image with 5 clusters [62] (e.g. Figure 3.6).

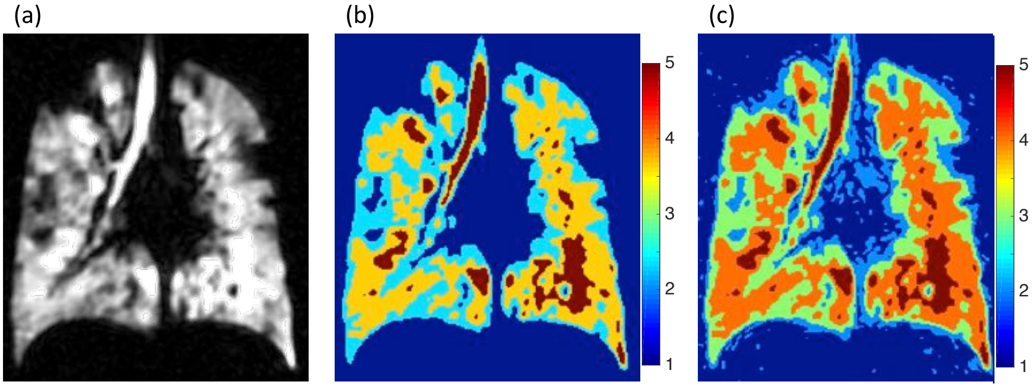

Figure 3.6 Example K-means clustering algorithm output. (a) ^{3}He ventilation-weighted image, (b) result of first clustering stage and (c) final clustering result

3.3.2.2.2 ^{1}H anatomical segmentation

^{1}H anatomical image segmentation is carried out by first Gaussian filtering the image and then thresholding the image by half the maximum value obtained from the lowest intensity cluster by k-means clustering [62]. Following this seed points for the region growing algorithm are selected as those with only 20 vertical adjacent neighbours and the region-growing algorithm is applied followed by morphological operations (*imclose – Matlab function)* to close any small holes within the image [62].

3.3.2.3 Semi-automated approach based on Spatial Fuzzy C-means

The pipeline described in Figure 3.4 was used for segmentation.

3.3.2.4 Performance evaluation

Quantitative performance analysis was carried out on the computed values for TLV, VV and %VV as expressed previously in equation (3.7). Intra-class correlation (ICC), Bland-Altman analysis and Pearson's / Spearman's correlation of the segmentation methods was carried out on a slice-by-slice basis using GraphPad Prism (GraphPad Software, La Jolla, CA, US). In addition, the limits of agreement (LOA) provided by the Bland-Altman analysis were also analysed to test for an improvement in the consistency of results when using the semi-automated method when compared to the manual method. Spatial similarity analysis was carried out on VV and TLV masks using the DSC [312]. Friedman's test was used to test for statistical significance in global %VV values.

3.4 Results

3.4.1 ^{3}He results

Figures 3.7 to 3.9 show the results of the global values of %VV, TLV and VV respectively, as measured by the pipeline proposed here (semi-auto), the basic method and the k-means method. As can be seen the k-means method overestimated %VV compared to all other methods.

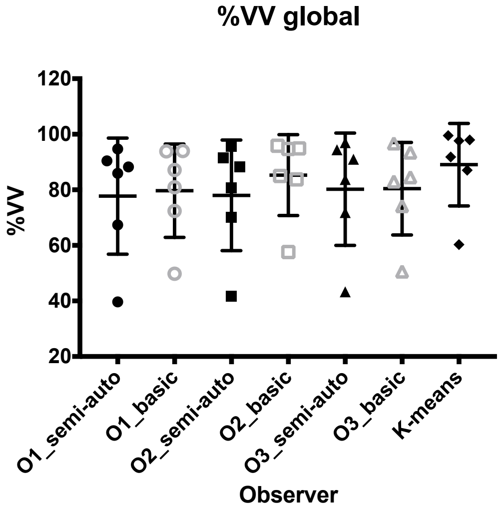

Figure 3.7 Plot of global values of %VV for all 6 patients scanned with ^{3}He

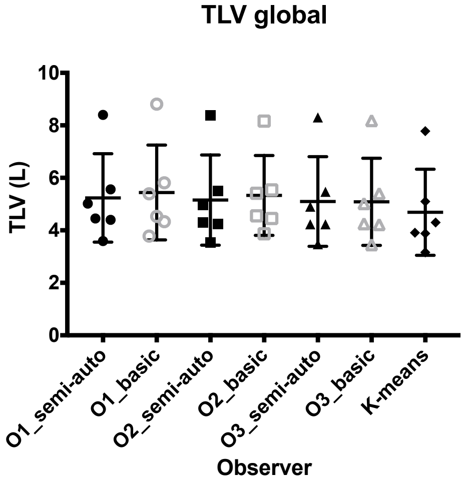

Figure 3.8 Plot of global values of TLV for all 6 patients scanned with ^{3}He

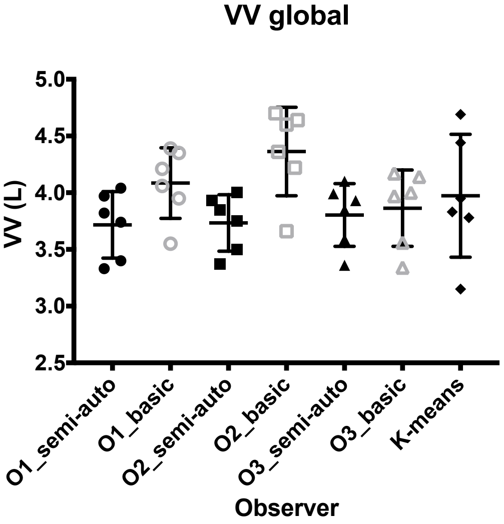

Figure 3.9 Plot of global values of VV for all 6 patients scanned with ^{3}He

Correlation improved (p=0.25) between observers when using the semi-automated method (%VV mean R = 0.984) when compared to the basic method (%VV mean R = 0.863) whilst mean ICC also increased (p=0.25) from 0.873 using the basic method to 0.980 using the semi-automated method. LOA (p=0.50) and %VV bias magnitude (p=0.25) were reduced when using the semi-automated method (%VV mean LOA = 7.5%, mean |bias| = 2.3%) when compared to the basic method (%VV mean LOA = 14.2%, mean |bias| = 4.6%). These improvements were also seen in the VV and TLV measures. DSC significantly improved using the semi-automated method (VV mean DSC = 0.973, TLV mean DSC = 0.980) when compared to the basic method (VV mean DSC = 0.947, TLV mean DSC = 0.957) ($p<0.01$ for both VV and TLV DSC).

The K-means method underestimated TLV when compared to both other methods. %VV was overestimated when compared to the basic (mean bias = 5.0%) and semi-automated (mean bias = 9.7%) methods. The Bland-Altman plot in Figure 3.10a(iii) shows poor agreement of the K-means method %VV with the basic method for O2 and is representative of the pattern seen when comparing K-means with both the basic (%VV mean LOA = 29.8%) and semi-automated (%VV mean LOA = 28.2%) methods for all observers.

On average the semi-automated method underestimated %VV by 4.6% compared to the basic method carried out by the same observer, with a mean LOA of 19.7%. The semi-automated method reduced average segmentation time from 1 hour (basic) to 25 minutes.

Table 3.9 shows the correlation, Intraclass correlation (ICC), DSC and LOA for TLV and VV and %VV on a slice-by-slice basis for ^{3}He data. Table 3.10 shows the same analysis for each observer inter-method (basic, semi-automated) values.

Table 3.9 Correlation, Bland-Altman and DSC analysis of TLV, VV and %VV of ^{3}He data. VV and TLV in litres

Parameter	O1 v O2	O1 v O3	O2 v O3	O1 v K-means	O2 v K-means	O3 v K-means
TLV Basic method						
R	0.904	0.998	0.907	0.913	0.983	0.914
ICC	0.906	0.989	0.905	0.883	0.960	0.906
bias ± LOA	0.003±0.062	0.009±0.010	-0.006±0.061	0.019±0.060	0.016±0.030	0.009±0.030
DSC	0.960	0.960	0.950	0.918	0.920	0.949
TLV Semi-automated method						
R	0.999	0.994	0.993	0.994	0.994	0.996
ICC	0.999	0.992	0.992	0.975	0.980	0.985
bias ± LOA	0.002±0.007	0.003±0.017	-0.002±0.018	0.013±0.020	0.012±0.020	0.010±0.010
DSC	0.990	0.980	0.970	0.942	0.941	0.953
VV Basic method						
R	0.829	0.991	0.824	0.830	0.980	0.828
ICC	0.845	0.985	0.820	0.843	0.965	0.837
bias ± LOA	-0.007±0.060	0.006±0.014	-0.013±0.061	0.002±0.060	0.009±0.020	-0.004±0.060
DSC	0.950	0.960	0.930	0.896	0.918	0.906
VV Semi-automated method						
R	0.997	0.993	0.993	0.940	0.950	0.961
ICC	0.998	0.992	0.993	0.930	0.940	0.960
bias ± LOA	-0.0004±0.007	-0.002±0.012	0.002±0.012	-0.007±0.040	-0.007±0.030	-0.005±0.030
DSC	0.980	0.970	0.970	0.887	0.897	0.911
%VV Basic method						
R	0.909	0.859	0.819	0.905	0.850	0.894
ICC	0.850	0.920	0.850	0.726	0.660	0.670
bias ± LOA	-6.9%±12.9%	-1.7%±14.2%	-5.3%±15.5%	-8.0%±27.4%	-11.2%±30.0%	-0.8%±32.0%
%VV Semi-automated method						
R	0.988	0.981	0.978	0.901	0.905	0.926
ICC	0.990	0.970	0.980	0.702	0.730	0.788
bias ± LOA	-1.1%±5.6%	-3.5%±8.3%	2.4%±8.7%	-11.2%±29.6%	-10.1%±28.4%	-7.7%26.5%

Table 3.10 Correlation, Bland-Altman and DSC analysis of TLV, VV and %VV of ^{3}He data (inter-method). VV and TLV in litres

Parameter	O1 basic v O1 semi-automatic	O2 basic v O2 semi-automatic	O3 basic v O3 semi-automatic
TLV			
R	0.918	0.991	0.914
ICC	0.987	0.918	0.914
bias ± LOA	0.006±0.060	0.005±0.020	-0.0002±0.059
DSC	0.956	0.947	0.966
VV			
R	0.814	0.972	0.821
ICC	0.825	0.931	0.839
bias ± LOA	0.010±0.060	0.016±0.026	0.002±0.059
DSC	0.946	0.913	0.944
%VV			
R	0.938	0.864	0.898
ICC	0.900	0.730	0.860
bias ± LOA	3.4%±16.6%	9.3%±23.2%	1.5%±21.3%

Figure 3.10a(iv) shows the inter-method agreement for O1 and is representative of the inter-method agreement seen between all observers.

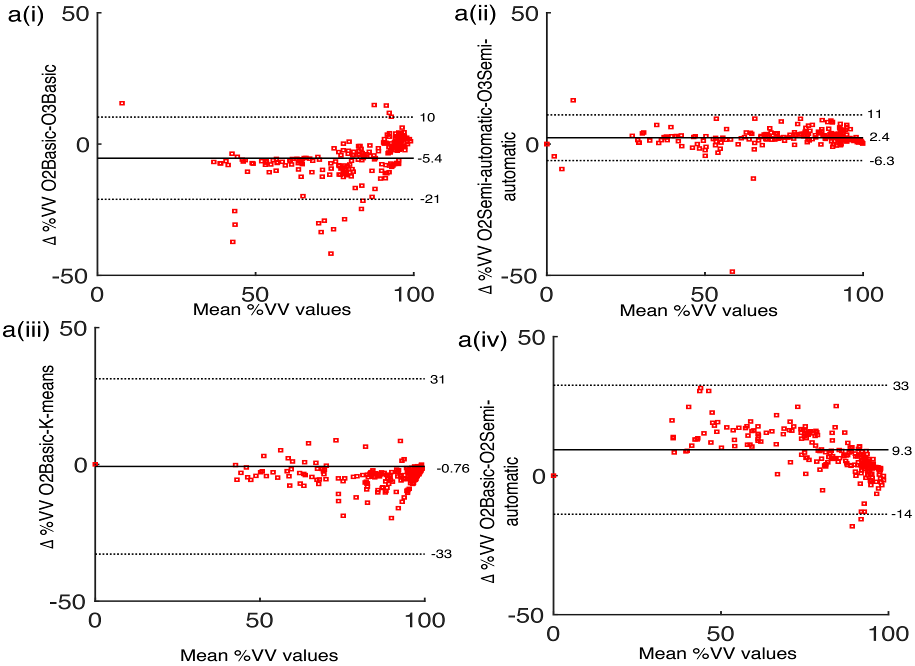

Figure 3.10 Bland-Altman analysis of 3He %VV on a slice-by-slice basis. a(i) O1vO2 basic, a(ii) O1vO2 semi-automatic, a(iii) O1 basic v K-means, a(iv) O1 semi-automatic v K-means

Table 3.11 shows the results of the Friedman test when comparing global %VV values. As can be seen the K-means method result is significantly different to the basic segmentation values of O1 and O3 and the semi-automatic method results of O1 and O2. No significant differences were found between observers using either method (basic or semi-automatic) and no intermethod statistical difference was found.

Table 3.11 Friedman test results when comparing global %VV values for ^{3}He data

Comparison	%VV p value
O1 basic vs. O1 semi-auto	>0.9999
O2 basic vs. O2 semi-auto	0.2033
O3 basic vs. O3 semi-auto	>0.9999
O1 basic vs. O2 basic	0.1521
O1 basic vs. O3 basic	>0.9999
O2 basic vs. O3 basic	>0.9999
O1 semi-auto vs. O2 semi-auto	>0.9999
O1 semi-auto vs. O3 semi-auto	0.2650
O2 semi-auto vs. O3 semi-auto	>0.9999
O1 basic vs. K-means	0.0009
O2 basic vs. K-means	0.7051
O3 basic vs. K-means	0.0437
O1 semi-auto vs. K-means	0.0021
O2 semi-auto vs. K-means	0.0219
O3 semi-auto vs. K-means	0.7051

3.4.2 ^{129}Xe results

Figures 3.11 to 3.13 show the distribution of global values of %VV, TLV and VV for both observers and the K-means method.

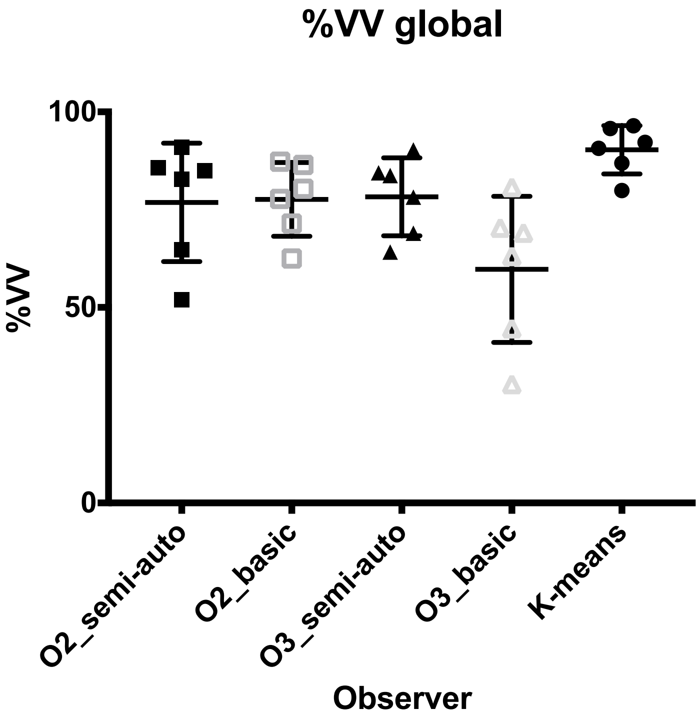

Figure 3.11 Plot of global values of %VV for all 6 patients scanned with ^{129}Xe

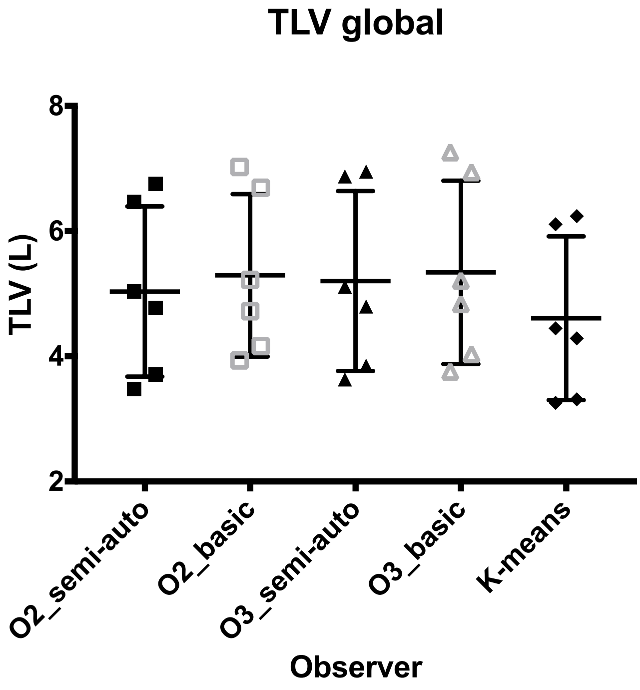

Figure 3.12 Plot of global values of TLV for all 6 patients scanned with ^{129}Xe

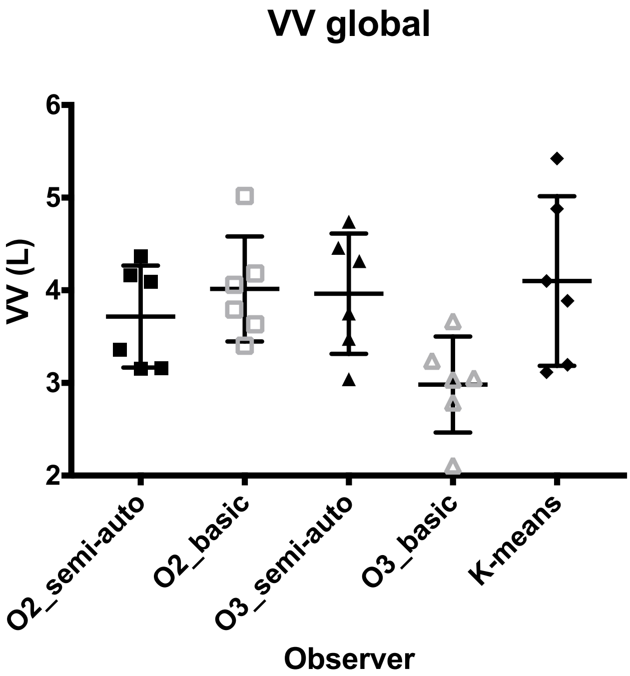

Figure 3.13 Plot of global values of VV for all 6 patients scanned with ^{129}Xe

Correlation, LOA, bias magnitude and DSC improved between observers when using the semi-automated method compared to the basic method (Figure 3.14a(i, ii), Table 3.12). The K-means method underestimated TLV and overestimated %VV compared to the other methods to a greater extent than for the ^{3}He data. The semi-automatic method underestimated %VV by 2.3% compared to the basic method for O2 (Figure 3.14 a(iv)) and overestimated %VV by 18.6% for O3. The mean LOA for %VV calculated by the same observer between the basic and semi-automatic methods was 26.4%.

Table 3.12 Correlation, Bland-Altman and DSC analysis of TLV, VV and %VV of ^{129}Xe data (inter-method). VV and TLV in litres

Parameter	O2 v O3	O2 v K-means	O3 v K-means	Parameter	O2 v O3	O2 v K-means	O3 v K-means
		TLV basic method				**TLV semi-automated method**	
R	0.981	0.896	0.904	**R**	0.984	0.930	0.930
ICC	0.930	0.950	0.638	**ICC**	0.950	0.897	0.899
bias±LOA	0.014±0.103	0.035±0.056	0.021±0.106	**bias±LOA**	0.007±0.088	0.022±0.050	0.015±0.102
DSC	0.960	0.920	0.923	**DSC**	0.980	0.947	0.935
		VV basic method				**VV semi-automated method**	
R	0.977	0.892	0.893	**R**	0.977	0.922	0.930
ICC	0.710	0.950	0.915	**ICC**	0.890	0.970	0.926
bias±LOA	0.016±0.093	-0.005±0.072	-0.020±0.098	**bias±LOA**	0.052±0.080	-0.020±0.095	-0.072±0.136
DSC	0.838	0.888	0.782	**DSC**	0.928	0.892	0.895
		%VV basic method				**%VV semi-automated method**	
R	0.884	0.836	0.740	**R**	0.929	0.860	0.883
ICC	0.579	0.610	0.356	**ICC**	0.905	0.589	0.660
bias±LOA	20.0%±24.3%	-10.9%±30.4%	-31.0%±34.6%	**bias±LOA**	-0.9%±19.1%	-13.3%±33.8%	-12.4%±28.5%

Table 3.13 Correlation, Bland-Altman and DSC analysis of TLV, VV and %VV of ^{129}Xe data (inter-method). VV and TLV in litres

Parameter	O2 basic v O2 semi-automatic	O3 basic v O3 semi-automatic
TLV		
R	0.959	0.966
ICC	0.989	0.995
bias ± LOA	0.013±0.030	0.007±0.034
DSC	0.948	0.965
VV		
R	0.956	0.956
ICC	0.962	0.781
bias ± LOA	0.015±0.052	0.051±0.100
DSC	0.917	0.831
%VV		
R	0.862	0.824
ICC	0.877	0.661
bias ± LOA	2.3%±20.0%	-18.6%±21.78%

Figure 3.14 shows Bland-Altman plots for ^{129}Xe %VV on a slice-by-slice basis. As can be seen there was improved agreement between O2 and O3 using the semi-automated method and also for the inter-method plot for O2.

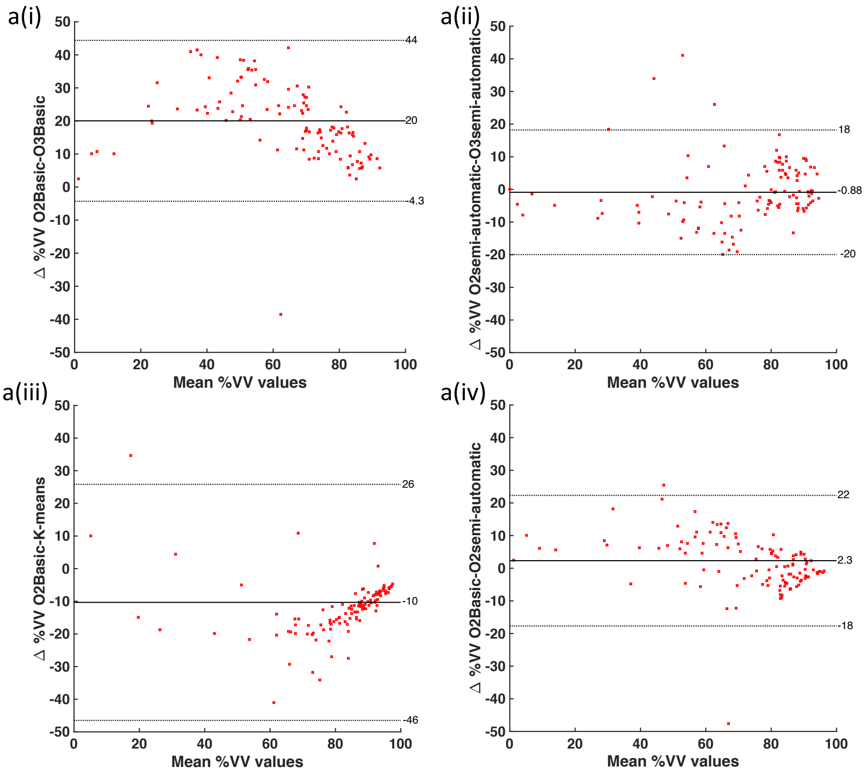

Figure 3.14 Bland-Altman analysis of ^{129}Xe %VV on a slice-by-slice basis. a(i) O2vO3 basic, a(ii) O2vO3 semi-automatic, a(iii) O2 basic v K-means and a(iv) O2 semi-automatic v K-means

Table 3.14 shows the results of the Friedman test when comparing global values of %VV derived from the ^{129}Xe data. As can be seen the K-means method is significantly different to O2's semi-automatic segmentation results and the basic segmentation result of O3. No significant intermethod difference was found for O2, and no significant difference was seen when comparing the results between users for the basic and semi-automatic segmentation methods. O3 had a significant intermethod difference in global %VV values.

Table 3.14 Friedman test results when comparing global %VV values for ^{129}Xe data

Comparison	%VV p value
O2 basic vs. O2 semi-auto	>0.9999
O3 basic vs. O3 semi-auto	0.0219
O2 basic vs. O3 basic	0.2498
O2 semi-auto vs. O3 semi-auto	>0.9999
O2 basic vs. K-means	0.2498
O3 basic vs. K-means	0.0016
O2 semi-auto vs. K-means	0.0117
O3 semi-auto vs. K-means	0.0628

3.5 Discussion

The focus of this study was the development and evaluation of a graphical tool for semi-automated %VV calculation. The tool developed reduces inter-observer variability and also provides similar results to the manual segmentation output. With longitudinal and multiple centre studies becoming more commonplace, developing novel and reproducible semi/fully-automatic analysis techniques are becoming the focus of many research groups.

The use of a co-registered multinuclear image acquisition [66] removes the need for image registration, which is commonly used for %VV analysis in other publications [62, 291, 285]. However, this software was written to be fully compatible with image registration software (section 3.2.7) if needed for breath-to-breath registration as shown here with the 3D ^{129}Xe ventilation images. This tool also has the ability to include bias field correction for image processing however due to issues discussed in Chapter 4 it was not used in this work.

Results obtained using the semi-automated approach proposed here were more similar to manual segmentation results than those obtained using the K-means method [62]. This is partially due to underestimation of TLV via heavy Gaussian filtering of the K-means method and also due to the inclusion of areas of noise as ventilated lung (e.g. Figure 3.6c). The remaining differences between the semi-automated and manual segmentation results could be explained by a few factors, among which is the treatment of partial volume effects at the lung border. Whilst the manual method would include neighbouring pixels corresponding to tissue where ^{3}He signal is present in the ^{1}H mask the method developed here would exclude these areas and consider the edge of the lung from the ^{1}H image as the ground truth.

However, this method is not without its drawbacks, principally the need for manual editing. Although segmentations are usually to a high standard as seen in Figure 3.4, there is still a need for airway removal and large vessel removal. Vessel removal may be overcome by the addition of a vesselness filter to the processing pipeline [314], whilst airway removal could be achieved with a region growing algorithm. Additionally, manual selection of clusters is a possible source of user bias that needs to be automated. This could be based on the range of the data being analysed or possibly SNR, however in practice there is rarely need to change the number of clusters from those found empirically.

The limitations of this technical development study are the small numbers of patients analysed as well as the reduced number of observers who segmented the ^{129}Xe images and the lack of comparison to other established techniques for %VV calculation.

3.6 Conclusion

In conclusion, the semi-automated method proposed here reduced image segmentation time for the author from 1 hour to less than 25 minutes on average. A semi-automatic segmentation robust to noise was demonstrated on both ^{3}He and ^{129}Xe ventilation images. Improvements were seen in agreement between users' values of TLV, VV and %VV using the semi-automatic method compared to the basic method, and the limitations of the K-means method were discussed.

The semi-automated method presented is encapsulated in a custom-built graphical interface that is easily portable between sites and easy to use. This software also allows for data which is misregistered to be analysed by interfacing with the well-known registration software ANTS [84]. This tool may be a step towards moving HP gas ventilation MRI into routine clinical use however further work for automation is needed before this can tool can be considered clinically useful.

CHAPTER 4. HISTOGRAM-BASED ANALYSIS OF VENTILATION HETEROGENEITY MEASURED BY THE COEFFICIENT OF VARIATION OF SIGNAL INTENSITY[2]

4.1 Introduction

As outlined in Chapter 3 the measurement of %VV (or its counterpart VDP) are well known and often used methods of evaluating lung ventilation that can be derived from HP gas MRI [315-318, 283, 62, 60, 63, 66, 284]. They are however binary measures derived from segmenting images that contain rich functional and spatial information about the lung. In this chapter, other metrics derived from HP gas ventilation images that provide information on ventilation heterogeneity in the lungs are explored.

The signal in ventilation-weighted HP gas images acquired with an SPGR or SSFP sequence is directly proportional to the gas spin density, which in turn is directly proportional to the ventilation in that voxel and thus these images provide information on ventilation on a continuous scale. Images are also weighted by the square of the coil sensitivity profile (Transmit (T) and receive (R) using a T/R coil, equation 4.1), whilst coils for HP gas imaging would ideally have a uniform B_1 field there is some inevitable coil inhomogeneity [319-321, 75].

$$S(r) \propto V(r) \cdot B_1^T(r) \cdot B_1^R(r) \cdot e^{-\frac{TE}{T_2^*(r)}} \cdot e^{-\frac{T_{acq}(r)}{T_1(r)}} \tag{4.1}$$

Where $S(r)$ is the signal in a voxel, $V(r)$ is the 'ventilation', the volume of gas within the voxel/breath hold, B_1^T and B_1^R are the transmit and receive fields, TE is the echo time of the acquisition, T_2^* and T_1 are intrinsic properties of the gas in the lung voxel at the magnetic field used and T_{acq} is the time at which the centre of k-space is acquired post gas inhalation for the pulse sequence used. In most applications of ventilation image analysis [322, 283, 291, 285, 78] coil bias is corrected using either a flip angle map [323] or the popular N3 or N4 bias field correction methods [324, 293] which require no prior information on the acquisition and calculate the bias field in a non-parametric way.

---

[2] I would like to acknowledge the efforts of Dr Helen Marshall for segmenting the images from healthy children, mild cystic fibrosis and asthma patients scanned with a 2D sequence.

One method to analyse ventilation image signal heterogeneity is the coefficient of variation of signal intensity (CV), a measure which describes the amount of variability relative to the mean of the sample being analysed and is calculated as the ratio of the standard deviation to the mean value of the sample [325]. This measure has previously been used to describe the ventilation heterogeneity in patients with asthma and healthy subjects, pre and post methacholine challenge and after a series of deep inspirations [326]. In this work the final heterogeneity score was generated by averaging all non-zero values within the heterogeneity map. The heterogeneity map was generated by first calculating a length scale to define as the neighbourhood for CV calculation, this neighbourhood was defined as 10% of the average of the maximum width of the left and right lungs. A sliding window was then applied over the fractional ventilation image, centred on each voxel within the lung ROI and excluding voxels dominated by defects with SNR<2.

Ventilation heterogeneity may also be assessed via imaging fractional ventilation using wash-in [327] or wash-out [67, 69, 70] MRI. These methods of acquisition measure the build-up (wash-in) or decay (wash-out) of MR signal in the lungs. An advantage to these methods are the dynamic nature of the acquisitions allowing a more complete picture of ventilation heterogeneity to be measured rather than a single static breath hold. However, the acquisitions are generally complicated and require good patient compliance, with post-processing techniques also being fairly complex although these techniques may be more easily implemented using fluorinated gases as they do not need to be hyperpolarised before use [328-332].

He et al. also quantified the pulmonary ventilation distribution [285] compared to a reference of healthy volunteers' distributions using the normalised ventilation signal, and also calculated the CV of the rescaled distribution. This method made use of histogram bins, defined from a set of 10 healthy volunteers, and then applied the same bin width to patient cohorts. The difference in the standard deviation and mean of the distributions was compared with the healthy reference values.

Sa et al. [333] made use of proton MRI to estimate the heterogeneity of the specific ventilation measured in humans and carried out a comparison with MBW metrics. The heterogeneity here was described as the width of the fitted log(Gaussian) function to the distribution of the specific ventilation values.

Additionally metrics using SPECT ventilation imaging have been suggested [334, 30]. Norberg [30] developed a metric known as CV_T which is the area under the curve of the CV histogram at a particular threshold, represented as a percentage of the total area under the curve whilst Walsh et al. [335] calculated CV locally using SPECT images in patients with asthma.

The MBW pulmonary function test has recently become more established for analysing ventilation heterogeneity by deriving the measures of lung clearance index (LCI) [120, 33] S_{cond}, and S_{acin} [123]. During the MBW pulmonary function test, which uses inert extrinsic gases, there is a wash-in phase where a known concentration of the test gas is administered and this phase is completed when the expired gas concentration reaches the level of the delivered gas concentration [122]. The wash-out phase then begins with the subject breathing room air until the gas concentration is 1/40th the initial concentration for at least 3 consecutive breaths [7]. Following this LCI is calculated using FRC and the cumulative expired volume from the MBW data [6]. S_{cond} and S_{acin} are then calculated as described in Chapter 2, section 2.2.3, and these metrics represent the heterogeneity in the conducting and transitional zones of the airway tree respectively.

The aim of this work was to utilise the spatial ventilation heterogeneity information provided by the coefficient of variation of signal intensity from HP gas ventilation images by analysing CV histogram metrics including skewness (s), kurtosis (k) and the interquartile range (IQR). We go on to compare these metrics of image derived ventilation heterogeneity with those derived from the MBW test.

Skewness is a measure of the asymmetry of the data around the mean (sample mean) and a normal distribution has s=0. The more left skewed a data distribution the more negative s and the more right skewed the more positive s will be [325]. The Skewness of data is defined by equation 4.2:

$$s = \frac{E(x-\mu)^3}{\sigma^3} \tag{4.2}$$

Where $E(M)$ is the expected value of the quantity M, μ is the mean and σ is the standard deviation of the data x. Kurtosis on the other hand is a measure of how outlier prone the data is, where the normal distribution has k=3. Data that is less outlier prone have k<3 while data which is more outlier prone have k>3 [325]. Kurtosis is defined by equation 4.3:

$$k = \frac{E(x-\mu)^4}{\sigma^4} \tag{4.3}$$

Finally the IQR of data is defined as the lower quartile of the data subtracted from the upper quartile of the data [325]. Figure 4.1 represents skewness (a), kurtosis (b) and the interquartile range (c) visually with distributions generated using MATLAB.

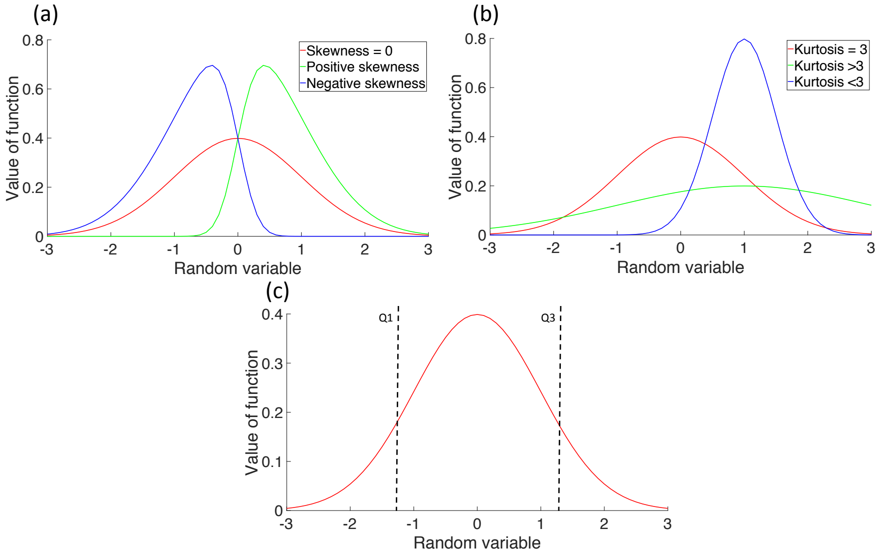

Figure 4.1 Graphical representation of (a) skewness, (b) kurtosis and (c) the IQR

The next sections of this chapter discuss the experimentation carried out in order to determine the final analysis pipeline for coefficient of variation histogram (CVH) calculation.

4.2 Calculation of the coefficient of variation of signal intensity (CV)

The coefficient of variation of signal intensity of a spatially variant image data set can be calculated in two or three dimensions (in-plane over a square region or in-plane and through-plane as a cube) and also over different length scales. The length scale is the size of the kernel used to cluster data and calculate the local CV. In addition, partial volume effects at the edges of the lungs and low SNR will increase the CV and alter the distribution of CV values. It is therefore important to understand the effect of the kernel size, dimension and the effect of image SNR on the measures being reported. In this work the CV was calculated using two different techniques, both of which are described below.

For calculating CV over the ventilated lung, defined by the ventilated volume mask, both HP gas ventilation and ^{1}H anatomical images were segmented. The segmentation method developed in Chapter 3 was used for the 3D imaging data and the manual segmentation method was used for the older 2D imaging data. The ^{1}H anatomical image mask was then eroded by 1 pixel to account for the partial volume effects at the edge of the lung and to ensure no high values of CV at the edges (see Figure 4.2 for an example). The ventilated volume mask, generated from the HP gas image, was then multiplied by the total lung volume mask, generated from the ^{1}H anatomical image, to ensure that CV was calculated only within the lung cavity. Following segmentation, the HP gas ventilation image, HP gas ventilation mask and ^{1}H anatomical masks were downsampled from 256x256xN_{slices} to 128x128xN_{slices} for 2D CV calculation or 86x86xN_{slices} for 3D CV calculation. This downsampling was chosen so that the smallest possible kernel used for experimentation, 3x3 or 3x3x3 voxels, would still encompass multiple acini in the CV measure based on previously reported values for the size (path length, the distance from the terminal bronchiole to the end of the acinus) of acini (ranging from ~4mm to 8mm depending on inflation level) [336-338]. Also, downsampling is performed to ensure that the subsampled image is closer to the actual acquisition matrix size. CV is then calculated by dividing the standard deviation of the voxels within the neighbourhood with the mean of the voxels within the neighbourhood and generating an image where the voxel on which the sliding window is centred is replaced by the CV value. The sliding window then only operates on voxels defined as ventilated by the ventilated volume mask. For CV metrics generated over the ventilated lung histograms were generated using 100 equispaced bins ranging from 0-1.

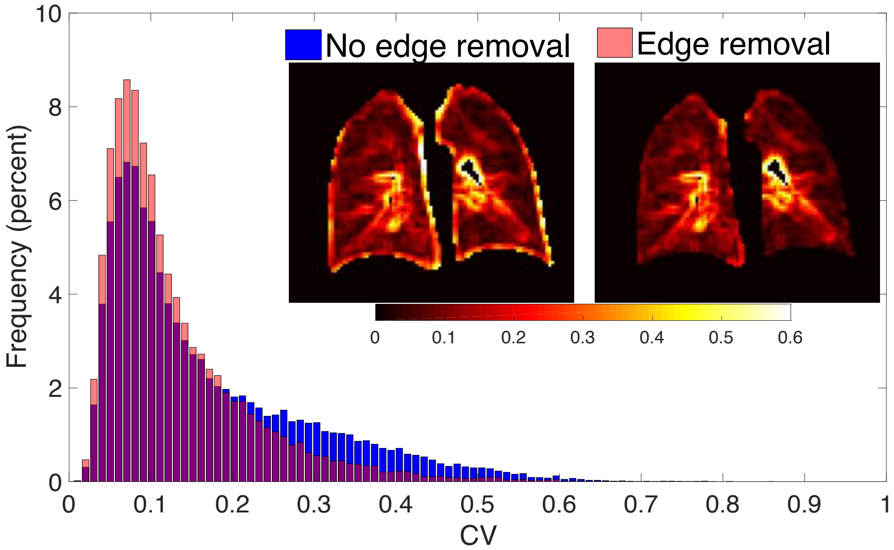

Figure 4.2 Example histograms and CV maps from a healthy subjects 2D SPGR ^{3}He image with (red) and without (blue) edge removal

Figure 4.2 demonstrates increased histogram skewness and a decreased peak with no edge removal when compared to the CV histogram generated following edge removal. The aim of the measurement of CV in these neighbourhoods was to attempt to capture the heterogeneity present in mild disease that using the standard metric of VDP would not be visualised as it would simply be included as ventilated lung e.g. Figure 4.3.

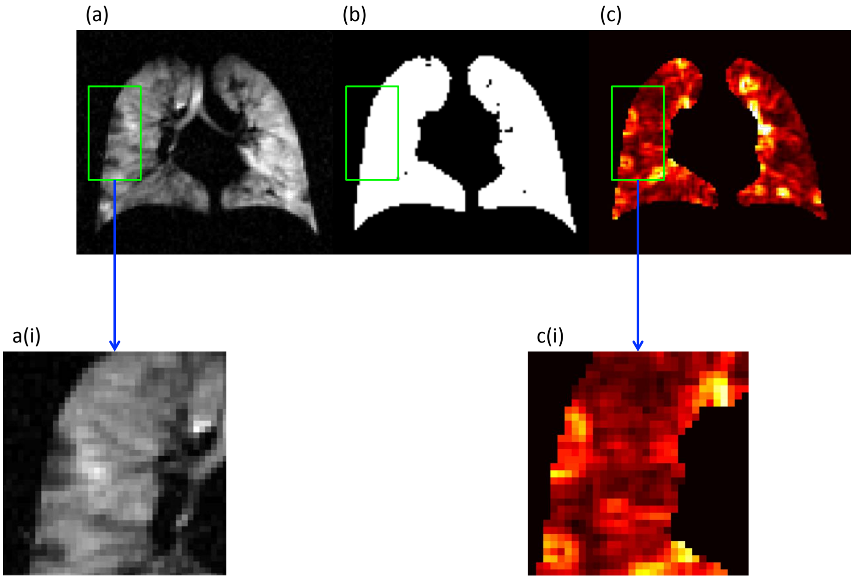

Figure 4.3 Example images showing local heterogeneity not visible on the ventilated volume mask. (a) original ^{3}He image, a(i) focused area of original image, (b) ventilated volume mask, (c) CV map and c(i) focused area of the CV map

For calculating CV over the total lung volume the method by Tzeng et al. [326] was implemented where only voxels with an SNR<2 and/or mean neighbourhood SNR<2 were excluded e.g. Figure 5.4.

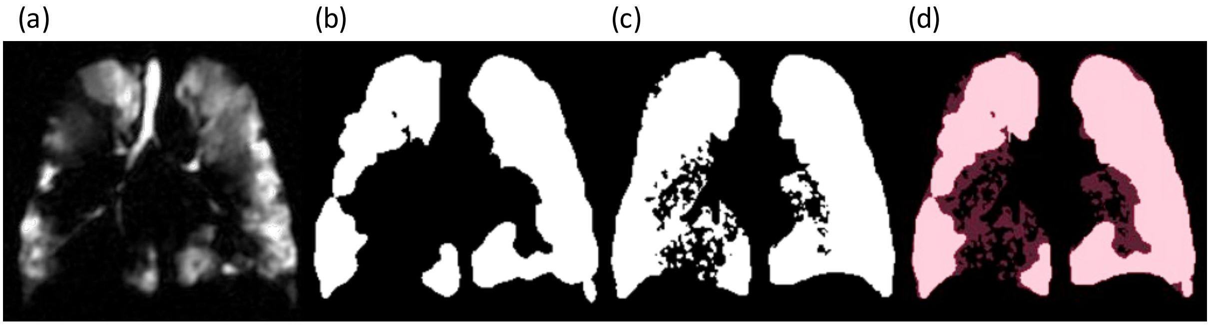

Figure 4.4 Example images showing regions included when calculating CV on the ventilated volume mask and the total lung volume mask from a patient with COPD. (a) original image, (b) ventilated volume mask, (c) ventilated volume mask generated using the SNR threshold and (d) voxels included in the CV calculation using the ventilated volume mask (white) and regions with SNR>2 (pink)

SNR was calculated using the *colfilt* routine in MATLAB and a sliding window of 3x3 voxels, where the SNR was calculated on the central voxel as well as the mean SNR of the neighbourhood and voxels with an SNR<2 and/or mean neighbourhood SNR<2 were excluded. Noise was estimated by taking the standard deviation of an area of the image with no signal. The *imcomplement* function was then used to generate a mask of voxels to be analysed, generating an SNR based ventilated volume mask (Figure 4.4c). This SNR based ventilated volume mask was then multiplied by the total lung volume mask to exclude any background voxels outside the lung that may have had an SNR>2. Any voxels outside the SNR based ventilated volume mask, but within the total lung volume were set to 0 and included in the CV calculation whilst all voxels outside the total lung volume were set to not a number (NaN) and excluded from the CV calculation.

4.3 Effect of image acquisition sequence, signal to noise ratio, kernel size and kernel dimensionality on CV

4.3.1 Overview

The next section presents the participants and imaging strategies used throughout this chapter. Section 4.3.3 discusses the effect of the imaging sequence used and its effect on CV histogram metrics in three healthy volunteers. Section 4.3.4 discusses the effect of image SNR on CV histogram (CVH) metrics. For CV metrics generated over the total lung histograms were generated using 200 equispaced bins ranging from 0-2, as the method introduced an increased number of values above 1 compared to estimating the CV on the ventilated lung. Section 4.3.5 demonstrates the effect of changing the size of the kernel used in the CV calculation, whilst section 4.3.6 demonstrates the effect of changing the dimensionality of the kernel on CV histogram metrics. Section 4.4 presents comparisons between health and disease using all kernel sizes and dimensionalities and presents the optimal choice for use in these cohorts and also demonstrates the correlations of the metrics derived using the optimal kernel size and dimensionality with spirometry and MBW outcomes. In addition, a method similar to that developed by Norberg et al. [339, 30] is investigated for its usefulness in differentiating health from disease. Finally, section 4.5 presents a comparison of metrics derived using HP ^{129}Xe and HP ^{3}He images.

4.3.2 Participants and imaging

Existing images from previous studies and a database of clinical imaging data were analysed. Healthy adults [66], healthy children [33], patients with asthma [71], COPD [340] and CF [33] were the selected cohorts. Five patients with asthma and five with COPD were chosen from the clinical database that had been segmented using the method described in chapter 3. Subject demographics are shown in Table 4.1. Table 4.2 shows the imaging parameters for all participants. HP gas ventilation-weighted images were acquired using HP ^{3}He polarized on site to approximately 25% using a rubidium spin exchange polarizer (GE Healthcare, Amersham, UK). Images were acquired using a ^{3}He transmit-receive flexible vest coil tuned to 48.62 MHz (Clinical MR Solutions, Brookfield, WI, USA) and the ^{1}H system body coil as previously described [321, 66, 71]. Gas was inhaled from a Tedlar bag (Jensen Inert Products, Coral Springs, Florida, USA).

Table 4.1 Subject overview

Patients (acronym)	Description	Age range	Number	^{3}He sequence	^{1}H sequence
Healthy children (HC)	9 healthy paediatric controls, separate study[b], normal FEV$_1$ z-score	7-16	9	2D SPGR	2D SSFP
Cystic fibrosis (CF)	19 mild CF paediatric patients, separate study[b], normal FEV$_1$ z-score	7-16	19	2D SPGR	2D SSFP
Healthy adults (HA)	11 healthy volunteers, separate study[a]	24-70	11	3D bSSFP	3D SPGR
Asthma normal FEV$_1$ (asthma_norm)	16 patients with asthma, separate study, normal FEV$_1$ z-score[c]	21-65	16	2D SPGR	2D SSFP
Asthma abnormal FEV$_1$ (asthma_abnorm)	18 patients with asthma, separate study, abnormal FEV$_1$ z-score[c]	34-73	18	2D SPGR	2D SSFP
Asthma clinical (asthma_clinical)	5 Clinical referrals from Sheffield database	33-72	5	3D bSSFP	3D SPGR
Chronic obstructive pulmonary disease (COPD)	5 patients from a separate study[d] and 5 clinical referrals from Sheffield database	59-76	10	3D bSSFP	3D SPGR

a - reference [66]; b - reference [33]; c - reference [71]; d - reference [340]

Table 4.2 Imaging parameters for the 3D and 2D scans used in this work. TR = Repetition time, TE = echo time, FA = flip angle. Note that slice number and field of view (FOV) was adjusted per patient to ensure full lung coverage

Acquisition	Sequence	TR (ms)	TE (ms)	FA (°)	Bandwidth (kHz)	Matrix size (frequency x phase)	FOV (cm)	Voxel size (mm)	Slice thickness (mm)	Slices
^{1}H (3D)	SPGR	1.5	0.6	5	167	100x100	40-48	4x4-4.8x4.8	5	46-50
^{3}He (3D)	SSFP	1.9	0.6	10	167	100x80	40-48	4x3.2-4.8x3.8	5	46-50
^{1}H (2D)	SSFP	2.4	0.7	50	167	128x64	32-42	2.3x3.5-3.2x4.9	10	16-24
^{3}He (2D)	SPGR	3.6	1.1	8	62.5	128x102	32-42	2.3x1.8-3.2x2.5	10	16-24

4.3.2.1 Healthy children, children with CF and patients with asthma (2D sequences)

34 patients with asthma, 19 children with CF and 9 healthy children underwent multi-slice 2D spoiled gradient echo HP ^{3}He ventilation imaging. Patients with asthma inhaled of 350ml ^{3}He mixed with 650ml N_2 from FRC. CF and HC subjects inhaled an amount of ^{3}He based empirically on their FRC [341] mixed with an equal amount of N_2 from FRC. Prior to the ^{3}He scan a ^{1}H anatomical image at the same inflation level as the ^{3}He scan was acquired. In addition all subjects underwent spirometry and multiple breath washout (MBW) [120] in the supine position to calculate LCI, S_{cond} and S_{acin} [342]. See Table 4.2 for imaging sequence parameters.

4.3.2.2 Healthy adults, patients with COPD and patients with asthma (3D sequence)

Three-dimensional ^{1}H anatomical (SPGR) and HP ^{3}He ventilation-weighted (bSSFP) images were acquired during the same breath hold for 11 healthy volunteers, 10 patients with COPD and 5 patients with asthma, [73, 66]. Imaging parameters can be seen in Table 4.2. HP gas ventilation-weighted images were acquired followed immediately by ^{1}H anatomical images. Patients inhaled 200mL HP ^{3}He mixed with 800mL N_2 from FRC prior to the scan.

4.3.3 Imaging sequence effects on CV

4.3.3.1 Participants and materials and methods

Three of the aforementioned 11 HAs were analysed to investigate the impact of a 2D and 3D sequence on CVH analysis. It was restricted to these subjects, since they were the only participants with 2D SPGR HP ^{3}He scans carried out on the same day. The method described in section 4.2 was used to calculate CV with a kernel size of 3 voxels, and CV was analysed in plane only. This kernel size was chosen based on the size of the voxels of the acquired images to allow a fair comparison by including approximately the same in-plane area and thus an approximately equal number of acini in the measurement of CV. HAs were scanned using the 2D and 3D HP ^{3}He sequences presented in section 4.3.1. A 3D SPGR ^{1}H image was acquired following the 2D ^{3}He image for the 2D acquisitions, rather than a 2D SSFP ^{1}H image acquired in a separate-breath.

4.3.3.2 Results

No statistical tests were carried out to compare SSFP and SPGR CV metrics due to the small sample size. When calculating the CV metrics using the VV mask mean and median CV were increased, CVH skewness and kurtosis increased and CVH IQR decreased for all participants when imaged using the 2D SPGR sequence compared to the 3D SSFP sequence. When calculating the CV metrics using the TLV mask mean and median CV were increased, CVH skewness and kurtosis decreased and CVH IQR increased for all participants when imaged using the 2D SPGR sequence compared to the 3D SSFP sequence. These changes are likely due to the generally lower SNR of the 2D SPGR data when compared to the 3D bSSFP data [72] and the fact the SPGR images are more heavily T2* weighted and thus show more contrast around regions of abrupt susceptibility difference e.g. next to the pulmonary blood vessels [343]. It should be noted that this change in SNR is affected mostly by the 2D and 3D nature of the sequences being acquired rather than the difference caused in signal generated using SPGR or SSFP imaging techniques. To assess the effect of imaging sequence on CV correctly a 3D SPGR and 3D bSSFP image should be acquired in healthy volunteers with the same dose of HP gas given to assess the change caused by the sequence.

4.3.4 SNR effect on CV

4.3.4.1 Participants and materials and methods

To simulate the effect of image SNR on CVH analysis the 3D images of the 11 HAs scanned were analysed along with the asthma_clinical cohort, 5 of the 10 COPD cohort and 5 of the 19 CF cohort. Gaussian white noise [344] was added to k-space to create images with approximately 75%, 50%, 25%, 10% and 5% of the original SNR. The k-space with noise added was then reconstructed into image space and analysed using the 2D CV code described in section 4.2 with a kernel size of 3x3 voxels.

4.3.4.2 Results – Healthy adults

Figure 4.5 shows an example image with an SNR of 42 (a) and 3 (d) with the corresponding CV maps generated on the ventilated lung volume mask (b,e) and the total lung volume mask (c,f). As can be seen the CV maps generated from the image with an SNR of 3 using the VV and TLV masks are quite different. This is because some voxels within the ventilated volume did not meet the SNR>2 criteria and thus are excluded from the SNR based ventilated volume mask (i.e. the black voxels within the lungs in Figure 4.5f). However, as they are within the total lung volume mask they are set to 0, causing the surrounding regions to have increased CV due to their inclusion in the CV calculation.

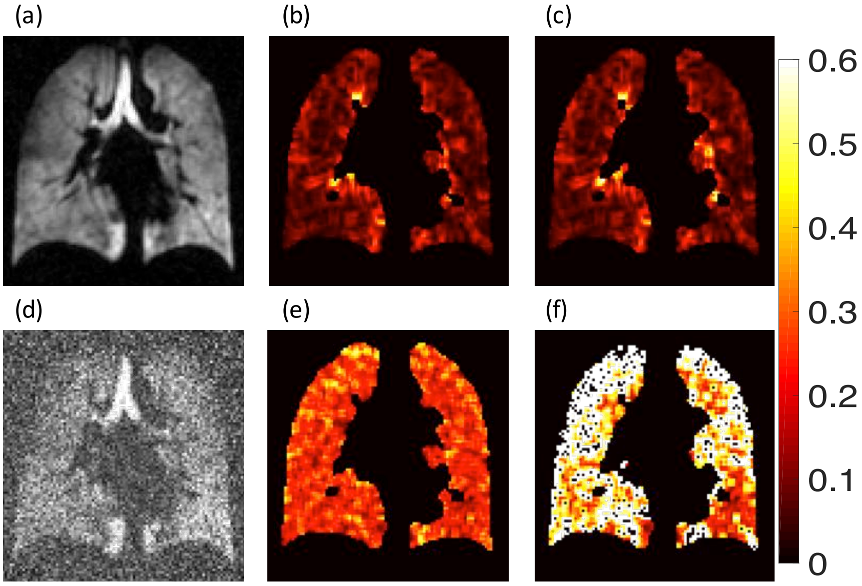

Figure 4.5 Example images from HA5 used to determine the effect of SNR on CV metrics. (a) original image with an SNR of 42 (b) the CV map generated from the original image and VV mask, (c) the CV map generated from the original image and TLV mask, (d) image with an SNR of 3, (e) the CV map generated from the image with an SNR of 3 and VV mask and (f) the CV map generated from the image with an SNR of 3 and TLV mask

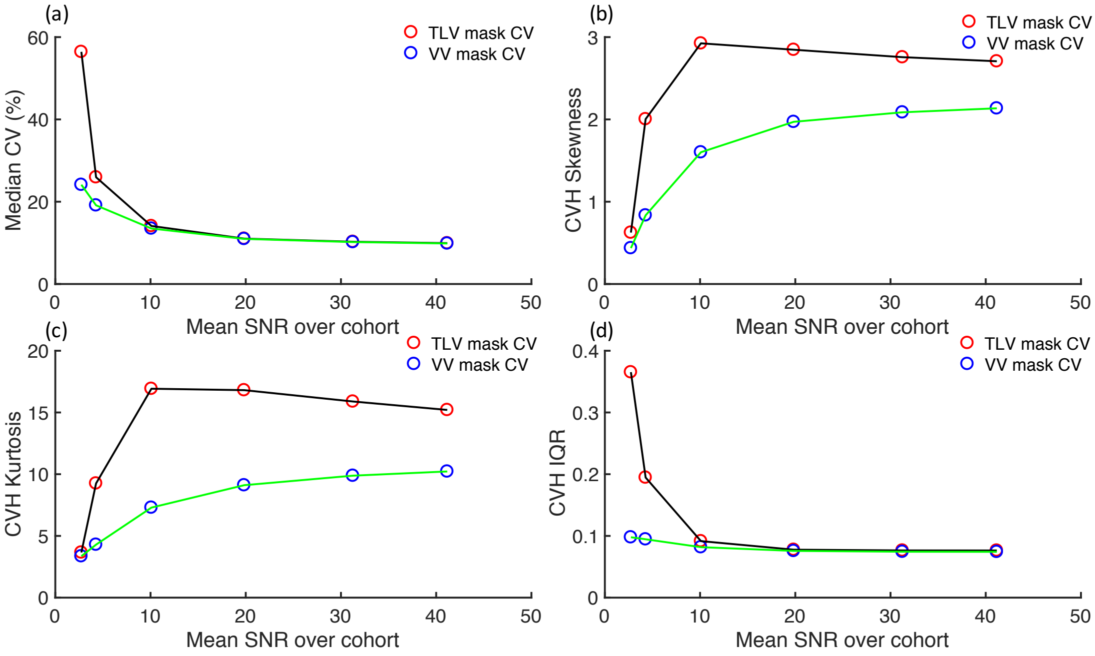

Figure 4.6 HA cohort average values CV metrics plotted as a function of SNR. (a) median CV, (b) CVH skewness, (c) CVH kurtosis and (d) CVH IQR generated from the VV and TLV masks. Note that each point represents the mean of all 11 HAs at each SNR level

As SNR decreased median CV increased as did CVH IQR whilst CVH skewness and kurtosis decreased, this is true for both VV and TLV mask generated CV metrics.

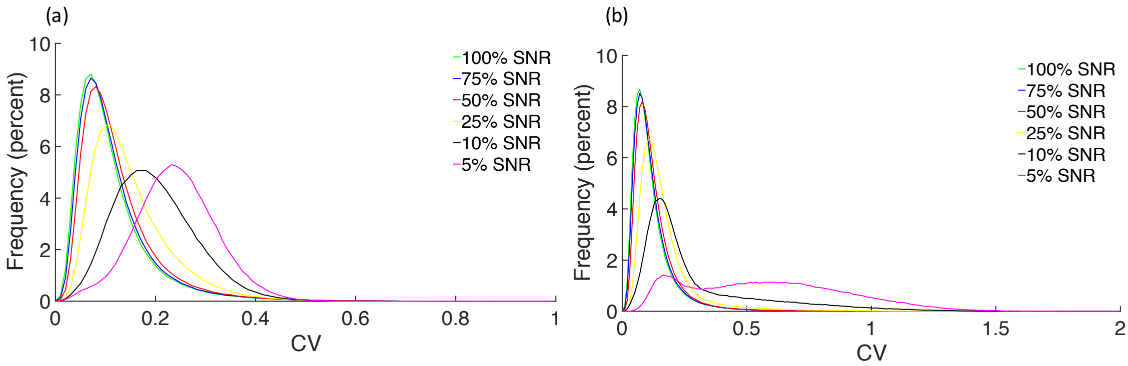

Figure 4.7 HA cohort average histograms for all 6 SNR levels generated from the (a) VV mask and (b) TLV mask

The histograms shown in Figure 4.7 shows little variation between 100% and 75% SNR with almost no movement in the peak location and very similar shapes. As SNR decreases, there is a clear shift to a higher peak location and a more Gaussian distribution, seen most clearly in the 5% SNR histogram when considering the CV histograms generated from the VV mask. When considering the CV histograms generated from the TLV masks there is the addition of a second peak at the lowest SNR value, with a similar pattern of a shifted peak as the SNR drops. The Friedman's test summary for CV metrics generated using the VV and TLV masks can be seen in Table 4.3.

Table 4.3 P-values returned by the multiple comparisons of the Friedman test comparing each SNR level to the control (100% SNR) when considering CV metrics generated from the VV mask and TLV mask

Comparison	Mean CV	Median CV	CVH skewness	CVH kurtosis	CVH IQR
100% SNR vs. 75% SNR	0.8573	0.8573	>0. 9999	>0. 9999	>0. 9999
100% SNR vs. 50% SNR	0.0438	0.0438	0.0835	0.0835	>0.9999
100% SNR vs. 25% SNR	0.0025	0.0025	0.0039	0.0039	0.7715
100% SNR vs. 10% SNR	<0.0001	<0.0001	<0.0001	<0.0001	0.0017
100% SNR vs. 5% SNR	<0.0001	<0.0001	<0.0001	<0.0001	0.0021
TLV metrics					
100% SNR vs. 75% SNR	0.9501	0.9501	>0.9999	>0.9999	>0.9999
100% SNR vs. 50% SNR	0.0517	0.0517	>0.9999	0.7715	>0.9999
100% SNR vs. 25% SNR	0.0007	0.0007	>0.9999	0.9501	0.8573
100% SNR vs. 10% SNR	<0.0001	<0.0001	>0.9999	>0.9999	0.0058
100% SNR vs. 5% SNR	<0.0001	<0.0001	0.0183	0.0058	<0.0001

Table 4.3 documents that there was no significant difference between any CV metric when image SNR is reduced to 75% of its original value when considering the metrics generated using the VV mask, with the lowest SNR seen in these healthy volunteers being 22 (at 100% SNR). Additionally, there was no significant difference between CV histogram metrics (skewness, kurtosis and IQR) as the image SNR was reduced to 50% of the original SNR. Once the image reaches 25% of the original SNR all metrics bar IQR had significant differences and as one would expect once the image SNR was 10% of the original value there were significant differences in all metrics. These differences of course depend on the original

value of the image SNR. When considering the TLV metrics mean and median CV did not become significantly different until the image reached 25% of its SNR level whilst CVH metrics do not become significantly different until the image reached 10% of its original value for IQR and 5% of its original value for skewness and kurtosis. The TLV mask based method of calculating CV is of course more heavily influenced by the image SNR as is demonstrated with the large changes seen as image SNR drops below 10 (Figure 4.6), which also demonstrated the relative stability of the VV based method even at these low SNR values. The primary reason for this is of course the defined ventilated volume mask remains the same whilst the voxels included based on the SNR threshold will vary greatly. There is also a clear offset in values of CVH skewness and kurtosis which narrows as the SNR drops below 10, suggesting much more similar distributions, even with the introduction of a second peak using the TLV based CV method. As analysing the mean and median of this cohort resulted in identical p-values it was decided to continue the analysis by analysing the median values of the CV maps only.

4.3.4.3 Results – Patients with asthma

Figure 4.8 shows an example image with an SNR of 70 (a) and 4 (d) with the corresponding CV maps generated using the ventilated lung volume mask (b,e) and the total lung volume mask (c,f). As can be seen the same pattern of increased overall heterogeneity was seen in this patient with asthma as was seen in the healthy adult shown in Figure 4.5.

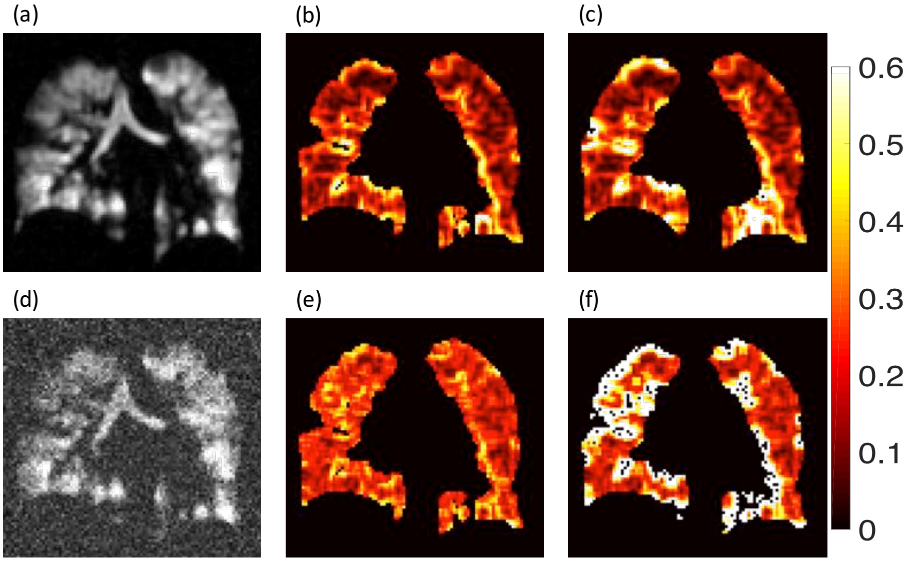

Figure 4.8 Example images from a patient with asthma used to determine the effect of SNR on CV metrics. (a) original image with an SNR of 70 (b) the CV map generated from the original image and VV mask, (c) the CV map generated from the original image and TLV mask, (d) image with an SNR of 4, (e) the CV map generated from the image with an SNR of 4 and VV mask and (f) the CV map generated from the image with an SNR of 4 and TLV mask

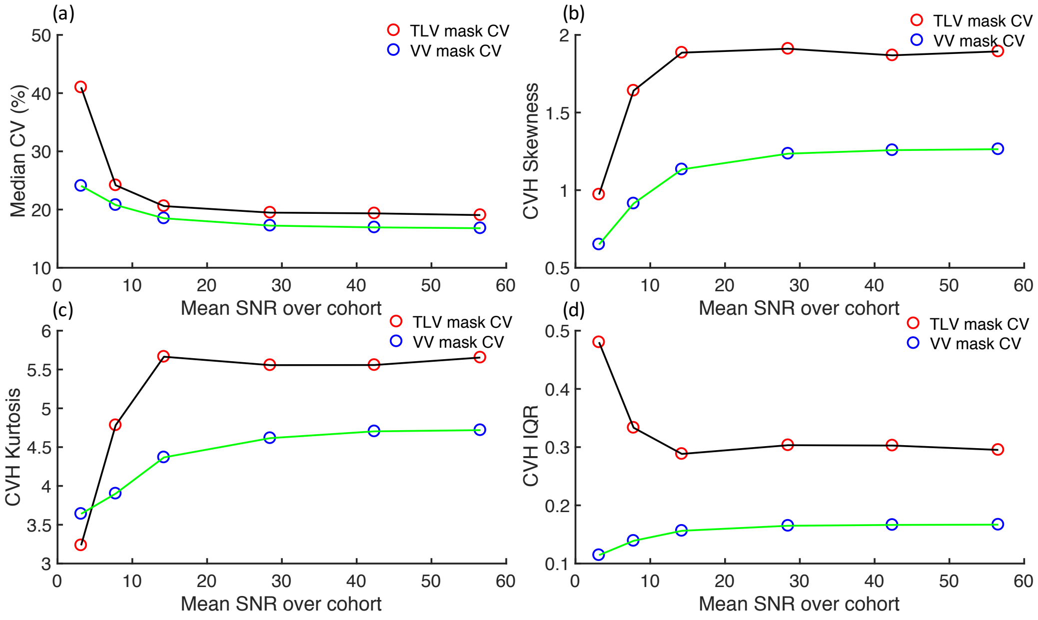

Figure 4.9 Asthma_clinical cohort average values CV metrics plotted as a function of SNR. (a) median CV, (b) CVH skewness, (c) CVH kurtosis and (d) CVH IQR generated from the VV and TLV masks. Each point represents all 5 patients with asthma

For patients with asthma the trends were similar for median CV, CVH skewness and kurtosis as those reported for the healthy adults. However, CVH IQR decreased as the SNR decreased when using the values from the VV mask and increased when using the TLV mask. In addition, the peak shifted to a higher CV value, and a more Gaussian distribution at lower SNR is observed when considering the histograms generated from the VV mask. Figure 4.10 shows increased high CV tails compared to the HAs histograms. This is due to the fact that patients with obstructive airways disease in general will have a higher fraction of pixels with higher CV (CV>0.3). Histograms generated from the TLV mask do not change in the same way as those generated from the VV mask with an increased number of high CV values seen rather than a more Gaussian distribution.

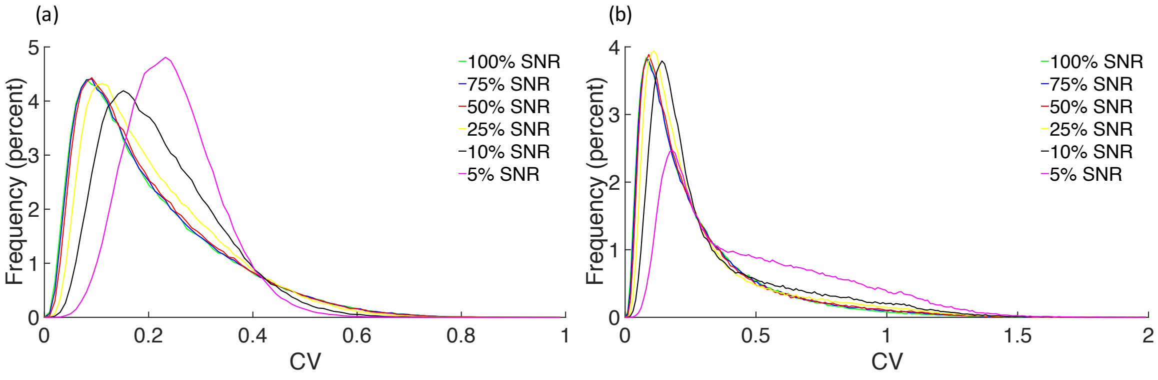

Figure 4.10 Asthma_clinical cohort average histograms for all 6 SNR levels generated from the (a) VV mask and (b) TLV mask

4.3.4.4 Results – Patients with COPD

Figure 4.11 shows an example image with an SNR of 66 (a) and 4 (d) with the corresponding CV maps.

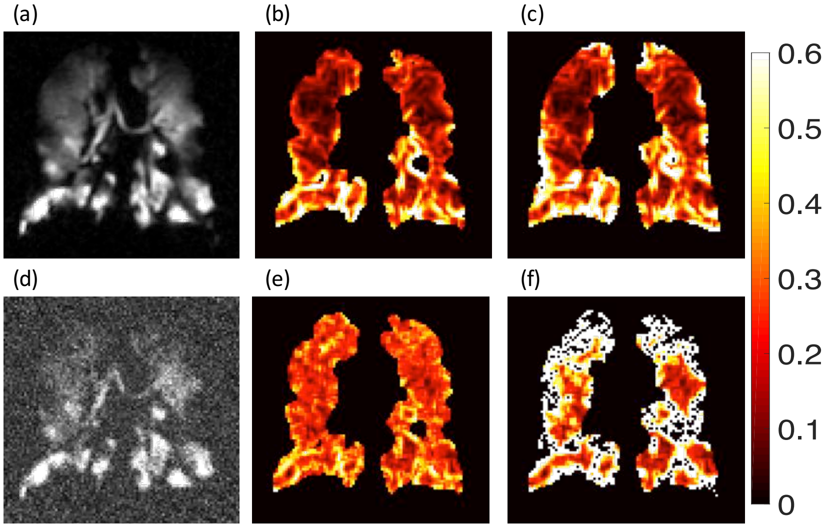

Figure 4.11 Example images from a patient with COPD used to determine the effect of SNR on CV metrics. (a) original image with an SNR of 66 (b) the CV map generated from the original image and VV mask, (c) the CV map generated from the original image and TLV mask, (d) image with an SNR of 4, (e) the CV map generated from the image with an SNR of 4 and VV mask and (f) the CV map generated from the image with an SNR of 4 and TLV mask

The trends for median CV, CVH skewness, kurtosis and IQR are similar to those seen for the patients with asthma as seen in Figure 4.12.

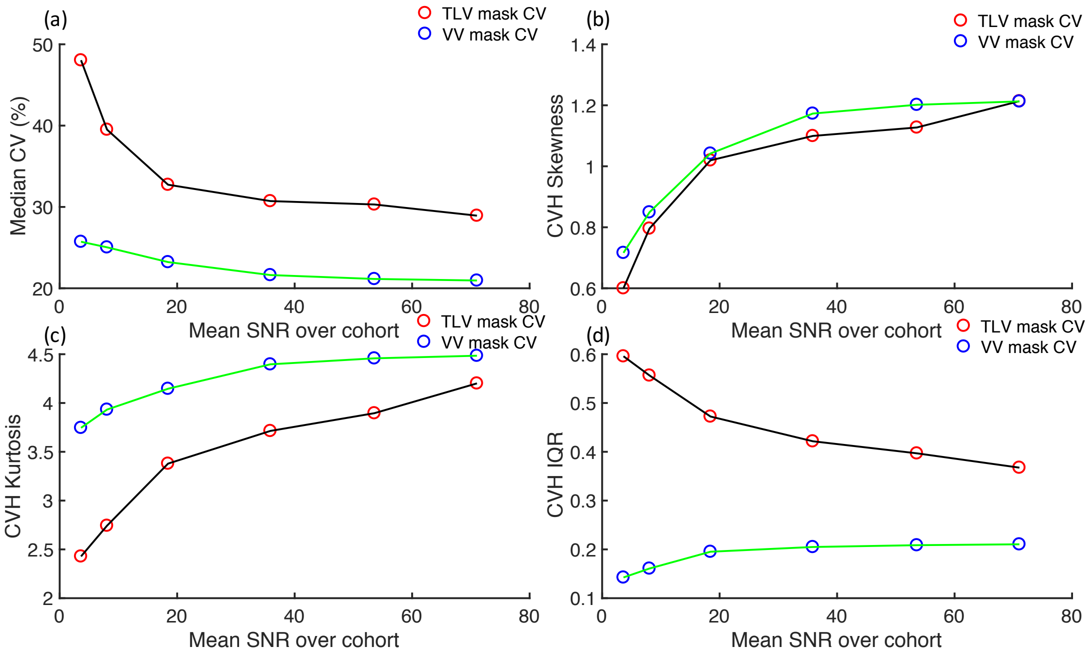

Figure 4.12 COPD cohort average values CV metrics plotted as a function of SNR. (a) median CV, (b) CVH skewness, (c) CVH kurtosis and (d) CVH IQR generated from the VV and TLV masks. Each point represents all 5 patients with COPD

Furthermore, the shapes of the histograms for the patients with COPD (Figure 4.13) are similar to those for the patients with asthma, up until the image reaches 10% of the original SNR with the appearance of a second peak occurring at this point in these COPD patients when considering the histograms generated using the TLV mask.

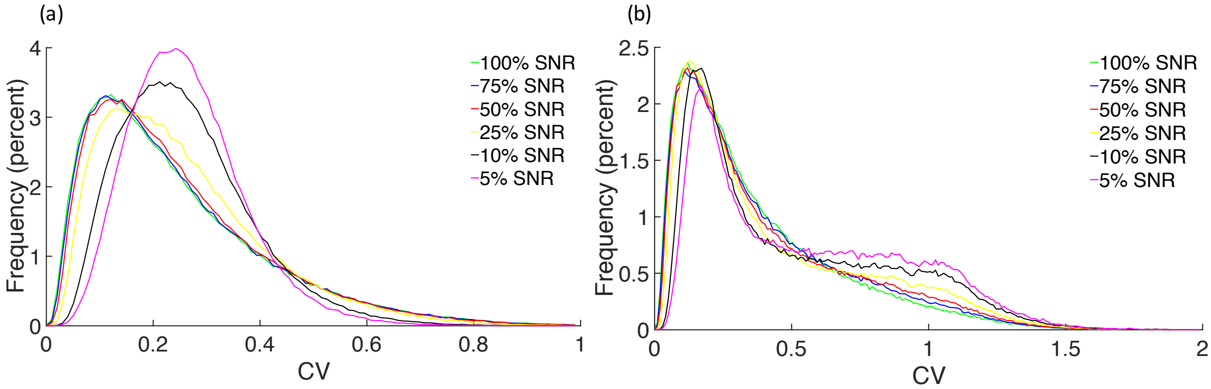

Figure 4.13 COPD cohort average histograms for all 6 SNR levels levels generated from the (a) VV mask and (b) TLV mask

4.3.4.5 Results – Children with CF

Figure 4.14 shows an example image with an SNR of 53 (a) and 3 (d) with the corresponding CV maps.

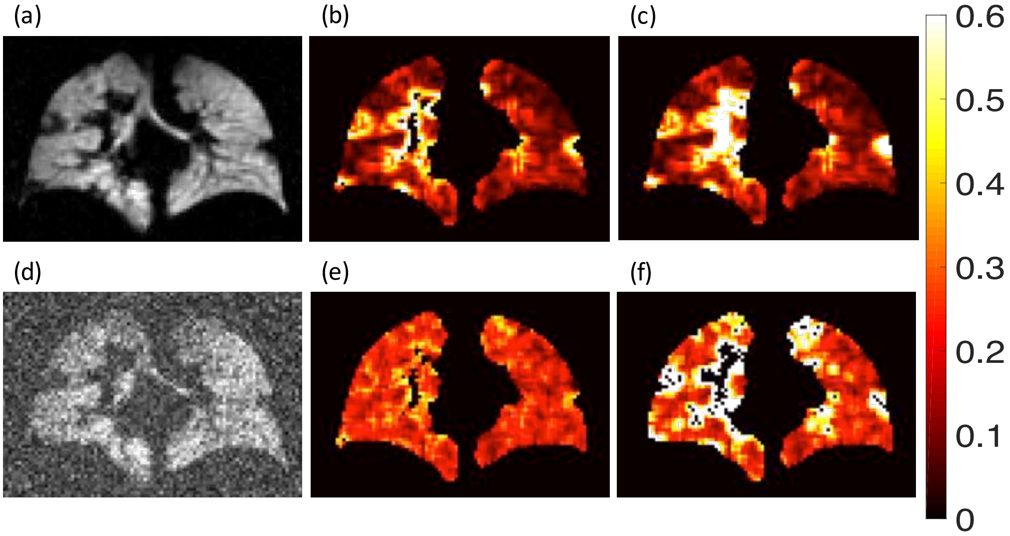

Figure 4.14 Example images from a patient with CF used to determine the effect of SNR on CV metrics. (a) original image with an SNR of 53 (b) the CV map generated from the original image and VV mask, (c) the CV map generated from the original image and TLV mask, (d) image with an SNR of 3, (e) the CV map generated from the image with an SNR of 3 and VV mask and (f) the CV map generated from the image with an SNR of 3 and TLV mask

Figure 4.15 shows the effect of changing SNR on median CV, skewness, kurtosis and IQR when generated from the VV mask and the TLV masks over the CF cohort analysed.

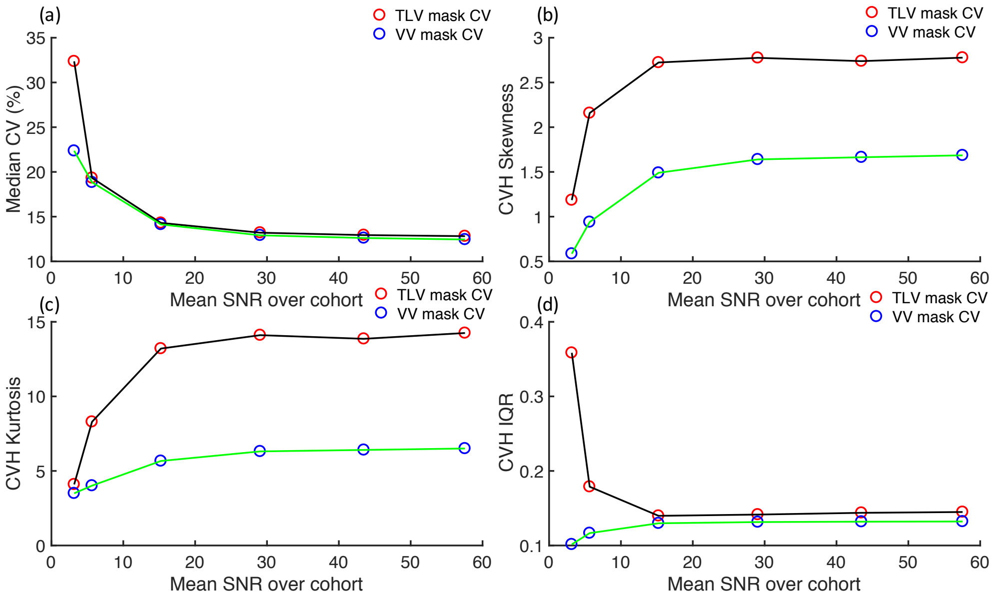

Figure 4.15 CF cohort average values CV metrics plotted as a function of SNR. (a) median CV, (b) CVH skewness, (c) CVH kurtosis and (d) CVH IQR generated from the VV and TLV masks. Each point represents all 5 patients with CF

The patterns seen in are similar to those seen in the HAs. Figure 4.16 shows the results of changing the SNR on the cohort average histograms of the CF patients when generated using VV and TLV masks. As can be seen the peak shifts to the right as the SNR decreases with an increased number of CV values >0.3, rather than a shift to a more Gaussian distribution when visually assessing the CV histograms generated from the TLV mask and comparing them to those generated from the VV mask.

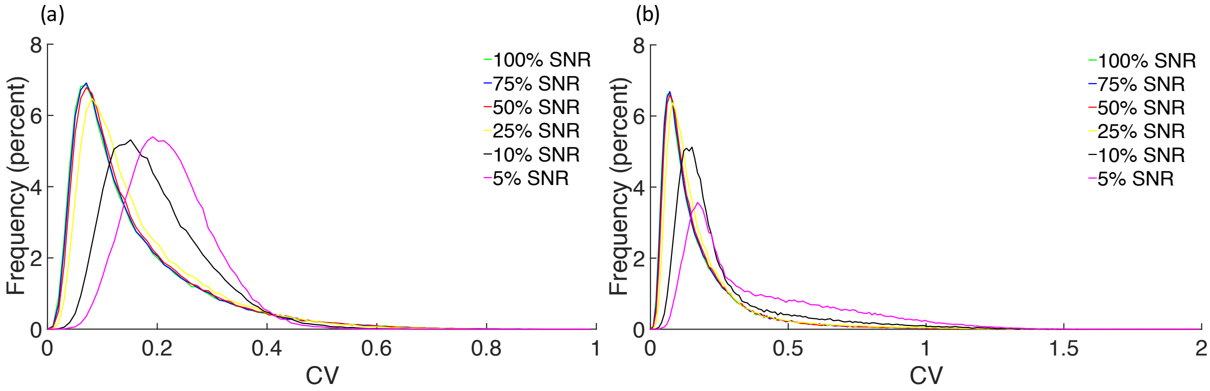

Figure 4.16 CF cohort average histograms for all 6 SNR levels generated from the (a) VV mask and (b) TLV mask

CF histograms do not display the same frequency of high CV values as the other disease cohorts analysed when using the VV mask, possibly due to the mild nature and limited lung obstruction of these patients when compared to the other disease cohorts.

4.3.5 Effect of kernel size on CV

4.3.5.1 Participants and materials and methods

All aforementioned datasets were analysed using the CV method mentioned in section 4.2 to study the effect of kernel size on CV and CVH metrics. Kernel sizes of 3, 5, 7 and 9 voxels were investigated for 2D CV calculation. Note that these kernel sizes were based on the resolution of the images used here as well as the size of the human acini [336-338].

4.3.5.2 Results

Figure 4.17 shows the effect of changing kernel size on the CV map of a patient with COPD, generated using both the VV and TLV masks. With increasing kernel size the CV map becomes smoothed as more voxels are contained within the neighbourhood with any areas of high CV being exaggerated as the kernel size increases from 3x3 to 9x9 voxels.

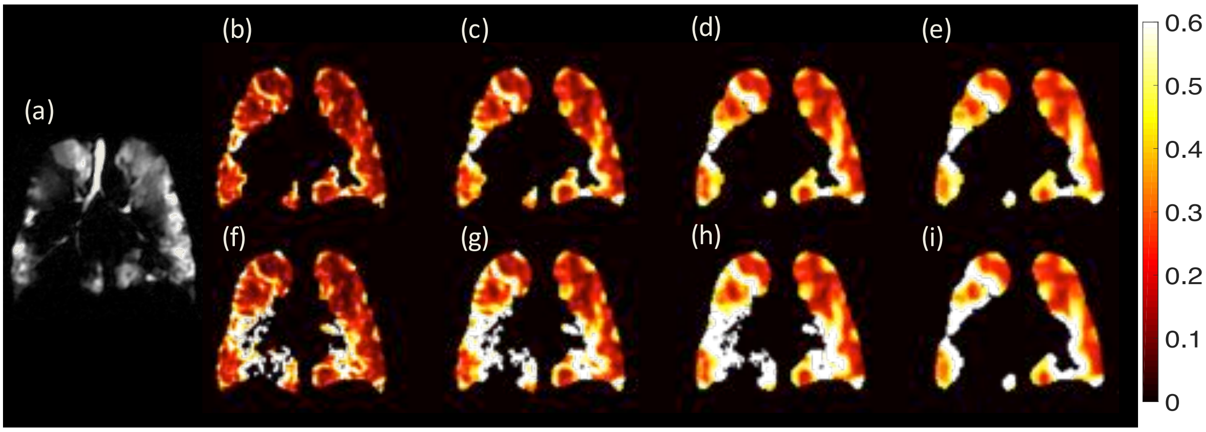

Figure 4.17 Examples of the original image and CV maps after increasing the kernel size from a patient with COPD. (a) original ventilation image, (b) 3 by 3 voxel kernel CV map generated from the VV mask, (c) 5 by 5 voxel kernel CV map generated from the VV mask, (d) 7 by 7 voxel kernel CV map generated from the VV mask, (e) 9 by 9 voxel kernel CV map generated from the VV mask, (f) 3 by 3 voxel kernel CV map generated from the TLV mask, (g) 5 by 5 voxel kernel CV map generated from the TLV mask, (h) 7 by 7 voxel kernel CV map generated from the TLV mask and (i) 9 by 9 voxel kernel CV map generated from the TLV mask

Additionally, the median CV over the whole map increases as the kernel size increases as represented by the shifting peak seen in the example histograms (Figure 4.18).

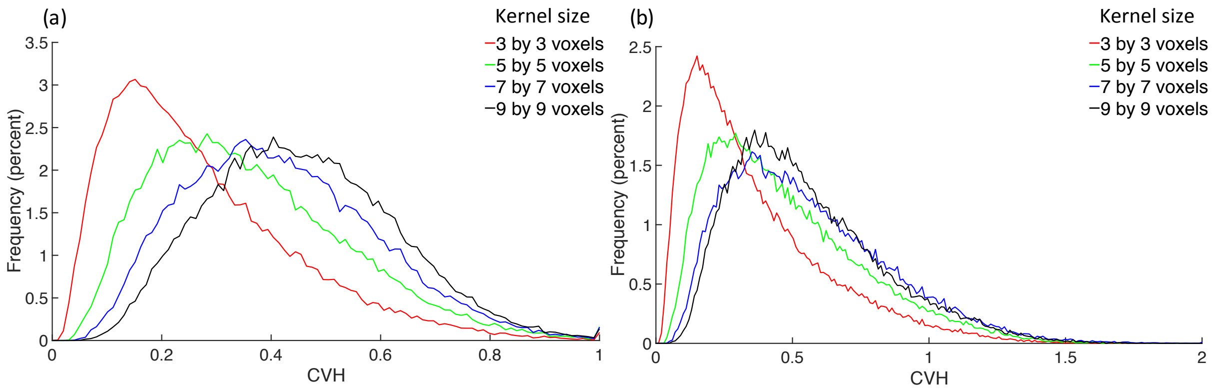

Figure 4.18 CV histograms generated using different kernel sizes from a patient with COPD generated using the (a) VV mask and (b) TLV mask

Figure 4.19 shows the effect of increasing kernel size for all groups on median CV measurements generated from the VV mask and Figure 4.20 shows the change when considering metrics generated from the TLV mask. There is a clear trend of increasing median CV in all groups as the kernel size increases.

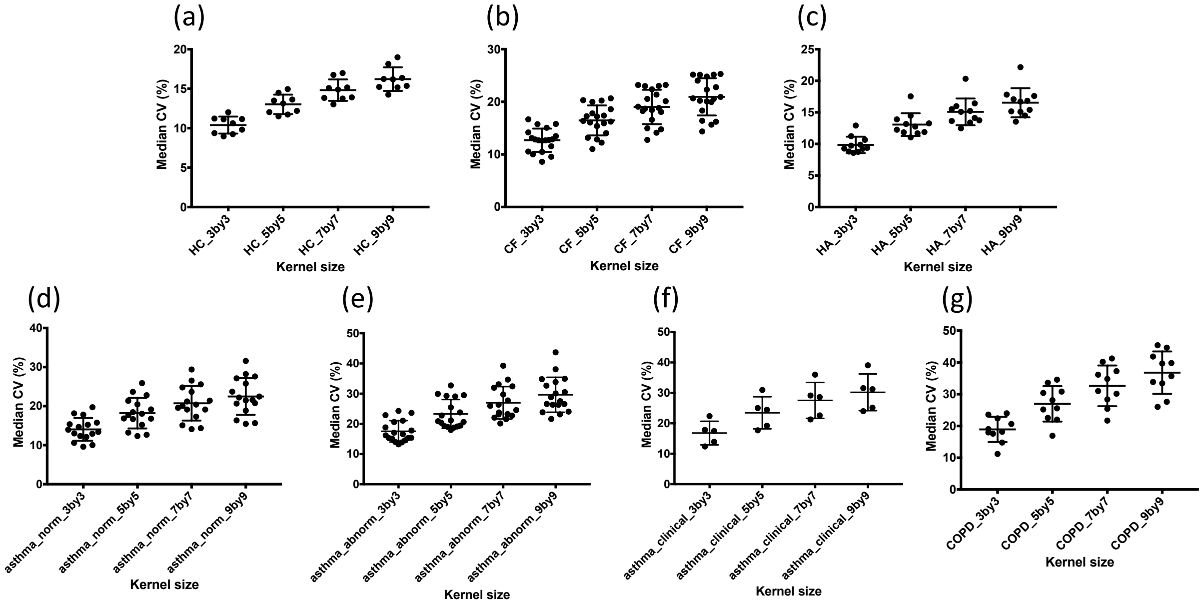

Figure 4.19 Plots of median CV for different kernel sizes for all groups generated from the VV mask. (a) HC, (b) CF, (c) HV, (d) asthma_clincial, (e) COPD, (f) asthma_norm and (g) asthma_abnorm. Each point represents a measurement from a single subject, error bars represent group means and standard deviations

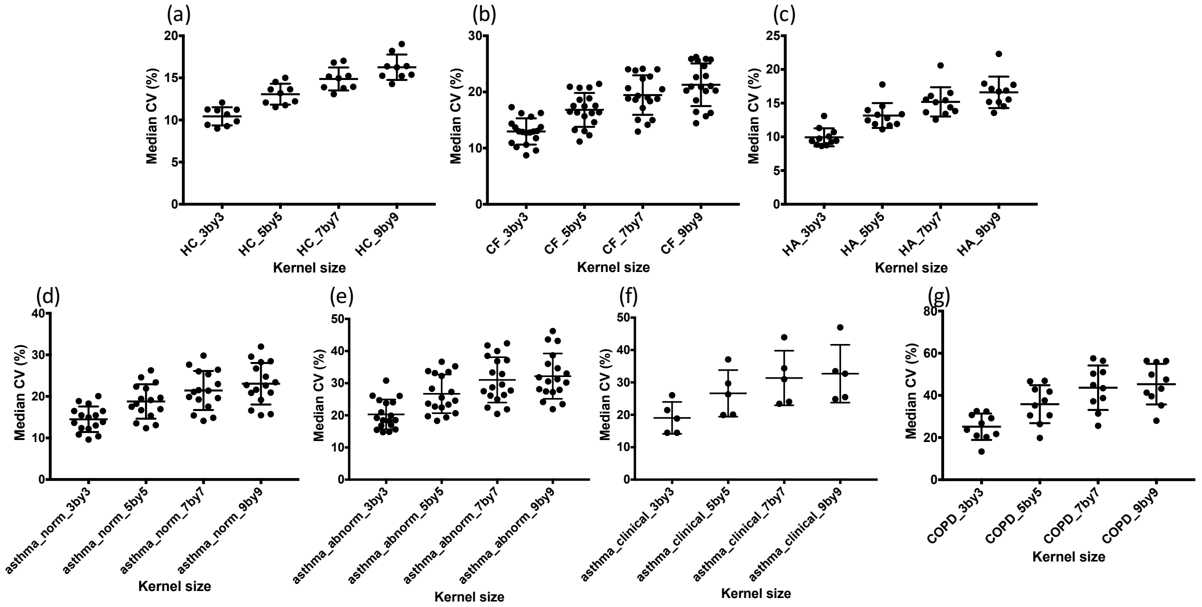

Figure 4.20 Plots of median CV for different kernel sizes for all groups generated from the TLV mask. (a) HC, (b) CF, (c) HV, (d) asthma_clincial, (e) COPD, (f) asthma_norm and (g) asthma_abnorm. Each point represents a measurement from a single subject, error bars represent group means and standard deviations

Increase in kernel size causes a decrease in CVH skewness for all groups as shown in Figures 4.21 and 4.22 and this pattern is seen when the CV metrics are generated from both the VV and TLV masks.

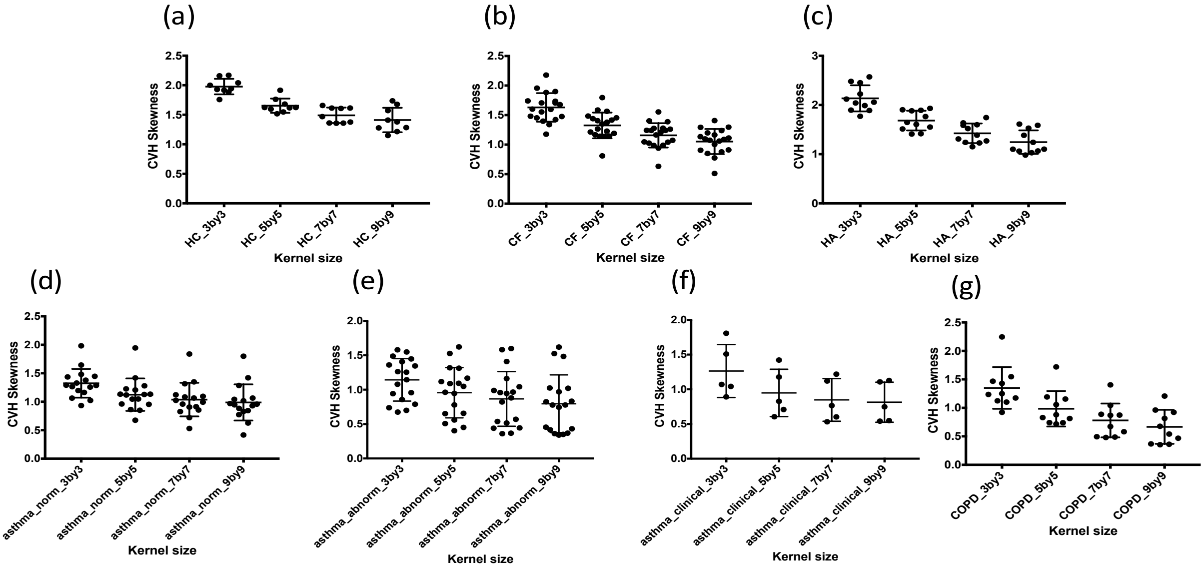

Figure 4.21 Plots of CVH skewness at different kernel sizes for each of the groups of subjects imaged generated from the VV mask. (a) HA, (b) HC, (c) asthma_clinical, (d) COPD, (e) CF, (f) asthma_norm and (g) asthma2Dabnorm. Each point represents a measurement from a single subject, error bars represent group means and standard deviations

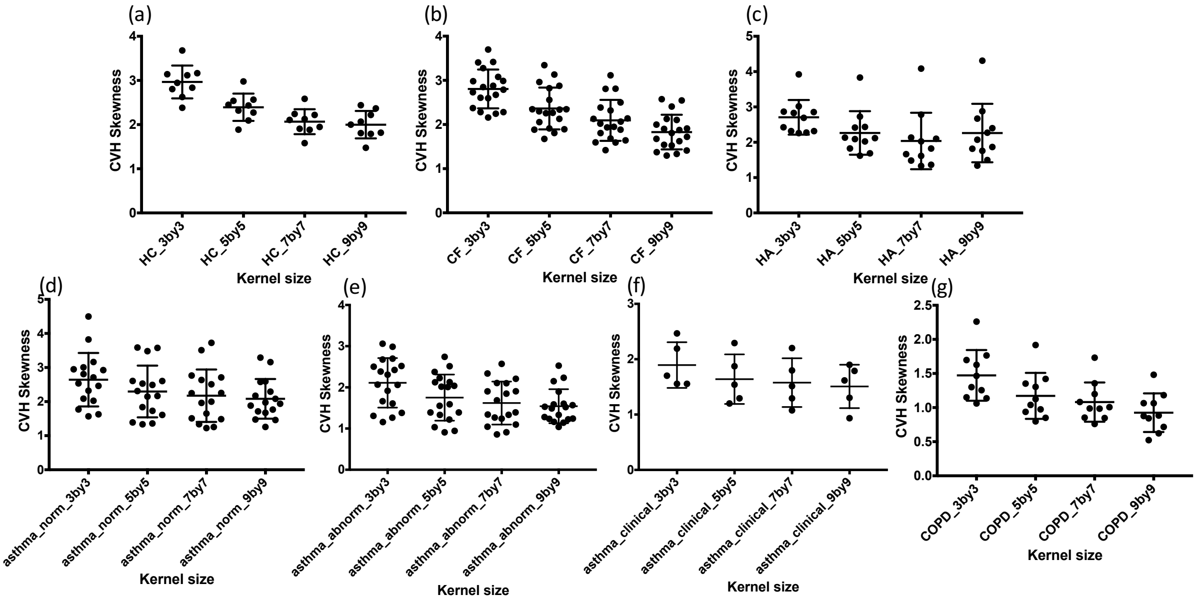

Figure 4.22 Plots of CVH skewness at different kernel sizes for each of the groups of subjects imaged generated from the TLV mask. (a) HA, (b) HC, (c) asthma_clinical, (d) COPD, (e) CF, (f) asthma_norm and (g) asthma2Dabnorm. Each point represents a measurement from a single subject, error bars represent group means and standard deviations

CVH kurtosis also decreases as the kernel size increases (Figures 4.23 to 4.24) with the most marked change being seen between the kernel sizes of 3 and 5 voxels for all groups and this pattern is seen when the CV metrics are generated from both the VV and TLV masks.

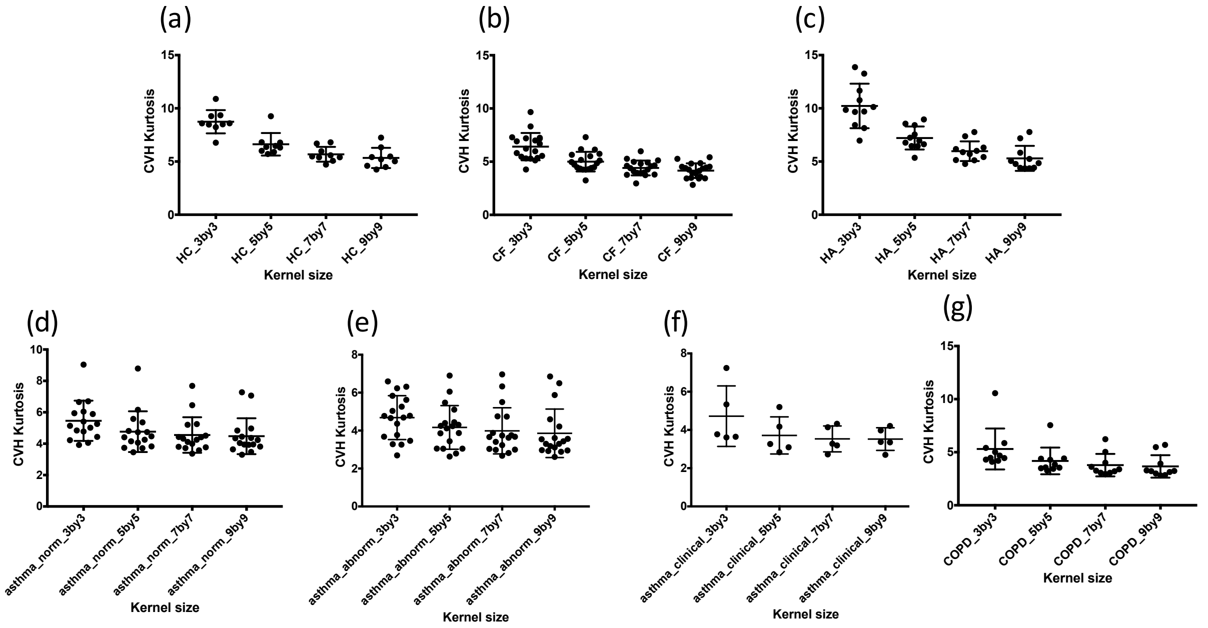

Figure 4.23 Plots of CVH kurtosis at different kernel sizes for all groups generated from the VV mask. (a) HC, (b) CF, (c) HV, (d) asthma_clincial, (e) COPD, (f) asthma_norm and (g) asthma_abnorm. Each point represents a measurement from a single subject, error bars represent group means and standard deviations

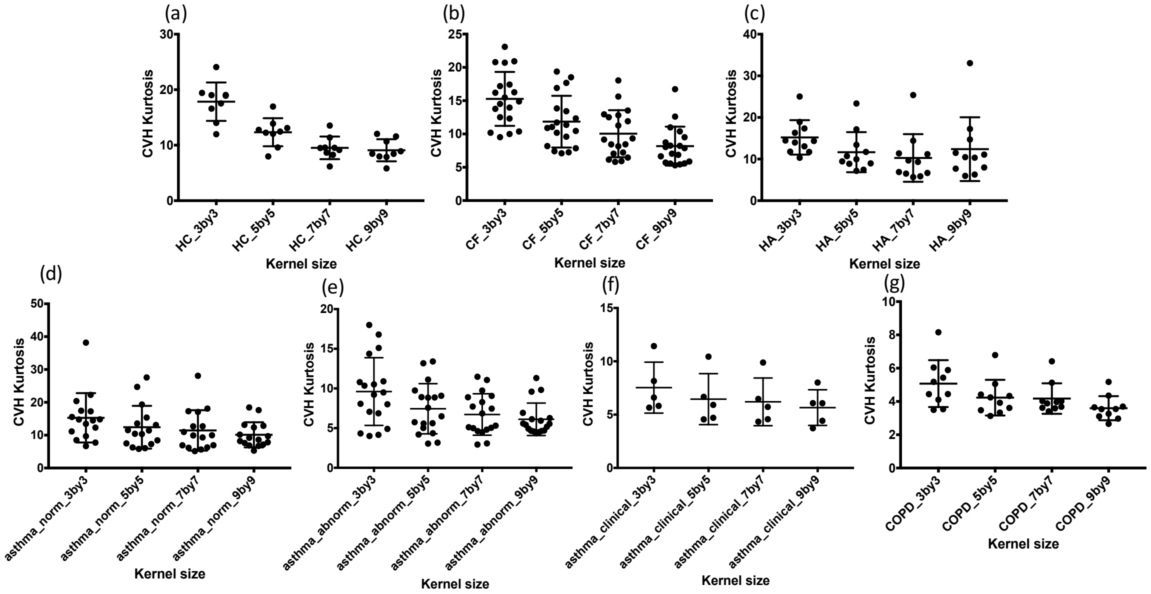

Figure 4.24 Plots of CVH kurtosis at different kernel sizes for all groups generated from the TLV mask. (a) HC, (b) CF, (c) HV, (d) asthma_clincial, (e) COPD, (f) asthma_norm and (g) asthma_abnorm. Each point represents a measurement from a single subject, error bars represent group means and standard deviations

CVH IQR increases as kernel size increases for HA, HC and COPD groups (Figures 4.25 to 4.26). However, for the asthma_clinical group there is an increase between 3 and 7 voxels and then a decrease at 9 voxels, this pattern is also seen, but not to the same extent, in both asthma groups scanned with the 2D sequence. CF patients have an increase when the kernel size increases from 3 to 5 voxels, with the values at a kernel size of 5 and 7 voxels being similar before a slight decrease at a kernel size of 9 voxels occurs when generated from the VV mask.

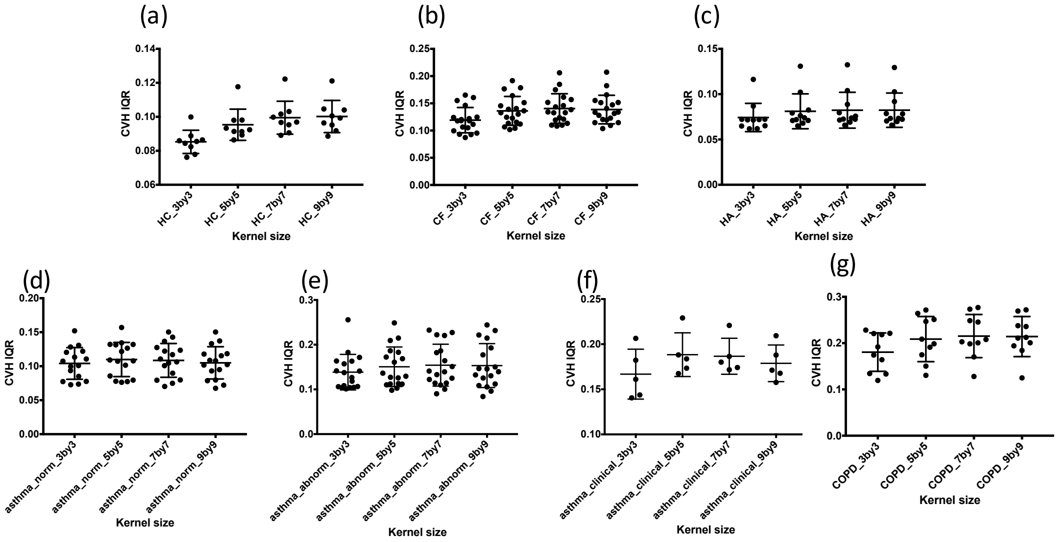

Figure 4.25 Plots of CVH IQR at different kernel sizes for each of the groups of subjects imaged generated from the VV mask. (a) HC, (b) CF, (c) HV, (d) asthma_clincial, (e) COPD, (f) asthma_norm and (g) asthma_abnorm. Each point represents a measurement from a single subject, error bars represent group means and standard deviations

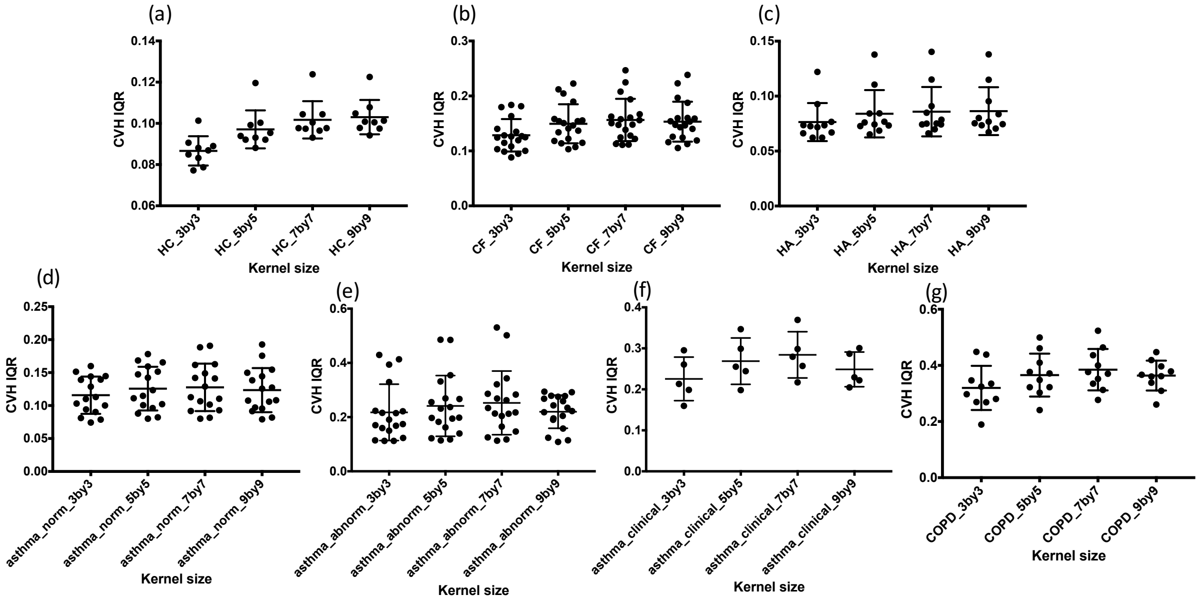

Figure 4.26 Plots of CVH IQR at different kernel sizes for each of the groups of subjects imaged generated from the TLV mask. (a) HC, (b) CF, (c) HV, (d) asthma_clincial, (e) COPD, (f) asthma_norm and (g) asthma_abnorm. Each point represents a measurement from a single subject, error bars represent group means and standard deviations

When considering the metrics generated from the TLV mask CVH IQR increases as kernel size increases for the HC and HA groups, although the increase is minimal in the HA group when compared to the HC group. Patients with CF and asthma CVH IQR values increase as the kernel increases from 3 to 7 voxels with a small reduction in CVH IQR between the kernel sizes of 7 and 9 voxels. Interestingly COPD patients follow this pattern when the metrics are generated from the TLV mask.

4.3.6 2D vs 3D dimensionality - effect on CV

4.3.6.1 Participants and materials and methods

All participants scanned with the 3D bSSFP ^{3}He sequence were analysed to compare the effect of the dimensionality of the kernel used on CV and CVH metrics. A kernel size of 3x3 voxels was used for 2D CV calculation, and a kernel size of 3x3x3 voxels (~9x9x10mm) was used for 3D CV calculation – this resulted in an approximately isotropic cube once the 3D image was subsampled.

4.3.6.2 Results

Figure 4.27 shows the results of changing the dimensionality of the kernel used to generate CV maps from images of a healthy volunteer and patients with COPD and asthma. Changing from a 2D to a 3D kernel introduced pronounced smoothing. Additionally, areas of high CV became more pronounced in the 3D CV map, particularly for the patients with asthma and COPD (note that the same pattern is seen when considering the CV map generated using the TLV mask).

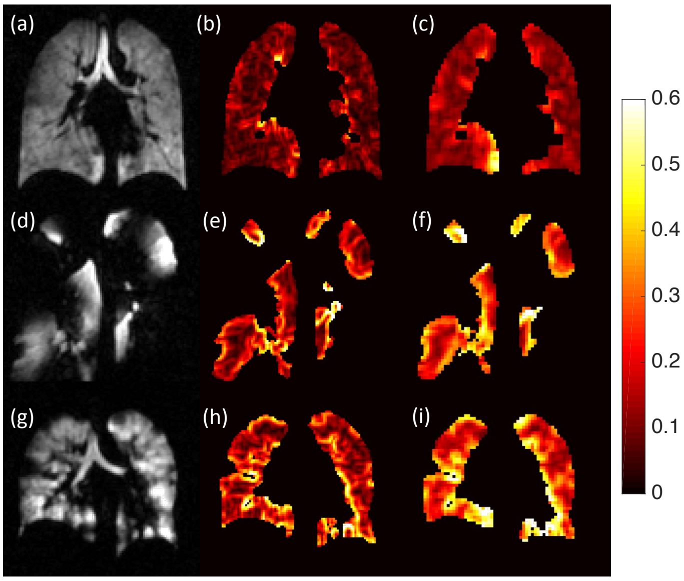

Figure 4.27 Example slices of a 3D ventilation image dataset and the corresponding CV maps generated from 2 and 3 dimensional kernels and the VV mask generated from a healthy volunteer (a-c) a patient with COPD (d-f) and a patient with asthma (g-i). (a) HA ventilation image, (b) HA 2D CV map, (c) HA 3D CV map, (d) COPD ventilation image, (e) COPD 2D CV map, (f) COPD 3D CV map, (g) patient with asthma ventilation image, (h) patient with asthma 2D CV map and (i) patient with asthma 3D CV map

This change can also be seen in the histograms for these examples (Figure 4.28), with a broader shape and peak shifted to the right indicating higher CV overall in the 3D map when compared to the 2D map.

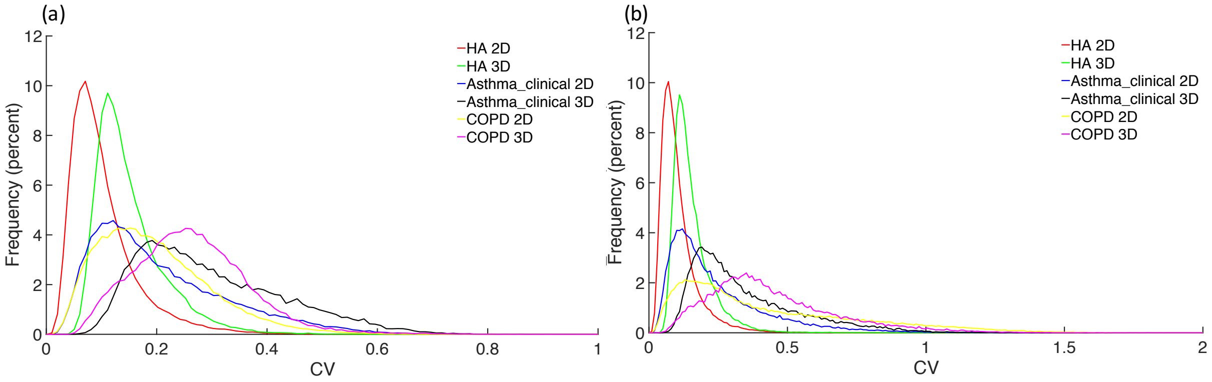

Figure 4.28 Example histograms for the HA, asthma and COPD patients shown in Figure 4.27 generated using the (a) VV mask and (b) the TLV mask

Figure 4.29 shows plots for the three patient groups analysed to compare the effect of dimensionality on the CV metrics. When comparing the 2D and 3D metrics generated from the VV mask a significant increase was seen in median CV for HAs (p=0.0010) when a 3D kernel was used compared to a 2D kernel, as well as a significant decrease in both CVH skewness and kurtosis (p=0.0010 for both). CVH IQR changed non-significantly for HAs (p=0.2402). No significant changes were seen in median CV, CVH skewness or CVH kurtosis for the asthma_clinical group (p=0.0625 for all), but this may be due to the small sample size, and similar to the HA group no significant difference was seen in CVH IQR (p=0.1250). All metrics were significantly different using 2D and 3D kernels for the COPD group; median CV (p=0.002), CVH skewness (p=0.002), CVH kurtosis (p=0.0039) and CVH IQR (p=0.0039). When considering the 2D and 3D metrics generated from the TLV mask median CV, CVH skewness and kurtosis all increased significantly for the HAs (p=0.0010 for all) whilst CVH IQR was not significantly different (p=0.2305). No metric changed significantly for the asthma_clinical cohort (p=0.0625 for median CV, CVH skewness and kurtosis, p>0.9999 for CVH IQR). When considering the 2D and 3D metrics generated from the TLV mask for the COPD cohort median CV and CVH skewness were significantly different (p=0.0020 and p=0.0059 respectively) whilst CVH kurtosis was not significantly different (p=0.5566). In contrast to the two other cohorts analysed CVH IQR was significantly different (p=0.0195).

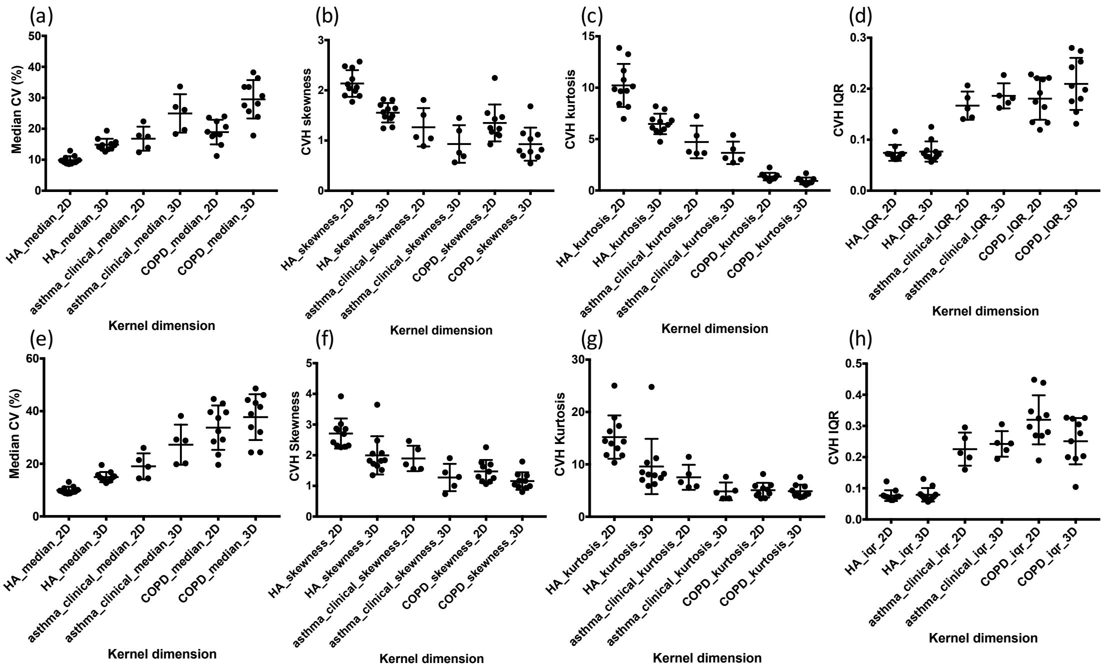

Figure 4.29 Plots of CV metrics for 2D and 3D CV calculation for all groups analysed generated from VV (a-d) and TLV(e-h) masks. (a) median CV, (b) CVH skewness, (c) CVH kurtosis, (d) CVH IQR, (e) median CV, (f) CVH skewness, (g) CVH kurtosis and (h) CVH IQR. Each point represents measurements from a single subject, error bars represent group means and standard deviations

4.4 CVH metrics as a tool to differentiate health from disease

The aim of this work was to use CVH metrics to differentiate different disease groups from healthy volunteers. For this study the 2D CVH metrics are reported with the healthy children when compared to the mild cystic fibrosis patients only, and the healthy adults are compared to the remaining groups. It is not yet clear what effect age might have on the heterogeneity of ventilation as measured using the CVH metrics.

4.4.1 Participants and imaging

All participants (HA, HC, CF, asthma_norm, asthma_abnorm, asthma_clinical and COPD) were analysed for this section of the work. Imaging parameters are listed in section 4.3.

4.4.2 Analysis

All images were analysed using the 2D CV methodology (section 4.2) with all aforementioned kernel sizes investigated to establish which provided the best distinction between health and disease. Additionally, the participants scanned with the 3D bSSFP ^{3}He sequence were compared via the optimal 2D kernel size and the 3D kernel to establish which dimension kernel best separated health from disease. The Kruskal-Wallis test was used to compare the HA to patient groups, whilst the Mann-Whitney test was used to compare HC to CF. In addition, the HC, CF, asthma_norm and asthma_abnorm datasets were analysed for correlations with LCI and S_{cond} metrics derived from MBW, as well as correlation with FEV_1 and the FEV_1/FVC ratio.

4.4.3 Results

4.4.3.1 Differentiating health from disease by kernel size

Figure 4.27 shows a plot of the metrics (generated from both the VV and TLV masks) found for the disparate groups when analysed with the 2D CV methodology and a kernel size of 3x3 voxels. Median CV was found to increase in all patient groups when compared to the HA/HC groups. Additionally, all patient groups had lower CVH skewness and kurtosis and increased CVH IQR when compared to the corresponding healthy groups. VDP is also increased in all patient groups when compared to the HA/HC groups as has been shown previously [77, 33].

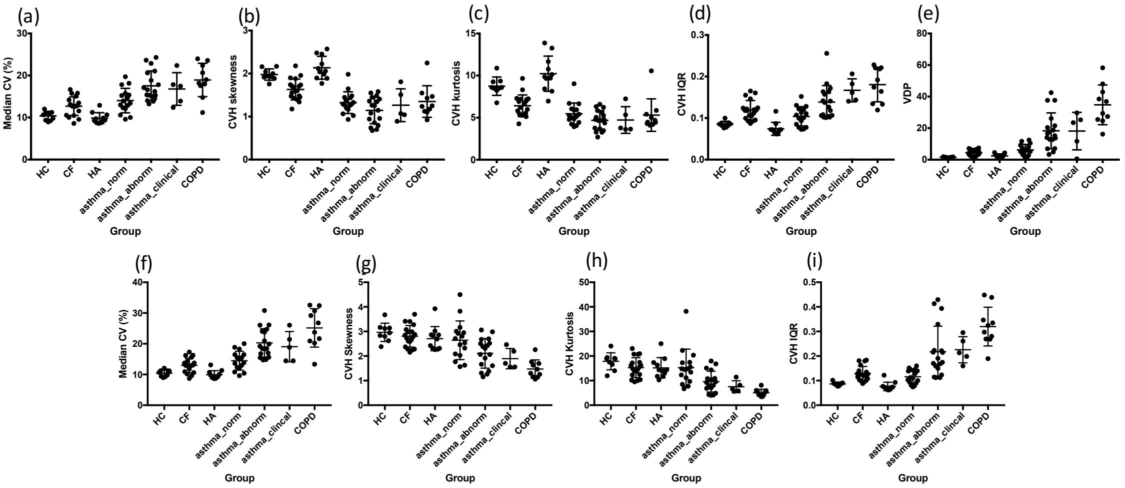

Figure 4.30 Plots of CV metrics for all groups analysed generated using a kernel size of 3 voxels generated from VV (a-d) and TLV(f-i) masks. (a) median CV, (b) CVH skewness, (c) CVH kurtosis, (d) CVH IQR, (e) VDP, (f) median CV, (g) CVH skewness, (h) CVH kurtosis and (i) CVH IQR. Ventilation defect percent (VDP) is shown for comparison. Each point represents a measurement from a single subject, error bars represent group means and standard deviations

Table 4.4 shows the results of the Kruskal-Wallis test to compare differences seen between CV metrics for the healthy adults and the asthmatic and COPD groups, and the Mann-Whitney test to compare the healthy children and CF group using CV metrics generated by both VV and TLV masks. The Kruskal-Wallis test was used as the comparisons made were between 4 groups and the Mann-Whitney test used as the comparison was between two groups only.

Table 4.4 Kruskal-Wallis test results comparing the healthy adults to the asthmatic and COPD groups, as well as Mann-Whitney results comparing the healthy children and CF group using CV metrics. Results are calculated using a kernel size of 3 voxels and the standard measure of lung function in pulmonary MRI, VDP

Comparison	Median CV	CVH Skewness	CVH Kurtosis	CVH IQR	VDP
HC vs. CF	<0.0001	0.0003	0.0016	<0.0001	<0.0001
HA vs. asthma_norm	0.0918	0.0012	0.0036	0.1508	0.4767
HA vs. asthma_abnorm	<0.0001	<0.0001	<0.0001	0.0003	<0.0001
HA vs. asthma_clinical	0.0302	0.0082	0.0016	0.0002	0.0288
HA vs. COPD	<0.0001	0.0006	0.0013	<0.0001	<0.0001
TLV comparison					
HC vs. CF	0.0051	0.3079	0.1054	<0.0001	-
HA vs. asthma_norm	0.0850	>0.9999	>0.9999	0.2142	-
HA vs. asthma_abnorm	<0.0001	0.1451	0.0343	<0.0001	-
HA vs. asthma_clinical	0.0089	0.1127	0.0386	0.0010	-
HA vs. COPD	<0.0001	0.0002	<0.0001	<0.0001	-

When considering metrics generated from the VV mask all CVH metrics can differentiated the healthy children from the CF cohort, with CVH IQR providing the same significance level as VDP. CVH skewness and CVH kurtosis were the only metrics, including VDP, that differentiated the healthy adults from the patients with asthma and normal FEV_1 z-score. All

CV metrics also significantly differentiated the healthy adults from the remaining groups, with median CV, CVH skewness and kurtosis at the same significance as VDP when comparing the healthy adults and the patients with asthma and abnormal FEV_1 z-score. Additionally, CVH metrics differentiated the healthy adults from the clinical asthma group more significantly than VDP. CVH IQR and median CV also differentiated the healthy adults from the COPD group to the same significance level as VDP, whilst CVH skewness and kurtosis separated them to a lesser extent than VDP. When considering metrics generated from the TLV mask only median CV and CVH IQR separated the healthy children from the children with CF, with CVH IQR providing the same significance level as VDP. No CVH metric could differentiate the healthy adults from the patients with asthma and normal FEV_1 z-score. Median CV, CVH kurtosis and CVH IQR were the only metrics able to differentiate the healthy adults from the patients with asthma and abnormal FEV_1 z-score and the healthy adults from the asthma_clinical cohort. CVH IQR separated the healthy adults from the patients with asthma and abnormal FEV_1 z-score to the same level of significance as VDP. All CVH metrics differentiated the healthy adults from the patients with COPD with median CV, CVH kurtosis and CVH IQR providing the same significance level as VDP.

Figure 4.31 shows a plot of all metrics for all groups when analysed with the 2D CV methodology and a kernel size of 5 voxels. Similar patterns of change in each of the CV metrics were seen using this kernel size as were seen using a kernel size of 3 voxels.

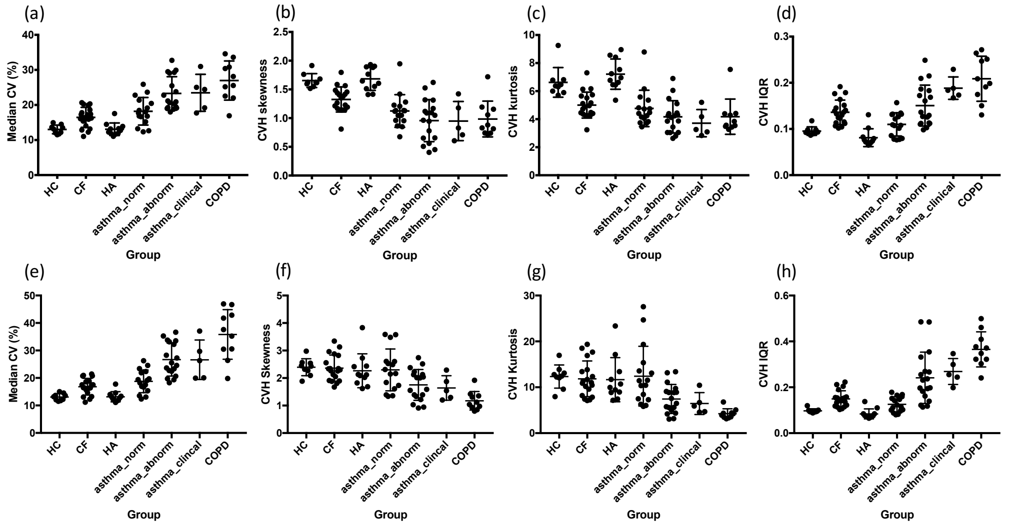

Figure 4.31 Plots of CV metrics for all groups analysed generated using a kernel size of 5 voxels generated from VV (a-d) and TLV(e-h) masks. (a) median CV, (b) CVH skewness, (c) CVH kurtosis, (d) CVH IQR, (e) median CV, (f) CVH skewness, (g) CVH kurtosis and (h) CVH IQR. Ventilation defect percent (VDP) is shown for comparison. Each point represents a measurement from a single subject, error bars represent group means and standard deviations

Table 4.5 shows the results of the Kruskal-Wallis test to compare the healthy adults to the asthmatic and COPD groups, and the Mann-Whitney test to compare the healthy children and CF group using both CV metrics.

Table 4.5 Kruskal-Wallis test results comparing the healthy adults to the asthmatic and COPD groups and the Mann-Whitney results comparing the healthy children and CF group using CV metrics calculated using a kernel size of 5 voxels

Comparison	Median CV	CVH Skewness	CVH Kurtosis	CVH IQR
HC vs. CF	0.0020	<0.0001	0.0002	<0.0001
HA vs. asthma_norm	0.2007	0.0061	0.0118	0.2116
HA vs. asthma_abnorm	<0.0001	<0.0001	<0.0001	0.0004
HA vs. asthma_clinical	0.0089	0.0063	0.0006	0.0002
HA vs. COPD	<0.0001	0.0007	0.0005	<0.0001
TLV comparison				
HC vs. CF	0.0016	0.5619	0.3829	<0.0001
HA vs. asthma_norm	0.1651	>0.9999	>0.9999	0.2705
HA vs. asthma_abnorm	<0.0001	0.2591	0.0631	<0.0001
HA vs. asthma_clinical	0.0033	0.3226	0.1645	0.0007
HA vs. COPD	<0.0001	0.0005	<0.0001	<0.0001

When considering metrics generated from the VV mask all CVH metrics differentiated the healthy children from the patients with CF. Only CVH skewness and kurtosis were able to differentiate the healthy adults from the patients with asthma and normal FEV_1 z-score at a kernel size of 5 voxels. All CV metrics also significantly differentiated the healthy adults from the remaining groups, with all CVH metrics bar IQR providing the same level of significance as VDP at a kernel size of 5 voxels to differentiate the healthy adults from the patients with asthma and abnormal FEV_1 z-score. Additionally, CVH metrics differentiated the healthy adults from the asthma_clinical cohort more significantly than VDP at a kernel size of 5 voxels. CVH IQR and median CV also differentiate the healthy adults from the COPD group to the same significance level as VDP, whilst CVH skewness and kurtosis separated them to a lesser extent than VDP. When considering metrics generated from the TLV mask, median CV and CVH IQR were the only metrics that separated the healthy children from the children with CF, the healthy adults from the patients with asthma and abnormal FEV_1 z-score, and the healthy adults from the asthma_clinical cohort. All CVH metrics differentiated the healthy adults from the patients with COPD. As with a kernel size of 3 voxels no CVH metric differentiated the healthy adults from the patients with asthma and normal FEV_1 z-score.

Figure 4.32 shows a plot of all metrics for all groups when analysed with the 2D CV methodology and a kernel size of 7 voxels. As with using a kernel size of 3 or 5 voxels there is the same pattern of change seen when comparing the CV metrics between the groups.

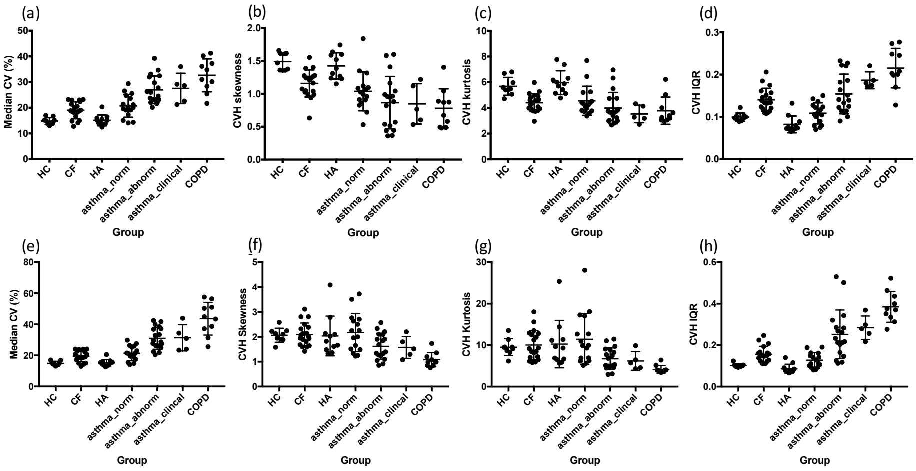

Figure 4.32 Plots of CV metrics for all groups analysed generated using a kernel size of 7 voxels generated from the VV (a-d) and TLV(e-h) masks. (a) median CV, (b) CVH skewness, (c) CVH kurtosis, (d) CVH IQR, (e) median CV, (f) CVH skewness, (g) CVH kurtosis and (h) CVH IQR. Ventilation defect percent (VDP) is shown for comparison. Each point represents a measurement from a single subject, error bars represent group means and standard deviations

Table 4.6 shows the results of the Kruskal-Wallis test comparing the healthy adults to the asthmatic and COPD groups, and the Mann-Whitney test comparing the healthy children and CF group.

Table 4.6 Kruskal-Wallis test results comparing the healthy adults to the asthmatic and COPD groups and the Mann-Whitney results comparing the healthy children and CF group using CV metrics calculated using a kernel size of 7 voxels

Comparison	Median CV	CVH Skewness	CVH Kurtosis	CVH IQR
HC vs. CF	0.0020	0.0001	0.0001	<0.0001
HA vs. asthma_norm	0.3670	0.0326	0.0994	0.3575
HA vs. asthma_abnorm	<0.0001	0.0004	0.0004	0.0004
HA vs. asthma_clinical	0.0111	0.0246	0.0036	0.0005
HA vs. COPD	<0.0001	0.0003	0.0005	<0.0001
TLV comparison				
HC vs. CF	0.0010	>0.9999	0.8470	<0.0001
HA vs. asthma_norm	0.2130	>0.9999	>0.9999	0.3326
HA vs. asthma_abnorm	<0.0001	0.6837	0.1832	<0.0001
HA vs. asthma_clinical	0.0045	>0.9999	0.3754	0.0008
HA vs. COPD	<0.0001	0.0016	0.0003	<0.0001

When considering metrics generated from the VV mask all CVH metrics differentiated the healthy children from the CF. Only CVH skewness was able to differentiate the healthy adults from the patients with asthma and normal FEV_1 z-score at a kernel size of 7 voxels. All CV metrics also significantly differentiated the healthy adults from the remaining groups, with median CV and CVH IQR differentiating the healthy adults from the patients with asthma and abnormal FEV_1 z-score to the same level of significance as VDP. Additionally, CVH metrics differentiated the healthy adults from the clinical asthma group more significantly than VDP at a kernel size of 7 voxels, although the p value of CVH skewness is very similar to that of VDP for this group. CVH IQR and median CV also differentiate the healthy adults from the COPD group to the same significance level as VDP, whilst CVH skewness and kurtosis separate them to a lesser extent than VDP. When considering metrics generated from the TLV mask no CVH metric differentiated the healthy adults from the patients with asthma and normal FEV_1 z-score, median CV and CVH IQR separated the healthy children from the children with CF, the healthy adults from the patients with asthma and abnormal FEV_1 z-score, and the healthy adults from the asthma_clinical cohort, whilst all CVH metrics differentiated the healthy adults from the patients with COPD.

Figure 4.33 shows a plot of all metrics for all groups when analysed with the 2D CV methodology and a kernel size of 9 voxels.

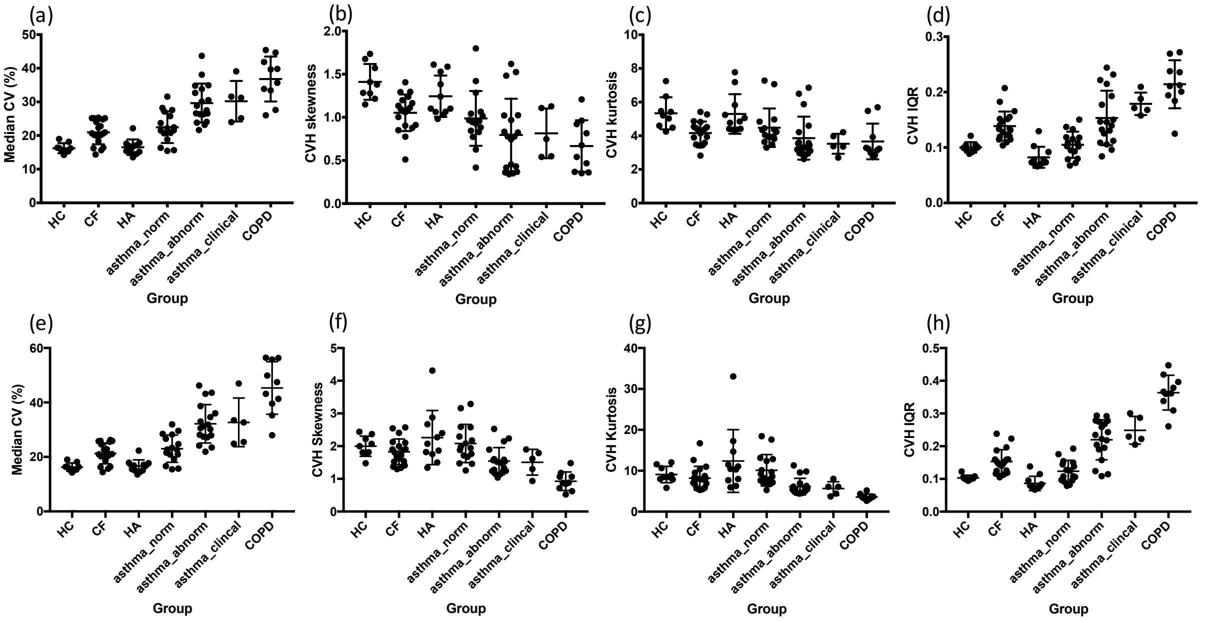

Figure 4.33 Plots of CV metrics for all groups analysed generated using a kernel size of 9 voxels generated from the VV (a-d) and TLV(e-h) masks. (a) median CV, (b) CVH skewness, (c) CVH kurtosis and (d) CVH IQR. Each point represents a measurement from a single subject, error bars represent group means and standard deviations

Table 4.7 shows the results of the Kruskal-Wallis in comparing healthy adults to asthmatic and COPD groups. Results of the Mann-Whitney test in comparing healthy children to the CF group using CV metrics are also shown.

Table 4.7 Kruskal-Wallis test results comparing the healthy adults to the asthmatic and COPD groups and the Mann-Whitney results comparing the healthy children and CF group using CV metrics calculated using a kernel size of 9 voxels

Comparison	Median CV	CVH Skewness	CVH Kurtosis	CVH IQR
HC vs. CF	0.0007	0.0003	0.0016	<0.0001
HA vs. asthma_norm	0.4337	0.1453	0.4057	0.4890
HA vs. asthma_abnorm	<0.0001	0.0017	0.0013	0.0004
HA vs. asthma_clinical	0.0099	0.1653	0.0227	0.0012
HA vs. COPD	<0.0001	0.0006	0.0013	<0.0001
TLV comparison				
HC vs. CF	0.0007	0.2634	0.1564	<0.0001
HA vs. asthma_norm	0.2061	>0.9999	>0.9999	0.4247
HA vs. asthma_abnorm	<0.0001	0.0401	0.0072	<0.0001
HA vs. asthma_clinical	0.0046	0.3461	0.0637	0.0016
HA vs. COPD	<0.0001	<0.0001	<0.0001	<0.0001

When considering metrics generated from the VV mask all CVH metrics differentiated the healthy children from the CF. No CVH metrics were able to differentiate the healthy adults from the patients with asthma and normal FEV_1 z-score at a kernel size of 9 voxels. Only median CV provided the same level of significance as VDP at a kernel size of 9 voxels to differentiate the healthy adults from the patients with asthma and abnormal FEV_1 z-score, although all other metrics still differentiated these groups. Median CV, CVH kurtosis and IQR differentiated the healthy adults from the asthma_clincial cohort at a kernel size of 9 voxels. CVH IQR and median CV also differentiated the healthy adults from the COPD group to the same significance level as VDP, whilst CVH skewness and kurtosis separated them to a lesser extent than VDP. When considering metrics generated from the TLV mask only median CV and CVH IQR separated the healthy children from the children with CF. No CVH metrics were able to differentiate the healthy adults from the patients with asthma and normal FEV_1 z-score. All CVH metrics can differentiate the healthy adults from the patients with asthma and abnormal FEV_1 z-score. Median CV and CVH IQR differentiated the healthy adults from the asthma_clincial cohort. All CVH metrics differentiated the healthy adults from the COPD group to the same significance level as VDP.

Generally, the level of significance between the healthy children and patients with CF remained at similar levels or became less significant when increasing the kernel size from 3 to 9 voxels, although at a kernel size of 7 voxels CVH kurtosis and skewness differentiated the groups more significantly than at 3 voxels. CVH IQR remained at the same significance level ($p<0.0001$) and significant differences remained between all other metrics generated using the VV mask.

The level of significance when comparing the healthy adults to the patients with asthma and normal FEV_1 z-scores decreased as the kernel size increases with median CV not being able to differentiate these groups at any kernel size. When comparing the healthy adults to the patients with asthma and abnormal FEV_1 z-scores median CV remained at the same significance level regardless of kernel size, while CVH skewness and kurtosis became less significantly different at a kernel size of 7 voxels. CVH IQR became less significantly different at a kernel size of 5 voxels. When comparing the healthy adults to the asthma_clinical cohort median CV became more significantly different as kernel size increased while CVH IQR became less significant. CVH skewness and kurtosis became more significantly different at a kernel size of 5 voxels when compared to a kernel size of 3 voxels before becoming less significant at kernel sizes of 7 and 9 voxels. When comparing the healthy adults to the patients with COPD the difference in median CV and CVH IQR remained at the same significance ($p<0.0001$). CVH skewness became more significantly different at a kernel size of 5 and 7 voxels before decreasing at 9 voxels, although at all kernel sizes the difference was more significant than that seen at a kernel size of 3 voxels. CVH kurtosis became more significantly different at a kernel size of 5 voxels compared to 3 voxels and remained at this significance level at a kernel size of 7 voxels before becoming less significantly different at a kernel size of 9 voxels.

When considering the metrics generated using the TLV mask, the difference in median CV became more significant as kernel size increases, whilst the level of significance of CVH IQR remained at $p<0.0001$. The level of significance when comparing the healthy adults to the patients with asthma and normal FEV_1 z-scores decreased as the kernel size increased with no CV metric being able to differentiate these groups at any kernel size. When comparing the healthy adults to the patients with asthma and abnormal FEV_1 z-scores median CV and CVH IQR remained at the same significance level regardless of kernel size, while CVH skewness and kurtosis did not separate these groups at a kernel size of 5 and 7 voxels but was able to at kernel sizes of 3 and 9 voxels. When comparing the healthy adults to the asthma_clinical cohort median CV became more significantly different between a kernel size of 3 and 5 voxels, and then became less significantly different, and CVH IQR follows this pattern in differentiating these groups. CVH skewness did not separate these groups at any kernel size, whilst CVH kurtosis only separated these groups at a kernel size of 3 voxels. When comparing the healthy adults to the patients with COPD the difference in median CV and CVH IQR remained at the same significance ($p<0.0001$) regardless of kernel size. CVH skewness became less significantly different between a kernel size of 3 and 7 voxels, before becoming more significantly different at a kernel size of 9 voxels, with CVH kurtosis following the same pattern. In summary based on these results it seems the most logical kernel size to use in CV calculations is 3 voxels as it was best able to differentiate the healthy adults from the patients with asthma and normal FEV_1 z-scores whilst all other kernel sizes are either less significantly different or fail to differentiate these groups. Furthermore, it appears using metrics generated using the VV mask is optimal as using those generated from the TLV mask could not differentiate these groups, and in most cases the level of significance is decreased when analysing the CV metrics generated on the TLV mask, although the metrics generated using this mask are more significantly different in some cases. The next stage was to determine whether a 2D or 3D kernel was optimum and if this would alter the choice of using the VV or TLV masks.

4.4.3.2 Differentiating ventilation heterogeneity in health and disease by kernel dimensionality

4.4.3.2.1 Participants and materials and methods

The participants for this study were the same as those listed in section 4.3.5 with the same methodology for CV calculation (section 4.2) also being used and a kernel size of 3x3 voxels for the 2D calculation and 3x3x3 for the 3D calculation.

4.4.3.2.2 Results

Table 4.8 shows the results of comparing the HA group to the asthma_clinical and COPD groups with metrics calculated using the 2D and 3D CV methodologies.

Table 4.8 Kruskal-Wallis test results comparing groups using 2D and 3D CV metrics

Comparison	Median CV	CVH Skewness	CVH Kurtosis	CVH IQR
2D metrics				
HA vs. asthma_clinical	0.0246	0.0028	0.0015	0.0073
HA vs. COPD	<0.0001	0.0025	0.0028	0.0001
3D metrics				
HA vs. asthma_clinical	0.0175	0.0098	0.0021	0.0098
HA vs. COPD	<0.0001	0.0018	0.0038	<0.0001
TLV comparison				
2D metrics				
HA vs. asthma_clinical	0.0268	0.0718	0.0481	0.0453
HA vs. COPD	<0.0001	<0.0001	<0.0001	<0.0001
3D metrics				
HA vs. asthma_clinical	0.0153	0.0509	0.0074	0.0083
HA vs. COPD	<0.0001	0.0008	0.0013	0.0002

When considering the metrics generated from the VV mask and comparing the HA group to the asthma_clinical group using the 3D CV methodology the difference in median CV became more significant when compared to the 2D method, whilst CVH skewness, kurtosis and IQR differences became less significant. When comparing the HA group to the COPD group using the 3D CV methodology there was no change in the significance of difference between the median CV of the two groups. CVH skewness and IQR differences became more significant, whilst CVH kurtosis differences became less significant. When considering the metrics generated from the TLV mask and comparing the HA group to the asthma_clinical group using the 3D CV methodology the difference in median CV became more significantly different when compared to the 2D method, as did CVH skewness, kurtosis and IQR, although CVH skewness was not able to differentiate these groups using either method. When comparing the HA group to the COPD group using the 3D CV methodology there was no change in the significance of difference between the median CV of the two groups. CVH skewness, kurtosis and IQR differences became less significant. Taking into account all metrics these results further corroborate the results of the previous section in suggesting that based on the data used here the 2D CV methodology with a kernel size of 3 voxels is the most suitable to differentiate health from disease, with the metrics being generated on the ventilated lung mask rather than the total lung volume mask. However, it should be noted that this becomes a more complex with the 3D CV metrics and metrics generated using the TLV mask increasing the significance in some situations when compared to the 2D metrics.

4.4.3.3 Correlations with Spirometry and MBW metrics

4.4.3.3.1 __Participants and materials and methods__

The participants for this study were the healthy children, patients with CF and the patients with asthma listed in section 4.3.2.1 (subjects scanned with the 2D sequence). Spearman correlations were carried out to determine if CVH metrics reflected multi-breath washout metrics and standard clinical measurements of lung function. The 2D CV methodology calculated on the ventilated lung and total lung masks.

4.4.3.3.2 __Results__

Figure 4.34 shows the correlations of CV metrics with LCI. Median CV had the highest correlation with the LCI metric whilst CVH kurtosis had the next best correlation, for metrics generated using the VV mask and median CV and CVH IQR had the best correlations for metrics generated using the TLV mask. All correlations were significant with p<0.001.

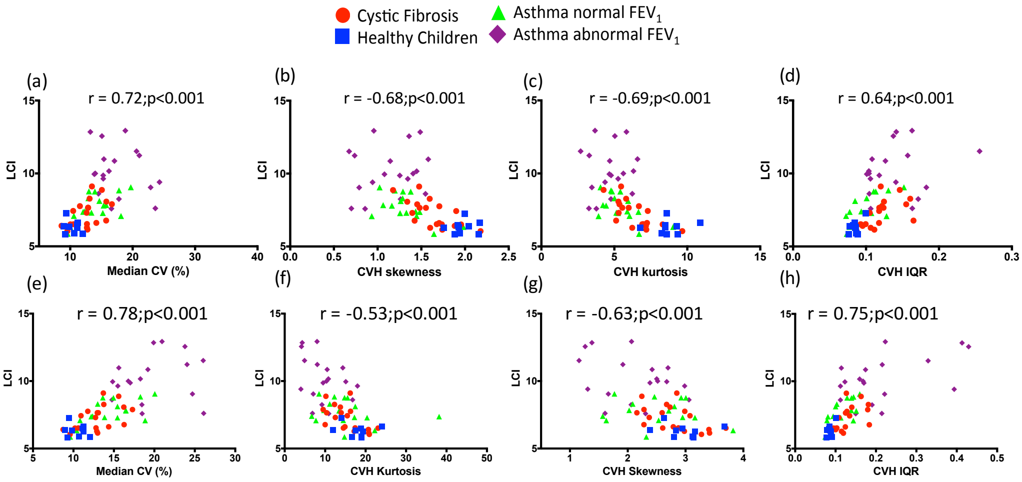

Figure 4.34 Spearman correlations of coefficient of variation histogram metrics with LCI generated from VV (a-d) and TLV(e-h) masks. (a) correlation of median CV with LCI, (b) correlation of CVH skewness with LCI, (c) correlation of CVH kurtosis with LCI, (d) correlation of CVH IQR with LCI, (e) correlation of median CV with LCI, (f) correlation of CVH skewness with LCI, (g) correlation of CVH kurtosis with LCI and (h) correlation of CVH IQR with LCI

Figure 4.35 shows the correlations of CV metrics with S_{cond}. CVH IQR had the highest correlation with S_{cond} whilst median CV had the second highest correlation for both metrics generated from the VV and TLV masks. As with the correlations with LCI all were significant with p<0.001.

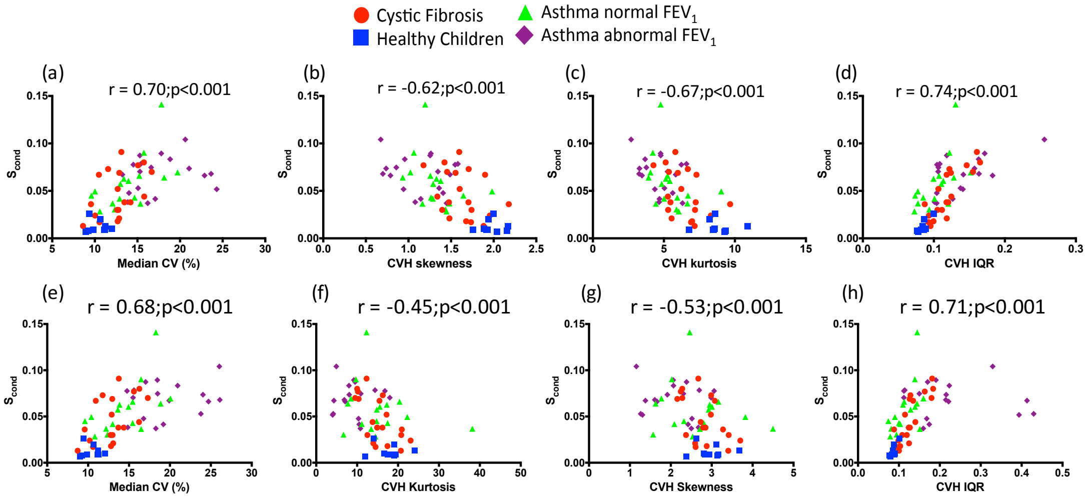

Figure 4.35 Spearman correlations of coefficient of variation histogram metrics with S_{cond} generated from VV (a-d) and TLV(e-h) masks. (a) correlation of median CV with S_{cond}, (b) correlation of CVH skewness with S_{cond}, (c) correlation of CVH kurtosis with S_{cond}, (d) correlation of CVH IQR with S_{cond}, (e) correlation of median CV with S_{cond}, (f) correlation of CVH skewness with S_{cond}, (g) correlation of CVH kurtosis with S_{cond} and (h) correlation of CVH IQR with S_{cond}

Figure 4.36 shows the correlation of CVH metrics with S_{acin}. All correlations are significant with median CV and CVH kurtosis having p<0.001 whilst CVH skewness had a p value of 0.0014, all correlations had p<0.001 for the metrics generated from the TLV mask.

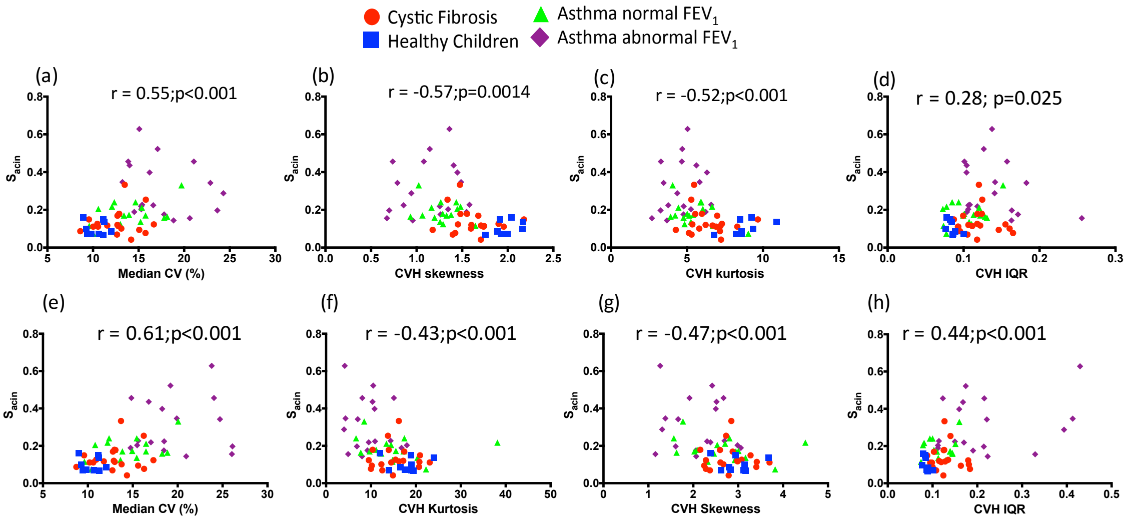

Figure 4.36 Spearman correlations of coefficient of variation histogram metrics with S_{acin} generated from VV (a-d) and TLV(e-h) masks. (a) correlation of median CV with S_{acin}, (b) correlation of CVH skewness with S_{acin}, (c) correlation of CVH kurtosis with S_{acin}, (d) correlation of CVH IQR with S_{acin}, (e) correlation of median CV with S_{acin}, (f) correlation of CVH skewness with S_{acin}, (g) correlation of CVH kurtosis with S_{acin} and (h) correlation of CVH IQR with S_{acin}

Figure 4.37 shows the correlations of CV metrics with the standard measure used in clinic to evaluate lung function – FEV_1 and Figure 4.38 shows the correlations with the FEV_1/FVC ratio.

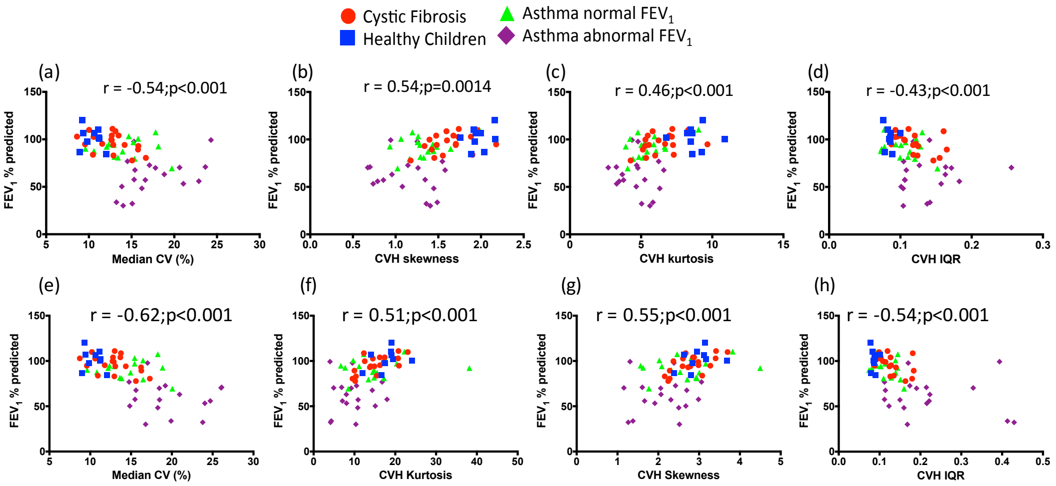

Figure 4.37 Spearman correlations of coefficient of variation histogram metrics with FEV_1 generated from VV (a-d) and TLV(e-h) masks. (a) correlation of median CV with FEV_1, (b) correlation of CVH skewness with FEV_1, (c) correlation of CVH kurtosis with FEV_1, (d) correlation of CVH IQR with FEV_1, (e) correlation of median CV with FEV_1, (f) correlation of CVH skewness with FEV_1, (g) correlation of CVH kurtosis with FEV_1 and (h) correlation of CVH IQR with FEV_1

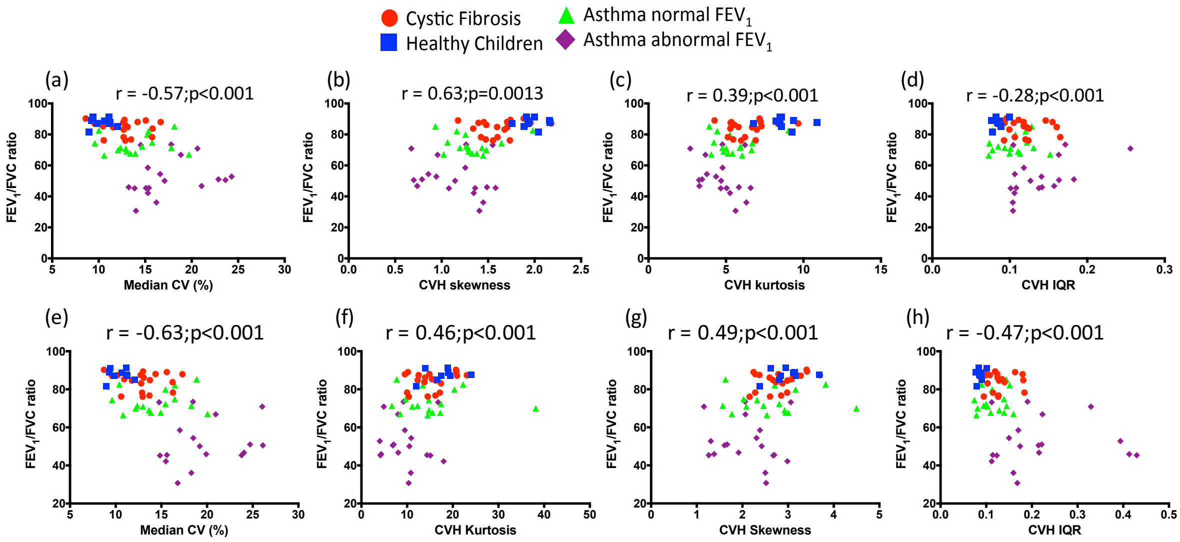

Figure 4.38 Spearman correlations of coefficient of variation histogram metrics with the FEV_1/FVC ratio generated from VV (a-d) and TLV(e-h) masks. (a) correlation of median CV with FEV_1/FVC, (b) correlation of CVH skewness with FEV_1/FVC, (c) correlation of CVH kurtosis with FEV_1/FVC, (d) correlation of CVH IQR with FEV_1/FVC, (e) correlation of median CV with FEV_1/FVC, (f) correlation of CVH skewness with FEV_1/FVC, (g) correlation of CVH kurtosis with FEV_1/FVC and (h) correlation of CVH IQR with FEV_1/FVC

All CV metrics had lower correlations with FEV_1 than with LCI and S_{cond}, however all correlations were significant. The correlations with FEV_1/FVC were lower than with LCI and S_{cond}, although again all correlations were significant. It should be noted that S_{acin} has moderate correlation with CVH metrics similar to FEV_1 and FEV_1/FVC.

4.4.3.4 Differentiating health from disease by area under the curve of the CV histogram

4.4.3.4.1 Participants and materials and methods

The participants for this study are the same as those listed in section 4.4.1. The area under the curve (AUC) of the CV histogram was calculated using MATLAB. To determine threshold values mean histograms of the healthy children and healthy adults populations were calculated similar to the method developed by Norberg et al. [30] and then the mean, median and 95th percentile values of these mean histograms were calculated. The AUC greater than each of these threshold values was then defined by taking the number of counts in each bin larger than the threshold value defined and less than one and multiplying by the step size of the bins in order to calculate an area.

The AUC measures of healthy children and patients with CF were compared via an unpaired t-test with Welch's correction, whilst the AUC measures of patients with asthma and COPD were compared to those of the healthy adults via the Kruskal-Wallis test when using the 95th percentile as a threshold and via a one-way ANOVA when using the mean and median population CV as a threshold. AUC values from patients with CF and asthma were compared to lung function values of FEV_1 % predicted, FEV_1/FVC ratio, LCI, S_{cond} and S_{acin} using Spearman's correlation.

4.4.3.4.2 Results

Figure 4.39 shows the histograms of the healthy children and Figure 4.40 shows histograms of the healthy adults, along with the mean population histogram (black line with star markers), location of the mean, median and 95th percentiles of the mean population histogram. There was some variation seen in the histograms of these healthy cohorts, with one of the healthy adults (HA8) having a broader CV histogram than the others, due to some small defects in the posterior of the lung. Table 4.9 gives the mean, median and 95th percentile values for the healthy children and adults used as thresholds to calculate the area under the curve measures of the CV histogram generated from the VV mask (a) and (b) TLV mask.

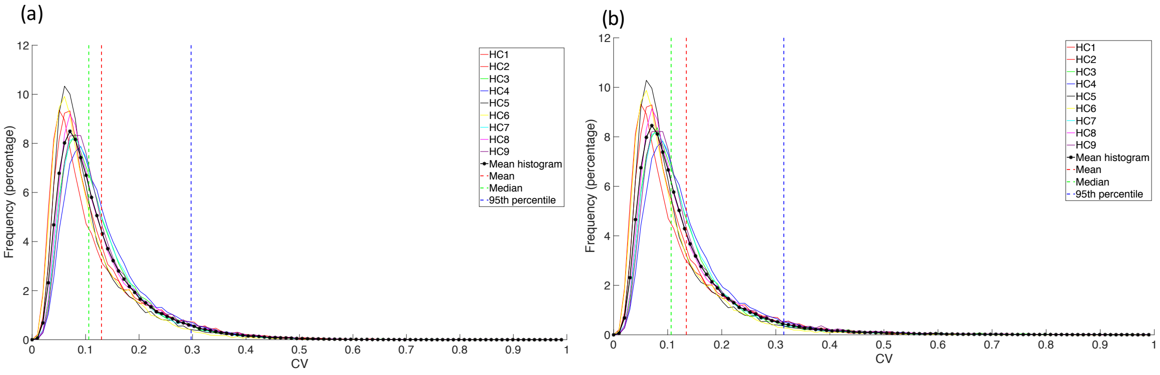

Figure 4.39 Histograms of all healthy children analysed along with the mean histogram generated from the population distributions.generated from the VV mask and (b) generated from the TLV mask

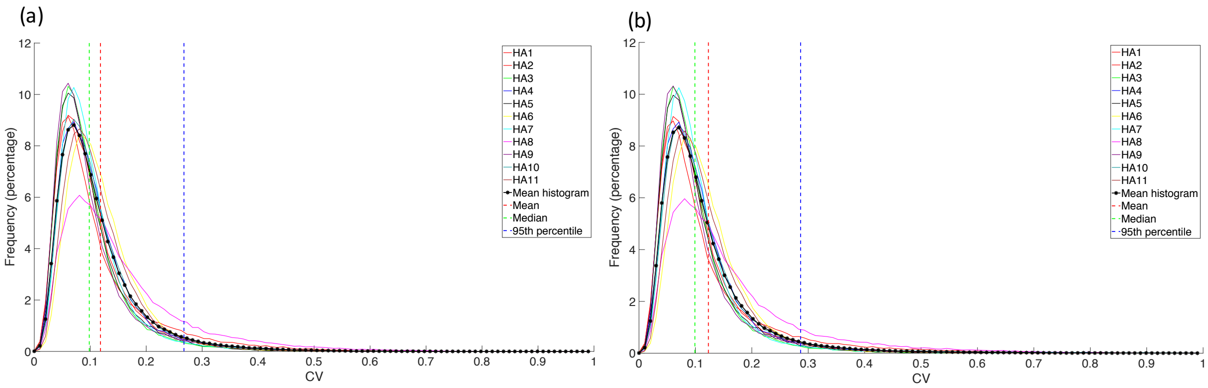

Figure 4.40 Histograms of all healthy adults analysed along with the mean histogram generated from the population distributions. (a) generated from the VV mask and (b) generated from the TLV mask

Table 4.9 Mean, median and 95th percentile values derived from mean histograms

Value	Healthy children	Healthy adults
Mean	0.1298	0.1183
Median	0.1060	0.0983
95th percentile	0.2974	0.2675
	TLV values	
Mean	0.1346	0.1231
Median	0.1064	0.0991
95th percentile	0.3148	0.2864

The mean, median and 95th percentile values were slightly higher in healthy children than those values seen in the healthy adults. The children were scanned with an SPGR sequence, resulting in lower SNR than images acquired in the adults using an SSFP sequence. Figure 4.41 shows plots of the area under the curve of the CV histogram using the thresholds listed in

Table 4.9. As can be seen the patients with asthma from the clinical database in Sheffield and the patients with COPD had both the highest value of AUC and the highest variability in AUC when compared to all other cohorts. As can be seen the patterns for AUC generated from either the VV or TLV masks have the same pattern with patient cohorts generally demonstrating higher AUC values.

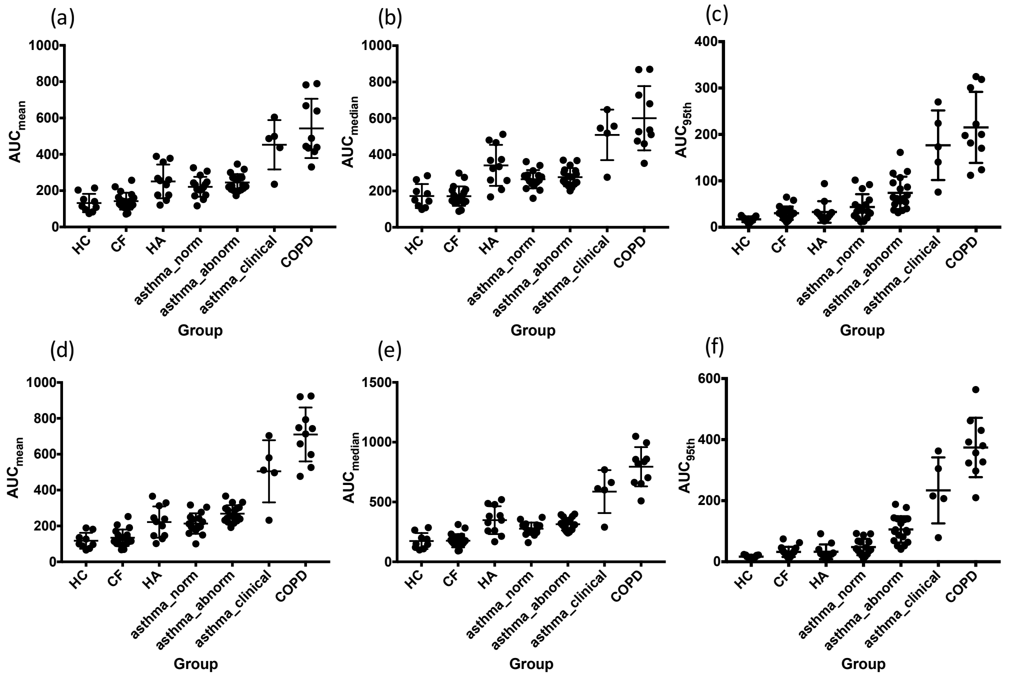

Figure 4.41 Plots of area under the histogram curve using the thresholds listed in

Table 4.9 generated from the VV mask (a-c) and TLV mask (d-f). (a) mean, (b) median, (c) 95th percentile, (d) mean, (e) median and (f) 95th percentile. Each point represents a measurement from a single subject, error bars represent group means and standard deviations

Table 4.10 shows the results of the statistical comparisons of the area under the curve of the CV histogram using the threshold values presented in
Table 4.9.

Table 4.10 Kruskal-Wallis/One-way ANOVA test results comparing the healthy adults to the asthmatic and COPD groups and the unpaired t-test results comparing the healthy children and CF group using area under the curve of the CV histogram

Comparison	Mean	Median	95th percentile
HC vs. CF	0.6079	0.9838	0.0022
HA vs. asthma_norm	0.8338	0.1816	>0.9999
HA vs. asthma_abnorm	0.9993	0.2850	0.0189
HA vs. asthma_clinical	0.0007	0.0122	0.0006
HA vs. COPD	0.0001	0.0001	<0.0001
TLV values			
HC vs. CF	0.3639	0.9205	0.0013
HA vs. asthma_norm	0.9980	0.2433	>0.9999
HA vs. asthma_abnorm	0.5021	0.8088	0.0026
HA vs. asthma_clinical	0.0001	0.0003	0.0011
HA vs. COPD	0.0001	0.0001	<0.0001

Using the mean and median value of the population histogram as a limit of integration to calculate area under the curve of the CV histogram did not separate patients with CF from the healthy children significantly. However, using the 95th percentile values as a threshold did enable separation. Healthy adults were significantly different from the clinical patients with asthma and COPD patients using all thresholds, however the healthy adults were not significantly different from the patients with asthma and normal FEV_1 using any threshold. Healthy adults were significantly different from patients with asthma and abnormal FEV_1 only when using the 95th percentile value as a threshold to calculate area under the curve of the CV histogram. When considering the metrics generated from the TLV mask it is interesting to see that using the 95th percentile as a threshold is able to differentiate the healthy adults from the patients with asthma and abnormal FEV_1 z-score more significantly than the metrics generated from the VV mask. In addition, using the median or mean as a threshold is able to more significantly differentiate the asthma_clincial cohort from the healthy adults.

Figure 4.42 shows the correlation of the area under the curve of the CV histogram, using the 95th percentile as a threshold, with LCI, S_{cond}, S_{acin}, FEV_1 % predicted and the FEV_1/FVC ratio for metrics generated using the VV mask.

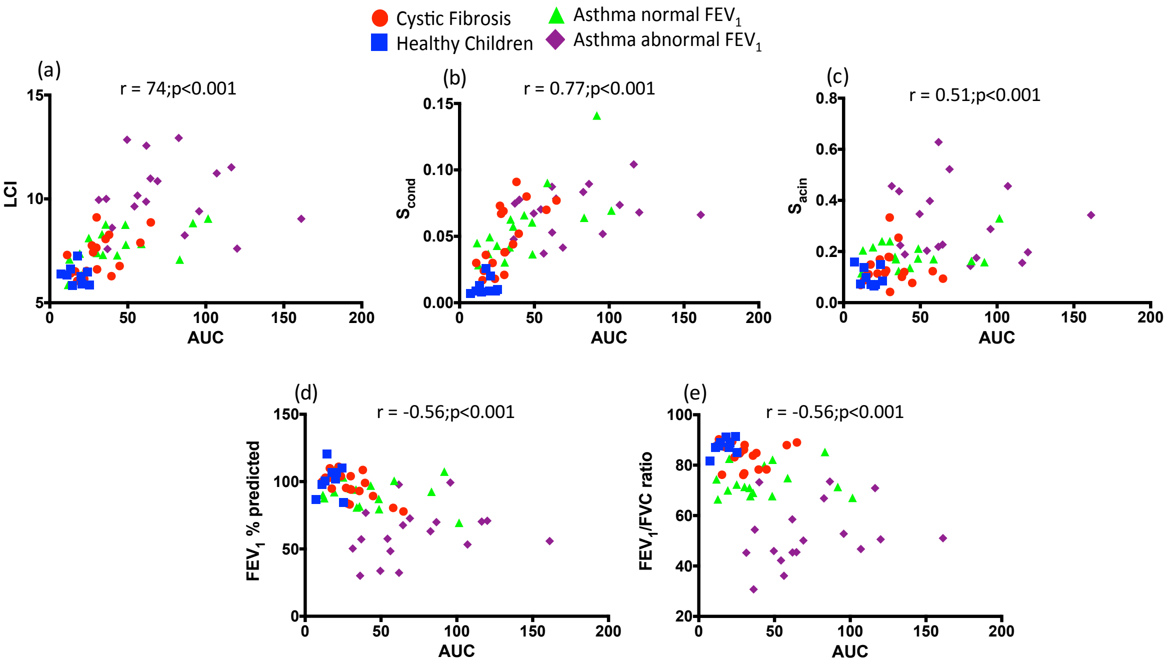

Figure 4.42 Spearman correlations of the area under the curve of the CV histogram generated from the VV mask with (a) LCI, (b) S_{cond}, (c) S_{acin}, (d) FEV$_1$ % predicted and (e) FEV$_1$/FVC ratio

The strongest correlations of the area under the curve of the CV histogram were with LCI and S_{cond}. A moderate correlation is seen with FEV$_1$ % predicted whilst a weak correlation was seen with the FEV$_1$/FVC ratio and S_{acin}. Figure 4.43 shows the same correlations for the metrics generated using the TLV mask. AUC metrics generated using the TLV mask had stronger correlations with LCI, S_{acin}, FEV$_1$ % predicted and the FEV$_1$/FVC ratio when compared to the metrics generated using the TLV mask. A weaker correlation was seen with S_{cond}.

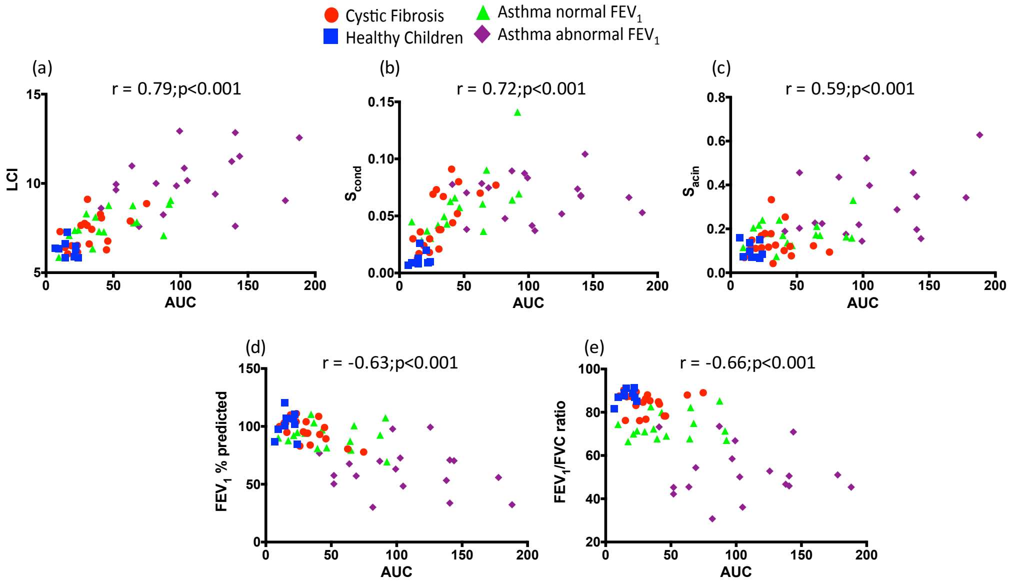

Figure 4.43 Spearman correlations of the area under the curve of the CV histogram generated from the TLV mask with (a) LCI, (b) S_{cond}, (c) S_{acin}, (d) FEV$_1$ % predicted and (e) FEV$_1$/FVC ratio

4.5 ^{3}He vs. ^{129}Xe CVH metrics

With the growing cost of ^{3}He [221], and improving methods of increasing the signal obtained using HP ^{129}Xe [246, 221], more research is focused on quantifying lung function using ^{129}Xe [63, 237, 70, 340, 285, 242]. Therefore, it is necessary to ensure that the proposed CV metrics are suitable for use with the lower SNR images generated when using ^{129}Xe in place of ^{3}He. The aim here was to compare the metrics generated from ^{129}Xe and ^{3}He images acquired on the same day in the same session.

4.5.1 Participants

To compare the metrics from ^{3}He and ^{129}Xe images 11 patients with NSCLC were analysed. PFTs were not carried out as part of this study.

4.5.2 Imaging

4.5.2.1 ^{3}He imaging

^{3}He imaging was carried out using the method presented in section 4.3.2.2.

4.5.2.2 ^{129}Xe imaging

HP ^{129}Xe ventilation-weighted images were acquired using HP ^{129}Xe polarized on site [76]. Images were acquired using a ^{129}Xe transmit-receive flexible vest coil tuned to 17.65 MHz (Clinical MR Solutions, Brookfield, WI, USA) and the ^{1}H system body coil. ^{1}H anatomical images were acquired in a separate breath prior to the HP gas ventilation images. Patients inhaled 550mL HP ^{129}Xe mixed with 450mL N_2 from a Tedlar bag from FRC prior to the ventilation scan. Images were registered using ANTs registration software [84].

4.5.3 Analysis

Images were analysed using the 2D CVH method discussed in section 4.2 with a kernel size of 3. Wilcoxon matched-pairs signed rank tests were used to compare the metrics from NSCLC patients ^{3}He and ^{129}Xe ventilation images.

4.5.4 Results

Figure 4.44 shows plots of all CVH metrics for the 11 NSCLC patients analysed generated from both the VV (a-d) and TLV (e-h) masks. CVH skewness and kurtosis decreased when analysing ^{129}Xe images compared to ^{3}He images ($p_{skewness}$ = 0.0098, $p_{kurtosis}$ =0.0137) whilst median CV and CVH IQR increased (p_{median} = 0.0010, p_{iqr} = 0.0059). When considering the metrics generated from the TLV mask the same patterns were seen. CVH skewness and kurtosis decreased when analysing ^{129}Xe images compared to ^{3}He images ($p_{skewness}$ = <0.0001, $p_{kurtosis}$ =0.0010) whilst median CV and CVH IQR increased (p_{median} = 0.0010, p_{iqr} = 0.0020).

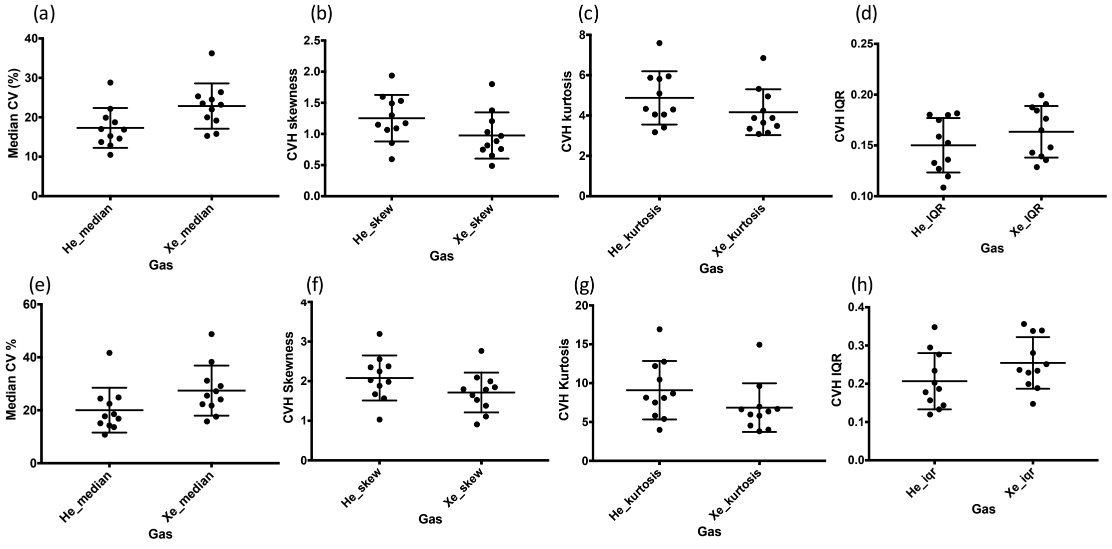

Figure 4.44 Plots of CV metrics for all NSCLC patients analysed generated from the VV mask (a-d) and TLV mask (e-h). (a) Median CV, (b) CVH skewness, (c) CVH kurtosis and (d) CVH IQR. Each point represents a measurement from a single subject, error bars represent group means and standard deviations

These changes are clear when comparing the cohort average histograms from ^{3}He and ^{129}Xe acquisitions (Figure 4.45). This follows the pattern of decreasing the image SNR shown in section 4.3.4, which is logical considering the significant (p=0.0068) difference in SNR between the ^{3}He and ^{129}Xe acquisitions for these patients (Figure 4.46). Additionally, a longer high CV tail is seen when considering the average histograms generated from the TLV mask when compared to the VV mask.

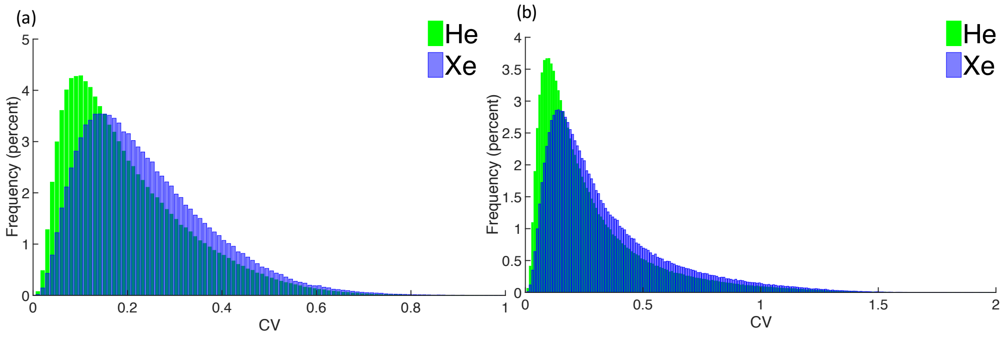

Figure 4.45 Average histograms for NSCLC patients comparing ^{3}He and ^{129}Xe CVH values generated from the (a) VV mask and (b) TLV mask

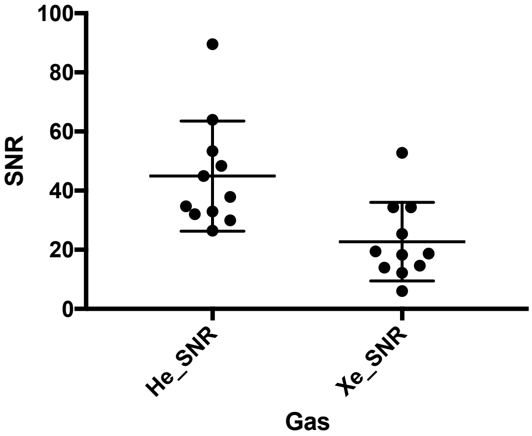

Figure 4.46 Plots of ^{3}He and ^{129}Xe SNR for NSCLC patients. Each point represents measurements from a single subject, error bars represent group means and standard deviations

4.6 Discussion and conclusion

The main limitation of the studies carried out here is the small number of participants scanned with both SPGR and SSFP ventilation-weighted imaging and the small sample size of the patient groups on which the CVH metrics were tested. Additionally no bias field correction for RF coil sensitivity was carried out, unlike other studies utilizing the ventilation image signal [285]. The reason the popular N4 bias field correction [293] was not carried out is mainly due to the frequent disappearance of what appear to be defects when the bias field correction is carried out, such as the reduced ventilation in the upper lobe, exemplified in Figure 4.47. Additionally, there is a large difference in the fractional ventilation (FV) histogram calculated following N4 correction when compared to the original uncorrected image histogram (Figure 4.47c).

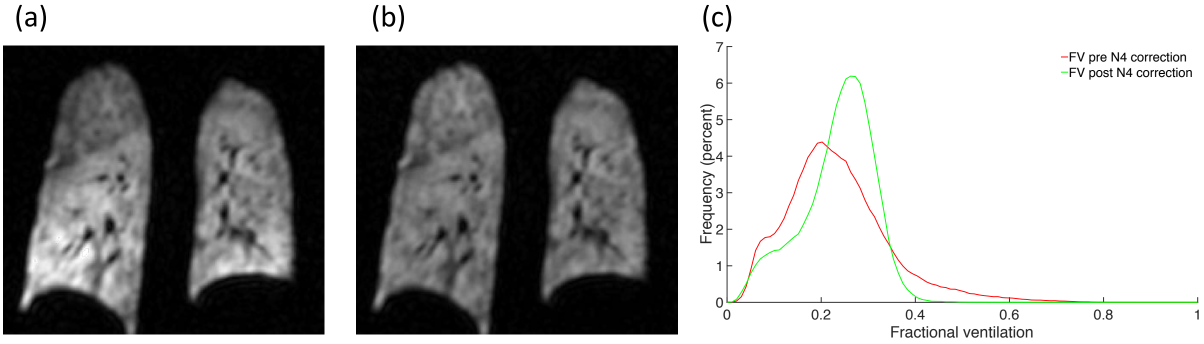

Figure 4.47 Example slices from an uncorrected ^{3}He and bias field corrected image from a healthy volunteer. (a) original image, (b) corrected image and (c) comparison of the fractional ventilation histograms pre and post bias field correction

Due to these changes, it would appear that the N4 bias field correction method would reduce the local variation in these areas, which may hide physiologically relevant information, thus in future work acquisition of a B1 map and correction of the image using this method should be applied and compared to the results obtained using the N4 method commonly used [283, 291, 285]. However, there are of course trade-offs in acquiring a B1 map – the most obvious being the additional dose of gas and extra scan. Additionally, were the B1 map to be acquired in a separate breath-hold there is the inherent difficulty of registering this image to the ventilation image being used for analysis. There exists the option to acquire the B1 map in the same breath-hold as the ventilation scan as was done by Miller et al. [323], however using the technique there would result in a longer breath-hold time and require the use of a smaller flip angle to maintain magnetisation for the B1 mapping, resulting in lower quality diagnostic images.

From the cohorts analysed in the previous sections the total lung volume method excluded significantly fewer voxels ($p<0.0001$) than the ventilated lung based method with a mean±SD of 23771 ± 38100 voxels excluded per patient for the total lung volume method and 49685 ± 72229 voxels excluded per patient for the ventilated lung volume method. Note that this is the number of voxels excluded within the total lung volume. To calculate these values the ventilated volume mask or SNR based ventilated volume mask was multiplied by the total lung volume mask, then the ventilated volume or SNR based ventilated volume masks were subtracted from the total lung volume mask and the number of values greater than zero counted to find the number of voxels excluded.

4.6.1 Effect of sequence and SNR on CV metrics

Imaging parameters along with gas dose have an effect on CV metrics. This is clearly visualized by comparing the 3 healthy adults analysed with both SPGR and SSFP imaging. It is clear that the reduced image SNR and T_2^* weighted contrast (susceptibility weighted image texture) of the SPGR sequence leads to increased median CV and CVH IQR values and decreased CVH skewness and kurtosis. Artificially reducing the SNR of ventilation images also caused these changes in the HAs scanned with SSFP imaging only. An interesting finding was the reduction in CVH IQR at lower SNR in the patient cohorts analysed, suggesting that as the SNR decreases in these patient cohorts the CV values become more tightly grouped, moving towards a more Gaussian distribution with the histogram peak shifted to a higher CV value.

Throughout this study it was also noted that there were no significant differences between CV metrics in healthy volunteers measured from simulated SNR of 75% of the original image, although this could be due to the small numbers. This is an important finding in the context of longitudinal and repeat studies if CVH metrics are to be used in conjunction with the standard metric of VDP to represent lung function as this can be considered the cut-off point of image SNR difference between time points to compare the metrics. This means that, from the data analysed here, a difference in SNR of approximately 20 between acquisitions is acceptable based on the metrics from the VV mask whereas the metrics from the TLV mask show no significant differences at 50% image SNR – although mean and median CV are approaching a p value of 0.05 suggesting from this data that using the TLV mask generated metrics would allow a difference of closer to 30.

4.6.2 Effect of kernel size on CV metrics

As one would expect modifying the kernel size to calculate CV will modify CVH metrics as signal variation is then analysed on different length scales. As expected, the median CV increased as the kernel size increased due to more of the lung being involved in the CV calculation, with a greater likelihood of increased standard deviation in the neighbourhood being analysed in patients. CVH skewness and kurtosis decreased with greater kernel size due to the smoothing of the CV maps. A decrease of CVH IQR in the asthmatic cohorts using a neighbourhood of 9x9 voxels when compared to 7x7 voxels was found, whilst there was a slight increase or no difference in all other groups analysed. This suggests a tighter grouping of values at this neighbourhood size compared to the other sizes used in this work.

The neighbourhood of 9x9 voxels is more similar to the size used in previous work [326] analysing images of asthmatic patients, where 10% of the maximum width of the lung was chosen as the neighbourhood size for CV calculation although histogram metrics were not reported in that work. As reported above the optimal kernel for the images analysed here seems to be 3x3 voxels based on the significance of differentiating patient groups with mild disease from healthy volunteers.

4.6.3 Effect of kernel dimensionality on CV metrics

Modifying the kernel from 2D to 3D increased median CV and produced a CV map that is smoothed due to the inclusion of through-plane voxels and having to increase in-plane downsampling from 2 to 3 to allow for CV calculation in an approximately isotropic cube. CVH skewness and kurtosis did not change to the same extent as median CV whilst CVH IQR has a minor change for all cohorts analysed. This is an interesting finding as although the median CV increased, suggesting a shift of the peak, the values are similarly grouped between the 2D and 3D CVH histograms.

4.6.4 CV metrics as a tool to differentiate groups

One key point to consider is that the differences in CV metrics seen between the healthy adults, scanned with a 3D bSSFP sequence, and the asthma_norm/asthma_abnorm cohorts, scanned with a 2D SPGR sequence, are of a similar magnitude to those seen when comparing the healthy adults scanned with both the 3D bSSFP and 2D SPGR sequences. However, one key difference with the asthma cohort is a generally higher SNR for the participants as exemplified in Figure 4.48 , suggesting that although there is an SNR difference as one would expect it is not to the same extent as that seen in the healthy volunteers 2D SPGR v 3D SSFP image SNR, hence the differences seen may be caused by the effects of the disease rather than imaging methods. An important consideration here is the lower dose of HP ^{3}He given for the HA scans due to increased polarisation of ^{3}He at the time of the experiment for the 2D SPGR scans.

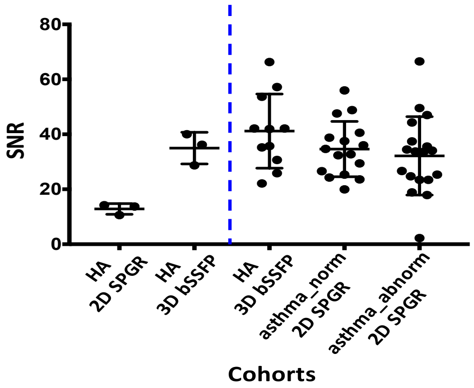

Figure 4.48 Plots of SNR values for the three healthy adults scanned on the same day with SPGR and SSFP and the healthy adults scanned with a 2D SPGR sequence and the asthma_norm and asthma_abnorm cohorts. Each point represents a measurement from a single subject, error bars represent group means and standard deviations.

The main limitation in this study is the lack of FEV_1 values for the HA, COPD and asthma_clinical cohorts to assess if CV metrics are able to distinguish patient groups from healthy volunteers to the same extent as the clinical gold standard for evaluating respiratory disease. However, when comparing imaging methods to differentiate patient groups it appears CV metrics are a useful tool to accompany the standard method of VDP analysis and can differentiate health from disease more strongly than VDP in some cases. Additionally, by comparing CV metrics alone the asthma_norm cohort had similar values of median CV and CVH IQR to the mild CF cohort analysed for this study.

The moderate and significant correlations of the CV metrics with MBW metrics for the HC, CF and asthma2D cohorts suggest that these metrics may be a useful tool to differentiate patient groups and also reflect disease severity as clinically measured by spirometry. These correlations suggest that imaging ventilation heterogeneity measured by CV and MBW ventilation heterogeneity metrics may be reflecting a similar underlying pathophysiology. The moderate correlations of median CV and CVH skewness with FEV_1 and the FEV_1/FVC ratio also support this statement. LCI appears to be the best MBW metric to represent ventilation heterogeneity derived using the coefficient of variation of signal intensity. One possible reason for this is the fact that LCI represents early changes to the small airways, as does the imaging methodology used in this work [33]. S_{cond} also appears to be a good representative of ventilation heterogeneity, possibly due to the fact that the heterogeneity of the conducting zone in the lung can be more clearly distinguished using imaging than that in the acinar zones. The ventilated lung volume based method provided improved separation of patients with mild disease from healthy controls possibly due to the exclusion of voxels which result in high CV values, leading to reduced median, skewness and kurtosis values when compared to the total lung volume method e.g. Figure 4.49. The example in Figure 4.49 from a patient with CF shows increased CV at the ‘transitional’ areas of the defect, and it is these areas which lead to histogram metrics more similar to the healthy controls in the mild disease cohorts used here.

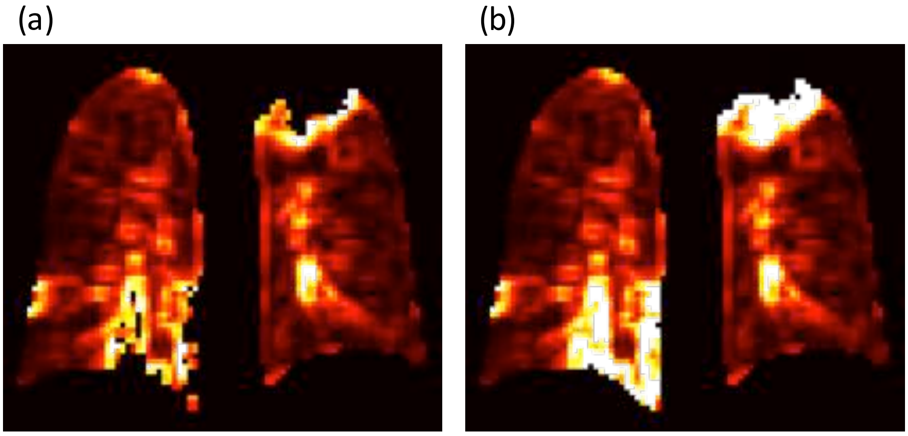

Figure 4.49 Example CV maps generated using the (a) VV mask and (b) the TLV mask from a ptient with CF

As seen in the work of Norberg et al. [339, 30, 345] area under the curve of the CV histogram is a useful metric to differentiate patient groups, although it was not successful in separating health from disease in all cohorts. By using the 95th percentile rather than the mean as a threshold, improved differentiation was seen between groups. However, the healthy cohorts from whom the values were determined are small in this work.

4.6.5 ^{3}He vs. ^{129}Xe CVH metrics

^{129}Xe and ^{3}He CVH metrics were significantly different in the 11 NSCLC patients analysed in this study, likely due to the lower SNR in the ^{129}Xe images. Therefore, the different intrinsic gas properties and imaging quality are important factors to consider when developing analysis techniques for quantifying these images. One possible solution could be to remove noise from the image using a method similar to that developed in [326], where the mean noise level was subtracted from all pixels, and evaluate whether this will result in more similar metrics when comparing these two gases. Of course, the small sample size and specificity of the patients included in this study mean that these results are not generalizable and should be considered only in the context of the comparisons carries out here.

4.7 Conclusion

The histogram-based method of CV analysis has the ability to differentiate patient groups from healthy volunteers to the same, or in some cases more significant, extent as the commonplace measure of VDP. Additionally, CV metrics had strong correlations with MBW outputs and moderate correlations with spirometry measures suggesting that these metrics may be useful in clinical assessment of patients. Unlike VDP, CVH analysis makes use of the rich spatial information available in HP gas ventilation-weighted images. From the small numbers of data sets analysed in this work it seems that using 2D CV metrics seems to better differentiate health from disease when considering only CVH kurtosis with mixed results seen when comparing CVH skewness and IQR. One important consideration here is the small number of asthmatic and COPD patients and lack of other disease groups being analysed. Additionally, by comparing the metrics generated over the ventilated volume and total lung volume masks it was shown that using the ventilated volume mask allows improved differentiation, particularly of the healthy adults and asthma_norm group – although in certain instances the metrics generated from the total lung volume mask outperformed those generated from the ventilated volume mask.

Additional work is necessary to determine if CV metrics derived from ^{129}Xe ventilation images are able to differentiate to the same extent as ^{3}He between health and disease and also to refine the methodology and reduce the effect image SNR has on the derived quantities. CV metrics are more sensitive to image SNR than %VV and thus more care must be taken when calculating and making use of CV metrics.

CHAPTER 5. ASSESSMENT OF THE INFLUENCE OF LUNG INFLATION STATE ON THE QUANTITATIVE PARAMETERS DERIVED FROM HP GAS LUNG VENTILATION MRI[3]

5.1 Introduction

The lung has a dynamic range of volumes as presented in Figure 2.3 and will change shape during inspiration and expiration within the thorax. Lung volumes are indicated on Figure 2.3 along with one of the standard metrics used in analysing pulmonary function, FEV_1.

As shown in Figure 2.3 there are a number of quantities that can be measured by either spirometry or body plethysmography. The results of these tests are compared to reference values predicted for the subject undergoing the tests based on numerous factors including age and height [118, 346]. For both spirometry and body plethysmography there are international standards to be followed that ensure repeatable measures of the quantities derived from these methods. Indeed for spirometry there are strict guidelines where measured values must be within an accepted threshold over the repetitions within the exam, whilst measurement of lung volumes using body plethysmography also have their own detailed standards [112] to be followed during examinations. Reported within a day, week to week and year to year changes for FEV_1 and FVC in normal subjects measured using spirometry are considered significant if they are over 5%, 11% and 15% respectively [5].

The lung volumes at which HP MRI or even computed tomography (CT) are performed are usually obtained by training and instructing the patient on the manoeuvre beforehand, however it has been shown that the use of spirometrically-gated CT and non-gated CT provide different estimates for lung density due to the difference in volume [347-352] and provide improved repeatability of lung inflation level. Additionally, as gas trapping is

---

[3] I would like to acknowledge the efforts of Laurie Smith, Fung Chan, Oliver Rodgers, Dr Guilhem Collier and Dr Graham Norquay for their help in acquiring the healthy volunteer data for this study. I also acknowledge the efforts of Dr Bilal Tahir in aiding with registration for the analysis of this data.

assessed using the difference of attenuation between an inspiratory and expiratory scan controlling the volumes these are acquired at is a key factor to ensure that this dynamic process is assessed correctly [353, 354].

5.1.1 Review of HP gas methods to assess ventilation heterogeneity at different states of lung inflation

Most HP gas studies carried out to evaluate lung function are acquired at a single fixed volume, generally functional residual capacity plus 1L (FRC+1L), to ensure repeatability in longitudinal studies [58-60, 62, 63, 355, 221, 78, 71]. These images are 'snapshots' of the ventilation distribution at a fixed point of the respiratory cycle and may not truly be representative of the dynamic nature of the lung. However, dynamic imaging methodologies enable visualisation of the lung ventilation over a range of volumes [356, 226, 227], whilst wash-in/wash-out techniques allow for assessment of gas turnover [67, 327].

Salerno et al. [357] developed a dynamic spiral HP MRI sequence capable of visualizing gas flow during breathing in healthy volunteers and patients with a variety of lung pathologies. Their method built on a number of previous studies to produce a pulse sequence that had similar spatial resolution to the static ventilation imaging available at the time. The method developed by Salerno et al. was capable of identifying the difference in filling of the parenchyma between patients and healthy volunteers and also could characterise ventilation defects. Wild et al. [356] developed an alternative methodology of monitoring the lung using a dynamic HP gas sequence where rather than an interleaved spiral acquisition a radial sequence was used. Koumellis et al. [358] built on this work by quantitatively evaluating the signal kinetics of HP ^{3}He in the lungs of patients with CF to derive metrics of gas flow. This was accomplished by imaging paediatric CF patients during inhalation and expiration of HP gas with a dynamic radial sequence, and showed that flow rate was altered in this cohort. Holmes et al. [226, 359, 227] developed protocols to assess ventilation impairment, including gas trapping, using dynamic HP gas MRI. A 3D multi-echo projection acquisition was used to dynamically scan a participant throughout respiration, breath hold, a forced expiratory manoeuvre to residual volume (RV) and tidal breathing [227]. Gas trapping was indicated by a consistent signal in a voxel rather than loss of signal, as one would expect whilst exhaling the HP gas. These areas of gas trapping were then compared to results from MDCT, showing strong agreement in the areas defined as gas trapping from HP MRI and MDCT. Kyriazis et al. [228] imaged rats dynamically during inspiration of HP gas to develop a metric of regional inflation rate, which they showed was altered in elastase-treated rats compared to normal rats.

Horn et al. [67, 70] developed a multiple breath washout imaging protocol to assess gas turnover in the lung using HP gases to derive a quantitative estimation of fractional ventilation. The method developed by Horn et al. [67, 70] differs from Holmes et al. [226, 359, 227] as the images are acquired while the subject holds their breath in between normal tidal breathing, and a lower resolution, Cartesian pulse sequence is used. Additionally, Horn et al. correct for the change in T_1 and RF decay and this provides quantitative measures of fractional ventilation. Hamedani et al. [327] recently developed a technique where the wash-in curve of HP gas is fitted to derive fractional ventilation using a 2D gradient-echo pulse sequence that employed parallel imaging.

Of course, with the availability of these dynamic imaging methods and wash-in/wash-out techniques it appears as though static ventilation imaging might become obsolete, however there are reasons that this technique is still being used in the pulmonary MRI community. One reason is that although washout imaging provides quantification of gas turnover it is limited in spatial resolution, with the in-plane resolution being ~12mm^2 [67], whereas static ventilation images have a resolution of ~3.2mm^2 [66], allowing for improved detection of small defects with this static methodology. With the dynamic sequences, there are also temporal resolution limits based on the speed of inhalation and expiration, requiring rapid image sampling which in itself is constrained by the choice of sequence and the considerations of HP gas imaging discussed in Chapter 2, section 2.4.4.

In a pilot study from our group in patients with asthma it was previously shown that there is a marked difference in %VV between HP gas ventilation images acquired at FRC+1L and total lung capacity (TLC) [360]. Additionally, the gas distribution within the lung improved at TLC when compared to FRC+1L suggesting that for better impact of treatment patients with asthma should inhale deeply to open the more vulnerable airways which would close at lower lung volumes due to inflammation and remodelling [99, 361, 362]. Increased ventilation heterogeneity has been observed in elite divers imaged close to their RV, after inhalation from sub RV volumes, when compared to normal control subjects imaged following inhalation from RV, resulting in volumes close to FRC [363]. In this work two elite divers were imaged after inhaling a small volume from sub RV (0.9 and 0.4L respectively of a mix of HP ^{129}Xe and O_2) and a larger volume (1.3 and 0.9L respectively of a mix of HP ^{129}Xe and O_2) with higher heterogeneity being seen after inhalation of the smaller volumes of gas. The healthy controls on the other hand had a lower heterogeneity score after inhaling from RV. The cause of this heterogeneity in the elite divers is assumed to be punctate opening of the airways; that is a reopening of frankly closed airways rather than functionally closed airways, although this was not seen in the volunteers possibly due to not being able to match the manoeuvre performed by the divers.

It is therefore important to assess the effect of lung inflation state on the qualitative appearance of HP gas ventilation images when imaging at breath hold and also to assess the effect of lung inflation state on the values and inter scan reproducibility of quantitative parameters derived from HP gas images. As covered in Chapter 3, the most widely used quantitative index of lung ventilation derived from HP gas and ^{1}H images is %VV and its counterpart VDP. These measures have been used to differentiate mild CF patients from age-matched healthy controls [33], to detect early obstructive changes in smokers [77] and have also been shown to be sensitive to disease severity and treatment [58-60, 63]. Additionally, they have been used to monitor patients with asthma in longitudinal studies [315, 316] to allow for disease monitoring and response to therapy and have correlation with spirometric findings [364, 60]. With the adoption of HP gas imaging for quantitative clinical assessment of lung obstruction [365] it is important to understand the effect of the inflation level of the lung on this measure. Additional measures of ventilation heterogeneity such as the coefficient of variation of ventilation signal intensity (CV, Chapter 4) [326] might also be expected to change with lung inflation particularly in partially obstructed lungs.

5.1.2 Aims of the study

The aim of the work performed in this chapter was to assess the effect of lung inflation on 3D HP gas lung ventilation images in a group of healthy subjects, a small cohort of patients with CF and a small cohort of patients with asthma by scanning at different lung inflation levels using same breath hyperpolarised ^{3}He and ^{1}H imaging. Additionally, a subgroup of the healthy subjects was scanned using separate breath hyperpolarised ^{129}Xe and ^{1}H imaging to determine if the same changes were seen using ^{129}Xe.

As a secondary aim the volumes obtained from the MRI data were compared with those obtained from body plethysmography. One important difference between these tests is that MRI was performed supine whilst body plethysmography was performed sitting. The values obtained from body plethysmography were RV, FRC and TLC. As it is not standard practice to measure FRC+1L and RV+1L using this technique, FRC+1L and RV+1L values were excluded from this comparison. Note that body plethysmography was carried out once for all healthy volunteers on the same day as the HP ^{3}He imaging session, except for HV6 where body plethysmography was carried out on the same day as the HP ^{129}Xe imaging session.

5.2 Materials and methods

5.2.1 Participants

Six healthy volunteers (one current smoker, one former smoker, two occasional smokers and two never smokers, all male) were recruited for this study with no exclusion criteria applied. The volunteers ranged in age from 27 to 35. The study was performed with National Research Ethics Committee and MHRA approval with informed consent from all volunteers. 6 patients with CF (3 male, 3 female) were selected from a separate study where images were acquired at FRC+1L and TLC with informed consent given by parents or participants depending on age. Additionally, 6 patients with asthma (3 male, 3 female) were selected from a separate study [71] where images were also acquired at FRC+1L and TLC. CF patients FEV_1 % predicted ranged from 39% to 112%, and age from 11 to 37, whilst asthmatic patients' FEV_1 % predicted ranged from 32% to 95% and age ranged from 41 to 64. Table 5.1 shows the demographics of the healthy volunteers and patients analysed here.

Table 5.1 Patient demographics for the multiple inflation level study

Patient	Age (years)	Sex	Height (cm)	Weight (kg)	FEV_1 (% predicted)
HV1	32	M	183.0	87.0	102.0
HV2	35	M	184.0	76.0	77.2
HV3	31	M	182.0	83.0	105.0
HV4	34	M	185.6	94.0	83.6
HV5	27	M	189.5	74.0	102.9
HV6	28	M	187.6	90.0	99.9
CF1	37	M	167.9	59.0	57.5
CF2	25	F	153.2	45.0	39.7
CF3	26	F	160.9	52.0	96.6
CF4	24	M	174.4	59.0	112.7
CF5	25	M	166.4	55.4	100.6
CF6	11	F	143.7	30.0	92.3
Asthma1	41	M	173.0	77.0	84.9
Asthma2	51	F	158.0	62.4	31.0
Asthma3	45	M	174.0	88.3	99.1
Asthma4	64	F	156.0	57.8	96.2
Asthma5	62	M	177.0	90.6	66.1
Asthma6	52	F	152.0	51.4	89.2

5.2.2 Study protocol

Healthy volunteers were imaged with a ^{3}He transmit-receive flexible chest coil (Clinical MR Solutions, Brookfield, WI, USA). Imaging was carried out on a GE HDx 1.5T MRI scanner (GE Healthcare, Milwaukee, IL, USA). HP ^{3}He and ^{1}H images were acquired in the same breath at five different inflation levels: RV, RV+1L, FRC, FRC+1L and TLC (Figure 2.3, Figure 5.1). All breathing manoeuvres started with inhalation of the 1L bag from FRC, except for the RV+1L image where the inhalation started after first exhaling to RV. To acquire images at TLC, volunteers first inhaled the 1L bag from FRC to reach FRC+1L and then topped up the volume with room air. For imaging at FRC, volunteers inhaled the 1L bag from FRC and then exhaled back to FRC. For RV imaging, volunteers inhaled the bag from FRC and then exhaled to RV.

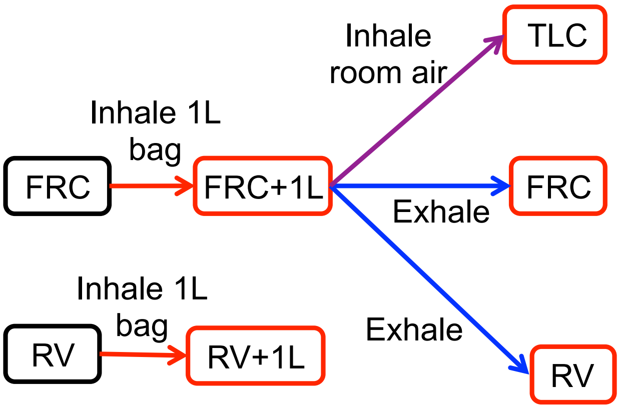

Figure 5.1 Breathing manoeuvres and acquisition volumes. RV = residual volume, FRC = Functional residual capacity, TLC = total lung capacity. Blue lines indicate an exhalation; red lines indicate an inhalation from a 1L bag and purple lines represent an inhalation of room air following inhalation from a bag

Same-breath 3D bSSFP ^{3}He and ^{1}H SPGR images were acquired using the gas doses given in Table 5.2. Imaging sequence parameters can be found in Chapter 3, section 3.3.1.3.

Table 5.2 Gas doses for ^{3}He acquisitions

	HV		Asthma		CF	
Acquisition	**^{3}He**	**N_2**	**^{3}He**	**N_2**	**^{3}He**	**N_2**
RV	200	800	-	-	-	-
RV+1L	150	850	-	-	-	-
FRC	200	800	-	-	-	-
FRC+1L	150	850	350	650	110-150	290-850
TLC	200	800	400	600	160-200	240-800

The gas doses for healthy volunteers were chosen empirically with the aim being to achieve approximately the same gas nuclear spin density, and hence, SNR in all images due to gas dilution at TLC and gas exhalation with the exhalation scans. Images were acquired in two sessions with a 10-minute break between the first and second set of acquisitions, with patients remaining in the scanner throughout. A qualified respiratory physiologist gave breathing instructions. Following all acquisitions patients underwent spirometry and body plethysmography performed to international standards [112].

^{3}He doses for patients with CF were scaled by height and predicted values of FRC and TLC based on normal values [341, 33] and they underwent the same image acquisition protocol as the healthy volunteers [66] but scans were not repeated and were only acquired at FRC+1L and TLC. Patients with asthma underwent multi-slice 2D spoiled gradient echo HP ^{3}He ventilation imaging following inhalation of 350ml ^{3}He mixed with 650ml N_2 from a Tedlar bag (Jensen Inert Products, Coral Springs, Florida, USA) from FRC. The imaging matrix was fixed at 128x102 resulting in resolutions of ~3x3x10mm. Same-breath 2D balanced steady state free precession ^{1}H anatomical images were acquired using the system body coil with a lower resolution. For TLC imaging patients inhaled a gas mixture consisting of 400ml ^{3}He mixed with 600ml N_2 and inhaled room air to reach TLC. Asthma patients were imaged with a 2D sequence as this study was carried out prior to the 3D HP ^{3}He imaging being optimised for use.

Three of the five healthy volunteers (HV2, HV3 and HV6) were scanned using HP ^{129}Xe at the aforementioned five lung volumes twice. ^{129}Xe was polarized on site [23]. Images were acquired using a ^{129}Xe transmit-receive flexible vest coil (Clinical MR Solutions, Brookfield, WI, USA) and the ^{1}H system body coil. ^{1}H anatomical images were acquired in a separate breath prior to the HP gas ventilation images. Between each session, patients were removed from the scanner as the waiting time was increased due to production limitations of the ^{129}Xe. Gas doses are given in Table 5.3 and were chosen to achieve the highest possible SNR in the images and ensure they were comparable to the images acquired with ^{3}He.

Table 5.3 Gas doses for ^{129}Xe acquisitions

Acquisition	^{129}Xe	N_2
RV	1000	0
RV+1L	750	250
FRC	1000	0
FRC+1L	600	400
TLC	750	250

5.2.3 Image analysis

The parameters TLV, VV and %VV were calculated from all images using the segmentation method introduced in Chapter 3 (Figure 5.2). Secondly measures of CV were acquired using the method discussed in Chapter 4. CV measures were also generated from the TLV mask as in Chapter 4.

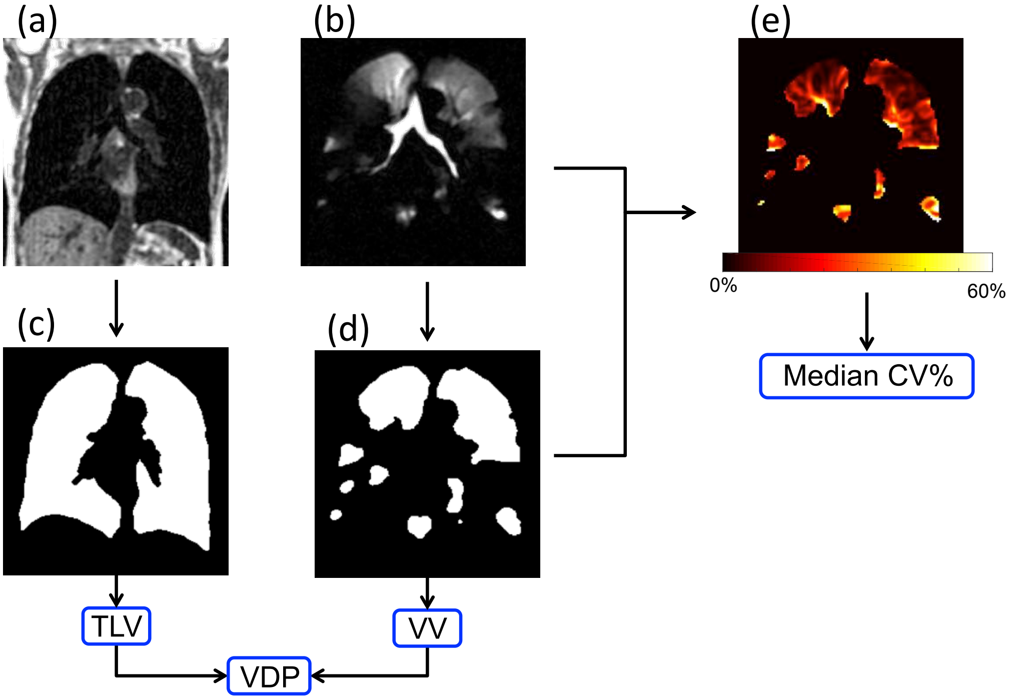

Figure 5.2 Workflow of image segmentation and CV metric calculation from the VV mask. (a) Example ^{1}H anatomical image slice from a 3D data set, (b) Example ^{3}He image slice from a 3D data set, (c) and (d) corresponding segmentation slices and (e) example slice of a CV map generated from the ^{3}He image

5.2.4 Reproducibility and statistical analysis

As measures of reproducibility between repeated measurements, that is the measurements obtained in the healthy volunteers in each imaging session, the coefficient of variation (CoV) was calculated [366] along with the percentage difference (%Δ, defined as ((session2-session1)/session1)*100) and Bland-Altman analysis [367].

Additionally, the voxel-wise Spearman rank correlation coefficient was used to compare inflation levels over both sessions, and to compare all inflation levels to FRC+1L for each session, that is RV_S1 was registered to FRC+1L_S1 and RV_S2 registered to FRC+1L_S2 and so on. For this analysis images acquired in session 2 were registered to their corresponding image in session 1, that is RV_S2 was registered to RV_S1 and so on. All registrations were carried out using the ANTs registration toolbox [84]. Ventilation images were registered directly to one another and only voxels within the ventilated volume were used in calculating the correlation coefficient.

TLVs calculated from the ^{1}H anatomical images were compared to the volumes from body plethysmography. Wilcoxon matched-pairs signed rank tests were carried out to determine if there were any significant differences in TLV, VV, %VV and CV metrics between each imaging session per inflation level and also between lung volume metrics obtained from MRI and body plethysmography for healthy volunteers. Wilcoxon matched-pairs signed rank tests were used to evaluate the change in volunteers/patients' metrics between FRC+1L and TLC. Healthy volunteers' metrics at FRC+1L and TLC were compared to those obtained in patients with asthma and CF using Mann-Whitney unpaired t-tests.

Finally, median CV (%) values from the images acquired at RV, RV+1L, FRC and TLC were compared to the median CV (%) value from the image acquired at FRC+1L via the mean absolute %Δ. Here, mean absolute %Δ is defined as:

$$\frac{abs(\%\Delta S1) + abs(\%\Delta S2)}{2} \tag{5.1}$$

where %Δ is defined as, for example:

$$\frac{CV\_RV - CV\_FRC + 1L}{CV\_FRC + 1L} \times 100 \tag{5.2}$$

5.3 Results

Section 5.3.1 discusses the repeatability of quantitative parameters of lung function acquired in a small cohort of healthy volunteers. Section 5.3.2 discusses the results of using hyperpolarised ^{129}Xe in place of ^{3}He in three of the six healthy volunteers analysed in section 5.3.1, demonstrating the applicability of using hyperpolarised ^{129}Xe in place of ^{3}He. Section 5.3.3 compares lung volumes obtained using MRI to those obtained using body plethysmography from the healthy volunteers presented in section 5.3.1. Finally, section 5.3.4 presents the effect of imaging patients at different lung inflation levels.

5.3.1 Repeatability in healthy volunteers

Figure 5.3 shows example images from all healthy volunteers. As can be seen by qualitatively evaluating the images, generally ventilation heterogeneity reduces as the volume increases, particularly at TLC.

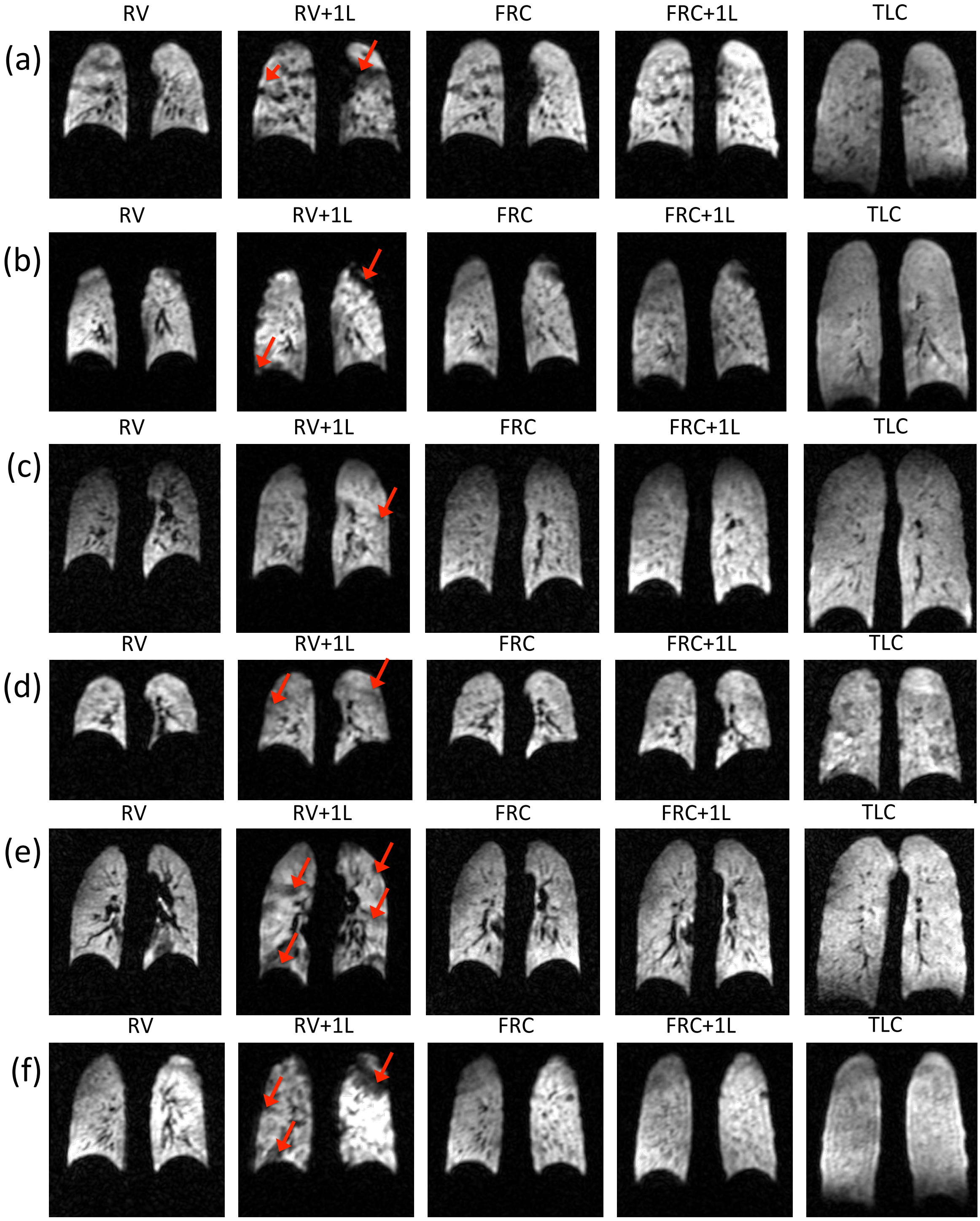

Figure 5.3 Example slices from all 6 healthy volunteers' datasets (acquired with HP ^{3}He). (a) HV1, (b) HV2, (c) HV3, (d) HV4, (e) HV5 and (f) HV6. Red arrows indicate apparent ventilation defects/areas of low ventilation present at RV+1L but that appear to fully/partially resolve at higher volumes

Figures 5.4 to 5.7 show plots of the metrics obtained from the images from the 6 HVs analysed here. The group mean TLVs at RV+1L and FRC are similar, which is logical considering that FRC reduces supine and thus is closer to RV.

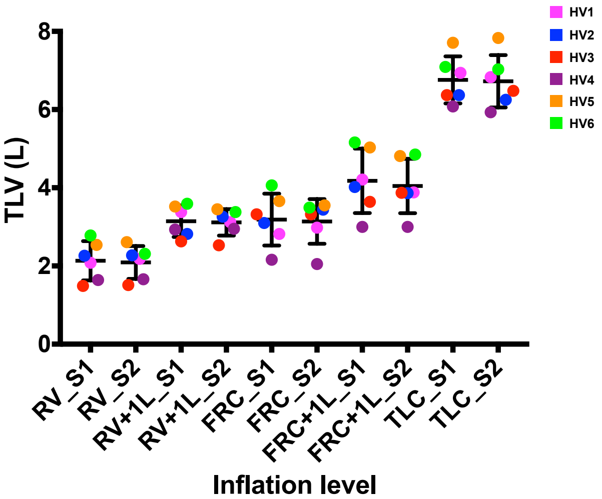

Figure 5.4 Plot of total lung volume at each inflation level from the 6 healthy adults scanned here. Each point represents a measurement from a single subject, error bars represent group means and standard deviations

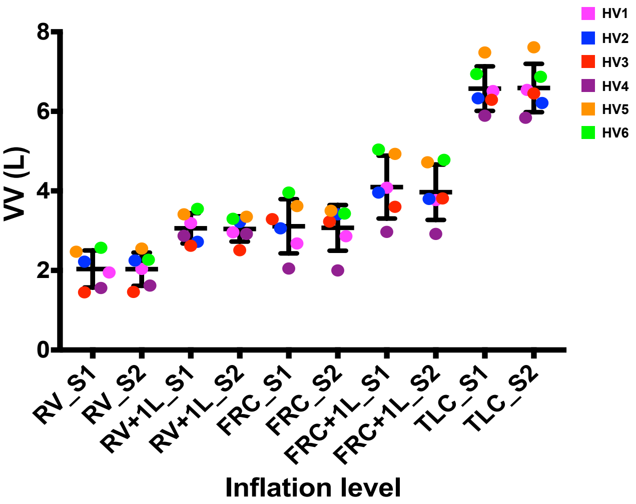

Figure 5.5 Plot of ventilated lung volume at each inflation level from the 6 healthy adults scanned here. Each point represents a measurement from a single subject, error bars represent group means and standard deviations

Overall, ventilated lung volume (Figure 5.5) appears to track the total lung volume (Figure 5.4) in these healthy volunteers, whereas %VV (Figure 5.6) highlights that there are differences in ventilated lung volume between inflation levels.

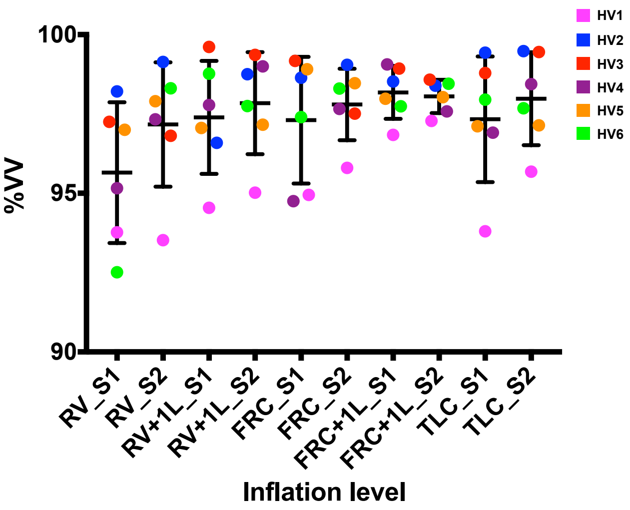

Figure 5.6 Plot of %VV at each inflation level from the 6 healthy adults scanned here. Each point represents a measurement from a single subject, error bars represent group means and standard deviations

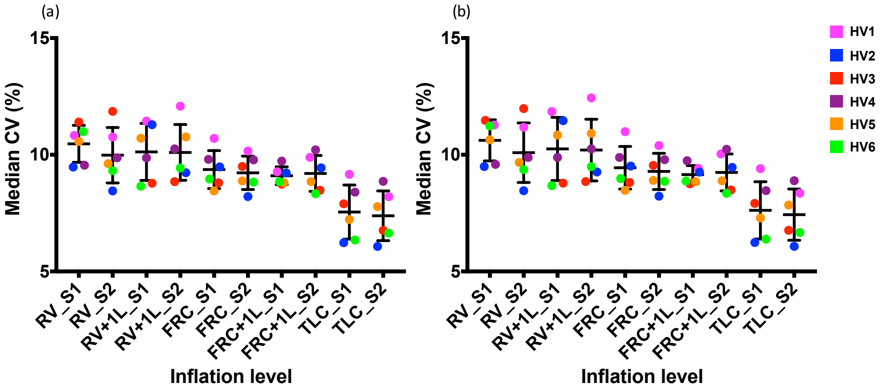

Figure 5.7 Plot of median CV at each inflation level from the 6 healthy adults scanned here generated using the (a) VV mask and (b) the TLV mask. Each point represents a measurement from a single subject, error bars represent group means and standard deviations

Median CV% (Figure 5.7) changed with inflation level; median CV is lowest at TLC and highest at RV and RV+1L. Table 5.4 shows the mean CoV, of TLV, VV and %VV, over all 6 volunteers at each inflation level. Regarding TLV and VV, the most repeatable volumes appear to be FRC+1L and TLC. When considering %VV FRC+1L is the most reproducible whilst RV has the most variation over all 6 volunteers.

Table 5.5 shows the mean CoV for all CV metrics generated using both TLV and VV masks, where FRC+1L has the lowest CoV in al CV metrics when generated from the VV mask. When considering metrics generated from the TLV mask median CV and CVH IQR are most repeatable at FRC+1L and CVH skewness and kurtosis are most repeatable at RV+1L.

Table 5.4 Mean CoV for TLV, VV and %VV over all volunteers between each session

Acquisition	TLV	VV	%VV
RV	3.40	3.05	1.29
RV+1L	4.13	4.64	0.63
FRC	4.63	4.64	0.87
FRC+1L	3.42	3.42	0.38
TLC	1.19	1.00	0.54

Table 5.5 CV metrics CoV over all volunteers between each session

Acquisition	Median CV	CVH skewness	CVH kurtosis	CVH IQR
RV	5.32	9.59	15.16	7.45
RV+1L	4.62	5.99	10.46	6.46
FRC	3.99	6.63	11.52	3.95
FRC+1L	2.74	3.68	5.88	3.03
TLC	5.46	4.99	7.63	4.19
TLV metrics				
RV	5.60	7.86	17.71	8.59
RV+1L	4.74	4.87	10.67	7.26
FRC	4.16	9.27	17.14	4.52
FRC+1L	2.72	7.71	15.06	2.97
TLC	5.52	6.66	14.30	4.50

Figure 5.8 shows the Bland-Altman plots for TLV, VV and %VV whilst Figure 5.9 shows the Bland-Altman plots for median CV (%), CVH skewness, kurtosis and IQR generated using the VV and TLV masks.

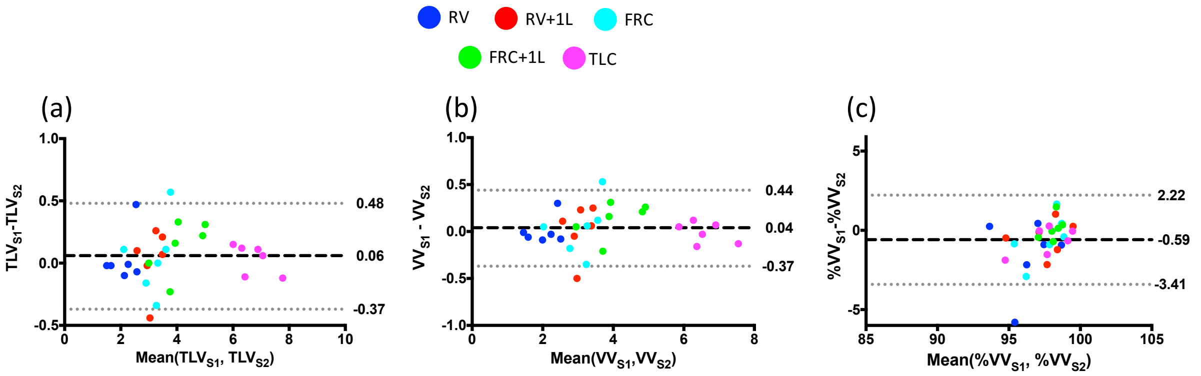

Figure 5.8 Bland-Altman plots of (a) TLV, (b) VV and (c) %VV for all 6 volunteers

TLV and VV had Bland-Altman bias±limits of agreement (LOA) of 60ml±420ml and 40ml±400ml respectively, suggesting almost a litre of change between imaging sessions occurs over all 6 volunteers at all inflation levels. %VV had bias±LOA of -0.60%±2.81%.

Median CV (%) had bias±LOA of 0.14%±1.50% when generated from the VV mask and 0.16%±1.54%, suggesting very little change in median CV (%) and a moderate change in %VV. CVH skewness, kurtosis and IQR also have very little variation when generated from the VV mask with similar values of bias±LOA seen in the metrics generated from the TLV mask when compared to the VV mask suggesting good agreement using both methods.

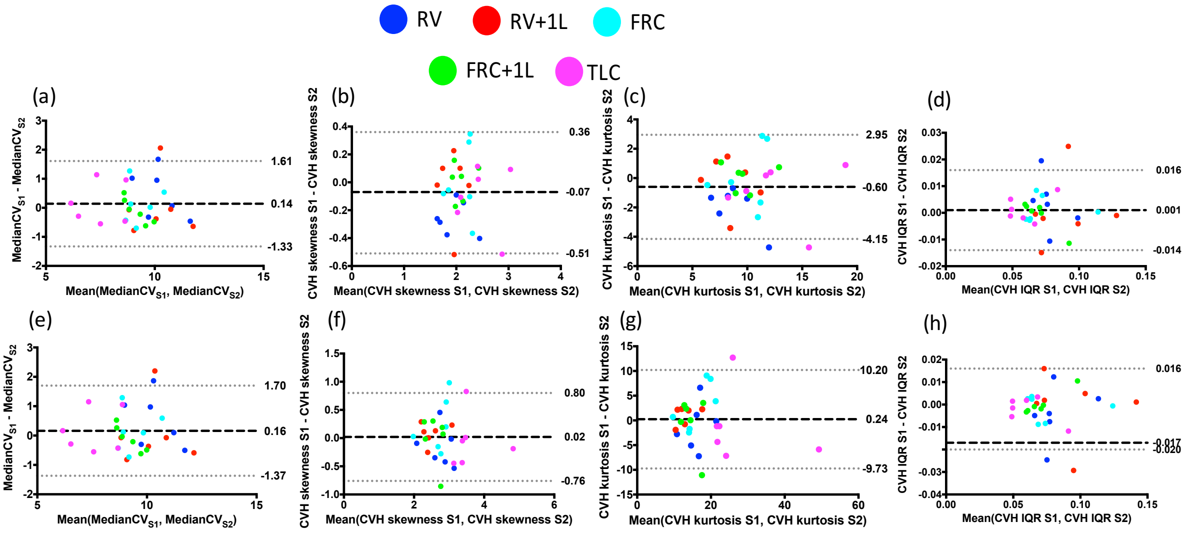

Figure 5.9 Bland-Altman plots of CVH metrics generated from the VV mask (a-d) and TLV mask (e-h). (a) Median CV, (b) CVH skewness, (c) CVH kurtosis, (d) CVH IQR, (e) Median CV, (f) CVH skewness, (g) CVH kurtosis, and (h) CVH IQR

As can be seen from Table 5.6 there is a clear pattern of increased % change over the two sessions, as defined in section 5.2.3, of TLV and VV when compared to %VV. This implies that although the volumes measured change between each session the measure of %VV is not affected to the same extent.

Table 5.6 %Δ of TLV, VV and %VV over both sessions for all volunteers

		HV1			HV2	
Acquisition	**TLV**	**VV**	**%VV**	**TLV**	**VV**	**%VV**
RV	5.04	4.76	-0.26	0.26	1.21	0.95
RV+1	-7.76	-7.30	0.50	15.79	18.38	2.24
FRC	5.87	6.82	0.90	10.99	11.45	0.41
FRC+1	-7.83	-7.41	0.46	-4.06	-4.19	-0.13
TLC	-1.54	0.44	2.01	-1.88	-1.82	0.05
		HV3			**HV4**	
Acquisition	**TLV**	**VV**	**%VV**	**TLV**	**VV**	**%VV**
RV	1.63	1.16	-0.45	1.67	3.99	2.28
RV+1	-3.93	-4.17	-0.25	0.50	1.76	1.25
FRC	-0.07	-1.75	-1.68	-5.22	-2.30	3.08
FRC+1	6.22	5.85	-0.35	-0.24	-1.73	-1.49
TLC	1.76	2.44	0.66	-2.52	-0.98	1.58
		HV5			**HV6**	
Acquisition	**TLV**	**VV**	**%VV**	**TLV**	**VV**	**%VV**
RV	1.67	3.99	2.28	-16.95	-11.65	6.27
RV+1	0.50	1.76	1.25	-5.95	-6.92	-1.03
FRC	-5.22	-2.30	3.08	-14.19	-13.40	0.92
FRC+1	-0.24	-1.73	-1.49	-5.90	-5.22	0.73
TLC	-2.52	-0.98	1.58	-0.79	-1.05	-0.27

Tables 5.7 to 5.8 shows the %Δ of CVH metrics from the VV and TLV masks respectively.

Table 5.7 %Δ of CVH metrics generated from the VV mask

Acquisition	Median CV	CVH skewness	CVH kurtosis	CVH IQR	Median CV	CVH skewness	CVH kurtosis	CVH IQR
		HV1				HV2		
RV	-15.16	17.33	38.56	-23.96	-0.67	18.54	22.20	1.94
RV+1L	9.03	-5.59	-14.61	23.17	5.56	1.21	2.14	0.78
FRC	-1.43	2.99	3.30	3.53	-5.00	4.75	7.72	-0.26
FRC+1L	-5.90	-1.89	-3.86	-5.25	6.64	-7.73	-13.18	13.13
TLC	4.42	5.28	9.34	2.51	-10.44	11.27	17.46	-9.86
Acquisition	**Median CV**	**CVH skewness**	**CVH kurtosis**	**CVH IQR**	**Median CV**	**CVH skewness**	**CVH kurtosis**	**CVH IQR**
		HV3				HV4		
RV	-10.76	7.09	15.14	-6.78	4.01	22.99	15.92	14.58
RV+1L	-18.22	30.47	50.51	-23.85	0.85	1.02	9.14	0.75
FRC	-13.37	17.19	27.65	-11.3	8.06	-14.21	-20.36	4.55
FRC+1L	2.43	-2.01	-3.00	0.14	4.90	6.53	12.21	-2.80
TLC	-2.61	19.66	35.69	-2.60	-14.46	-2.99	-4.59	-9.96
Acquisition	**Median CV**	**CVH skewness**	**CVH kurtosis**	**CVH IQR**	**Median CV**	**CVH skewness**	**CVH kurtosis**	**CVH IQR**
		HV5				HV6		
RV	3.25	17.93	49.20	-4.11	-8.95	4.66	8.32	-8.87
RV+1L	3.81	-4.75	-3.83	2.92	0.45	-10.99	-16.46	4.22
FRC	-0.22	4.68	16.03	-8.59	5.08	-12.09	-22.44	4.07
FRC+1L	4.90	6.52	12.21	-2.80	0.56	9.12	12.25	-1.08
TLC	5.48	-0.88	-1.53	6.50	7.59	-4.65	-3.20	3.33

Table 5.8 %Δ of CVH metrics generated from the TLV mask

Acquisition	Median CV	CVH skewness	CVH kurtosis	CVH IQR	Median CV	CVH skewness	CVH kurtosis	CVH IQR
		HV1				HV2		
RV	-0.89	0.53	-6.70	-2.27	-10.93	-15.34	-32.49	7.72
RV+1L	4.96	11.19	20.25	-0.77	-19.19	-4.84	-13.47	36.49
FRC	-5.40	10.57	18.99	0.48	-13.55	5.84	12.95	13.71
FRC+1L	6.56	-2.51	-0.31	-10.18	2.25	-11.26	-16.48	0.41
TLC	-11.21	-0.28	5.54	13.85	-2.66	13.79	22.26	3.07
Acquisition	**Median CV**	**CVH skewness**	**CVH kurtosis**	**CVH IQR**	**Median CV**	**CVH skewness**	**CVH kurtosis**	**CVH IQR**
		HV3				HV4		
RV	4.38	18.64	0.77	-14.25	3.12	15.74	55.23	5.35
RV+1L	0.79	-0.24	6.11	-0.74	3.72	-12.31	-18.08	-2.56
FRC	8.30	-6.62	-16.76	-5.49	-0.96	-28.07	-38.81	12.05
FRC+1L	-3.00	-6.50	-18.00	4.54	5.03	0.67	2.53	2.72
TLC	-14.54	-21.19	-39.39	11.69	5.05	1.44	5.40	-4.87
Acquisition	**Median CV**	**CVH skewness**	**CVH kurtosis**	**CVH IQR**	**Median CV**	**CVH skewness**	**CVH kurtosis**	**CVH IQR**
		HV5				HV6		
RV	-9.15	14.41	42.11	10.37	-16.61	4.53	29.55	39.17
RV+1L	0.67	-7.22	-12.01	-4.62	9.43	-4.82	-17.46	-19.75
FRC	5.03	-19.77	-34.89	-4.19	-1.33	-1.45	-7.00	-3.69
FRC+1L	0.41	36.65	92.16	1.38	-5.92	-11.82	-21.54	5.68
TLC	7.58	3.96	12.65	-3.13	4.50	15.38	34.95	-2.99

Generally, TLV metrics demonstrate less %Δ between each session when compared to those metrics derived from the VV mask. Tables 5.9 to 5.11 shows the results of the voxel-wise Spearman correlation of ventilation image signal when considering the inter-session correlation and correlation of all inflation levels with FRC+1L for each session respectively.

Table 5.9 Results of the inter-session voxel-wise Spearman correlation

Subject	RV	RV+1L	FRC	FRC+1L	TLC
HV1	0.88	0.91	0.91	0.89	0.90
HV2	0.94	0.94	0.97	0.98	0.94
HV3	0.95	0.97	0.95	0.96	0.91
HV4	0.95	0.97	0.96	0.95	0.93
HV5	0.94	0.93	0.95	0.95	0.96
HV6	0.88	0.92	0.96	0.96	0.95
Mean(SD)	0.92(0.03)	0.94(0.03)	0.95(0.02)	0.95(0.03)	0.93(0.02)

In this cohort of healthy volunteers there was strong correlation between images acquired in different sessions, suggesting very little change in the distribution of gas in ventilated regions over the two sessions at each inflation level.

Table 5.10 Results of the voxel-wise correlation of all other inflation levels to FRC+1L from the first imaging session

Subject	RV	RV+1L	FRC	TLC
HV1	0.80	0.58	0.85	0.68
HV2	0.86	0.51	0.94	0.71
HV3	0.84	0.68	0.97	0.80
HV4	0.83	0.88	0.88	0.70
HV5	0.78	0.41	0.91	0.68
HV6	0.82	0.60	0.94	0.85
Mean(SD)	0.82(0.03)	0.61(0.16)	0.91(0.05)	0.74(0.07)

Table 5.11 Results of the voxel-wise correlation of all other inflation levels to FRC+1L from the second imaging session

Subject	RV	RV+1L	FRC	TLC
HV1	0.79	0.56	0.89	0.73
HV2	0.89	0.60	0.97	0.80
HV3	0.82	0.63	0.95	0.83
HV4	0.82	0.79	0.87	0.61
HV5	0.76	0.39	0.88	0.73
HV6	0.85	0.52	0.92	0.86
Mean(SD)	0.82(0.05)	0.58(0.13)	0.91(0.04)	0.76(0.09)

As can be seen from tables 5.10 and 5.11 the image with the highest correlation to FRC+1L is FRC, which is logical considering the small inhalation from FRC+1L to FRC. Additionally, RV and TLC had good correlations with FRC+1L and, as one would expect from comparing the images visually and the different breathing manoeuvre employed prior to imaging, RV+1L had a lower correlation with FRC+1L when compared to all other inflation levels.

As an additional measure of repeatability, lung volumes over all volunteers were compared via a paired t-test/Wilcoxon matched-pairs signed rank tests (depending on the normality of the data). Table 5.12 shows the summary of comparisons. As can be seen all comparisons have a p-value >0.1, showing that there is no significant difference between the lung volumes over the sessions in this cohort of healthy volunteers.

Table 5.12 P-value comparing TLV, VV and %VV

Acquisition	TLV	VV	%VV
RV	0.5655	0.9778	0.2435
RV+1L	0.7815	0.8883	0.3725
FRC	>0.9999	0.8438	0.4630
FRC+1L	0.1913	0.1528	0.7022
TLC	0.5062	0.7846	0.1320

Table 5.13 P-value comparing CVH metrics generated from the VV mask between each session

Acquisition	Median CV	CVH skewness	CVH kurtosis	CVH IQR
RV	0.2162	<0.001	0.0682	<0.001
RV+1L	0.9579	0.8433	0.7403	0.9458
FRC	0.6571	0.9649	0.9352	0.8438
FRC+1L	0.6030	0.9239	0.9152	0.8202
TLC	0.6115	0.3435	0.3242	0.5377

Table 5.14 P-values comparing CVH metrics generated from the TLV mask between each session

Acquisition	Median CV	CVH skewness	CVH kurtosis	CVH IQR
RV	0.2155	0.3265	0.5609	0.4214
RV+1L	0.9196	0.3260	0.2407	0.8998
FRC	0.6182	0.2859	0.2022	0.8438
FRC+1L	0.6211	0.9860	0.8691	0.9159
TLC	0.5752	0.5625	0.4375	0.7188

When considering the metrics generated from the VV mask the only significant differences were seen with CVH skewness and IQR at RV, whilst for the metrics generated from the TLV mask there were no significant differences seen in any metric between any sessions.

The most interesting discovery is that the highest observed CV is at RV+1L with Figure 5.10 showing an example from HV2. As can be seen at FRC+1L there are few small defects in this posterior slice yet at RV+1L there seems to be the appearance of defects and ventilation heterogeneity possibly caused by airways which have not reopened after inhalation from RV [89]. As discussed by West if only a small inspiration occurs from RV this does not sufficiently change the intrapleural pressure, particularly at the base, however it should be noted that in this cohort the lack of airway opening seems to occur throughout the lung and not only the base.

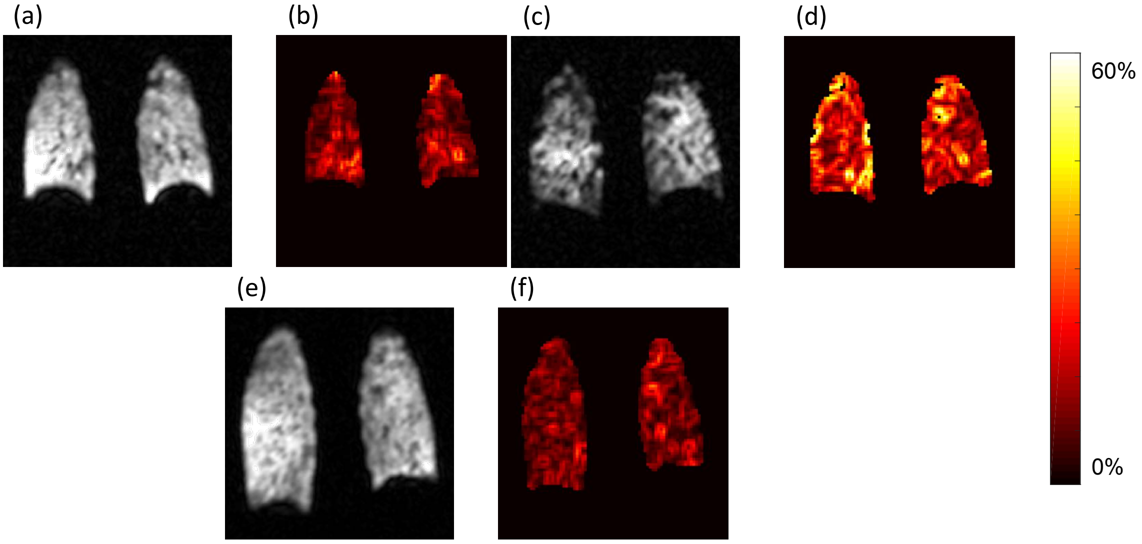

Figure 5.10 Example of differences seen in HP ^{3}He images acquired at RV, RV+1L and FRC+1L (posterior slices). (a) HP gas image slice acquired at RV, (b) corresponding CV map, (c) HP gas image slice acquired at RV+1L, (d) corresponding CV map, (e) HP gas image slice acquired at FRC+1L and (f) corresponding CV map generated from the VV mask

Median CV at FRC+1L and RV+1L differed in all volunteers as seen in Figure 5.7. Table 5.15 shows the mean absolute %Δ of median CV between FRC+1L and all other lung volumes.

Table 5.15 Mean absolute %Δ of median CV between FRC+1L and all other lung volumes

Volunteer	FRC+1L vs. RV	FRC+1L vs. RV+1L	FRC+1L vs. FRC	FRC+1L vs. TLC
HV1	12.81	22.78	9.08	9.14
HV2	6.60	12.34	7.92	34.06
HV3	35.15	2.41	6.36	14.95
HV4	2.59	0.92	2.47	13.45
HV5	14.41	21.64	2.16	14.97
HV6	18.03	7.73	3.62	24.27
Mean(SD)	14.93(11.36)	11.30(9.37)	5.27(2.93)	18.37(9.09)
		TLV values		
HV1	15.59	21.98	10.18	8.40
HV2	6.61	22.51	7.95	34.17
HV3	36.06	1.90	6.53	14.97
HV4	2.49	2.43	2.89	13.14
HV5	14.53	22.28	2.20	14.66
HV6	19.40	3.08	3.66	24.06
Mean(SD)	15.78(11.72)	12.36(10.85)	5.57(3.16)	18.23(9.32)

Two of the six volunteers had very small percentage increases in median CV between FRC+1L and RV+1L whilst four had comparatively large increases. Additionally, four of the 6 volunteers had a greater than 10% increase in median CV at RV when compared to FRC+1L whilst two had a less than 10% difference, with HV4 having only a 2.59% change in median CV. Median CV at TLC has a greater than 9% difference in all subjects with HV2 and HV6 having the greatest differences. This pattern of increased CV in the posterior slices was also seen when taking the median CV of every slice (Figure 5.11), from the images in the first imaging session. Additionally, as one would expect in healthy volunteers the pattern of change in the CV values calculated from the TLV mask is very similar to those calculated from the VV mask.

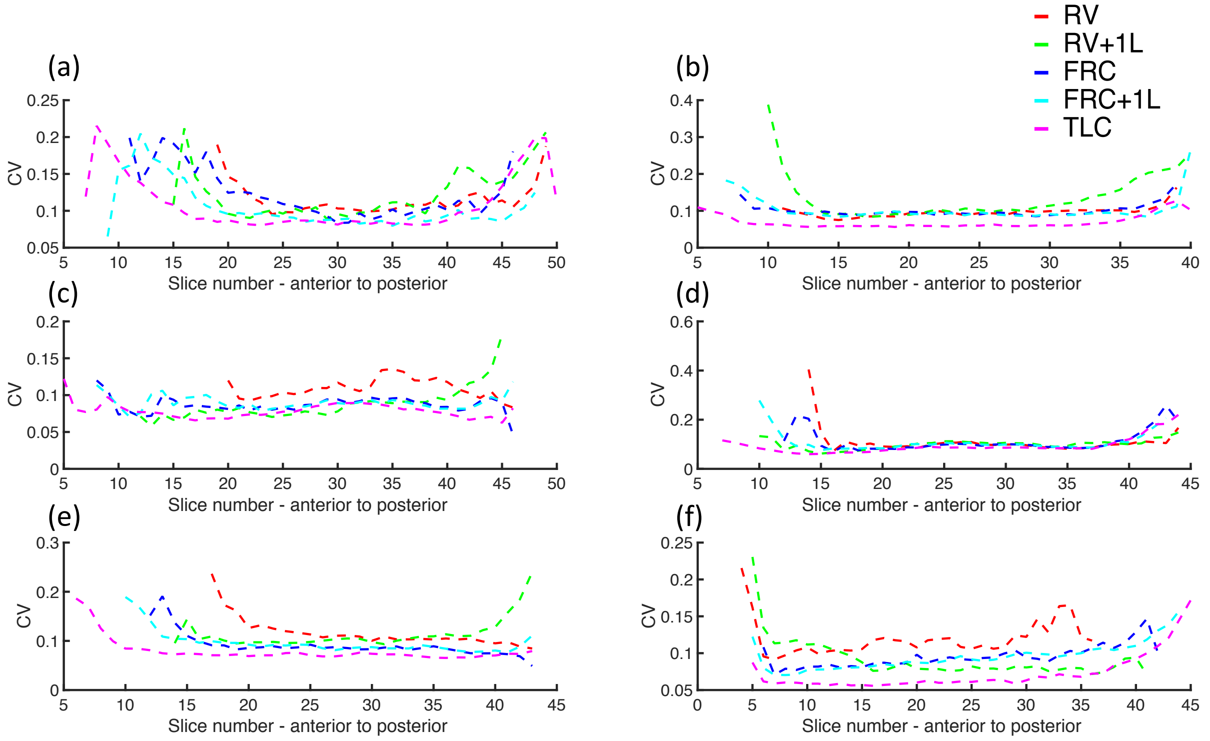

Figure 5.11 Plots of median CV per slice generated from the VV mask for all 6 healthy volunteers' images obtained with HP ^{3}He during imaging session 1. (a) HV1, (b) HV2, (c) HV3, (d) HV4, (e) HV5 and (f) HV6. All inflation levels were acquired using the same imaging volume with the number of slices and field of view being kept consistent

As can be seen from Figure 5.11 in five out of the six healthy volunteers there was increased median CV, with a steep incline, in the final ten or so posterior slices when comparing FRC+1L to RV+1L. High CV values were also seen in the anterior slices, although this may be due to less gas reaching this area of the lung due to gravitational dependence as well as partial volume effects. These patterns are also seen on the plots when generated from the TLV mask metrics (Figure 5.12).

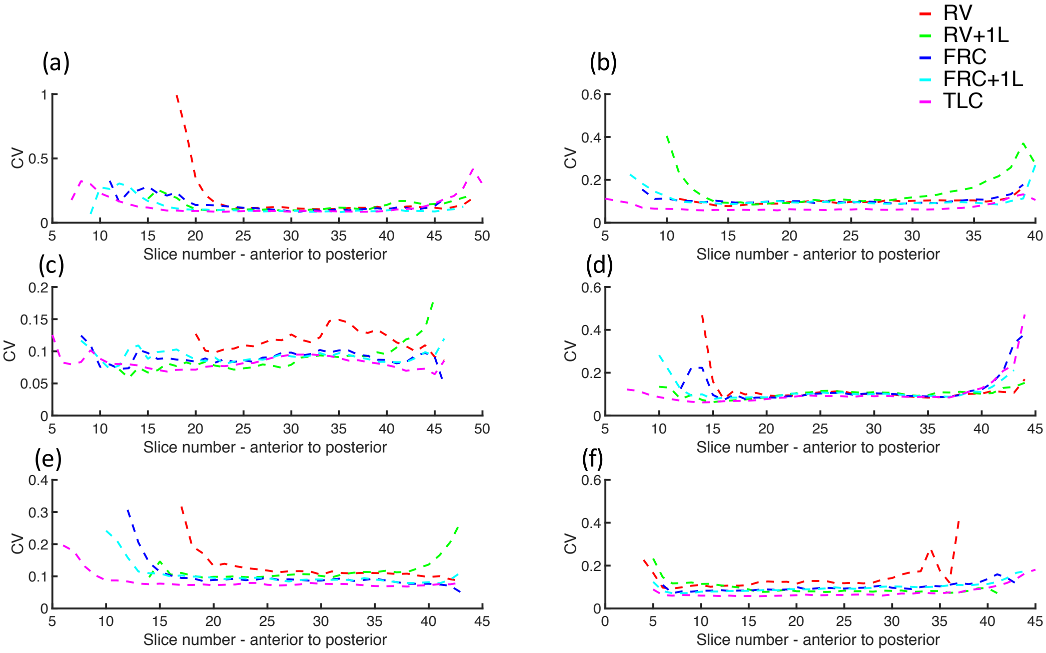

Figure 5.12 Plots of median CV per slice generated from the TLV mask for all 6 healthy volunteers' images obtained with HP ^{3}He during imaging session 1. (a) HV1, (b) HV2, (c) HV3, (d) HV4, (e) HV5 and (f) HV6. All inflation levels were acquired using the same imaging volume with the number of slices and field of view being kept consistent

Figure 5.13 shows a slice-by-slice plot of SNR from all 6 healthy volunteers.

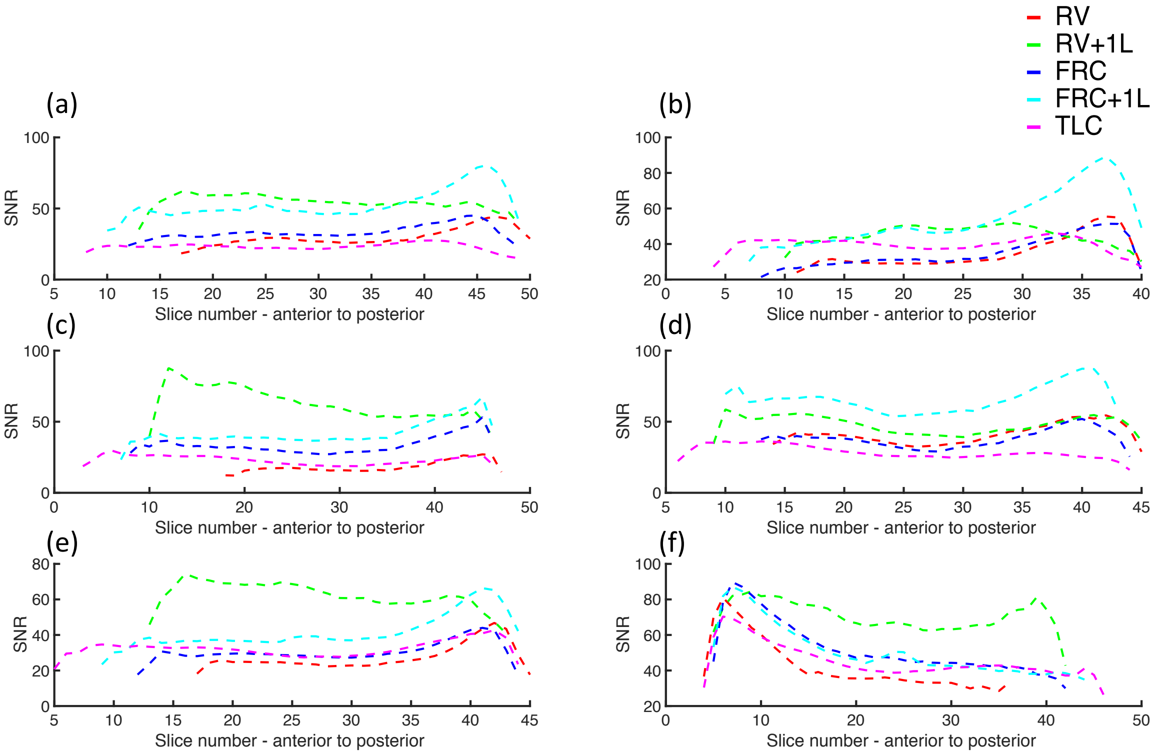

Figure 5.13 Plots of SNR per slice for all 6 healthy volunteers' images obtained with HP ^{3}He during imaging session 1. (a) HV1, (b) HV2, (c) HV3, (d) HV4, (e) HV5 and (f) HV6. All inflation levels were acquired using the same imaging volume with the number of slices and field of view being kept consistent

As the SNR drops sharply in the most posterior regions this coincides with the increased CV in all images. Additionally, the SNR of the anterior and posterior slices is similar in all scans, with a general trend of higher SNR in the posterior sections of the lung as one would expect due to the gravitational distribution of the gas when a volunteer is supine. Generally, CV increases before a noticeable decrease in SNR in the RV+1L images, suggesting this higher CV is due to airways not reopening upon inhalation of the 1L bag and not only the reduction in SNR.

5.3.2 Comparison with body plethysmography values

Figure 5.14 shows a plot of the values of RV, FRC and TLC values measured using MRI and body plethysmography (BPleth). To have an accurate comparison to BPleth, TLV masks including the major airways needed to be generated as BPleth measures the total compressible gas in the thorax. Therefore, following generation of the masks using the method described in chapter 3 only minor editing was carried out to ensure no leakage into non-lung areas, with the major airways remaining in the mask and contributing to the total lung volume reported in this section.

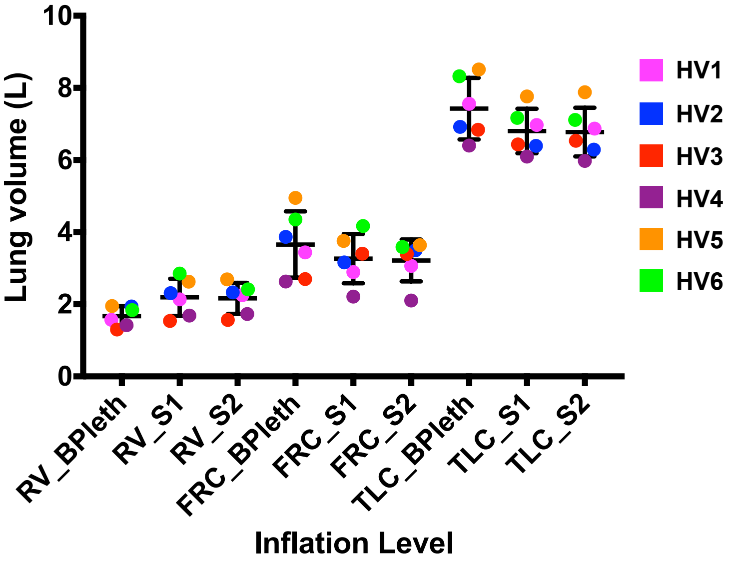

Figure 5.14 Plot of lung volumes measured using body plethysmography and MRI. Each point represents a measurement from a single subject, error bars represent group means and standard deviations

The values of FRC and TLC as measured using MRI are lower when compared to body plethysmography in this healthy cohort. This follows previously reported changes due to posture [368-370]. However, the residual volume as estimated by MRI is greater than that measured by BPleth, and MRI overestimates FRC compared to BPleth for HV3. Table 5.16

shows the difference in volume (L) between body plethysmography and MRI metrics, defined as MRI volume – body plethysmography volume.

Table 5.16 Volume difference between MRI derived measures and body plethysmography measures

	HV1					HV2				
Lung volume	**BP**	**S1**	**S2**	**S1-BP**	**S2-BP**	**BP**	**S1**	**S2**	**S1-BP**	**S2-BP**
RV	1.57	2.14	2.25	0.57	0.68	1.94	2.31	2.33	0.37	0.39
FRC	3.44	2.89	3.06	-0.55	-0.38	3.87	3.16	3.5	-0.71	-0.37
TLC	7.56	6.97	6.87	-0.59	-0.69	6.92	6.39	6.29	-0.53	-0.63
	HV3					**HV4**				
Lung volume	**BP**	**S1**	**S2**	**S1-BP**	**S2-BP**	**BP**	**S1**	**S2**	**S1-BP**	**S2-BP**
RV	1.30	1.54	1.56	0.24	0.26	1.42	1.69	1.73	0.27	0.31
FRC	2.70	3.40	3.39	0.70	0.69	2.63	2.21	2.11	-0.42	-0.52
TLC	6.84	6.43	6.53	-0.41	-0.31	6.40	6.09	5.97	-0.31	-0.43
	HV5					**HV6**				
Lung volume	**BP**	**S1**	**S2**	**S1-BP**	**S2-BP**	**BP**	**S1**	**S2**	**S1-BP**	**S2-BP**
RV	1.95	2.63	2.69	0.68	0.74	1.84	2.85	2.41	1.01	0.57
FRC	4.95	3.76	3.64	-1.19	-1.31	4.35	4.17	3.59	-0.18	-0.76
TLC	8.51	7.76	7.88	-0.75	-0.63	8.32	7.17	7.11	-1.15	-1.21

BP = body plethysmography, S1 = first imaging session, S2 = second imaging session

FRC and TLC from MRI are reduced when compared to body plethysmography with RV values being increased. Table 5.17 shows the summary of paired t-test/Wilcoxon matched-pairs signed rank tests comparing all 6 volunteers' body plethysmography values to the MRI derived metrics. RV and TLC volumes are significantly different from both MRI sessions compared to BPLETH whilst FRC values are not.

Table 5.17 P-values comparing Body plethysmography and sessions 1 and 2 (S1/S2) lung volumes

Volume/Ratio	BPleth v S1	BPleth v S2
RV	0.0074	0.0018
FRC	0.1910	0.2188
TLC	0.0039	0.0037

BPleth = body plethysmography, S1 = first imaging session lung volumes, S2 = second imaging session lung volumes

5.3.3 Results of multiple inflation analysis using hyperpolarised ^{129}Xe

Figure 5.15 shows example slices from ventilation images acquired with ^{3}He and ^{129}Xe from all volunteers.

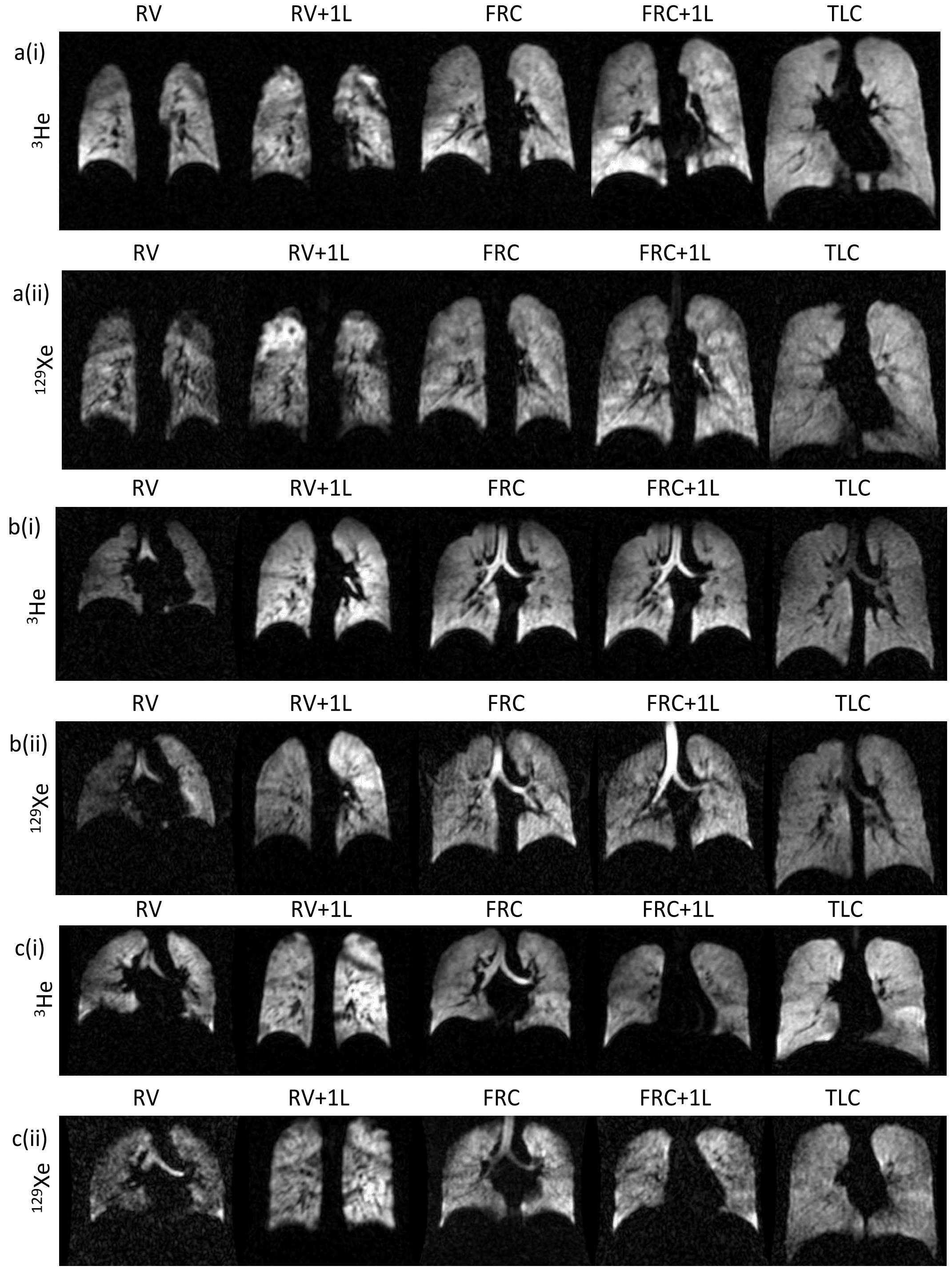

Figure 5.15 Example slices from all five inflation levels in all three healthy volunteers scanned with both HP ^{3}He and HP ^{129}Xe. a(i) HV2 ^{3}He, a(ii) HV2 ^{129}Xe, b(i) HV3 ^{3}He, b(ii) HV3 ^{129}Xe, c(i) HV6 ^{3}He and c(ii)HV6 ^{129}Xe

As can be seen the SNR of the ^{129}Xe images is generally slightly lower than that of the ^{3}He images particularly at the RV and RV+1L images, a pattern seen in all three volunteers. Additionally, there are more apparent defects appearing at RV+1L when using ^{129}Xe when compared to ^{3}He. Following analysis of the RV images acquired in HV3 it became apparent the coil was not receiving in the posterior right section due to almost complete disappearance of the right lung. Due to this the metrics acquired at RV using ^{129}Xe were considered unreliable and hence could not be compared to those values acquired with ^{3}He.

Figure 5.16 shows the (a) SNR change of all images acquired using ^{3}He and ^{129}Xe for the three volunteers analysed here and (b) the distribution of the SNR of images acquired using both gases. As can be seen ^{129}Xe SNR is generally lower for all acquisitions.

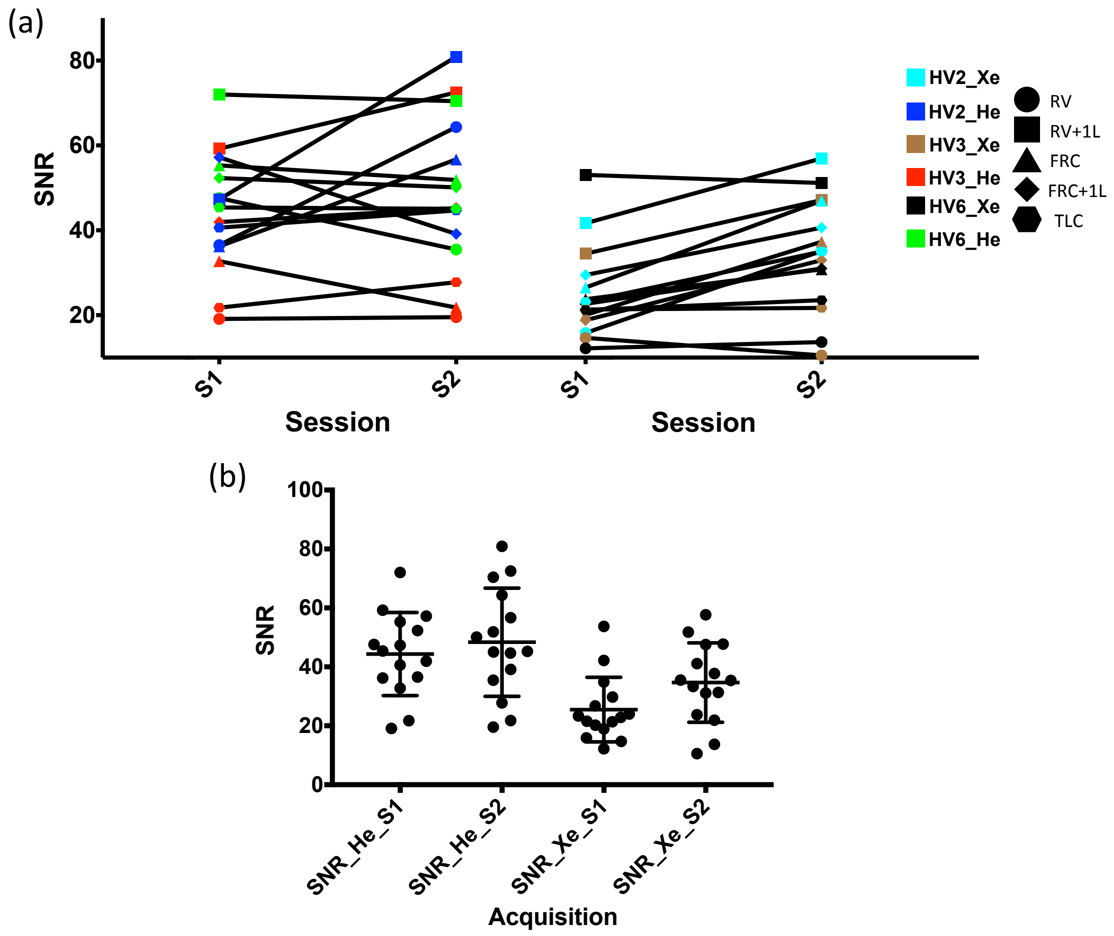

Figure 5.16 Plots comparing the SNR from each session using ^{129}Xe and ^{3}He for the three volunteers analysed using both gases. (a) the SNR change for ^{3}He and ^{129}Xe and (b) Plots comparing the SNR from each session. Each point represents a measurement from a single subject, error bars represent group means and standard deviations

Table 5.18 shows the coefficient of variation analysis results of TLV, VV and %VV. Note that HV3 data was excluded from CoV analysis at RV. %VV is highly reproducible at all inflation levels with TLC having the lowest CoV. TLC also has the best repeatability in terms of TLV and VV.

Table 5.18 Mean CoV over all volunteers between each session

Acquisition	TLV	VV	%VV
RV	3.33	1.34	3.98
RV+1L	2.19	2.26	1.16
FRC	5.88	4.80	1.49
FRC+1L	6.88	6.00	3.18
TLC	1.97	1.91	0.62

Table 5.19 CV metrics CoV over all volunteers between each session

Acquisition	Median CV	CVH skewness	CVH kurtosis	CVH IQR
RV	9.37	9.27	12.25	5.41
RV+1L	7.60	10.91	14.33	8.02
FRC	2.86	10.12	10.83	4.86
FRC+1L	3.74	7.75	10.10	4.02
TLC	4.62	9.51	10.30	3.21
TLV values				
RV	6.73	5.76	7.60	4.89
RV+1L	6.41	9.35	18.14	6.96
FRC	3.02	14.77	19.11	5.57
FRC+1L	3.88	34.39	41.91	4.28
TLC	4.48	12.84	38.73	2.94

Figure 5.17 shows Bland-Altman plots of TLV, VV and %VV. When compared to the Bland-Altman plots shown in Figure 5.8 it is clear that the intersession agreement of the metrics obtained using ^{129}Xe is poorer than the agreement of the metrics obtained when using ^{3}He.

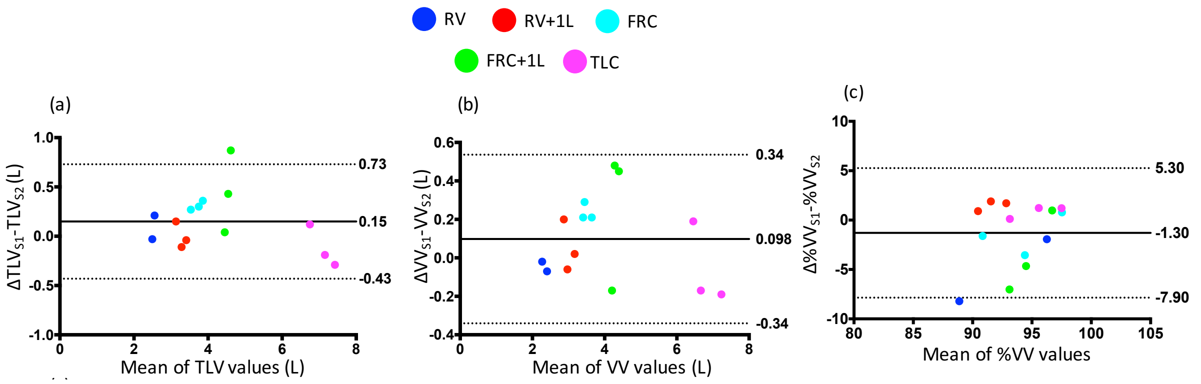

Figure 5.17 Bland-Altman plots of (a) TLV, (b) VV and (c) %VV for all 3 volunteers

Figure 5.18 shows the Bland-Altman plots of CVH metrics generated using the VV (a-d) and TLV mask (e-h). Generally, the agreement of these metrics is good with the IQR, as one would expect, being very reproducible across sessions. However, the TLV mask CVH skewness and kurtosis' reproducibility is substantially lower than that of the VV mask values.

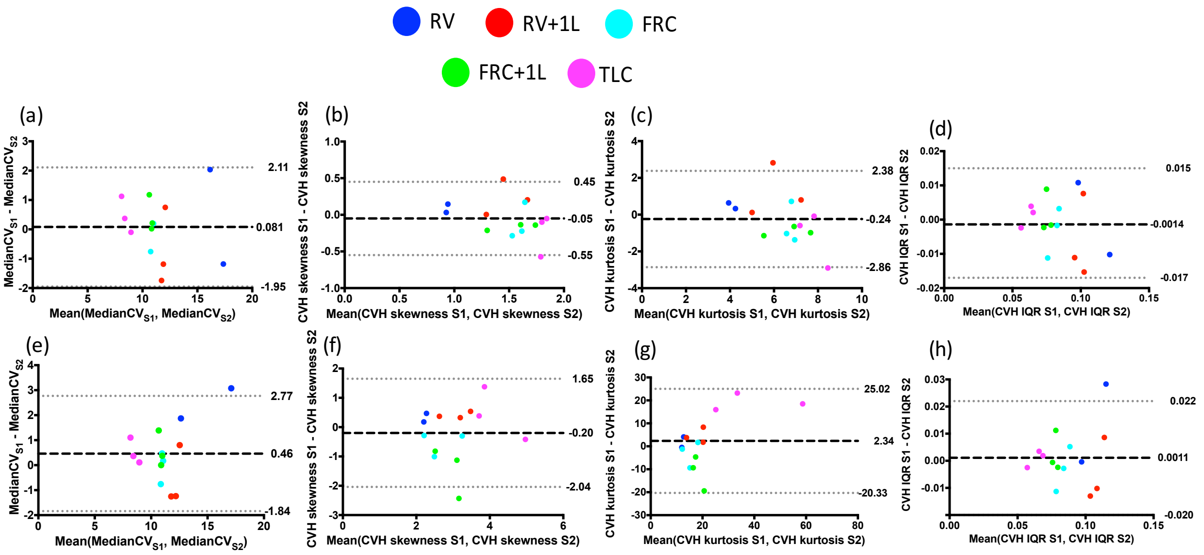

Figure 5.18 Bland-Altman plots of CVH metrics generated from the VV mask (a-d) and TLV mask (e-h). (a) Median CV, (b) CVH skewness, (c) CVH kurtosis, (d) CVH IQR, (e) Median CV, (f) CVH skewness, (g) CVH kurtosis, and (h) CVH IQR

Table 5.20 shows the %Δ over both sessions for TLV, VV and %VV derived from ^{129}Xe and ^{3}He ventilation-weighted and ^{1}H anatomical images in HV2, HV3 and HV6.

Table 5.20 Comparison of %Δ of TLV, VV and %VV calculated using ^{129}Xe and ^{3}He datasets

	HV2 ^{129}Xe			HV2 ^{3}He		
Acquisition	**TLV**	**VV**	**%VV**	**TLV**	**VV**	**%VV**
RV	-7.30	-8.04	-0.80	0.26	1.21	0.95
RV+1L	-8.95	-9.87	-1.01	15.79	18.38	2.24
FRC	1.16	3.23	2.04	-1.88	-1.82	0.05
FRC+1L	3.37	2.34	-1.00	10.99	11.45	0.41
TLC	-1.67	-2.92	-1.27	-4.06	-4.19	-0.13
	HV3 ^{129}Xe			**HV3 ^{3}He**		
Acquisition	**TLV**	**VV**	**%VV**	**TLV**	**VV**	**%VV**
RV	NA	NA	NA	1.63	1.16	-0.45
RV+1L	-0.84	4.15	5.04	-3.93	-4.17	-0.25
FRC	-7.10	-2.60	4.85	1.76	2.44	0.66
FRC+1L	-4.62	-6.57	-2.05	-0.07	-1.75	-1.68
TLC	2.63	2.50	-0.13	6.22	5.85	-0.35
	HV6 ^{129}Xe			**HV6 ^{3}He**		
Acquisition	**TLV**	**VV**	**%VV**	**TLV**	**VV**	**%VV**
RV	-8.03	0.89	9.69	-14.19	-13.40	0.92
RV+1L	1.19	-0.66	-1.83	-5.90	-5.22	0.73
FRC	-7.57	-5.92	1.79	-0.79	-1.05	-0.27
FRC+1L	-17.16	-10.66	7.84	-16.95	-11.65	6.27
TLC	3.98	2.70	-1.23	-5.95	-6.92	-1.03

Table 5.21 shows the %Δ of all CV metrics generated using both the VV and TLV masks.

Table 5.21 %Δ of CVH metrics generated from the VV and TLV masks

Acquisition	Median CV	CVH skewness	CVH kurtosis	CVH IQR	Median CV	CVH skewness	CVH kurtosis	CVH IQR
	HV2 VV metrics				HV2 TLV metrics			
RV	-11.84	-3.36	-7.45	-10.43	-13.77	-18.65	-27.77	0.41
RV+1L	10.48	-11.56	-10.48	12.33	-6.19	-13.15	-23.99	-7.28
FRC	7.31	20.66	16.98	15.95	-1.54	13.84	10.50	3.39
FRC+1L	-1.94	17.82	23.08	3.20	-0.02	38.99	79.54	3.06
TLC	-4.35	38.13	41.46	4.36	-12.63	-30.31	-51.47	-5.18
Acquisition	**Median CV**	**CVH skewness**	**CVH kurtosis**	**CVH IQR**	**Median CV**	**CVH skewness**	**CVH kurtosis**	**CVH IQR**
	HV3 VV metrics				HV3 TLV metrics			
RV	NA	NA	NA	NA	NA	NA	NA	NA
RV+1L	-6.02	-0.32	-2.36	-7.19	11.23	-14.38	-34.03	9.87
FRC	-1.77	14.79	21.87	2.08	-4.19	9.73	-8.85	-5.71
FRC+1L	-0.19	8.85	9.80	2.07	-12.21	44.37	31.02	-13.38
TLC	-13.00	2.82	1.11	-5.95	-1.22	-9.84	-48.21	-2.73
Acquisition	**Median CV**	**CVH skewness**	**CVH kurtosis**	**CVH IQR**	**Median CV**	**CVH skewness**	**CVH kurtosis**	**CVH IQR**
	HV6 VV metrics				HV6 TLV metrics			
RV	7.03	-14.38	-14.97	8.79	-16.5	-7.79	4.32	-21.9
RV+1L	16.04	-28.83	-38.29	16.14	10.71	-9.62	-8.32	13.40
FRC	-1.95	-9.94	-10.06	-3.73	7.23	50.68	89.51	15.54
FRC+1L	-10.50	8.39	13.69	-11.21	-3.37	125.05	177.49	0.80
TLC	1.11	5.68	8.63	-3.17	-4.22	8.76	-27.22	4.47

Figure 5.19 shows plots of TLV, VV and %VV calculated using ^{129}Xe and ^{3}He for HV2, HV3 and HV6 for sessions 1 and 2. %VV is generally lower when measured using ^{129}Xe compared to ^{3}He.

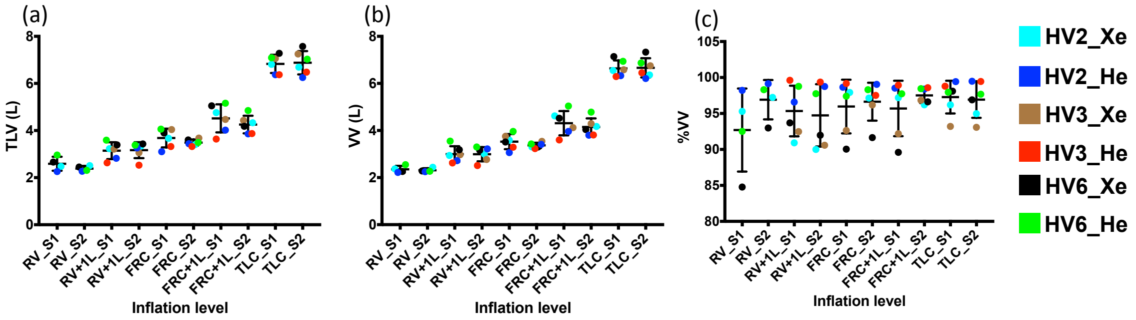

Figure 5.19 Plots of TLV, VV and %VV ^{129}Xe and ^{3}He datasets. (a) TLV, (b) VV and (c) %VV. Each point represents a measurement from a single subject, error bars represent group means and standard deviations

FG shows plots of median CV when generated from the VV mask (a) and the TLV mask (b) using both HP ^{129}Xe and ^{3}He. Median CV is generally increased in images acquired with HP ^{129}Xe when compared to HP ^{3}He.

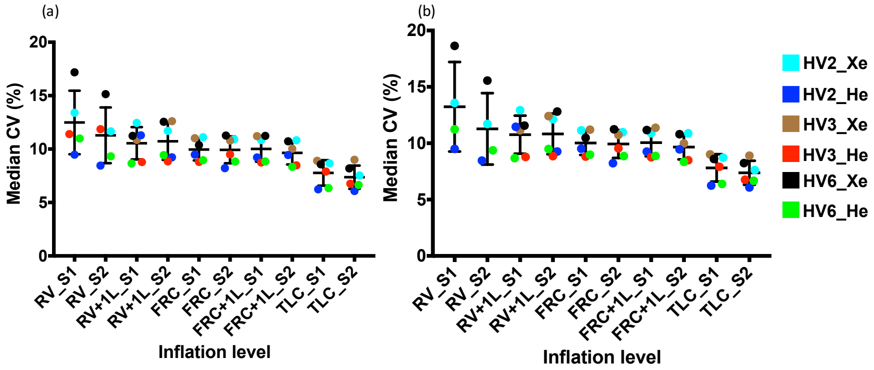

Figure 5.20 Plots of median CV generated from the (a) VV mask and (b) TLV mask. Each point represents a measurement from a single subject, error bars represent group means and standard deviations

Figure 5.21 shows scatter plots comparing TLV, VV and %VV acquired with ^{129}Xe and ^{3}He.

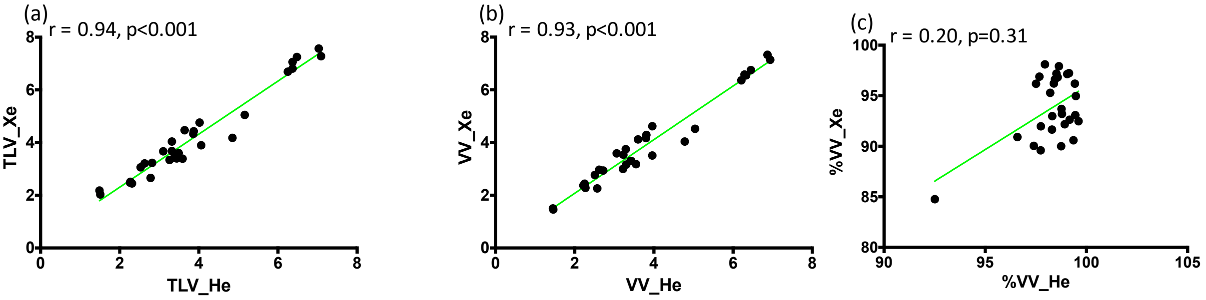

Figure 5.21 Scatter plots comparing (a) TLV, (b) VV and (c) %VV generated from images acquired with ^{129}Xe and ^{3}He

TLV and VV have strong correlations whilst %VV is poorly correlated. One possible cause for this was the requirement of registration to calculate %VV from the ^{129}Xe and ^{1}H anatomical images which may introduce error as discussed by Horn et al. in their paper discussing ventilation volume percentage calculation [66]. The poor correlation of %VV may be expected as it has previously been shown that any airway obstruction or even partial obstruction is present causing lower signal, and thus lower %VV, due to the poorer diffusivity of the xenon gas compared to helium [60].

Figure 5.22 shows scatter plots of median CV generated from both the VV and TLV masks. Median CV (%) will differ due to the generally lower SNR of the ^{129}Xe images compared to the ^{3}He images as was shown in chapter 4. What is interesting to note is that the correlation of median CV when generated from the TLV mask is slightly higher than the correlation of median CV generated from the VV mask in these healthy volunteers.

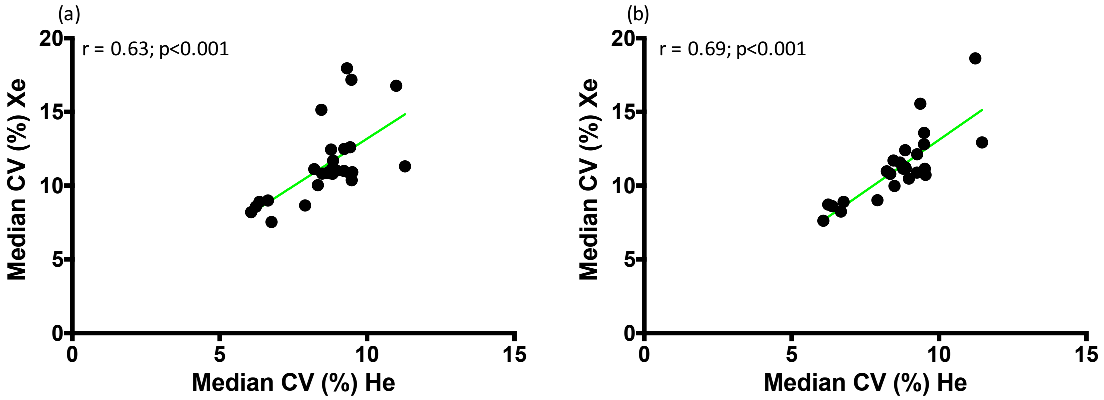

Figure 5.22 Scatter plots comparing (a) median CV generated from the VV mask and (b) median CV generated from the TLV mask from images acquired with ^{129}Xe and ^{3}He

5.3.4 The effect of inflation level on MRI-based measures of lung function demonstrated in patients with CF and asthma

Figure 5.23 shows plots of all metrics analysed in the cohorts presented at both FRC+1L and TLC generated from the VV mask. As can be seen VDP in both the patients with CF and asthma cohorts is higher than that seen in the HV cohort (Figure 5.23c). Additionally, CV metrics follow the same patterns as those discussed in Chapter 4.

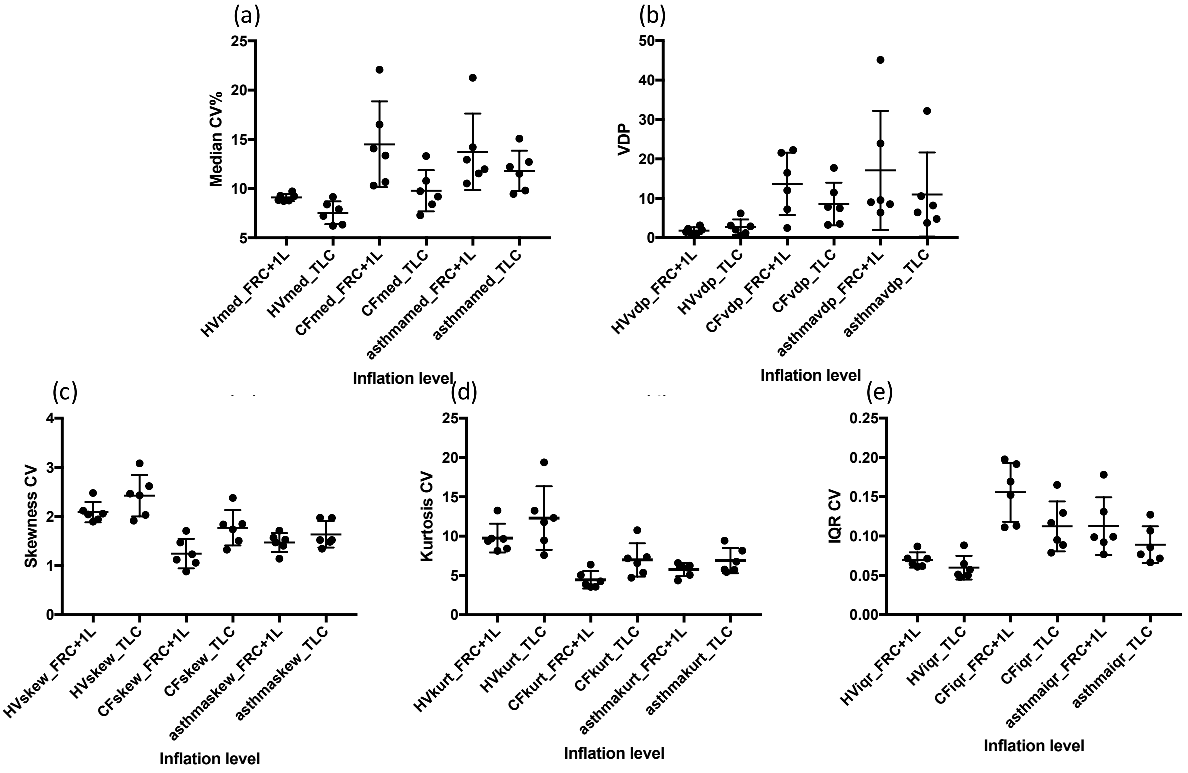

Figure 5.23 Plots of all metrics at both inflation levels analysed for all cohorts generated from the VV mask. (a) Median CV%, (b) VDP, (c) CVH skewness, (d) CVH kurtosis and (e) CVH IQR. Each point represents a measurement from a single subject, error bars represent group means and standard deviations.

Figure 5.24 shows the plots of all CV metrics generated using the TLV mask at FRC+1L and TLC. When considering the CVH kurtosis measured using the TLV mask the patients with asthma values become more widely spread when compared to the CVH kurtosis measured using the VV mask. It should be noted however that five of the six patients are very well grouped with only one patient having markedly different values at FRC+1L to the rest of the group and only two patients having different values at TLC to the rest of the group.

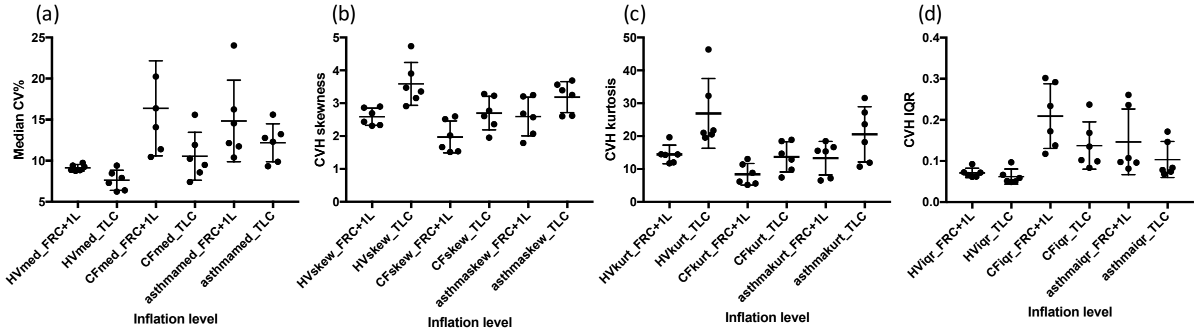

Figure 5.24 Plots of all CV metrics analysed at both inflation levels analysed for all cohorts generated from the TLV mask. (a) Median CV%, (b) VDP, (c) CVH skewness, (d) CVH kurtosis and (e) CVH IQR. Each point represents a measurement from a single subject, error bars represent group means and standard deviations.

Figure 5.25 shows example images at FRC+1L and TLC from the HV, patients with CF and asthma groups. As can be seen there is a decrease of ventilation heterogeneity as assessed visually with some defects resolving at TLC in the patients' images.

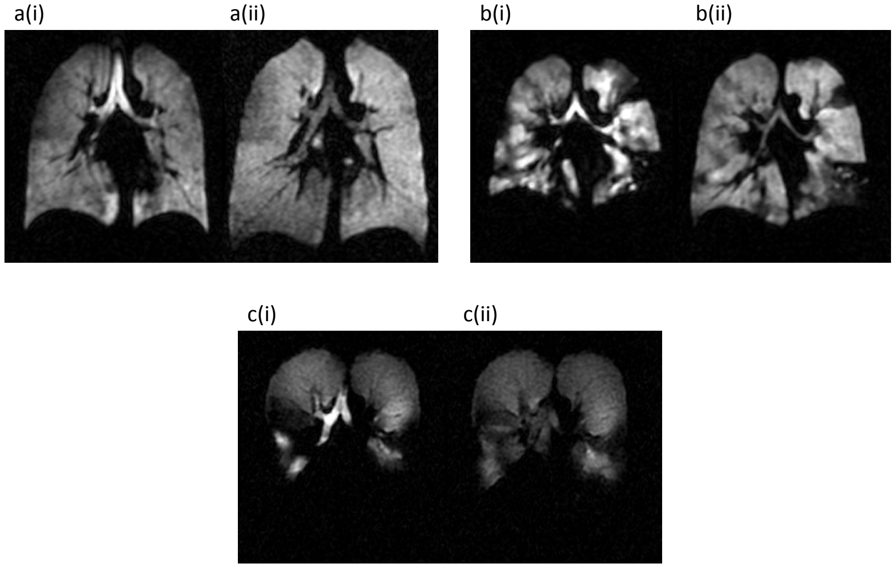

Figure 5.25 Example slices from datasets acquired at FRC+1L and TLC. a(i) healthy volunteer FRC+1L, a(ii) healthy volunteer TLC, b(i) CF FRC+1L, b(ii) CF TLC, c(i) asthma FRC+1L and c(ii) asthma TLC

This is further evidenced by the reduction in VDP at TLC in four out of six of the patients with CF and all six of the patients with asthma (Figure 5.26), however even with this reduction at TLC the VDP seen in both CF and patients with asthma is higher than that seen in the HVs at TLC. Increased VDP at TLC in some healthy volunteers is due to coil sensitivity effects at the diaphragm (e.g. see TLC images of HV1 and HV6, Figure 5.3).

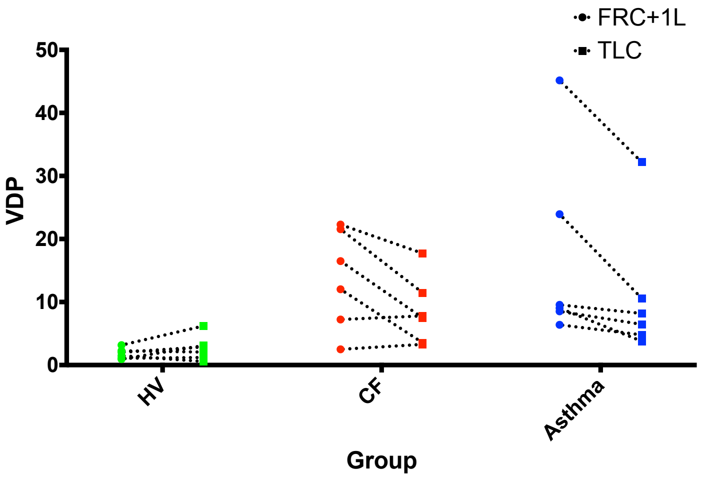

Figure 5.26 Change in VDP for all cohorts analysed

When considering CV metrics generated from the VV mask, CVH skewness increased in five out of the six healthy volunteers from FRC+1L to TLC, whilst it increased in all CF patients and five of the six patients with asthma (Figure 5.27) suggesting a shift of the peak location of the histogram towards 0 at TLC as confirmed by comparing histograms (Figure 5.28) from the datasets shown in Figure 5.25. When considering CVH skewness generated using the TLV mask all subjects demonstrated increased skewness at TLC when compared to FRC+1L.

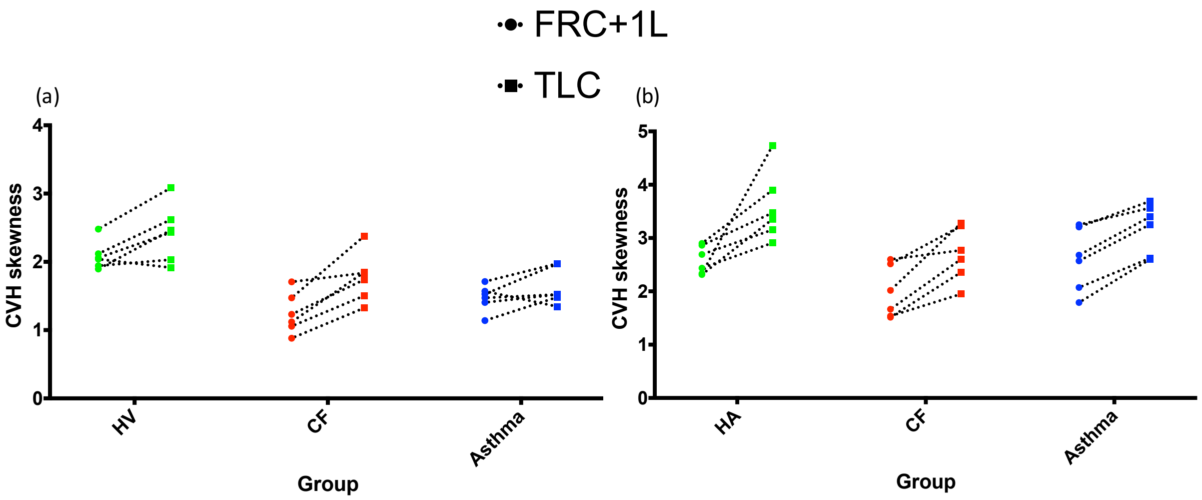

Figure 5.27 CVH Skewness change from FRC+1L to TLC for all cohorts generated from the (a) VV mask and (b) TLV mask

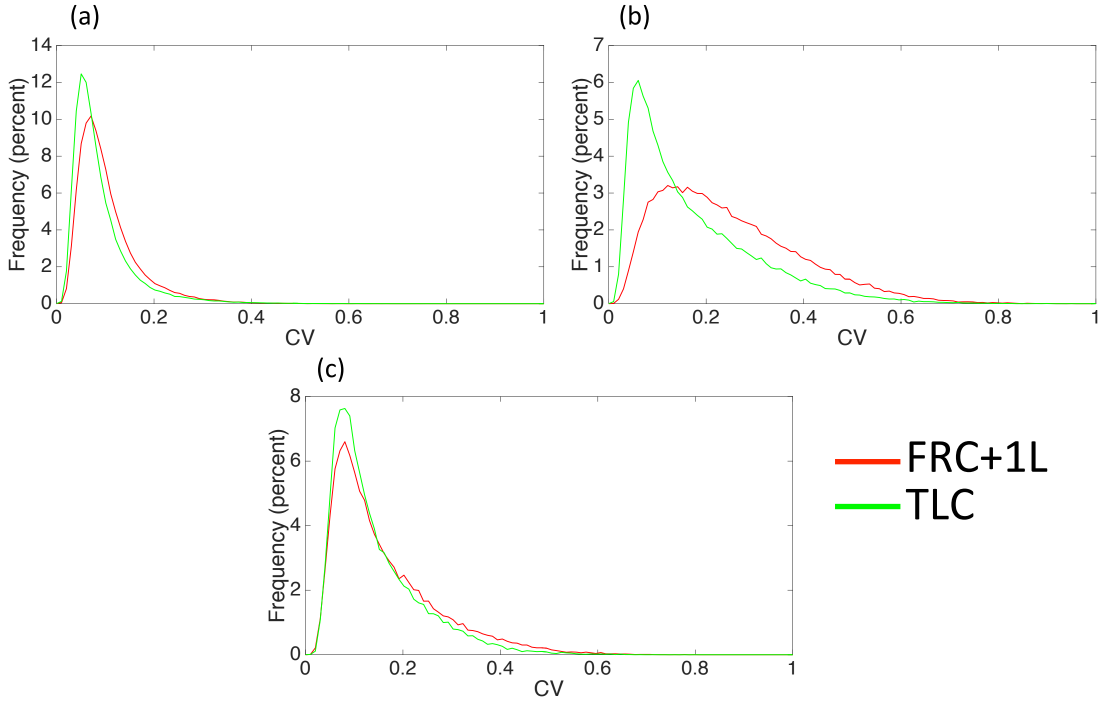

Figure 5.28 Example histograms for the datasets shown in Figure 5.25. (a) healthy volunteer, (b) patient with CF and (c) patient with asthma histograms generated from the VV mask. As shown in Figure 5.27 the pattern is the same for metrics generated using the TLV mask

CVH kurtosis followed the same pattern as skewness, increasing at TLC when compared to FRC+1L, in four out of the six healthy volunteers, all six CF patients and five of the six patients with asthma (Figure 5.29) when generated from the VV mask. When considering the metrics generated from the TLV mask one healthy volunteer has a marked increase of kurtosis at TLC compared to FRC+1L, whilst all other subjects have moderate increases as seen in the metrics generated from the VV mask.

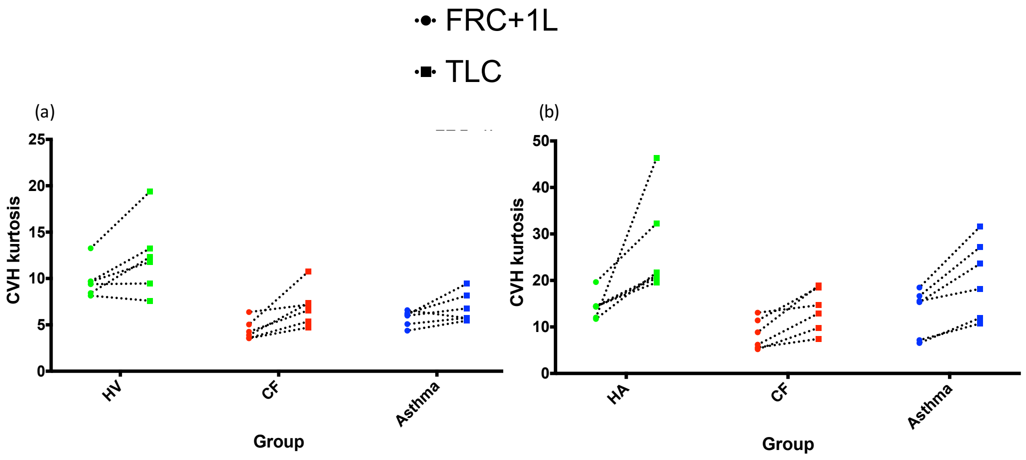

Figure 5.29 CV Kurtosis change from FRC+1L to TLC for all cohorts from the (a) VV mask and (b) TLV mask

CVH IQR (Figure 5.30) decreased in five of the six healthy volunteers and decreased in all 6 of the patients with CF and all 6 of the patients with asthma, this suggests a tighter grouping of values of CV at the higher inflation level when generated from the VV mask. When considering the metrics generated from the TLV mask the patterns were the same.

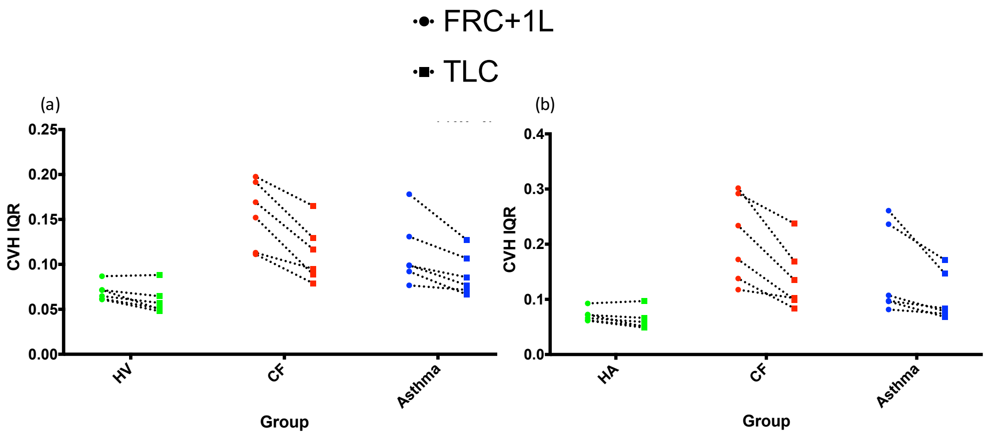

Figure 5.30 CV IQR change from FRC+1L to TLC for all cohorts from the (a) VV mask and (b) TLV mask

Marked decreases in four of the six CF patients and two of the six patients with asthma CVH IQR values suggest a drastic alteration in the distribution of the gas within the lung possibly due to improved ventilation in areas affected by mucus plugging in the patients with CF and possible airway opening due to increased pressure in the patients with asthma. Table 5.22 shows the results of comparing the metrics obtained at FRC+1L to TLC in all cohorts analysed. As can be seen there is a significant difference in all CV metrics in patients with CF, whilst for patients with asthma only CVH IQR is significantly different. Patients with asthma are the only group to display a significant difference in VDP. Median CV is the only metric to significantly change from FRC+1L to TLC for the HA group.

Table 5.22 Wilcoxon matched-pairs results of comparing metrics at FRC+1L and TLC in all cohorts analysed using CV metrics generated from both the VV and TLV masks

Metric	HA	CF	Asthma
VDP	0.4375	0.1562	0.0312
Median CV	0.0312	0.0312	0.0625
CVH skewness	0.0938	0.0312	0.1562
CVH kurtosis	0.0938	0.0312	0.1562
CVH IQR	0.0625	0.0312	0.0312
TLV values			
Median CV	0.0312	0.0312	0.0625
CVH skewness	0.0312	0.0312	0.0312
CVH kurtosis	0.0312	0.0312	0.0312
CVH IQR	0.0625	0.0312	0.0312

Table 5.23 shows the results of the Kruskal-Wallis test comparing healthy volunteers to the patient cohorts. When considering the metrics generated from the VV mask the difference in metrics at TLC between the healthy volunteers and patients with asthma became more significant in four of the six metrics, with a decreased significance in VDP when compared to those results obtained at FRC+1L. All metrics were more significantly different between healthy volunteers and patients with CF at FRC+1L when compared to those at TLC. When considering the metrics generated from the TLV mask the difference between median CV at TLC between the healthy volunteers and patients with asthma became more significant when compared to FRC+1L, as did CVH skewness and kurtosis although these metrics could not distinguish the groups. CVH IQR became less significantly different. Median CV and CVH IQR were more significantly different between healthy volunteers and patients with CF at FRC+1L when compared to those at TLC whilst CVH skewness and kurtosis became more significantly different at TLC when compared to FRC+1L.

Table 5.23 Results of the Kruskal-Wallis test comparing healthy volunteers to the patient cohorts

Metric	FRC+1L asthma	TLC asthma	FRC+1L CF	TLC CF
VDP	0.0070	0.0137	0.0116	0.0257
Median CV	0.0099	0.0024	0.0049	0.1032
CVH skewness	0.0299	0.0137	0.0013	0.0257
CVH kurtosis	0.0463	0.0221	0.0007	0.0161
CVH IQR	0.0611	0.1168	0.0009	0.0034
		TLV metrics		
Median CV	0.0116	0.0049	0.0041	0.0908
CVH skewness	>0.9999	0.8981	0.1032	0.0401
CVH kurtosis	>0.9999	0.4684	0.0463	0.0132
CVH IQR	0.0463	0.0908	0.0013	0.0049

When comparing the VV and TLV mask generated CV metrics ability to differentiate the patients with asthma and healthy adult groups at FRC+1L median CV was less significantly different using the TLV mask when compared to the VV mask metrics, whereas CVH skewness and kurtosis are unable to differentiate the groups using the TLV mask, although CVH IQR is significantly different where it is not using the VV mask. At TLC, median CV is more significantly different as is CVH IQR, although neither the VV mask or TLV mask generated IQR can differentiate the groups at TLC. When considering the healthy adults and CF group median CV is slightly more significantly different at FRC+1L using the TLV mask when compared to the VV mask, however CVH skewness, kurtosis and IQR are less significantly different, with the same pattern persisting at TLC.

5.4 Discussion

The finding of increased ventilation heterogeneity at lower lung volumes, specifically RV+1L, in healthy volunteers is interesting indicating partial airway closure in certain lung fields. This was mostly seen in the posterior section of the lung, consistent with the gravitational dependence of the lung in the supine position [371, 52]. The volume inhaled was 1L, which is similar to the volumes used by Muradyan et al. [363] in their experimentation, and the results seen here are very similar to those seen in this paper, with a patchier distribution of ventilation quantified by the increased CV at RV+1L when compared to FRC+1L.

Notice that at all inflation levels the lung has high CV towards the anterior portion, however in four out of six of the volunteers the posterior portion of the lung shows the highest CV. However, it should be noted that the higher CV seen at RV+1L is caused by the fact that this is the only image acquired from RV. This was done as the dependence of the metrics on inflation level was a secondary objective of the study with the prime objective being repeatability of metrics at different inflation levels. Were this experiment to be redesigned all images would be acquired from RV with the aid of spirometric gating. An additional limitation is the separate-breath acquisition of the anatomical and ^{129}Xe scans requiring registration between them to calculate %VV. As noted by Horn et al. [66] registration will introduce some error into the calculation of %VV and this may be particularly problematic in this study due to the participants being asked to inhale to the highest and exhale to the lowest volumes possible. Additionally, the lower diffusivity of xenon compared to helium may cause lower %VV values and in combination with lower SNR this may lead to the poorer repeatability of the %VV derived from xenon when compared to helium [60]. The increased median CV at all lung volumes is most likely due to the decreased SNR of the ^{129}Xe images.

The closing volume of healthy lungs is also a key point to consider when reviewing the results of this study, as it is known that with aging the lung becomes less elastic and hence the volume at which airway closure begins will increase, with airway closure occurring at FRC around 45 years of age [372]. Additionally, with some of the volunteers here being occasional or former smokers there may be some detrimental effect on the airways from this past activity, although there was still a change in ventilation heterogeneity at different lung inflation levels seen in the never smokers (HV5 and HV6).

By carrying out imaging acquisitions in patients at different inflation levels the fixed or temporally reversible nature of focal ventilation defects may be understood more clearly. Indeed, as seen in the patients with CF and patients with asthma at TLC there was decreased VDP in some patients suggesting resolution of defects by increasing the pressure in the airways with the deep inspiration. However, it is noted that not all defects resolved and there was a clearer improvement in ventilation homogeneity at TLC in the severe CF patients compared to the milder patients. Additional work to co-register high-resolution CT images of the airways and identify the cause of defects is needed in order to draw concrete conclusions on the cause of some defects resolving and others not in this cohort of patients.

The comparatively large between session CoV in TLV and VV derived from MR images and smaller between session CoV seen in measures of %VV further confirm the body of evidence [58, 60, 63, 66] that this measure is a robust global metric of lung ventilation. The good inter scan repeatability of %VV also suggests that it is a good candidate marker of lung ventilation change in response to treatment. However, the relatively large between session CoV seen in the median coefficient of variation of signal intensity suggests this measure of image texture may be less reliable as a global index of ventilation heterogeneity. It is possible that normalisation of the image, such as conversion to fractional ventilation values [326], may improve the repeatability of a normalised CV metric.

The differences between body plethysmography and MRI derived FRC and TLC are as one would expect to see from the literature due to the different postures adopted for each test [368-370]. However increased measures of RV when using MRI when compared to BPLETH (measured using BPLETH, supine RV is lower than sitting RV [373]) may be caused by the confounding factors of MRI segmentation e.g. inclusion of small vessels which will take up a higher proportion of the total lung volume at RV, discussed in more detail in the discussion section of chapter 3.

Generating CV metrics over the total lung volume mask following the method of Tzeng et al. [326] rather than over the ventilated volume mask yielded similar CVH metrics in most of the healthy volunteers and generally less reproducible metrics over two sessions. In addition, these metrics generally became less significantly different when comparing healthy adults to patients at FRC+1L and TLC, suggesting that from this specific group of data generating metrics over the ventilated volume mask is optimal for separation of health from disease.

5.5 Conclusion

This work has shown that although TLV and VV may vary relatively largely between imaging acquisitions there is little effect on the quantitative ratio of lung function (%VV) often used in the pulmonary MRI community in these healthy volunteers. Additionally, this work has shown that even in healthy volunteers, increased ventilation heterogeneity is seen at lower lung volumes, using both ^{3}He and ^{129}Xe. Patients with CF and asthma imaged at FRC+1L and TLC showed some resolution of ventilation defects at TLC with decreased ventilation heterogeneity also clearly seen and quantified using CV. This indicates that imaging patients over a range of inflation levels and with different gas inhalation/exhalation manoeuvres may allow for better understanding of ventilation defects and pulmonary mechanics.

CHAPTER 6. QUANTITATIVE MEASUREMENT OF THE VENTILATION-PERFUSION RATIO USING HP GAS AND DCE-^{1}H LUNG MRI

6.1 Introduction

The primary function of the lung is to facilitate gas exchange. Gas exchange is affected by changes in ventilation (V) and perfusion (Q) and pulmonary diseases may directly or indirectly affect the V/Q ratio due to issues such as thickening of the alveolar-capillary walls and reduced blood flow [374, 81, 64, 375] resulting in areas of shunt and wasted ventilation as shown in Figure 2.2. V/Q matching allows oxygen uptake and carbon dioxide excretion to occur most efficiently, as these are both passive mechanisms that depend on the concentration gradients over the alveolar-capillary barrier [376]. Therefore, if a detrimental change in ventilation occurs, a decrease in V/Q, poor alveolar ventilation and also removal of oxygen from the alveolus outweighing the delivery to it occurs. These changes cause a reduction in the partial pressure of oxygen whilst the partial pressure of carbon dioxide is increased. Additionally, if areas of the lung are poorly perfused, an increase in V/Q, the delivery of oxygen will increase relative to its removal, and the amount of carbon dioxide delivered back to the alveolus from the blood will decrease, with alveolar partial pressure of oxygen increasing and the partial pressure of carbon dioxide reducing.

Measurement of the V/Q ratio and quantification of gas exchange is a key area of research within the MR community as many diseases may affect both V and Q, for example recent work has shown that there is a vascular component (Q) involved in airway remodelling in asthma [361, 377, 378] as well as the well-known airways obstruction (V). Kelly et al. [379] have recently demonstrated that in asthma hypoxic pulmonary vasoconstriction (HPV) is not the only mechanism behind perfusion redistribution in asthma suggesting that multimodal imaging is necessary to truly understand this complex disease. There has also been evidence of perfusion defects present in patients with CF [380, 381]. Identification of perfusion defects in patients with COPD and emphysema is important, particularly if they are being considered for procedures such as lung volume reduction surgery. It is therefore important for the development of image processing workflows allowing the combination of multimodal imaging techniques including HP gas MRI, DCE-^{1}H MRI and possibly CT [256] to improve the current understanding of ventilation and perfusion in respiratory diseases. The next section of this chapter discusses previous methods for analysing V/Q relationships in the lung.

6.1.1 Review of PFT and imaging methods to analyse V/Q in the lung

To date only small patient numbers have been used in the attempt to quantify V/Q with HP gas and DCE-^{1}H MRI [95]. However quantification of regional V/Q with Positron Emission Tomography (PET) has been explored [97, 382-384], and the MIGET pulmonary function test has been demonstrated to provide highly valuable information on the V/Q ratio within the lung [385, 8]; albeit without regional information. The most commonly employed method for imaging V/Q in the clinic is V/Q scintigraphy [9, 12], followed by V/Q SPECT [27, 28, 162, 204, 386], whilst it is also possible to measure V/Q with dual-energy CT [163, 387, 164, 25]. There have been other methods to measure V/Q using MR imaging including the work of Henderson et al. [52] which combined specific ventilation (SV) imaging using oxygen enhanced ^{1}H MRI and ASL imaging simultaneously to calculate the V/Q ratio whilst HP gas MRI has also been combined with ASL to calculate V/Q [388, 56, 389].

6.1.1.1 Multiple Inert Gas Elimination Technique

Wagner developed the MIGET technique [385, 390] and analysis method in the mid 1970s. The MIGET technique [385] is based on the work of three different groups from which the V/Q equations approximated for oxygen and carbon dioxide were derived [8], which led to the realisation that the partial pressures of oxygen and carbon dioxide (PO_2 and PCO_2 respectively) are set by the local V/Q ratio for given boundary conditions, with the effects of V/Q matching on these quantities being discussed in the introduction to this chapter. The MIGET technique is based on applying these equations to inert gases. Due to the nature of these inert gases it is known that the fraction of the gas retained is a function of the blood-gas partition coefficient and the V/Q ratio. This has been researched extensively [8], with the most well-known work coming from Kety [391] and Farhi [392, 393]. The MIGET technique is invasive, as it requires venous injection of a mix of six inert gases, of variable solubility, and saline. The method also requires extraction of systemic and pulmonary blood to monitor gas retention and excretion. In addition, the levels of expired gas are analysed. Following the collection of these samples gas chromatography is used to analyse the levels of gas present and the data are analysed using the MIGET algorithms, which use a least squares fitting algorithm to find the best fit to the theoretical excretion and retention (from the equations) and the actual data (from the samples). The limitations of this technique are mainly theoretical as stated by Wagner [8]. However, the major practical limitations are the inherent invasiveness of drawing blood and the technique's ability to only provide whole lung measurements of V/Q.

With the desire for regional information and reduced invasiveness, V/Q analysis using imaging methods is particularly attractive. With established clinical perfusion imaging methods based on scintigraphy it is necessary for the injection of an ionizing contrast agent. The improved spatial resolution of MRI over nuclear scintigraphy and SPECT for assessment of vasculopathy [386] makes MR perfusion imaging combined with HP gas ventilation even more attractive in comparison to these techniques.

6.1.1.2 Nuclear scintigraphy

VQ scintigraphy is a well-established method and is still used widely in clinical practice since its introduction some 40 years ago. The inhalation of a gas contrast agent is used for ventilation imaging and intravenous administration of a ^{99}T labelled contrast agent is required for perfusion imaging [9, 12] with the radiation captured by a gamma camera.

During a SPECT V/Q scan the patient will inhale a radioactive inert gas or a labelled aerosol such as ^{99m}Tc-diethylenetriaminepentaacetic acid [27, 29] whilst the perfusion scan is usually carried out following the ventilation scan using ^{99m}Tc-macroaggregated albumin [29, 386]. V/Q SPECT is currently the preferred clinical screening test for chronic thromboembolic pulmonary hypertension [386] and has also been used in the analysis of patients with COPD [394]. SPECT provides improved visualisation of V/Q over scintigraphy as it allows for 3D imaging. Although both of these methods are well known in the clinic the radiation dose is an issue, particularly for longitudinal studies, as is the poor spatial resolution and lack of structural information.

6.1.1.3 Position emission tomography

PET has proven potential for measuring regional V/Q [395, 97, 396]. The method described in [97] is based on the kinetics of the tracer used (^{13}NN), which has advantages over MRI since both V and Q are measured with the same tracer. For this work Melo et al. began imaging sheep at apnoea following the injection of a bolus of the tracer for sixty seconds. They then resumed ventilation of the animal and analysed the washout of the tracer and based on the low solubility of their tracer in blood and tissues could estimate regional perfusion based on the radioactivity measured during apnoea. Ventilation was then estimated by taking the inverse of the time constant of their model. A limitation of PET is the spatial resolution but the temporal resolution of the tracer kinetics is high. The ionising nature of PET does not allow for longitudinal studies and although it provides functional information it is limited in its ability to deliver structural information, an area where MRI has been proven to be sensitive and capable [38, 176, 34, 208, 397].

6.1.1.4 CT

Dual energy CT is an emerging field and a recent publication demonstrated the feasibility of combined V/Q imaging [160] in patients with suspected pulmonary embolism (PE). To acquire the V scan an inhalation of radio-dense xenon is used to differentiate from tissue and for the Q scan an injection of iodinated contrast is used and the images are acquired in a single breath hold. The clear advantage of dual energy CT over MR is the increased image resolution, however again this is an ionising imaging modality, exposing patients to a significant amount of radiation when compared to SPECT or nuclear scintigraphy [398, 399].

6.1.1.5 Oxygen enhanced ^{1}H MRI

The method proposed by Henderson et al. [52] builds on some of their previous work [400, 371, 44] by incorporating quantifiable ASL imaging with specific ventilation (SV) imaging. The SV image is acquired in cycles of breathing room air and 100% oxygen with a single slice ^{1}H MRI acquisition. The volume of fresh gas in the voxels is then estimated, since oxygen changes the T_1 within the lung appreciably. This method builds upon previous studies [401-405, 44, 406], however with this method there are disadvantages. One key disadvantage is the basic registration method employed, where data is discarded if the movement in the lung is too large, which could lead to erroneous values in the final analysis. Furthermore, the SNR of the resulting images is low, although it does employ ^{1}H MRI, which is readily available for use in many medical institutions. An additional assumption is that the changes seen assume a constant perfusion input with all signal change being the result of changes in O_2 and ventilation, though this may not be the case in reality. Results with SV are promising, but clear and convincing comparisons to HP gas MRI have not yet been presented. Recent work by Sa et al. [407] compared the results from this methodology to the MIGET technique.

Close correlation of measures of the V/Q ratio were observed between the MRI and MIGET methods, and it was suggested that this non-contrast methodology is suitable for use in clinic [407]. However, the fact that only one slice of the lung is analysed and the lengthy acquisition time are clear disadvantages of this method.

6.1.1.6 Free-breathing ^{1}H MRI

Recent work has focused on non-contrast enhanced methods to measure V and Q with ^{1}H MRI using a methodology termed Fourier decomposition (FD) MRI [179-182, 184, 185]. To derive parametric maps from these images requires analysis of the signal change observed during inspiration and expiration, this can be separated from changes in signal intensity based on the cardiac pulsatility. These physiological processes can then be spectrally retrieved from the timeseries data and used to generate ventilation and perfusion weighted images [180]. Bauman et al. [180] compared FD MRI to nuclear medicine methods of SPECT and CT in porcine lung and found qualitative agreement between the techniques. A study comparing DCE-^{1}H MRI and perfusion-weighted FD MRI [181] in patients with CF determined that perfusion-weighted FD MRI provides equivalent diagnostic information to DCE-^{1}H MRI. Lederlin et al. [182] displayed good reproducibility of V and Q images derived from FD MRI in healthy volunteers suggesting that this may be a useful technique in future, particularly in patients with renal failure or small children. Kjorstad et al. [183] also developed a method to quantify perfusion using FD MRI which produced results comparable to other published methods, whilst Capaldi et al. compared ventilation images acquired using FD MRI to ^{3}He ventilation images [408] where they found a strong relation between FD MRI and ^{3}He ventilation images for COPD but not in bronchiectasis. Voskrebenzev et al. acquired images in two healthy volunteers and patients with CTEPH, COPD and CF [187]. This study did not compare the ventilation and perfusion weighted images acquired using the FD MRI technique to any other imaging technique.

6.1.1.7 Hyperpolarised gas PO_2 mapping

The method described by Rizi et al. [57] and Wild et al. [409] measures the regional alveolar partial pressure of oxygen within the lung (P_AO_2) by building on previous methods in which the oxygen-dependent decay of HP ^{3}He signal is described [410], and essentially the method developed allowed the conversion of regional P_AO_2 to regional V/Q measurements. To measure this HP ^{3}He was mixed with N_2 and pure O_2 gas and this mixture was injected into pig lungs and imaged at breath hold. One drawback to be seen from this method is that it requires two scans to be carried out to differentiate between RF induced depolarisation and O_2 induced T_1 decay, this is done by comparison of the two scans. Due to the model used to calculate this regional V/Q numerous sources of error can be introduced although from the results obtained it seems to match well with the literature [411, 412]. Although this study provided promising results the necessity of two HP gas scans and the complex model and analysis mean that it is not particularly feasible to include in everyday clinical use. However recent studies have acquired these images in the same breath-hold in human subjects [413, 64] meaning that this method could be adapted and used more frequently in the clinical research setting.

6.1.1.8 Dissolved phase ^{129}Xe MRI

Recent work with gaseous and dissolved phase ^{129}Xe MR imaging may be used to measure the regional gas exchange within the lung [80]. The results obtained in reference [97] show that prior to any embolism or bronchoconstriction that V/Q ratios are narrow and unimodal and these distributions become wider and bimodal after bronchoconstriction. The use of dissolved phase xenon for assessment of perfusion however relies on the fact that the lungs need to be ventilated in order to deliver xenon to the capillaries via alveolar gas exchange, the technique therefore shows perfusion where there is VQ matching but will be less effective at demonstrating a true picture of absolute perfusion.

6.1.1.9 Combined HP gas and DCE-^{1}H MRI

Crémillieux et al. [388] were among the first to display the possibility of combining DCE-^{1}H MRI and ^{3}He MRI and demonstrate the possibility of acquiring these types of images in rats. Lipson et al. [56] demonstrated the usefulness of acquiring V and Q images in humans in a small study using ASL and ^{3}He V images whilst Rizi et al. also acquired images in healthy volunteers [414]. Their qualitative analysis of the images again showed that these imaging modalities are sensitive to pulmonary disease and have improved resolution over the current gold standards in the clinic. However, the clear drawback here is the lack of quantitative analysis in comparison with the nuclear medicine methods, this is one of the key challenges in calculating V/Q with MRI. Marshall et al. [68, 415] developed a method to combine the information from ^{3}He MRI and DCE-^{1}H MRI to analyse the V/Q ratio in asthmatic patients in response to bronchodilator (BD) and also in patients with CTEPH before and after pulmonary endartorectomy [68].

In the work presented here quantitative ventilation [326] and perfusion metrics [83, 205] were generated from HP ^{3}He ventilation-weighted and DCE-^{1}H images which have been co-registered. The aim of this work was to compare metrics developed using these co-registered images from patients with asthma and COPD to healthy volunteers.

6.2 Quantitative perfusion analysis theory

As stated in chapter 2, section 2.4.2 tracer kinetic theory is often used to quantify pulmonary perfusion in terms of the primary hemodynamic parameters of pulmonary blood flow (PBF), pulmonary blood volume (PBV) and mean transit time (MTT). PBF, PBV and MTT are derived based on the kinetic theory of tracers in stationary or linear systems [416, 47, 144, 417, 202, 418]. By assuming a closed one-compartment model there is an assumption that the tracer will have negligible leakage into the extracellular space during the first pass [144]. Additionally, this model assumes conservation of volume of the tracer entering and exiting the system at a constant flow. There are numerous other models that can be used to examine pulmonary perfusion which can be used depending on the acquisition length and temporal resolution with a list found in table 3 of reference [205].

To obtain the aforementioned parameters it is necessary to know how the tracer behaves as it first enters the pulmonary vascular system and then how it behaves as it passes through the system and also to convert from signal intensity to contrast agent concentration. The initial behaviour in pulmonary perfusion is described by the arterial input function (AIF) where a region of interest (ROI) is usually drawn in the main pulmonary artery to extract a curve representing the passage of the bolus through the artery. To convert signal in a voxel to contrast agent concentration it is necessary to have the T_1 measurements from the same voxel pre, during and post contrast administration. Contrast concentration is proportional to the relaxation rate at time t (defined as $1/T_1$) minus the relaxation rate at time zero divided by the relaxivity of the contrast agent being used [419]:

$$[\mathrm{CA}](\mathrm{t}) = \frac{\frac{1}{T_1(t)} - \frac{1}{T_{1,0}}}{r_1} = \frac{1}{r_1} R_1 - R_{1,0} \tag{6.1}$$

Using this and a signal-formation model based on the sequence applied (in this work a 3D SPGR sequence was used which spatially matches the subsequent DCE time resolved imaging sequence) it is possible to calculate the T_1 at each time point for all voxels in the lung and convert the signal intensity to the contrast agent concentration. The first step is to estimate $T_{1,0}$ by acquiring images pre-contrast administration. The method used here was the variable flip angle method [420] with three different flip angles of 2, 10 and 30 degrees. Note that other T_1 mapping methods such as inversion recovery [421] and the Look-Locker method [422, 423] are available and the inversion recovery method is seen as the gold standard, whilst recent developments have also allowed the use of ultra-fast modified look-locker SSFP imaging to measure T_1 [424].

By fitting each voxel in the three flip angle maps using equation 6.2 and the Levenberg-Marquardt non-linear least squares fitting algorithm values of baseline T_1 ($T_{1,0}$) and proton spin density (M_0) can be extracted [420, 425].

$$\boldsymbol{s_{SPGR}} = M_0 \frac{\left(1 - e^{-TR/T_1}\right)}{\left(1 - e^{-TR/T_1}\right) \cdot \cos(\alpha)} \sin(\alpha) \tag{6.2}$$

To enable measurement of $T_{1,0}$ and M_0 the sequence TR must be kept constant and this will then result in a curve characterized by T_1 [145] with each point on the curve defined at each flip angle measured. To extract the values of $T_{1,0}$ and M_0 this equation can also be linearized and solved in the form of equation 6.3:

$$\frac{\boldsymbol{s_{SPGR}}}{\sin(\alpha)} = \boldsymbol{E_1} \frac{\boldsymbol{s_{SPGR}}}{\tan(\alpha)} . M_0(1 - \boldsymbol{E_1}) \tag{6.3}$$

Where $\boldsymbol{E_1}$ is e^{-TR/T_1}. Where the $T_{1,0}$ (equation 6.4a) and M_0 (equation 6.4b) are defined by the slope (m) and y-intercept (b) values obtained [145]:

$$T_{1,0} = \frac{-TR}{\ln(m)} \tag{6.4a}$$

$$M_0 = \frac{b}{1 - m} \tag{6.4b}$$

Following determination of these values, the $T_{1,0}$ and M_0 maps will need to be registered to the dynamic acquisition in order to convert signal intensity to contrast agent concentration. This is dependent on the sequence used and the conversion algorithm used is shown below. Relaxivity (r_1) of the Gd agent used here was assumed to be 5.2 L/mmol sec^{-1} as shown in the Gadovist™ (Bayer Schering Pharma, Germany) data sheet. The dynamic contrast enhanced sequence TR was 2.297ms and the flip angle was 30^{o}. Gadovist was administered at 0.05ml/kg at a rate of 4ml/s with a saline flush of 20ml/s. This dose was used over the recommended 0.2ml/kg as in some cases patients were scanned twice on the same day and hence it was necessary to remain within local hospital dosing rules. Secondly at higher concentrations the relationship between signal intensity and contrast agent concentration is non-linear [426, 419] and this would impact the analysis methodology introduced in this section. Of course the need to measure pre-contrast T_1 is determined by the relationship between the relative signal enhancement and contrast concentration – if this relationship is non-linear then the approach of normalising the signal time-course to the baseline signal time-course acquisition, as Nikolaou et al. [213] amongst others have used, would not be appropriate. To assess this relationship for the specific sequence parameters used here the approach of Schabel et al. was used [428], where relative signal enhancement is calculated by equation 6.5:

$$\frac{\Delta S}{S_0} = \frac{(E_1 - 1)(E_{1,0}\cos\alpha - 1)}{(E_{1,0} - 1)(E_1\cos\alpha - 1)}\left(\frac{E_2}{E_{2,0}}\right) - 1 \tag{6.5}$$

Where $E_{1,0} = \exp^{-TR \cdot R_{1,0}}$, $E_1 = \exp^{-TR \cdot R_1}$, $E_{2,0} = \exp^{-TE \cdot R^*_{2,0}}$, $E_2 = \exp^{-TE \cdot R^*_2}$, where $R_{1,0}$ and R_1 are defined as in equation 6.1 and $R^*_{2,0} = \frac{1}{T^*_{2,0}}$ and $R^*_2 = \frac{1}{T^*_2}$. Relaxation rates were assumed to scale linearly with contrast agent concentration [428] and thus $R_1 = R_{1,0} + (r_1 \cdot CA)$ and $R_2 = R_{2,0} + (r_2 \cdot CA)$. r_1 was set to 5.2 L/mmol^{-1}sec^{-1} and r_2 was set to 6.1 L/mmol^{-1}sec^{-1}. For both the simulations in Figures 6.1 and 6.2 $T^*_{2,0}$ was estimated as 1.4ms with a $T_{1,0}$ of lung and blood set as 1200ms, with the range of contrast concentrations being the same.

As is done in most work the T^*_2 component is ignored thus for the simulations to determine T_1 dependence this was done [428]. For simulations, the T_1 of lung tissue and blood was defined as an equispaced vector ranging from 200ms to 2500ms and contrast agent concentration (CA) was defined as an equispaced vector (with the same number of points as the T_1 vector) ranging from 0 mmol/litre to 10 mmol/litre. Figure 6.1 shows a plot of the percentage signal enhancement against a range of T_1 values for a number of contrast agent concentrations (a) and for a fixed contrast agent concentrations of 1 to 5mmol/litre (b). As can be seen there appears to be increased T_1 dependence at higher contrast agent concentrations with a CA of 10 mmol/litre causing anywhere from 5% to 70% enhancement depending on the T_1. These simulations show that measurement of pre-contrast T_1 is a necessary step, particularly in the lung where there is a large range of T_1 values.

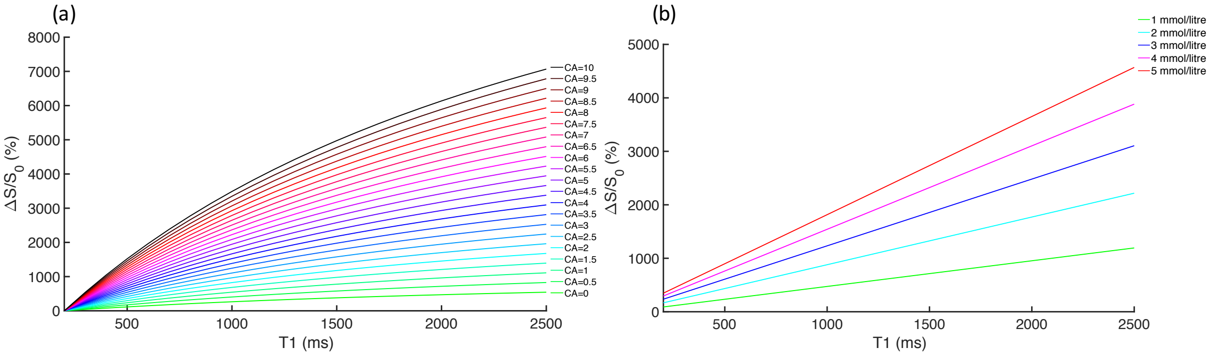

Figure 6.1 Simulated curves of relative signal enhancement as a function of concentration of contrast agent. (a) Varying T_1 and contrast agent concentration and (b) Varying T_1 and fixed contrast agent concentrations between 1 and 5mM

Additionally, not including the T_2^* effects may be detrimental to the calculation, particularly in the lung due to the low T_2^*, as discussed in Chapter 2, compared to other organs. For simulation of the effect of including/excluding this effect equation 6.5 was used with and without the T_2^* component to generate the curves in Figure 6.2. Figure 6.2 demonstrates that in the case of the flip angle used in this work (30°) there is little difference in the percentage signal enhancement when considering/not including the T_2^* effects with an average error of 64% over the range of contrast concentrations used in simulation, meaning that on average excluding the T_2^* leads to a 64% overestimation in percentage signal enhancement. Although this value seems large, when considering the percentage increase at a low concentration value of 1 mmol/litre this causes a 500% change in signal and thus 64% is negligible, as is proven by the near overlap in Figure 6.2, suggesting that it is reasonable to exclude the T_2^* component as has been done in previous publications [46, 144].

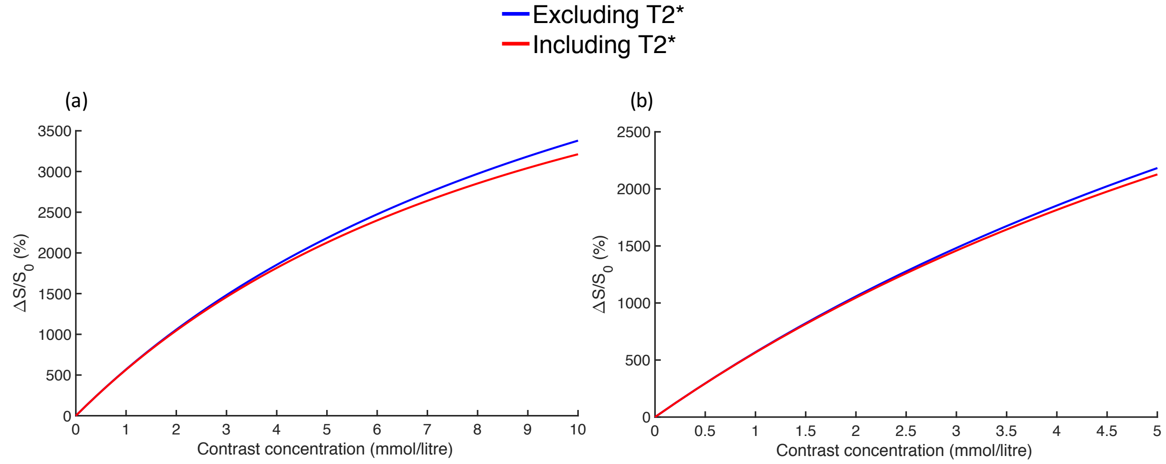

Figure 6.2 Simulated curves showing the effect of including/excluding the T_2^* component (a) over a large range of contrast concentrations and (b) an enhanced view of concentrations of 0-5 mmol/litre

Equations 6.6-6.11 show the way in which the contrast concentration was found [430]. Note that S here refers to the dynamic acquisition signal intensity.

$$A = \frac{S(t) - S(0)}{M_0 \sin(\alpha)} \tag{6.6}$$

$$B = \frac{\left(1 - e^{-TR/T_{1,0}}\right)}{1 - \cos(\alpha)\left(e^{-TR/T_{1,0}}\right)} \tag{6.7}$$

$$C = \frac{1 - (A + B)}{1 - \cos(\alpha)(A + B)} \tag{6.8}$$

$$R1_t = -\frac{1}{TR}\ln(\mathrm{C}) \tag{6.9}$$

$$R1_0 = \frac{1}{T_{1,0}} \tag{6.10}$$

$$Contrast\ concentration\ (CA) = \frac{R1_t - R1_0}{r_1} \tag{6.11}$$

Where CA will be in units of mmol/litre. The next stage of quantitative perfusion analysis is to extract the parameters PBF, PBV and MTT. Before applying any modelling techniques the data is smoothed via fitting to a Gamma-variate function [431, 82]:

$$CA_{lung}(t) = K_s(t - AT)^{\alpha} e^{-\frac{(t-AT)}{\beta}} \tag{6.12}$$

Where K_s is a constant scale factor, α and β are scale parameters; t is time after injection and AT is the appearance time of the contrast in the voxel being considered. Following the fitting of every voxels concentration-time curves the closed compartment model described in detail by Ostergaard et al. [83] can be used where the indicator dilution theory provides the fundamental method for volume calculation. The CA concentration in a lung voxel is defined by [46]:

$$CA_{lung}(t) = PBF(CA_{AIF}(t) \otimes R(t)) \tag{6.13}$$

Where ⊗ is the convolution operator, C_{AIF} is the concentration of the CA in the AIF (acquired from a region similar to the region of interest shown in Figure 2.13) at time t and R is the residue function, defined as the fraction of contrast agent concentration remaining in the lung after time t [83, 432, 46]. PBF is usually taken as the maximum value of the result of the deconvolution of the CA_{lung} and CA_{AIF} concentration-time curves [83].

Deconvolution is a complex procedure and there are different methods that may be used, however the most commonly used method of deconvolution in perfusion analysis was applied in this work, singular value decomposition (SVD) [83, 433, 434]. The SVD method of estimating PBF from contrast enhanced MRI data involves solving a matrix equation formed from [83]:

$$CA_{lung}(t) = PBF\Delta T \sum_{i=1}^{N} CA_{AIF}(ti)\, R(tj - ti) \tag{6.14}$$

Which can be represented in matrix form as equation 6.15:

$$R_{SVD} = \frac{1}{\Delta T} CA_{AIF}^{-1} CA_{tissue} \tag{6.15}$$

Where ti and N denote the time of the ith acquisition and total number of acquisitions respectively. ΔT is the sampling time of the dynamic acquisition and the matrix CA_{AIF} is generated from the sampled values of the AIF over time [435]:

$$\boldsymbol{A} = \begin{bmatrix} CA_{AIF}[t1] & 0 & 0 & \ldots & 0 \\ CA_{AIF}[t1 + \Delta T] & CA_{AIF}[t1] & 0 & \ldots & 0 \\ \vdots & \vdots & \ddots & \ddots & \vdots \\ \vdots & \vdots & & \ddots & 0 \\ CA_{AIF}[t1 + (N-1)\Delta T] & CA_{AIF}[t1 + (N-2)\Delta T] & \ldots & \ldots & CA_{AIF}[t1] \end{bmatrix}$$

N is the number of samples used to generate the AIF (the number of time frames in the dynamic acquisition) and $t1$ is the time at which sampling started. R_{SVD} ($\boldsymbol{b}$) and CA_{tissue} ($\boldsymbol{c}$) are Nx1 vectors representing the residue function multiplied by the PBF and ΔT and the contrast agent in the region of interest respectively. The aim is then to solve the matrix equation $\boldsymbol{c} = \boldsymbol{Ab}$ for the value of $\boldsymbol{b}$. Using the SVD methodology the inverse of $\boldsymbol{A}$ can be calculated as:

$$\boldsymbol{A^{-1}} = \boldsymbol{V}[diag(1/w_i)]\boldsymbol{U}^T \tag{6.16}$$

w_i are the diagonal elements of $\boldsymbol{W}$ and $\boldsymbol{U}^T$ is the transpose of $\boldsymbol{U}$**.**

This is possible as the SVD methodology expresses the matrix $\boldsymbol{A}$ as the product of the orthogonal matrix $\boldsymbol{U}$, the diagonal matrix $\boldsymbol{W}$ with a positive or zero element and the transpose of the orthogonal matrix $\boldsymbol{V}$ [436].

Note that it is possible to estimate functions for the residue function, for example a box function [83, 433], however these estimates may lead to a deconvolution with increased noise and affect the value of PBF found. For this work the residue function was assumed to have a value of 1 at the initial sampling time-point and was not estimated by any of the functions listed in [83, 433]. The matrix $\boldsymbol{b}$ can then be estimated by:

$$\boldsymbol{b} = \boldsymbol{V}[diag(1/w_i)](\boldsymbol{U}^T\boldsymbol{c}) \tag{6.17}$$

The values in the diagonal matrix $\boldsymbol{W}$ are usually thresholded by removing any values less than a threshold, typically this threshold is set around 20% of the largest singular values [437], to try and reduce the noise in the deconvolution. The maximal value of the matrix $\boldsymbol{b}$ is then taken as the PBF [433].

The PBV is then given by the time integrated concentration-time curve of the voxel of interest within the lung normalised by the time integrated concentration-time curve of the pulmonary artery:

$$PBV = \frac{\int_0^\infty CA_{lung}(t)\,dt}{\int_0^\infty CA_{AIF}(t)\,dt} = f \tag{6.18}$$

And from the central volume theorem [431, 83] the MTT can be calculated by simply dividing the PBV by PBF:

$$MTT = \frac{PBV}{PBF} \tag{6.19}$$

At this point the values returned are not in the standard reporting measures of ml/100ml for PBV and ml/100ml/min for PBF [199, 426, 438, 439, 200, 201, 191, 418, 203, 206]. PBV will be a dimensionless fraction whilst PBF will be in units of 1/time following deconvolution. When expressing these values, it is important to consider the density of the lung tissue and the haematocrit factor [83, 208, 419], however it should be noted that in much of the previous literature of DCE in lungs these values are not used to calculate PBV and PBF.

It is known that the concentration of the contrast agent will be reduced in tissue capillaries (C_{tc}) when compared to the intravascular space (C_{iv}) [440] and can be defined by equation 6.20 [431]:

$$C_{tc} = f.C_{iv} \tag{6.20}$$

Where f will be a fraction between 0 and 1 [441].

From the principle of conservation of mass, the amount of contrast agent input to a system must equal the amount leaving the system as defined by equation 6.21 [431, 441]:

$$F \int_0^t C_{artery}(t)\, dt = F \int_0^t C_{iv}(t)\, dt \tag{6.21}$$

Where F is the flow per unit volume. By combining equations 6.20 and 6.21 f is defined as fractional blood volume (equation 6.22):

$$f = \frac{\int_0^t C_{tissue}(t)\, dt}{\int_0^t C_{iv}(t)\, dt} \tag{6.22}$$

Therefore to calculate PBV in units of ml/100ml of tissue the fraction f must be multiplied by the hematocrit factor (H_f) (the difference between hematocrit in the artery and capillaries (equation 6.23a), usually not reported as it close to unity) divided by the tissue density (equation 6.23b) [442].

$$H_f = \frac{1 - H_{artery}}{1 - H_{capillary}} \tag{6.23a}$$

$$PBV = \frac{H_f}{\rho} f \tag{6.23b}$$

Whilst PBF is given by equation 6.23c [441] :

$$C_{tissue} = \frac{\rho}{H_f} . PBF . C_{AIF}(t) \otimes R(t) \tag{6.23c}$$

This means that whereas f is a dimensionless unit, PBV is the volume of blood per unit mass of tissue and PBF is the flow of blood per unit mass of tissue over time. Also, it should be noted that in many cases f and PBV are used interchangeably within the literature and particular care must be taken when reporting these values. Therefore prior to deconvolution it is important to transform the CA values from mM/litre to the correct units for flow. This transformation is accomplished by firstly converting the CA values to grams/ml by; (1) multiplying the CA values by the weight of the gadolinium chelate and (2) dividing by 1000. The second stage is to convert the mass into a volume by using a lung tissue density estimate

(0.2 g/cm^3 at inspiration for example) and applying the factor of 100 to get to the standard reporting values.

6.3 Materials and methods

6.3.1 Participant selection

To evaluate the V/Q mapping image-processing workflow developed, patient and normal subject imaging data was used. Four patients with asthma (denoted A-), five patients with COPD (denoted COPD-) and three healthy volunteers (denoted HV-) were scanned for this study. Patients with asthma underwent imaging pre and post administration of a bronchodilator to assess response to treatment. Subject demographics and PFTs are given in Table 6.1.

Table 6.1 Patient and volunteer demographics

Patient	Age	Gender	GINA*/GOLD	FEV_{1_base}**	FEV_{1_post}**
HV1	35	F	NA	98.2	NA
HV2	42	M	NA	107.2	NA
HV3	40	F	NA	99.9	NA
A1	60	F	4	110.3	115.1
A2	44	M	4	79.6	83.9
A3	52	F	4	90.1	90.0
A4	60	M	4	44.2	50.3
COPD1	61	M	-	-	NA
COPD2	69	F	-	-	NA
COPD3	57	M	-	-	NA
COPD4	59	F	-	48.9	NA
COPD5	67	F	-	43.9	NA

** GINA – global initiative for asthma score [443]; ** % predicted; - data not available; NA – not applicable*

6.3.2 Imaging

6.3.2.1 ^{1}H anatomical and ^{3}He ventilation-weighted imaging

Patients with asthma underwent multi-slice 2D spoiled gradient echo HP ^{3}He ventilation imaging following inhalation of 350ml ^{3}He mixed with 650ml N_2 from FRC. Prior to the ^{3}He scan a ^{1}H anatomical image at the same inflation level as the ^{3}He scan was acquired. For COPD patients and healthy volunteers three-dimensional ^{1}H anatomical (SPGR) and HP ^{3}He ventilation-weighted (bSSFP) images were acquired during the same breath hold following the methods in [73, 66]. HP gas ventilation-weighted images were acquired followed immediately by ^{1}H anatomical images. Patients inhaled 200mL HP ^{3}He mixed with 800mL N_2 from FRC prior to the scan. Imaging parameters can be seen in Table 6.2.

Table 6.2 Imaging parameters for the sequences used in this work. TR = Repetition time, TE = echo time, FA = flip angle. Note that slice number and field of view (FOV) were adjusted per patient to ensure full lung coverage

Acquisition	Sequence	TR (ms)	TE (ms)	FA (°)	Bandwidth (kHz)	Matrix size (frequency x phase)	FOV (cm)	Voxel size (mm)	Slice thickness (mm)	Slices
^{1}H (2D)	SSFP	2.4	0.7	50	167	128x64	32-42	2.3x3.5-3.2x4.9	10	16-24
^{3}He (2D)	SPGR	3.6	1.1	8	62.5	128x102	32-42	2.3x1.8-3.2x2.5	10	16-24
^{1}H (3D)	SPGR	1.5	0.6	5	167	100x100	40-48	4x4-4.8x4.8	5	46-50
^{3}He (3D)	SSFP	1.9	0.6	10	167	100x80	40-48	4x3.2-4.8x3.8	5	46-50

6.3.2.2 Variable flip angle imaging for T_1 mapping

All subjects had three-dimensional SPGR images acquired at flip angles of 2, 10 and 30 degrees during inspiratory breath-hold to estimate T_1 and proton spin density of the lungs pre contrast adminstration ($T_{1,0}$ and M_0). TR and TE were kept constant at 2.85ms and 0.9ms respectively. Bandwidth was $\pm$62.5 kHz, with an acquisition matrix of 200x80 and a slice thickness of 4mm [144].

6.3.2.3 DCE-^{1}H imaging

DCE-^{1}H perfusion-weighted images were acquired following all HP gas images so as not to affect the contrast of the ventilation-weighted images. DCE-^{1}H perfusion-weighted images were acquired during inspiratory breath-hold using a 3D spoiled gradient echo sequence with full lung coverage with an acquisition matrix of 200x80 and 36 time-frames of ~0.5s each [216, 214] following injection of 0.05ml/kg gadolinium contrast agent (Gadovist) at 4ml/s with 20ml saline flush. TR was 2.2ms, TE was 0.8ms and FA was 30°.

6.3.3 Image analysis

Figure 6.3 describes the co-registration and basic analysis steps used in this work. Briefly perfusion time-course images were co-registered to the initial time point of the dynamic acquisition to reduce motion artifact error in the quantitative pulmonary perfusion analysis. Following this, all dynamic contrast enhanced images are co-registered to the T_1-weighted image acquired using a flip angle of 2° to allow for conversion of signal intensity to contrast agent concentration. Following registration of the dynamic contrast enhanced images and the T_1-weighted image, quantitative pulmonary perfusion analysis is carried out to estimate the pulmonary blood volume. The pulmonary blood volume map and peak signal enhancement image are then indirectly registered to the same image space as the ventilation image. This registration is accomplished by registering the first time point of the dynamic contrast enhanced acquisition (which has been co-registered to the T_1-weighted image) to the same-breath ^{1}H anatomical image and applying the transform to the peak signal enhancement image and pulmonary blood volume map. Finally, the fractional ventilation and VQ metrics, discussed next, are derived.

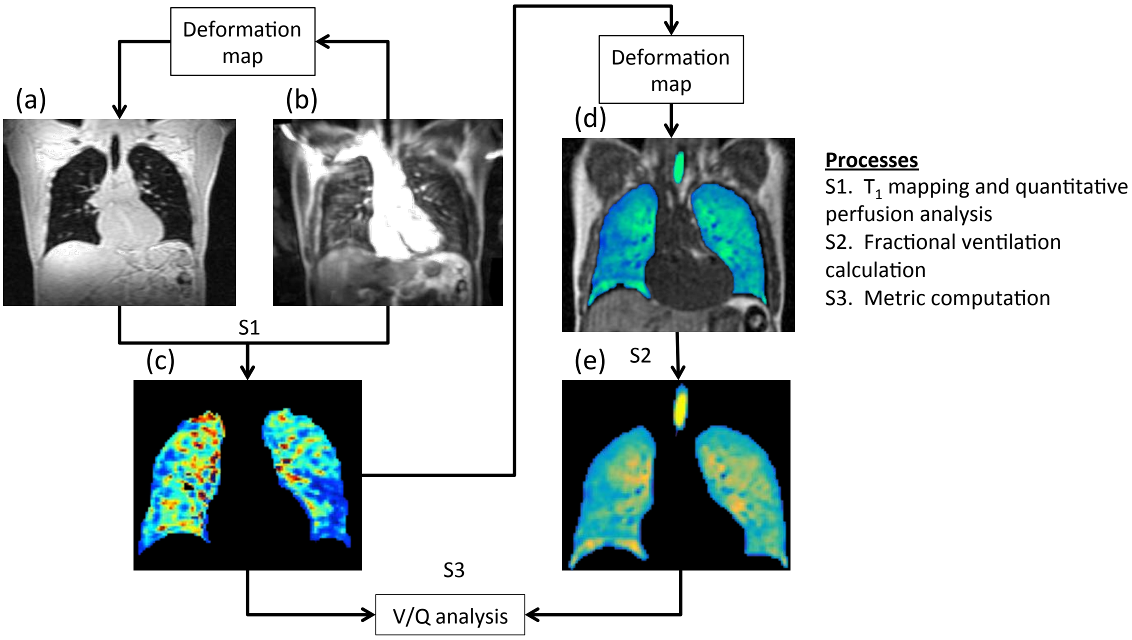

Figure 6.3 Basic representation of the workflow used to analyse V and Q images. Example slices from (a) T_1-weighted image used in T_1 mapping, (b) peak signal enhancement image, (c) Pulmonary blood volume map, (d) fused ventilation-weighted and 1H anatomical image and (e) Fractional ventilation map

6.3.3.1 Ventilation image analysis

Ventilation-weighted images were quantified using the method developed by Tzeng et al. [326], where the signal intensity of the ventilation image is converted to a fraction of gas in the voxel using equation 6.24:

$$\mathrm{FV} = \frac{1}{\sum S_{i,j,k}} \times \frac{S_{i,j,k}}{V_{voxel}} \tag{6.24}$$

Where FV is the fractional ventilation, $S_{i,j,k}$ is the signal intensity at voxel location i, j, k, $\sum S_{i,j,k}$ is the total signal including airways and V_{voxel} is the volume of the voxel. ^{1}H anatomical images were registered to ventilation-weighted images using the method presented in chapter 3, section 3.2.7 to compute %VV using the segmentation method described in chapter 3.

6.3.3.2 T_1 mapping

T_1 mapping was carried out following the variable flip angle method described in [144]. Images were registered using masked registration, that is masking out everything but the lung parenchyma and then registering these masked images, after which the deformation field was applied to the unmasked data. To calculate $T_{1,0}$ and M_0 images were then passed into a Matlab function to fit every voxel using a non-linear least squares Levenberg-Marquardt algorithm [430, 47, 420, 144]. $T_{1,0}$ and M_0 images were subsampled to the same number of slices as the DCE-^{1}H acquisition.

6.3.3.3 DCE-$_1$H image analysis

The DCE-^{1}H time series images were registered to the T_1-weighted image acquired with a flip angle of 2°. Following registration signal intensity was converted to contrast agent concentration and pulmonary blood volume (PBV) was calculated by fitting a gamma-variate to every voxel's concentration-time curve [431, 82, 83, 444, 46] as outlined in section 6.2 and applying the deconvolution methodology to estimate values of PBF and MTT, and using equation 6.19 PBV was defined as MTT*PBF. Finally, the quantitative PBV map, as well as T_1 and M_0 maps were registered to the ventilation image space, and as with the DCE-^{1}H to T_1 registration, ventilation images were subsampled to the same number of slices as the DCE-^{1}H acquisition. As in reference [442] PBV was multiplied with a factor κ to account for lung density at the level of inspiration during scanning. For this work κ = 0.2g/cm^3 was used, based on lung density measurements acquired from CT at inspiration [445]. Major blood vessels were segmented from the peak signal enhancement image by setting a threshold value by drawing an ROI in any vessel clearly seen in the lung followed by manual editing to ensure no parenchyma was removed.

The region of interest for the calculation of the AIF was manually drawn in the pulmonary artery. First DCE-^{1}H images were reviewed to assess at which time point and slice the pulmonary artery was most clearly seen. Second a region of interest was drawn using the Matlab command *roipoly*. Finally, all voxels greater or equal to the 95th percentile within the region of interest were used from every time point to construct the AIF.

6.3.3.4 V and Q metrics

Dividing the fractional ventilation image by the PBV map generated V/Q ratio maps. Additionally, measures of percent ventilated volume ($\% V_{vol}$), percent perfused volume ($\%Q_{vol}$) and percent ventilated and perfused volume (%V∩Q) were calculated. $\%Q_{vol}$ was calculated by first manually segmenting the whole lung from the peak signal enhancement image, generated by taking the maximum signal intensity over time for every voxel in the DCE-^{1}H images that were registered to the ventilation image. Following this the image was thresholded to calculate the perfusion defect area, this defect area was then subtracted from the whole lung perfusion mask to give the perfused volume (Q_{vol}). The threshold was defined by drawing an ROI in an area of noise and calculating the standard deviation over two slices (equation 6.25):

$$threshold = \sqrt{2}(mean(noiseROI_1 + noiseROI_2)) \tag{6.25}$$

Any voxel, within the whole lung perfusion mask, in the peak signal enhancement image with an intensity lower than the threshold was defined as perfusion defect.

$\%Q_{vol}$ is then defined by equation 6.26:

$$\%Q_{vol} = \frac{Q_{vol}}{TLV} \times 100\% \tag{6.26}$$

Where the TLV is defined as the registered ^{1}H anatomical image lung volume.

%V∩Q is defined by equation 6.27:

$$\%V \cap Q = \frac{V \cap Q}{TLV} \times 100\% \tag{6.27}$$

In addition to these metrics wasted ventilation (WV) and shunt were also defined using the 3-compartment model discussed by Peterson and Glenny [81] equations 6.28-6.31

$$Shunt\ volume\ (Sh_{vol}) = Q_{vol} \cap \overline{VV} \cap TLV \tag{6.28}$$

$$\%Shunt = \frac{Sh_{vol}}{TLV} \times 100\% \tag{6.29}$$

$$Wasted\ ventilation\ volume\ (WV_{vol}) = V_{vol} \cap \overline{Q_{vol}} \cap TLV \tag{6.30}$$

$$\%WV_{vol} = \frac{WV_{vol}}{TLV} \times 100\% \quad (6.31)$$

In addition to these metrics histograms were generated to assess the overlap of the FV and PBV histograms. To allow this analysis the ranges of the data needed to be made equal, this was done by normalising the PBV image to the minimum and maximum values of the FV image. Second both images were divided by their mean value and histograms generated using 100 bins. The location of the bin centres from the FV image were then used to generate the PBV image histogram. This normalisation process allowed for the area of the overlap to be calculated along with the mutual information (MI) of the histograms.

6.4 Results

6.4.1 Healthy volunteers

Table 6.3 shows the results of each of the aforementioned V and Q metrics for the three healthy volunteers. %VV are high as one would expect in healthy volunteers and is in line with previously reported results [66]. $\%Q_{vol}$ is also high but slightly lower than %VV in two out of the three volunteers, though this may be due to slight registration errors at the periphery of the lung. %V∩Q is above 90% for all three volunteers, as one would expect.

Table 6.3 Healthy volunteer V and Q metrics

Patient	$\%V_{vol}$	$\%Q_{vol}$	%V∩Q
HV1	98.20	93.90	93.32
HV2	94.49	94.15	90.85
HV3	98.02	94.29	93.31

Figure 6.4 shows an example FV, PBV and V/Q image from HV1. Both the FV and PBV maps are homogeneous with little heterogeneity seen in the V/Q map.

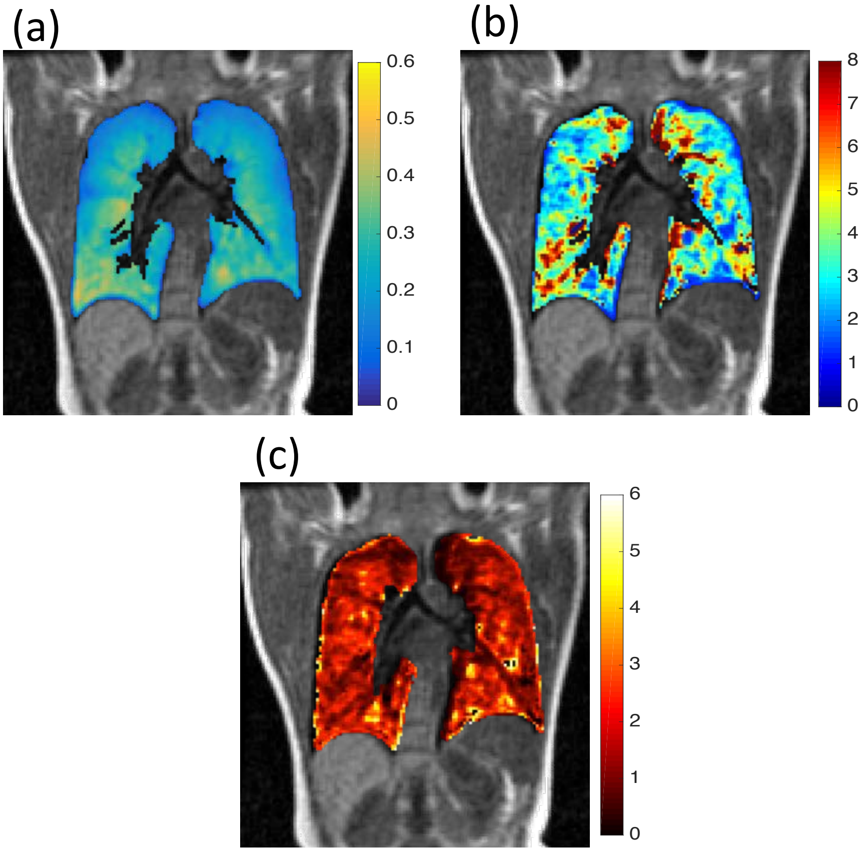

Figure 6.4 Example slices from a healthy volunteers (a) FV map, (b) PBV map and (c) V/Q map

Table 6.4 shows the mean values for PBV, FV and V/Q for each of the volunteers. Fractional ventilation values are similar to those estimated in healthy volunteers using the multiple breath washout technique [67]. It should also be noted that the mean V/Q ratio in two out of three of these healthy volunteers is higher than the reported range of 0.8-1.2 [376], although this could be due to the gravitational effect of the volunteers being supine and reduced ventilation and perfusion seen in the anterior slices, exemplified in the axial view of FV and PBV maps shown in Figure 6.5 , note that these are from the same volunteer shown in Figure 6.4. This pattern of increased PBV and FV towards the posterior section of the lung is representative of all volunteers analysed.

Table 6.4 Mean values of PBV, FV and V/Q for the three healthy volunteers

Patient	Mean PBV (ml/100ml)	Mean FV	Mean V/Q
HV1	3.72	0.25	2.34
HV2	6.47	0.23	1.21
HV3	5.41	0.22	1.99

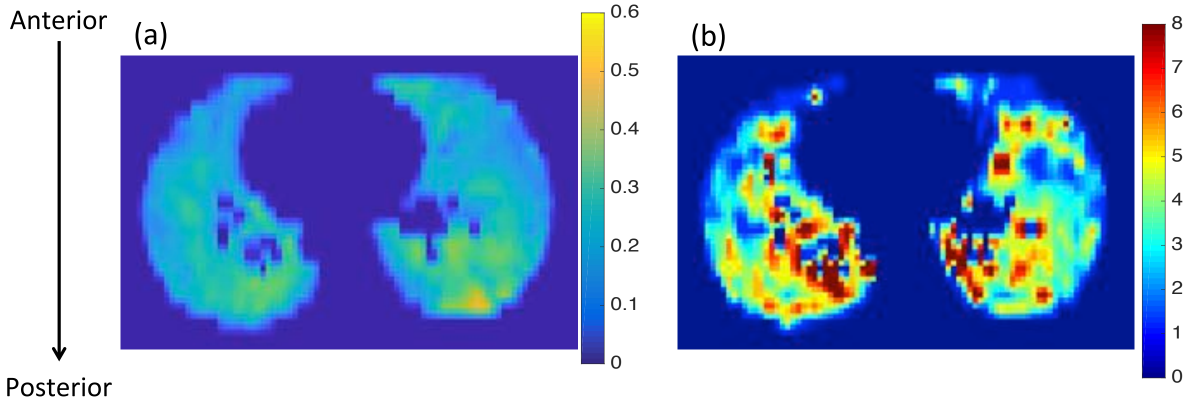

Figure 6.5 Example axial slices from a HV1s FV and PBV maps. (a) FV slice and (b) PBV slice

Figure 6.6 shows the FV and PBV histograms for all three healthy volunteers whilst Table 6.5 shows the overlap area and mutual information (MI) values.

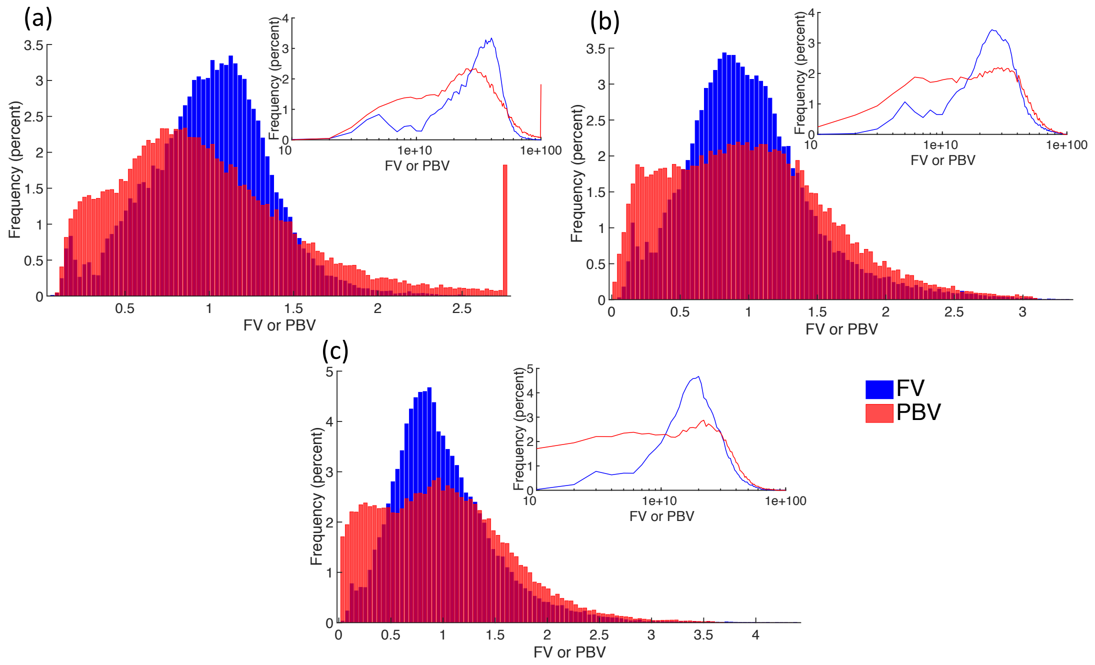

Figure 6.6 FV and PBV histograms from all three healthy volunteers. (a) HV1, (b) HV2 and (c) HV3. The inset on each graph is the FV and PBV histograms plotted on a log x axis

Table 6.5 MI and overlap area of histograms for healthy volunteers

Patient	MI	Overlap area
HV1	0.50	4164
HV2	0.48	1927
HV3	0.51	4018

Pulmonary blood volume in these healthy volunteers is slightly lower than previously reported values in healthy volunteers [46], however slight differences in deconvolution methodology and image registration will affect the values calculated from the fitted concentration-time curves. Additionally, the breath-hold at which the image is acquired will affect the perfusion parameters. When comparing our results and the study in [46] it is worth noting that in that work the contrast agent concentration was not calculated using $T_{1,0}$ and M_0 maps as there is no mention of the method used to convert the signal intensity to contrast agent concentration. In these healthy volunteers, it is clear that there is still some V/Q mismatch even after normalization of the data. However, there is a good level of overlap in the histograms as exemplified in Figure 6.6.

6.4.2 Patients with asthma – pre and post bronchodilator administration

Figure 6.7 shows image examples from a patient with asthma with a good ventilation response to bronchodilator.

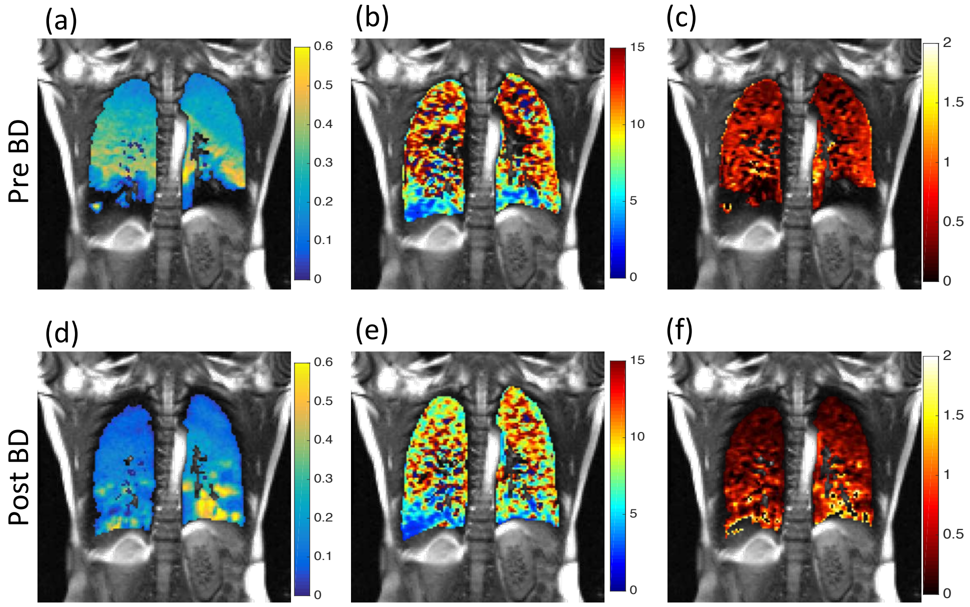

Figure 6.7 Example images from an asthmatic (A1) pre and post bronchodilator administration. (a) FV pre, (b) PBV pre, (c) V/Q pre, (d) FV post, (e) PBV post and (f) V/Q post

As can be seen in Figure 6.7 there is clearly a perfusion deficit in the base of the lung, with little improvement following the administration of the bronchodilator, this is likely due to hypoxic vasoconstriction and the pulmonary vasculature not responding to the increased lung ventilation on the time course of the post bronchodilator scan [446, 447, 98, 448]. Table 6.6, Figure 6.8 and Table 6.7 shows the V and Q metrics for the asthmatic patients pre and post bronchodilator administration, note that no statistical tests were carried out due to the small patient numbers.

Table 6.6 Asthmatic V and Q metrics pre and post bronchodilator

Patient	%V_{vol}	%Q_{vol}	%V∩Q
A1pre	90.81	87.84	82.02
A1post	94.43	87.01	84.91
A2pre	81.99	88.01	76.41
A2post	84.31	85.65	78.7
A3pre	95.28	75.36	74.91
A3post	96.74	90.62	90.1
A4pre	83.89	79.13	69.09
A4post	84.33	92.31	80.65

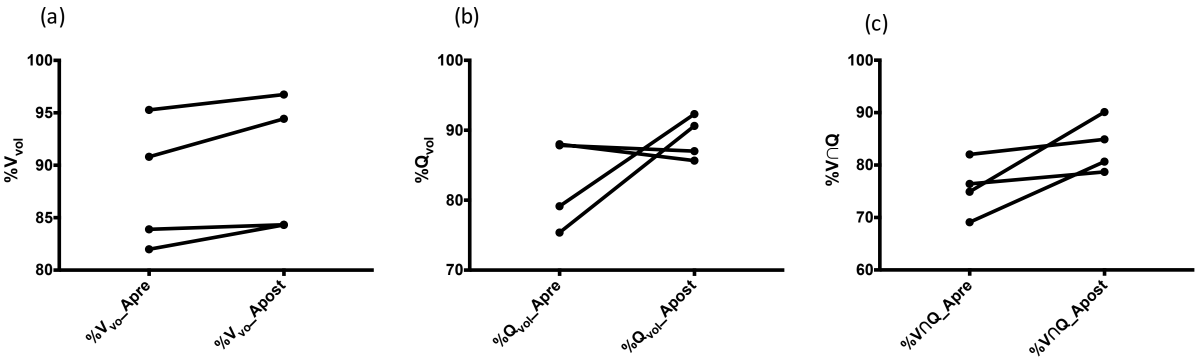

Figure 6.8 Change in %V_{vol}, %Q_{vol} and %V∩Q pre and post bronchodilator. (a) %V_{vol}, (b) %Q_{vol} and (c) %V∩Q

%V_{vol} shows increased in all patients, whilst %Q_{vol} increased in two patients and decreased in the remaining two. %V∩Q increases in all four patients. Table 6.7 shows the mean values for PBV, FV and V/Q for each of the asthmatic patients pre and post administration of the bronchodilator. The %VV values seen in these patients is slightly higher than previously reported values [63] however the difference in analysis methods may be a cause of this difference.

Table 6.7 Mean values of PBV and FV for the asthmatic patients

Patient	Mean PBV (ml/100ml)	Mean FV	Mean V/Q
A1pre	9.09	0.17	0.77
A1post	7.72	0.14	0.63
A2pre	6.52	0.17	2.29
A2post	8.18	0.30	3.27
A3pre	8.26	0.17	1.57
A3post	9.56	0.23	1.11
A4pre	7.04	0.15	1.20
A4post	6.52	0.19	1.32

Mean PBV over the whole lung increased post bronchodilator administration in two of the four asthmatics and decreased in the remaining two (Figure 6.9a). Mean fractional ventilation decreased in one subject (A1), and increases in patients A2, A3 and A4 increased (Figure 6.9), with a marked increase seen in patient A2. Mean V/Q increases in two patients (A2, A4) and decreases in the remaining two (A1, A3) suggesting an improvement in matching of V and Q for A1 and A3 and a worsening for A2 and A4.

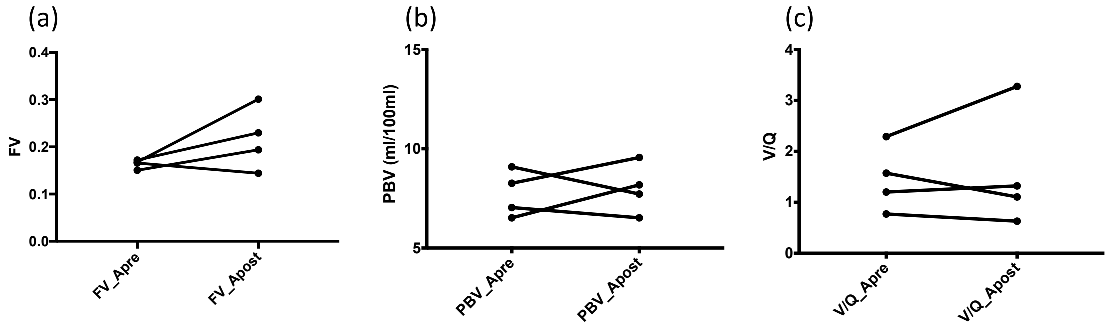

Figure 6.9 Change in PBV, FV and V/Q pre and post bronchodilator. (a) FV, (b) PBV and (c) V/Q

Figure 6.10 shows example axial slices from patient A1. Following administration of the bronchodilator there is almost no gravitational gradient seen in the FV images whilst PBV is much patchier and more heterogeneously distributed when compared to the healthy volunteer shown in Figure 6.5.

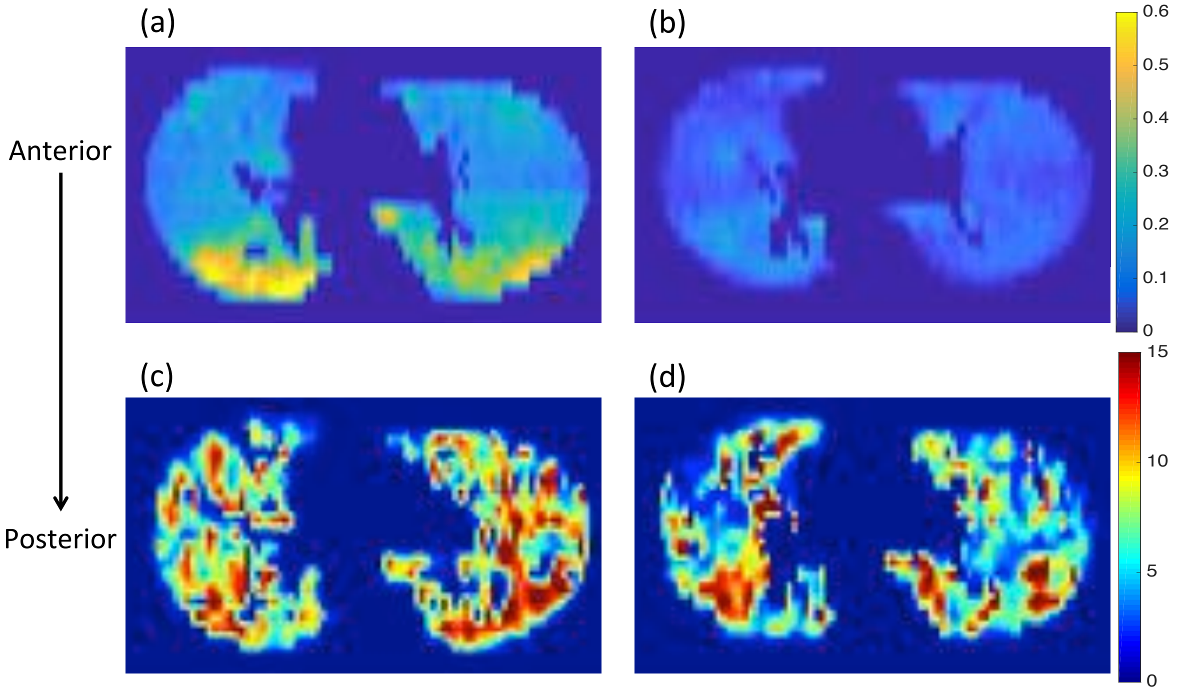

Figure 6.10 Example axial slices form patient A1. (a) FV pre, (b) FV post, (c) PBV pre and (d) PBV post

Figure 6.11 shows FV and PBV histograms for patients with asthma pre and post administration of a bronchodilator whilst Table 6.8 shows the overlap area and mutual information (MI) values. For this cohort of asthmatics there is slight improvement in the overlap of the histograms assessed visually although the overlap area metric does not represent this in one out of the four patients with asthma. MI between the FV and PBV histograms improves in three out of the four asthmatics, including A1 and A2 where there is a decrease in the overlap area of the histograms.

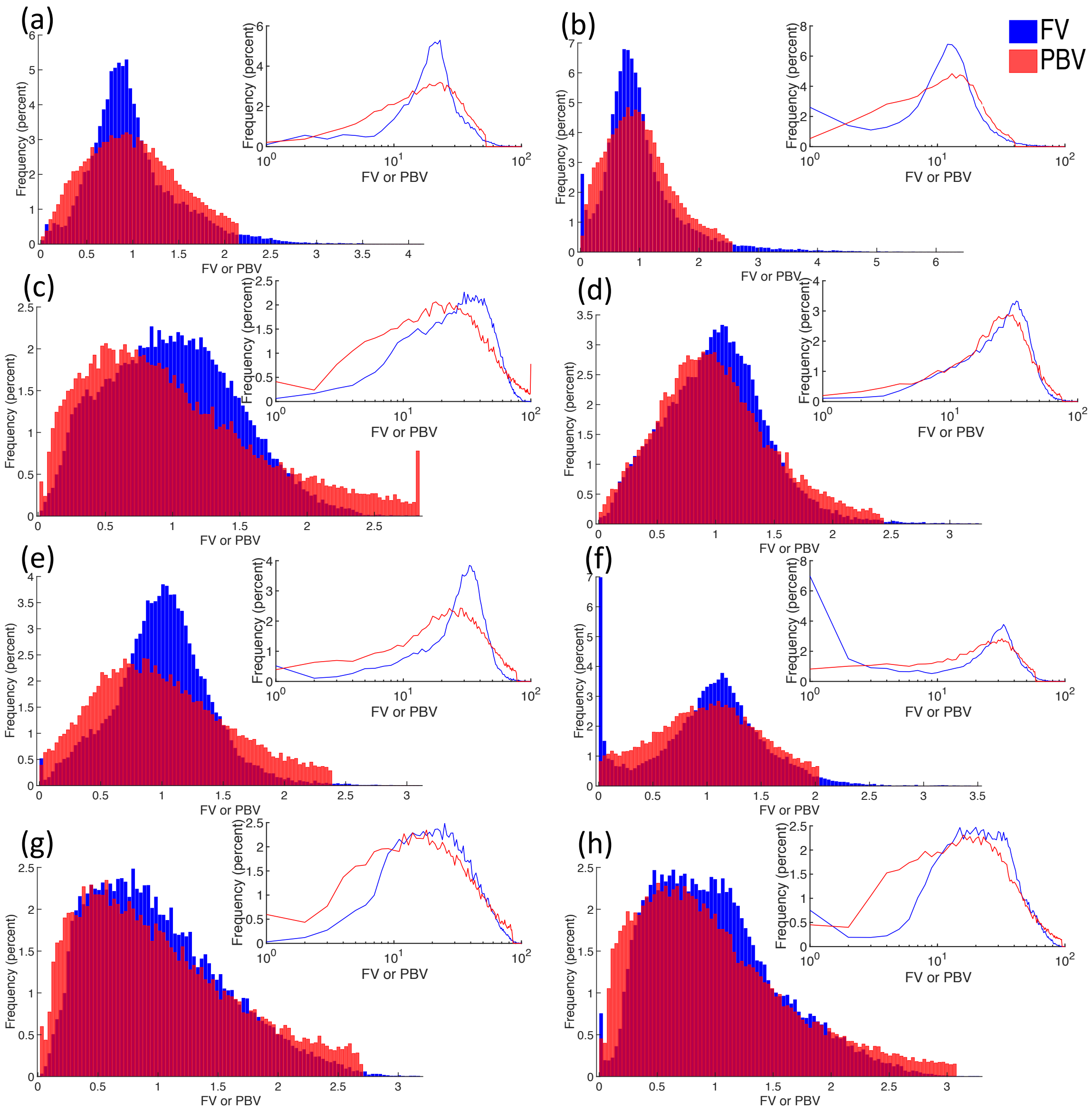

Figure 6.11 Example FV and PBV histograms for all patients with asthma. (a) A1 pre BD, (b) A1 post BD, (c) A2 pre BD, (d) A2 post BD, (e) A3 pre BD, (f) A3 post BD, (g) A4 pre BD and (h) A4 post BD. The inset on each graph is the FV and PBV histograms plotted on a log x axis

Table 6.8 MI and overlap area of histograms for patients with asthma

Patient	MI	Overlap area
A1pre	0.31	303
A1post	0.35	747
A2pre	0.27	1192
A2post	0.33	446
A3pre	0.33	582
A3post	0.31	730
A4pre	0.28	1179
A4post	0.34	1826

6.4.3 Patients with COPD

Figure 6.12 shows example images from a patient with COPD. This patient has a large amount of ventilation defects with some areas of reduced perfusion, with a heterogeneous V/Q map with large areas of high V/Q seen.

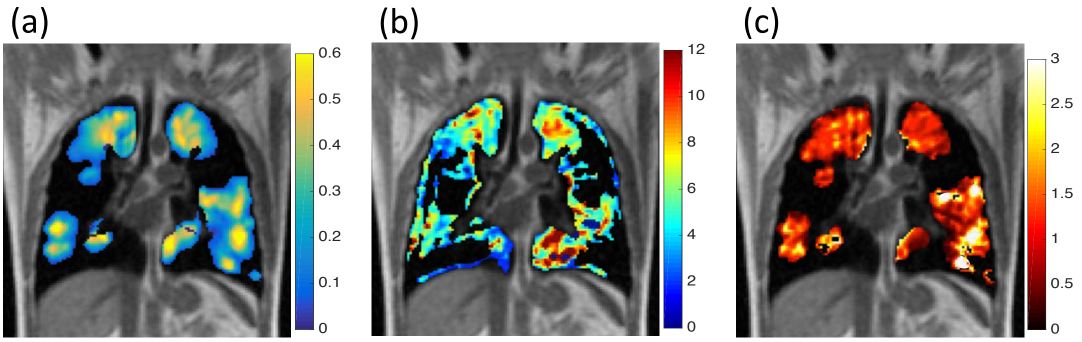

Figure 6.12 Example slices from a patient with COPD (COPD3) (a) FV map, (b) PBV map and (c) V/Q map

Table 6.9 shows the V and Q metrics from the patients with COPD. There is lower %V∩Q seen in this group of COPD patients compared to that seen in asthma, due to the increased number of defects seen in both the ventilation and perfusion images in the COPD patients when compared to the patients with asthma.

Table 6.9 COPD V and Q metrics

Patient	%V_{vol}	%Q_{vol}	%V∩Q
COPD1	80.36	72.04	64.10
COPD2	80.14	65.00	55.80
COPD3	54.26	68.63	41.26
COPD4	68.50	70.00	51.80
COPD5	84.80	74.44	66.81

%VV for these patients is within the range of previously reported values [58, 290]. Table 6.10 shows the mean PBV, FV and V/Q values from the patients with COPD. PBV is within previously reported values [449]. Mean V/Q is markedly increased in these COPD patients when compared to both asthmatic patients and healthy volunteers. One cause for this is the clearer mismatch in areas that are both ventilated and perfused compared to the healthy volunteers and patients with asthma. Additionally, the increased heterogeneity within ventilated lung contributes to these much higher mean V/Q values.

Table 6.10 Mean values of PBV, FV and V/Q for the patients with COPD

Patient	Mean PBV (ml/100ml)	Mean FV	Mean V/Q
COPD1	7.71	0.09	48.98
COPD2	6.31	0.14	22.97
COPD3	4.26	0.15	13.15
COPD4	4.87	0.13	64.88
COPD5	5.94	0.12	20.67

Figure 6.13 shows example axial slices of FV and PBV from patient COPD3. This patient has a similar perfusion gravitational gradient to the healthy volunteer, although this may simply be due to tissue destruction in the anterior portion of the lung.

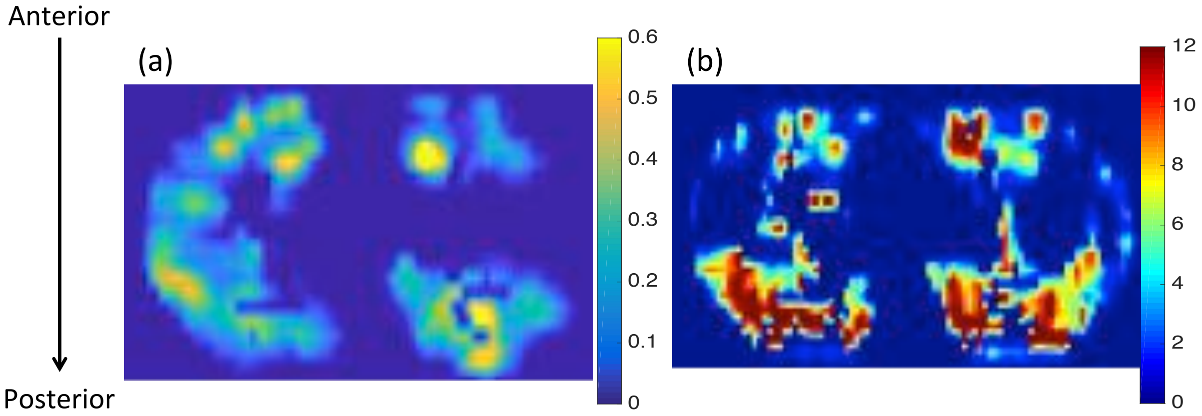

Figure 6.13 Example axial slices from patient COPD3s FV and PBV maps. (a) FV slice and (b) PBV slice

Figure 6.14 shows the FV and PBV histograms of all patients with COPD whilst Table 6.11 shows the overlap area and MI of these histograms. As can be seen the MI values are particularly small in these patients, partially due to the lack of perfused and ventilated tissue and the very different distributions seen in FV and PBV.

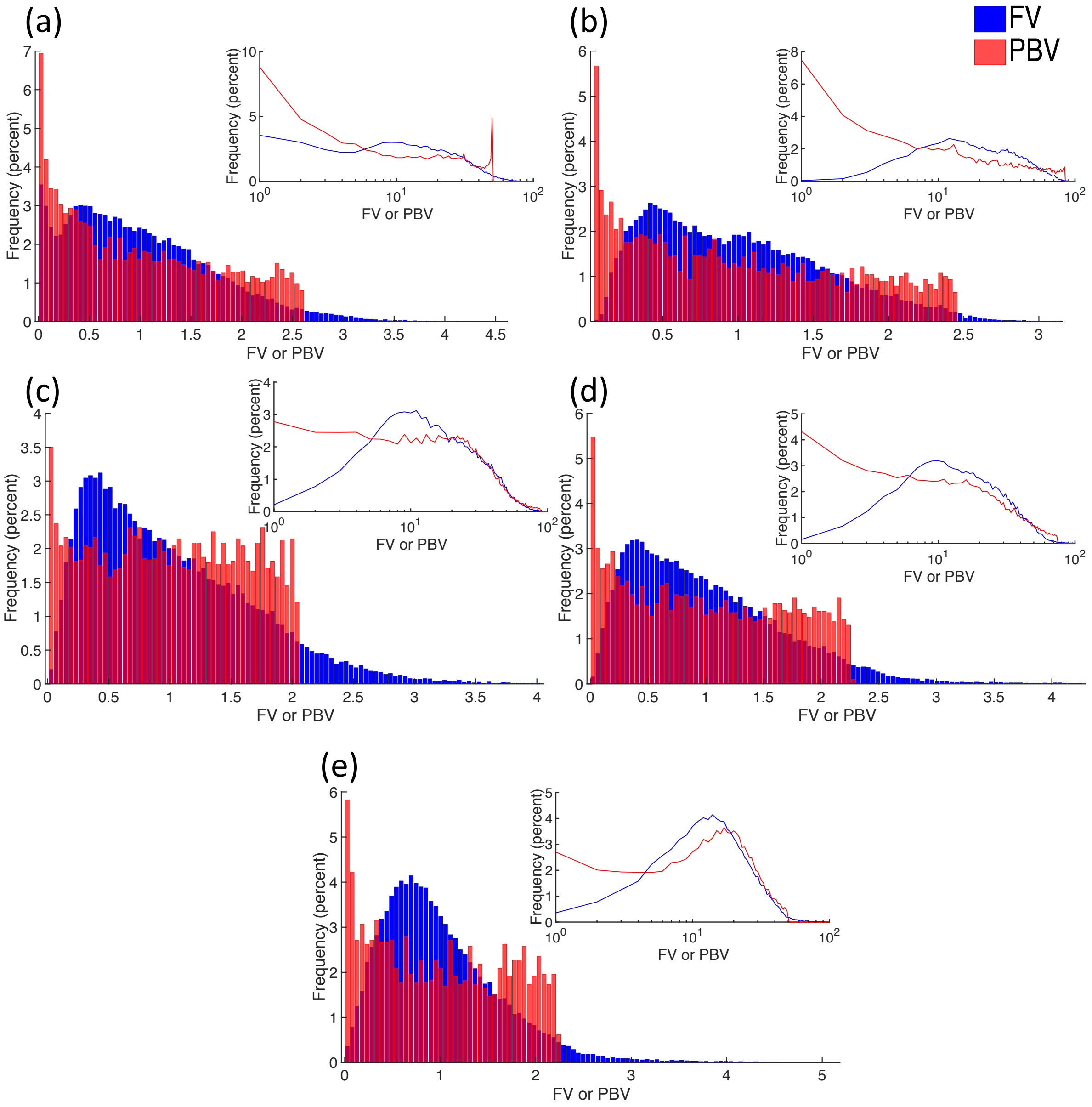

Figure 6.14 Example FV and PBV histograms for all patients with COPD. (a) COPD1, (b) COPD2, (c) COPD3, (d) COPD4 and (e) COPD5. The inset on each graph is the FV and PBV histograms plotted on a log x axis

Table 6.11 MI and overlap area of histograms for patients with COPD

Patient	MI	Overlap area
COPD1	0.09	48.98
COPD2	0.14	22.97
COPD3	0.15	13.15
COPD4	0.13	64.88
COPD5	0.12	20.67

These histograms follow the same pattern of high frequency of low PBV values and a broader spread of FV values when compared to healthy volunteers. Figure 6.15 shows the V and Q metrics of all three cohorts analysed. COPD patients have the highest variance in values of all three cohorts.

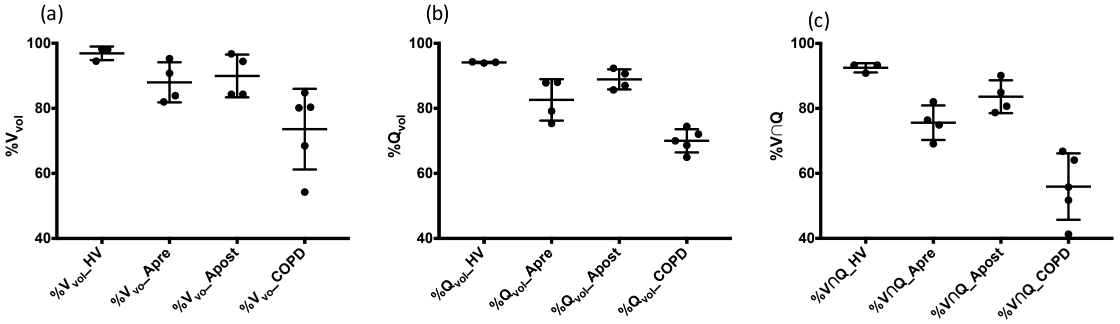

Figure 6.15 V and Q metrics for all cohorts analysed. (a) %V_{vol}, (b) %Q_{vol} and (c) %V∩Q. Each point represents a measurement from a single subject, error bars represent group means and standard deviations

Figure 6.16 shows the estimated percentages of shunt and wasted ventilation using the aforementioned techniques. As can be seen healthy volunteers have the lowest levels of shunt and wasted ventilation whilst patients with COPD have the highest values for these metrics. One interesting finding is the reduced value of shunt and wasted ventilation following administration of the bronchodilator to the patients with asthma.

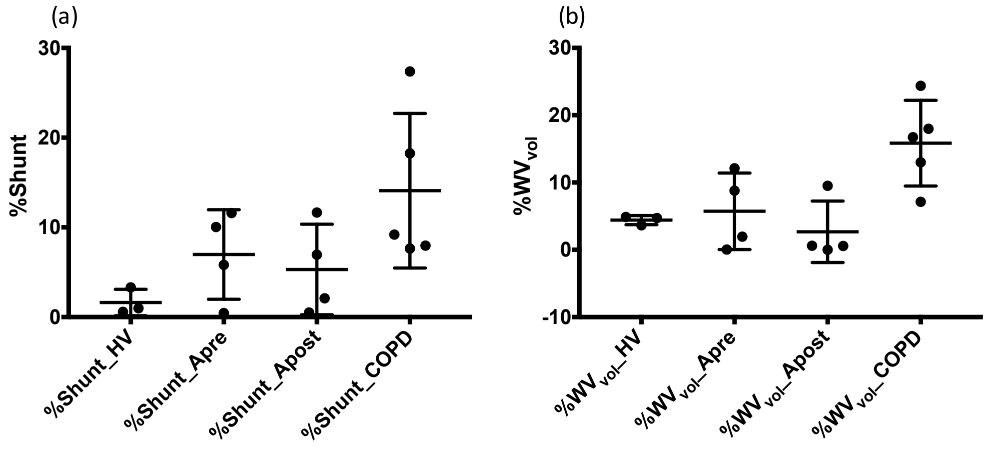

Figure 6.16 %Shunt and %WV_{vol} obtained from all cohorts analysed. (a) %Shunt and (b) %WV_{vol}. Each point represents a measurement from a single subject, error bars represent group means and standard deviations

Figure 6.17 shows plots of mean FV, PBV and V/Q as well as the mutual information and overlap area for all cohorts analysed. Healthy volunteers have the higher mean FV but lower mean PBV. Population means for the patients with asthma have a trend of improvement in all metrics following administration of the bronchodilator.

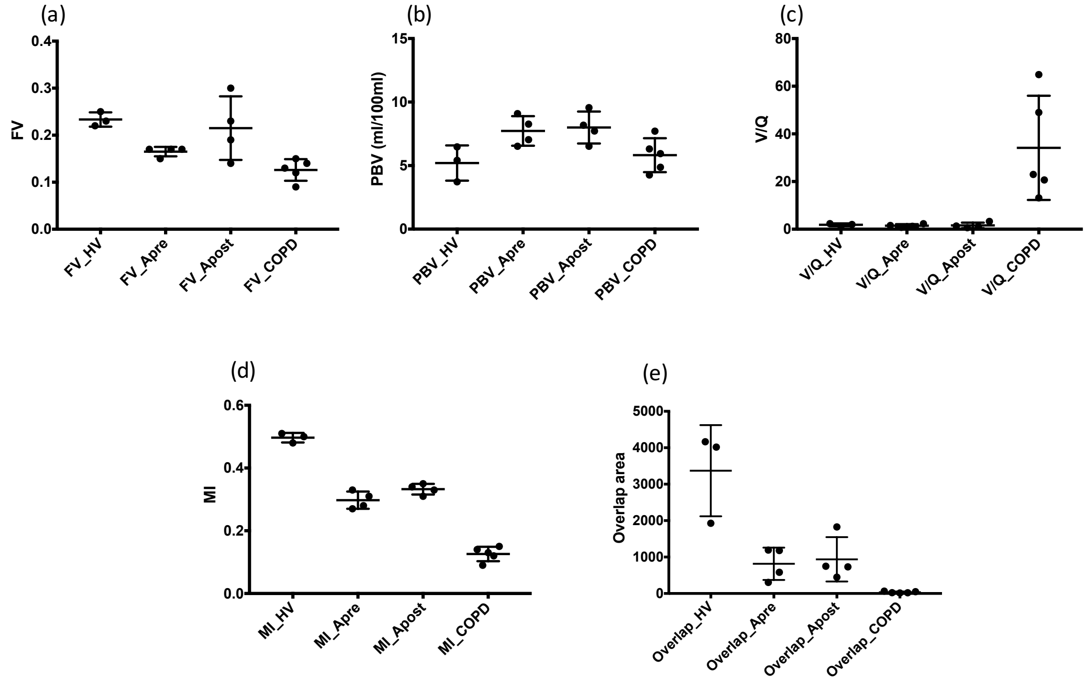

Figure 6.17 Plots of mean FV, PBV and V/Q along with MI and overlap area for all cohorts analysed. (a) FV, (b) PBV, (c) V/Q, (d) MI and (e) overlap area

Table 6.12 shows the results of statistical comparisons (p-values) of all metrics derived. All groups were compared to the healthy volunteer group via the Kruskal-Wallis test and the patients with asthma were then compared pre and post administration of the bronchodilator via a Wilcoxon matched-pairs signed rank test, the results of which are shown in Table 6.13.

Table 6.12 P-values from the Kruskal-Wallis multiple comparisons test comparing patient groups to healthy volunteers

Comparison	**$\%V_{vol}$**	**$\%Q_{vol}$**	**$\%V \cap Q$**	**$\%WV_{vol}$**	**%Shunt**
HV vs. A_{pre}	0.3260	0.2215	0.1627	>0.9999	0.8443
HV vs. A_{post}	0.7001	0.6477	0.8139	>0.9999	>0.9999
HV vs. COPD	0.0073	0.0017	0.0017	0.1970	0.0710
Comparison	**FV***	**PBV***	**V/Q ratio***	**MI**	**Overlap area**
HV vs. A_{pre}	0.5064	0.0906	>0.9999	0.1616	0.3414
HV vs. A_{post}	>0.9999	0.0635	>0.9999	0.8118	0.4464
HV vs. COPD	0.0091	>0.9999	0.2056	0.0016	0.0017

**Mean over whole lung*

Table 6.13 Wilcoxon matched-pairs signed rank test results

Comparison	**$\%V_{vol}$**	**$\%Q_{vol}$**	**$\%V \cap Q$**	**$\%WV_{vol}$**	**%Shunt**
A_{pre} vs. A_{post}	0.1250	0.6250	0.1250	0.3750	0.6250
Comparison	**FV***	**PBV***	**V/Q ratio***	**MI**	**Overlap area**
A_{pre} vs. A_{post}	0.2500	0.8750	>0.9999	0.2500	0.8750

**Mean over whole lung*

As can be seen from Table 6.12 the only significant differences were seen between healthy volunteers and COPD patients' values of $\%V_{vol}$, $\%Q_{vol}$, %V∩Q, %Shunt, FV, MI and overlap area. No significant differences were found between any metrics when comparing the patients with asthma pre and post bronchodilator.

6.5 Discussion

The main aim of this work was to develop and validate the proposed workflow however a limitation is the small numbers of healthy volunteers and patients analysed meaning a statistical significance cannot be derived and general conclusions may not be derived from the results presented.

Patients with COPD had lower %V∩Q than patients with asthma suggesting poorer matching of ventilation and perfusion in this small cohort of COPD patients than in the cohort of patients with asthma. %V∩Q improved in three of the four patients with asthma analysed and dropped by less than 1% in the remaining patient following administration of a bronchodilator.

Lower PBV was seen in the healthy volunteers when compared to some of the patients with asthma and COPD. One possible reason for this could be the difference in inspiration level as the volumes were not controlled for the DCE-^{1}H and T_1-mapping acquisitions and it has been shown that PBV increases at expiration compared to inspiration [199]. $\%Q_{vol}$ changed in all four patients with asthma following administration of a bronchodilator, with an increase seen in two and a decrease seen in the other two. One possible reason for the decrease may be the change in inspiration level, with the patient being able to take a larger breath in following administration of the bronchodilator. The increase may be caused by minor vasodilation effects of the bronchodilator [450] or simply that the breath hold was better held during the DCE-^{1}H acquisition meaning less motion induced errors are seen.

Perfusion defects occurred in the same regions of the lung as ventilation defects in most patients with asthma (Figure 6.7) and COPD (Figure 6.12), and in some cases in areas where there was no apparent ventilation defect. The patient exemplified in Figure 6.7 shows an example of HPV causing reduced perfusion in the base of the lung, which remains even after administration of a bronchodilator and increased ventilation in this area of the lung suggesting that reversing the effects of HPV may be more difficult in asthma than simply oxygenating previously hypoxic areas of the lung due to possible vascular remodelling caused by chronic hypoxia. This may help in the treatment of asthma and COPD by demonstrating that although %VV improves with treatment the vascular component of the disease may require more treatment or be beyond treatment due to the constriction that has taken place and possible destruction of the capillary bed, due to the time between the acquisition of the ventilation and perfusion images.

Another limitation is the lack of reproducibility data however Ingrisch et al. [206] demonstrated that in healthy volunteers PBV was fairly reproducible with moderate ICC, although PBF had a low ICC whilst other studies have shown good reproducibility of DCE-^{1}H MRI [451-453] in patients with cancer.

This method is not without its drawbacks as there are still the time consuming manual stages of segmentation of the first time-point of the DCE-^{1}H acquisition and the thresholding to determine the vessels and areas of perfusion deficit. Additionally, manual selection of the region of interest for the AIF will introduce a source of error into measurements between observers, due to the possibility of selecting different slices and region of interest sizes. However, the combination of V and Q metrics seems to provide improved difference in the patients with asthma pre and post administration of a bronchodilator and also provides good grouping of the healthy volunteers. The grouping of the patients with COPD does not improve.

6.6 Conclusion

A semi-automated workflow for quantitative evaluation of co-registered ventilation and perfusion images was developed and tested in a small cohort of healthy volunteers and patients with asthma and COPD. The method allows for voxel-by-voxel comparison of ventilation and perfusion whilst also allowing for novel metrics such as percentage ventilated and perfused lung to be examined.

Differences were seen between the healthy volunteers and the two patient cohorts analysed, although no statistical significance was found when comparing the healthy volunteers and patients with asthma. Increased numbers are needed to determine if this method can be used in conjunction with standard measures of the ventilation-perfusion ratio and if the metrics derived are capable of differentiating health from disease or detecting improvement following intervention in patients.

CHAPTER 7. CONCLUSIONS AND FUTURE WORK

7.1 Summary of the thesis and conclusions

This thesis investigated image-processing methods for quantitative evaluation of multinuclear magnetic resonance images of the lung. Three distinct analysis pipelines were developed and their utility in patients and healthy volunteers was demonstrated.

Chapter 3 introduced a semi-automatic segmentation method for lung MRI using a Spatial Fuzzy C-means methodology. This method reduced inter-observer differences when compared to the standard manual method and also provided more similar segmentations to the manual method than the well-known K-means method. Its utility was demonstrated in a small number of patients with diverse disease and also demonstrated on images acquired with both hyperpolarised ^{3}He and ^{129}Xe.

Chapter 4 investigated the use of the coefficient of variation of signal intensity histogram metrics in separating health from disease. Histogram metrics were used to differentiate healthy controls from patients and compared to the gold standard of ventilation defect percent and the standard global metric of median CV. In one case the CV histogram metrics were able to differentiate health from disease where VDP could not. In addition, the effect of sequence parameters, SNR, kernel size, dimensionality and gas used were investigated with the effect on CV metrics shown.

Chapter 5 made use of the segmentation software and the coefficient of variation of signal intensity to assess the effect of lung inflation level on quantitative metrics of lung function derived from hyperpolarised gas MRI. Six healthy volunteers were scanned to assess the repeatability of lung volumes and metrics whilst the effect of inflation level was also investigated in a small cohort of patients with asthma and cystic fibrosis. It was shown that although lung volumes may vary between sessions the quantitative measure of lung function (%VV) is very reproducible between sessions. Additionally, it was shown that %VV changes in disease when imaged at total lung capacity compared to functional residual capacity plus 1 litre, which may lead to better understanding of the nature of focal defects in patients with asthma and cystic fibrosis.

Chapter 6 discussed the development of a workflow for quantitative analysis of the ventilation-perfusion ratio using MRI. A workflow was developed to co-register hyperpolarised gas and DCE-^{1}H MRI to allow for a voxel-by-voxel comparison of quantitative metrics of ventilation and perfusion. Metrics were also developed using the co-registered images to analyse the severity of perfusion defects and the extent to which ventilation and perfusion are matched. This workflow was demonstrated on a small cohort of patients and volunteers.

7.2 Future work

Chapter 3

Further automation via addition of a vesselness filter and algorithm to automatically determine the optimum number of clusters to use in the Spatial Fuzzy C-means algorithm are the main areas to improve the methodology presented in chapter 3. Addition of a vesselness filter can be accomplished using the method developed by Frangi et al. [314] whilst determining the optimal number of clusters will require experimentation based on the distribution of signal intensity values within the lung.

Chapter 4

Developing a method to denoise the HP gas images and attempt to minimise the effect of noise on CV values is a key step to improve the reliability and sensitivity of the CV based metrics. Increased numbers of healthy volunteers imaged with both HP ^{129}Xe and ^{3}He are needed to determine normal values for each of the CV metrics presented. Additionally, increased numbers of patients with a range of pulmonary disease are needed to carry out the same simulations and comparisons of kernel size and dimensionality as was done for HP ^{3}He.

Chapter 5

Increasing the numbers of healthy volunteers and patients with different inflation levels is a key aspect of future work to ensure that the pattern of airway closure at lower lung volumes is seen in a cohort with a wider age range. Additional patient data may also allow for clearer understanding of what defects in different diseases are. A final stage of this work would be to add in a registration of high-resolution CT and proton anatomical images to the same space as the HP gas images to determine why certain defects resolve and others do not.

Chapter 6

Increased patient numbers analysed using the fully quantitative pipeline to show that the metrics developed may be useful in assessing patients, whilst more healthy volunteers are needed to determine a normal range for the metrics developed. Combining multiple breath washout MRI [69, 70] and free-breathing DCE-^{1}H MRI [203, 206] and comparing the output to that obtained from static breath hold images to determine if any changes are seen in the metrics developed is an interesting project and could allow for improved patient comfort for scanning if a free-breathing DCE-^{1}H MRI can be implemented. Finally comparing the metrics developed using HP ^{129}Xe and DCE-^{1}H to those obtained using HP ^{3}He and DCE-^{1}H MRI is an important development.

LIST OF PUBLICATIONS

Journal papers

1. Spatial fuzzy c-means thresholding for semiautomated calculation of percentage lung ventilated volume from hyperpolarised gas and ^{1}H MRI
   Paul J. C. Hughes, Felix Horn, Guilhem Collier, Alberto Biancardi, Helen Marshall and Jim Wild
   Journal Of Magnetic Resonance Imaging, 2017, DOI: 10.1002/jmri.25804; Epub ahead of print
2. Pulmonary MR angiography and Perfusion imaging – A review of methods and applications, Christopher S Johns, Andrew J Swift, **Paul J.C. Hughes**, Mark Schiebler and Jim M. Wild
   European Journal of Radiology, 2017, 86, 361-370
3. Lung Perfusion: MRI vs SPECT for screening in suspected Chronic Thromboembolic Pulmonary Hypertension, Christopher Johns, Andy Swift, Smitha Rajaram, **Paul J. C. Hughes**, Dave Capener, David Kiely and Jim Wild
   Journal Of Magnetic Resonance Imaging, 2017, DOI: 10.1002/jmri.25714; Epub ahead of print
4. Detection of early sub-clinical lung disease in children with cystic fibrosis by lung ventilation imaging with hyperpolarised gas MRI, Helen Marshall/Alex Horsley, Chris J Taylor, Laurie Smith, David Hughes, Felix C Horn, Andrew J Swift, Juan Parra-Robles, **Paul J.C. Hughes**, Graham Norquay, Neil J Stewart, Guilhem J Collier, Dawn Teare, Steve Cunningham, Ina Aldag and Jim M Wild
   Thorax, 2017, 72(8), 760-762

Abstracts

1. Ventilation-Perfusion Analysis with Co-Registered Hyperpolarized Gas and CE ^{1}H Perfusion MRI
   Paul J.C. Hughes, Bilal Tahir, Felix Horn, Helen Marshall, Rob Ireland and Jim Wild
   International Society of Magnetic Resonance in Medicine 23rd annual meeting, Toronto, 2015 – **Presented as traditional poster**
2. Spatial Fuzzy C-Means Thresholding for Semi-Automated Calculation of Percentage Lung Ventilated Volume from Hyperpolarised Gas and ^{1}H MRI **Paul J.C. Hughes**, Helen Marshall, Felix Horn, Guilhem Collier and Jim Wild
   International Society of Magnetic Resonance in Medicine 24th annual meeting, Singapore, 2016 – **Presented as traditional poster**
3. Assessment of Lung Inflation State on the Repeatability of Hyperpolarized Gas Ventilation MRI
   Paul J.C. Hughes, Laurie Smith, Felix Horn, Alberto Biancardi, Neil Stewart, Graham Norquay, Guilhem Collier and Jim Wild
   International Society of Magnetic Resonance in Medicine 25th annual meeting, Honolulu, 2017– **Presented as traditional poster**
4. Quantitative Ventilation-Perfusion Imaging Using Co-Registered Hyperpolarized Gas and Contrast Enhanced ^{1}H Perfusion MRI
   Paul J.C. Hughes, Bilal Tahir, Felix Horn, Alberto Biancardi, Rob Ireland, Helen Marshall and Jim Wild
   International Society of Magnetic Resonance in Medicine 25th annual meeting, Honolulu, 2017– **Oral presentation**
5. Ventilation heterogeneity assessed in patients with mild cystic fibrosis and asthma using Hyperpolarised gas MRI histogram analysis
   Paul J.C. Hughes, Laurie Smith, Felix Horn, Alberto Biancardi, Neil Stewart, Graham Norquay, Madhwesha Rao, Chris Taylor, Helen Marshall. Guilhem Collier and Jim Wild
   European Respiratory Society (ERS) International Congress, Milan, Sept 2017 – **Oral presentation**
6. Myocardial T_1 mapping MRI in patients with Pulmonary Hypertension and age-matched healthy volunteers
   Laura Hutchison, Neil Stewart, **Paul J. C. Hughes**, Charlotte Hammerton, Martin Graves, David Kiely, Jim Wild and Andrew Swift

European Respiratory Society (ERS) International Congress, Amsterdam, 2015

7. CT-based surrogates of pulmonary ventilation in lung cancer: A voxel-level comparison with HP gas MRI

   Bilal Tahir, **Paul J. C. Hughes**, Helen Marshall, Kerry Hart, James Swinscoe, Matthew Hatton, Jim Wild and Rob Ireland

   World Conference on Lung Cancer (WCLC), Vienna, 2016 [Submitted]

8. Ventilation CT: Voxel-level comparison with HP gas MRI

   Bilal Tahir, Helen Marshall, **Paul J. C. Hughes**, Neil Stewart, Felix Horn, Guilhem Collier, Graham Norquay, Kerry Hart, James Swinscoe, Matthew Hatton, Jim Wild and Rob Ireland

   European Respiratory Society (ERS) International Congress, London, 2016

9. Ventilation CT: Voxel-level comparison with hyperpolarized Helium-3 & Xenon-129 MRI

   Bilal Tahir, Helen Marshall, **Paul J. C. Hughes**, Neil Stewart, Felix Horn, Guilhem Collier, Graham Norquay, Kerry Hart, James Swinscoe, Matthew Hatton, Jim Wild and Rob Ireland

   American Association of Physicists in Medicine (AAPM), Washington DC, 2016

10. Comparison of ^{3}He and ^{129}Xe MRI for Evaluation of Lung Microstructure and Ventilation at 1.5 T.

    Neil J Stewart, Ho-Fung Chan, **Paul J. C. Hughes**, Guilhem J Collier, Felix C Horn, Graham Norquay, Juan Parra-Robles, Denise Yates, Paul Collini, Rod Lawson, Helen Marshall, Jim M Wild

    European Respiratory Society (ERS) International Congress, London, 2016

11. Comparison of phase III slope analysis from multiple breath washout with Hyperpolarised gas MRI in children with mild cystic fibrosis

    Laurie Smith, Felix Horn, Helen Marshall, Guilhem Collier' **Paul J. C. Hughes**, Ina Aldag, Chris Taylor, Alex Horsley, Jim Wild

    European Respiratory Society (ERS) International Congress, London, Sept 2016

12. Longitudinal changes in lung function in children with mild CF using hyperpolarised gas MRI and lung clearance index

    Laurie Smith, Ina Aldag, **Paul J. C. Hughes**, Felix Horn, Helen Marshall, Graham Norquay, Guilhem Collier, David Hughes, Chris Taylor, Alex Horsley and Jim Wild

    European Respiratory Society (ERS) International Congress, London, 2016

13. Hyperpolarised gas ventilation MRI detects Early ventilation heterogeneity in children with primary ciliary dyskinesia

Noreen West, Laurie Smith, David Hughes, Helen Marshall, Christopher Johns, Neil Stewart, Ho-Fung Chan, Madhwesha Rao, David Capener, Jody Bray, Guilhem Collier, **Paul J.C. Hughes**, Lynne Schofield, Felix Horn, Eduardo Moya, Phil Chetcuti and Jim Wild

European Respiratory Society (ERS) International Congress, Milan, 2017

14. Hyperpolarized Helium-3 MRI Insights Into Subtypes of Emphysema in Chronic Obstructive Pulmonary Disease (COPD)

    Sun Yanping, Christian Lo Cascio, Pallavi Balte, Jia Guo, Emilia Herman, Firas Ahmed, Belinda Dsouza, Robert Steiner, Jay Leb, Casandea Almonte, **Paul J. C. Hughes,** Stephen Dashnaw, Jim Wild, Martin Prince, Emlyn Hughes, Benjamin Smith, Eric Hoffman and Graham Barr

    International Society of Magnetic Resonance in Medicine 25th annual meeting, Honolulu, 2017

15. Longitudinal Monitoring of Disease Progression in Children with Mild Cystic Fibrosis Using Hyperpolarised Gas MRI and Lung Clearance Index

    Laurie Smith, **Paul J. C. Hughes**, Felix Horn, Helen Marshall, Graham Norquay, Guilhem Collier, David Hughes, Chris Taylor, Noreen West, Ina Aldag, Alex Horsley and Jim Wild

    International Society of Magnetic Resonance in Medicine 25th annual meeting, Honolulu, 2017

16. Rapid Acquisition of Co-Registered 3D Xenon-129 and Proton Images of the Human Lung in a Single Breath-Hold Using Compressed Sensing

    Guilhem Collier, **Paul J. C. Hughes**, Felix Horn, Ho-Fung Chan, Graham Norquay, Neil Stewart and Jim Wild

    International Society of Magnetic Resonance in Medicine 25th annual meeting, Honolulu, 2017

17. A Spatial Comparison of CT-Based Surrogates of Ventilation with Hyperpolarized Helium-3 & Xenon-129 MRI

    Bilal Tahir, **Paul J. C. Hughes**, Helen Marshall, Neil Stewart, Felix Horn, Guilhem Collier, Graham Norquay, Kerry Hart, James Swinscoe, Matthew Hatton, Jim Wild and Rob Ireland

    International Society of Magnetic Resonance in Medicine 25th annual meeting, Honolulu, 2017

REFERENCES

1. World Health Organization. *Chronic respiratory diseases, Burden of COPD.* [cited 2017; Available from: http://www.who.int/respiratory/copd/burden/en/.
2. Hubbard, R., *The burden of lung disease*. 2006, BMJ Publishing Group Ltd.
3. World Health Organization, *2008-2013 action plan for the global strategy for the prevention and control of noncommunicable diseases: prevent and control cardiovascular diseases, cancers, chronic respiratory diseases and diabetes.* 2009.
4. Ferkol, T. and D. Schraufnagel, *The global burden of respiratory disease.* Annals of the American Thoracic Society, 2014. **11**(3): p. 404-406.
5. Miller, M.R., et al., *Standardisation of spirometry.* European respiratory journal, 2005. **26**(2): p. 319-338.
6. Horsley, A., *Lung clearance index in the assessment of airways disease.* Respiratory medicine, 2009. **103**(6): p. 793-799.
7. Jensen, R., et al., *Multiple breath nitrogen washout: a feasible alternative to mass spectrometry.* PloS one, 2013. **8**(2): p. e56868.
8. Wagner, P.D., *The multiple inert gas elimination technique (MIGET).* Intensive care medicine, 2008. **34**(6): p. 994-1001.
9. Berthezene, Y., et al., *Prospective comparison of MR lung perfusion and lung scintigraphy.* Journal of Magnetic Resonance Imaging, 1999. **9**(1): p. 61-68.
10. Amundsen, T., et al., *Perfusion abnormalities in pulmonary embolism studied with perfusion MRI and ventilation-perfusion scintigraphy: An intra-modality and inter-modality agreement study.* Journal of Magnetic Resonance Imaging, 2002. **15**(4): p. 386-394.
11. Tiel-van Buul, M. and J. Verzijlbergen, *Ventilation–perfusion lung scintigraphy.* Imaging Decisions MRI, 2004. **8**(4): p. 3-14.
12. Tunariu, N., et al., *Ventilation–perfusion scintigraphy is more sensitive than multidetector CTPA in detecting chronic thromboembolic pulmonary disease as a treatable cause of pulmonary hypertension.* Journal of Nuclear Medicine, 2007. **48**(5): p. 680-684.
13. Parker, J., et al., *Society of Nuclear Medicine procedure guideline for lung scintigraphy. Version 3.0, approved February 7, 2004.* 2011.
14. Hofman, M.S., et al., *68Ga PET/CT ventilation–perfusion imaging for pulmonary embolism: a pilot study with comparison to conventional scintigraphy.* Journal of Nuclear Medicine, 2011. **52**(10): p. 1513-1519.
15. Park, W.J. and D.F. Worsley, *Ventilation/Perfusion Lung Scintigraphy.* Nuclear Medicine and PET/CT Cases, 2015: p. 61.
16. Simon, B.A., *Regional ventilation and lung mechanics using X-Ray CT.* Academic radiology, 2005. **12**(11): p. 1414-1422.
17. Guerrero, T., et al., *Quantification of regional ventilation from treatment planning CT.* International Journal of Radiation Oncology* Biology* Physics, 2005. **62**(3): p. 630-634.
18. Guerrero, T., et al., *Dynamic ventilation imaging from four-dimensional computed tomography.* Physics in medicine and biology, 2006. **51**(4): p. 777.
19. Fuld, M.K., et al., *CT-measured regional specific volume change reflects regional ventilation in supine sheep.* Journal of applied physiology, 2008. **104**(4): p. 1177-1184.
20. Reinhardt, J.M., et al., *Registration-based estimates of local lung tissue expansion compared to xenon CT measures of specific ventilation.* Medical image analysis, 2008. **12**(6): p. 752-763.
21. Chae, E.J., et al., *Xenon ventilation CT with a dual-energy technique of dual-source CT: initial experience.* Radiology, 2008. **248**(2): p. 615-624.

22. Castillo, R., et al., *Ventilation from four-dimensional computed tomography: density versus Jacobian methods.* Physics in medicine and biology, 2010. **55**(16): p. 4661.
23. Ding, K., et al., *Comparison of image registration based measures of regional lung ventilation from dynamic spiral CT with Xe-CT.* Medical physics, 2012. **39**(8): p. 5084-5098.
24. Kong, X., et al., *Xenon-enhanced dual-energy CT lung ventilation imaging: techniques and clinical applications.* American Journal of Roentgenology, 2014. **202**(2): p. 309-317.
25. Ohana, M., et al., *Thoracic dual energy CT: acquisition protocols, current applications and future developments.* Diagnostic and interventional imaging, 2014. **95**(11): p. 1017-1026.
26. Seeram, E., *Computed Tomography-E-Book: Physical Principles, Clinical Applications, and Quality Control*. 2015: Elsevier Health Sciences.
27. Roach, P.J., et al. *Spect/ct in v/q scanning*. in *Seminars in nuclear medicine*. 2010. Elsevier.
28. Bajc, M. and B. Jonson, *Ventilation/perfusion SPECT for diagnosis of pulmonary embolism and other diseases.* International journal of molecular imaging, 2010. **2011**.
29. Roach, P.J., G.P. Schembri, and D.L. Bailey, *V/q scanning using spect and spect/ct.* Journal of Nuclear Medicine, 2013. **54**(9): p. 1588-1596.
30. Norberg, P., *Quantification and optimisation of lung ventilation SPECT images*. 2014, Linköping University Electronic Press.
31. Bowen, S., et al., *Impact of Functional Lung Imaging Using Ventilation/Perfusion SPECT/CT on Planning Objectives in Thoracic Radiation Therapy.* International Journal of Radiation Oncology• Biology• Physics, 2014. **90**(1): p. S659.
32. Mazurek, A., et al., *The utility of hybrid SPECT/CT lung perfusion scintigraphy in pulmonary embolism diagnosis.* Respiration, 2015. **90**(5): p. 393-401.
33. Marshall, H., et al., *Detection of early subclinical lung disease in children with cystic fibrosis by lung ventilation imaging with hyperpolarised gas MRI.* Thorax, 2017: p. thoraxjnl-2016-208948.
34. Wild, J.M., et al., *Simultaneous imaging of lung structure and function with triple-nuclear hybrid MR imaging.* Radiology, 2013. **267**(1): p. 251-255.
35. Tofts, P., *Quantitative MRI of the brain: measuring changes caused by disease*. 2005: John Wiley & Sons.
36. Semelka, R.C., *Abdominal-pelvic MRI*. 2016: John Wiley & Sons.
37. Hatabu, H., et al., *Pulmonary perfusion: Qualitative assessment with dynamic contrast-enhanced MRI using ultra-short TE and inversion recovery turbo FLASH.* Magnetic resonance in medicine, 1996. **36**(4): p. 503-508.
38. Kauczor, H.-U., *MRI of the Lung.* 2009.
39. Hornak, J.P., *The basics of MRI.[Online book] Rochester Institute of Technology.* 2010.
40. Brown, M.A. and R.C. Semelka, *MRI: basic principles and applications*. 2011: John Wiley & Sons.
41. Wild, J., et al., *MRI of the lung (1/3): methods.* Insights into imaging, 2012. **3**(4): p. 345-353.
42. Currie, S., et al., *Understanding MRI: basic MR physics for physicians.* Postgraduate medical journal, 2013. **89**(1050): p. 209-223.
43. Ohno, Y., et al., *Dynamic oxygen-enhanced MRI versus quantitative CT: pulmonary functional loss assessment and clinical stage classification of smoking-related COPD.* American Journal of Roentgenology, 2008. **190**(2): p. W93-W99.
44. Sá, R.C., et al., *Vertical distribution of specific ventilation in normal supine humans measured by oxygen-enhanced proton MRI.* Journal of Applied Physiology, 2010. **109**(6): p. 1950-1959.

45. Zhang, W.-J., et al., *Dynamic oxygen-enhanced magnetic resonance imaging of the lung in asthma—Initial experience.* European journal of radiology, 2015. **84**(2): p. 318-326.
46. Ohno, Y., et al., *Quantitative assessment of regional pulmonary perfusion in the entire lung using three-dimensional ultrafast dynamic contrast-enhanced magnetic resonance imaging: Preliminary experience in 40 subjects.* Journal of Magnetic Resonance Imaging, 2004. **20**(3): p. 353-365.
47. Parker, G.J. and D.L. Buckley, *Tracer kinetic modelling for T1-weighted DCE-MRI*, in *Dynamic contrast-enhanced magnetic resonance imaging in oncology*. 2005, Springer. p. 81-92.
48. Cheng, H.L.M., *T1 measurement of flowing blood and arterial input function determination for quantitative 3D T1-weighted DCE-MRI.* Journal of Magnetic Resonance Imaging, 2007. **25**(5): p. 1073-1078.
49. Fan, L., et al., *Assessment of pulmonary parenchyma perfusion with FAIR in comparison with DCE-MRI—Initial results.* European journal of radiology, 2009. **70**(1): p. 41-48.
50. Henzler, T., et al., *Diffusion and perfusion MRI of the lung and mediastinum.* European journal of radiology, 2010. **76**(3): p. 329-336.
51. Ng, C.S., et al., *Reproducibility of perfusion parameters in dynamic contrast-enhanced MRI of lung and liver tumors: effect on estimates of patient sample size in clinical trials and on individual patient responses.* American Journal of Roentgenology, 2010. **194**(2): p. W134-W140.
52. Henderson, A.C., et al., *The gravitational distribution of ventilation-perfusion ratio is more uniform in prone than supine posture in the normal human lung.* Journal of Applied Physiology, 2013. **115**(3): p. 313-324.
53. Kohlmann, P., et al., *Automatic lung segmentation method for MRI-based lung perfusion studies of patients with chronic obstructive pulmonary disease.* International journal of computer assisted radiology and surgery, 2014. **10**(4): p. 403-417.
54. Zöllner, F.G., et al., *Semi-automatic lung segmentation of DCE-MRI data sets of 2-year old children after congenital diaphragmatic hernia repair: Initial results.* Magnetic resonance imaging, 2015. **33**(10): p. 1345-1349.
55. Sá, R.C., et al., *Measurement of the distribution of ventilation-perfusion ratios in the human lung with proton MRI: comparison with the multiple inert-gas elimination technique.* Journal of Applied Physiology, 2017. **123**(1): p. 136-146.
56. Lipson, D.A., et al., *Pulmonary ventilation and perfusion scanning using hyperpolarized helium-3 MRI and arterial spin tagging in healthy normal subjects and in pulmonary embolism and orthotopic lung transplant patients.* Magnetic resonance in medicine, 2002. **47**(6): p. 1073-1076.
57. Rizi, R.R., et al., *Determination of regional VA/Q by hyperpolarized 3He MRI.* Magnetic resonance in medicine, 2004. **52**(1): p. 65-72.
58. Kirby, M., et al., *Chronic obstructive pulmonary disease: longitudinal hyperpolarized 3He MR imaging.* Radiology, 2010. **256**(1): p. 280-289.
59. Kirby, M., et al., *Quantitative evaluation of hyperpolarized helium-3 magnetic resonance imaging of lung function variability in cystic fibrosis.* Academic radiology, 2011. **18**(8): p. 1006-1013.
60. Kirby, M., et al., *Hyperpolarized 3He and 129Xe MR imaging in healthy volunteers and patients with chronic obstructive pulmonary disease.* Radiology, 2012. **265**(2): p. 600-610.
61. Heydarian, M., et al. *Two and three-dimensional segmentation of hyperpolarized 3 He magnetic resonance imaging of pulmonary gas distribution*. in *SPIE Medical Imaging*. 2012. International Society for Optics and Photonics.

62. Kirby, M., et al., *Hyperpolarized 3He Magnetic Resonance Functional Imaging Semiautomated Segmentation.* Academic radiology, 2012. **19**(2): p. 141-152.
63. Svenningsen, S., et al., *Hyperpolarized 3He and 129Xe MRI: differences in asthma before bronchodilation.* Journal of Magnetic Resonance Imaging, 2013. **38**(6): p. 1521-1530.
64. Marshall, H., et al., *3He pO2 mapping is limited by delayed-ventilation and diffusion in chronic obstructive pulmonary disease.* Magnetic Resonance in Medicine, 2014. **71**(3): p. 1172-1178.
65. Sheikh, K., et al., *Pulmonary ventilation defects in older never-smokers.* Journal of applied physiology, 2014: p. jap. 00046.2014.
66. Horn, F., et al. *Lung ventilation volumetry with same-breath acquisition of hyperpolarized gas and proton MRI.* NMR in Biomedicine, 2014. DOI: doi: 10.1002/nbm.3187. Epub 2014 Sep 10.
67. Horn, F.C., et al., *Quantification of regional fractional ventilation in human subjects by measurement of hyperpolarized 3 He washout with 2D and 3D MRI.* Journal of applied physiology, 2014. **116**(2): p. 129-139.
68. Marshall, H., et al., *Magnetic Resonance Imaging of Ventilation and Perfusion Changes in Response to Pulmonary Endarterectomy in Chronic Thromboembolic Pulmonary Hypertension.* American journal of respiratory and critical care medicine, 2014. **190**(5): p. e18-e19.
69. Horn, F., et al., *Comparison of ventilation heterogeneity (VH) measured with multiple breath washout (MBW) imaging to whole lung MBW LCI and FEV1 in asthma and cystic fibrosis (CF).* 2015, Eur Respiratory Soc.
70. Horn, F.C., et al., *Multiple breath washout of hyperpolarized 129Xe and 3He in human lungs with three-dimensional balanced steady-state free-precession imaging.* Magnetic resonance in medicine, 2016.
71. Horn, F.C., et al., *Regional Ventilation Changes in the Lung: Treatment Response Mapping by Using Hyperpolarized Gas MR Imaging as a Quantitative Biomarker.* Radiology, 2017: p. 160532.
72. Wild, J.M., et al., *Steady-state free precession with hyperpolarized 3He: Experiments and theory.* Journal of Magnetic Resonance, 2006. **183**(1): p. 13-24.
73. Wild, J.M., et al., *Synchronous acquisition of hyperpolarised 3He and 1H MR images of the lungs–maximising mutual anatomical and functional information.* NMR in Biomedicine, 2011. **24**(2): p. 130-134.
74. Deppe, M.H. and J.M. Wild, *Variable flip angle schedules in bSSFP imaging of hyperpolarized noble gases.* Magnetic resonance in medicine, 2012. **67**(6): p. 1656-1664.
75. Deppe, M.H., et al., *A flexible 32-channel receive array combined with a homogeneous transmit coil for human lung imaging with hyperpolarized 3He at 1.5 T.* Magnetic resonance in medicine, 2011. **66**(6): p. 1788-1797.
76. Norquay, G., et al., *Optimized production of hyperpolarized 129Xe at 2 bars for in vivo lung magnetic resonance imaging.* Journal of Applied Physics, 2013. **113**(4): p. 044908.
77. Woodhouse, N., et al., *Combined helium-3/proton magnetic resonance imaging measurement of ventilated lung volumes in smokers compared to never-smokers.* Journal of magnetic resonance imaging, 2005. **21**(4): p. 365-369.
78. Zha, W., et al., *Semiautomated ventilation defect quantification in exercise-induced bronchoconstriction using hyperpolarized helium-3 magnetic resonance imaging: a repeatability study.* Academic radiology, 2016. **23**(9): p. 1104-1114.
79. Sun, Y., et al., *Using hyperpolarized 3He MRI to evaluate treatment efficacy in cystic fibrosis patients.* Journal of Magnetic Resonance Imaging, 2011. **34**(5): p. 1206-1211.

80. Kaushik, S.S., et al., *Probing the regional distribution of pulmonary gas exchange through single-breath gas-and dissolved-phase 129Xe MR imaging.* Journal of Applied Physiology, 2013. **115**(6): p. 850-860.
81. Petersson, J. and R.W. Glenny, *Gas exchange and ventilation-perfusion relationships in the lung.* Eur Respir J, 2014. **44**(4): p. 1023-41.
82. Thompson, H.K., et al., *Indicator transit time considered as a gamma variate.* Circ Res, 1964. **14**(6): p. 502-515.
83. Østergaard, L., et al., *High resolution measurement of cerebral blood flow using intravascular tracer bolus passages. Part I: Mathematical approach and statistical analysis.* Magnetic resonance in medicine, 1996. **36**(5): p. 715-725.
84. Avants, B.B., N. Tustison, and G. Song, *Advanced normalization tools (ANTS).* Insight J, 2009.
85. Drake, R., A.W. Vogl, and A.W.M. Mitchell, *Gray's anatomy for students*. 2009: Elsevier Health Sciences.
86. Porter, R.S., J.L. Kaplan, and B.P. Homeier, *The Merck manual home health handbook*. 2009: Merck & Company.
87. Pump, K., *The bronchial arteries and their anastomoses in the human lung.* CHEST Journal, 1963. **43**(3): p. 245-255.
88. Bruzzi, J.F., et al., *Multi–detector row CT of hemoptysis.* Radiographics, 2006. **26**(1): p. 3-22.
89. West, J.B., *Respiratory physiology: the essentials*. 2012: Lippincott Williams & Wilkins.
90. Cotes, J.E., D.J. Chinn, and M.R. Miller, *Lung function: physiology, measurement and application in medicine*. 2009: John Wiley & Sons.
91. van Beek, E.J., et al., *Functional MRI of the lung using hyperpolarized 3-helium gas.* Journal of Magnetic Resonance Imaging, 2004. **20**(4): p. 540-554.
92. Riley, R. and A. Cournand, *'Ideal'alveolar air and the analysis of ventilation-perfusion relationships in the lungs.* Journal of Applied Physiology, 1949. **1**(12): p. 825-847.
93. Rahn, H. and W.O. Fenn, *A Graphical Analysis of the Respiratory Gas Exchange: The Ob2-COb2 Diagram*. 1955: American Physiological Society.
94. Anderson, T.W., *Asymptotic theory for principal component analysis.* Annals of Mathematical Statistics, 1963: p. 122-148.
95. Marshall, H., et al., *Mutli-Nuclear Mr Imaging Of Vq Distribution Response To Bronchodilator In Asthma.* 2014.
96. Hartmann, E.K., et al., *Ventilation/perfusion ratios measured by multiple inert gas elimination during experimental cardiopulmonary resuscitation.* Acta Anaesthesiologica Scandinavica, 2014. **58**(8): p. 1032-1039.
97. Melo, M.F.V., et al., *Quantification of regional ventilation-perfusion ratios with PET.* Journal of Nuclear Medicine, 2003. **44**(12): p. 1982-1991.
98. Samuel, J. and C. Franklin, *Hypoxemia and hypoxia*, in *Common Surgical Diseases*. 2008, Springer. p. 391-394.
99. Saetta, M. and G. Turato, *Airway pathology in asthma.* European Respiratory Journal, 2001. **18**(34 suppl): p. 18s-23s.
100. Buist, A., *Similarities and differences between asthma and chronic obstructive pulmonary disease: treatment and early outcomes.* European Respiratory Journal, 2003. **21**(39 suppl): p. 30s-35s.
101. Barnes, P.J., et al., *Asthma and COPD: basic mechanisms and clinical management.* 2009: Elsevier.
102. Hamid, Q., *Pathogenesis of small airways in asthma.* Respiration, 2012. **84**(1): p. 4-11.
103. Szilasi, M., et al., *Pathology of chronic obstructive pulmonary disease.* Pathology & Oncology Research, 2006. **12**(1): p. 52-60.

104. Andersen, D.H., *Pathology of cystic fibrosis.* Annals of the New York Academy of Sciences, 1962. **93**(12): p. 500-517.
105. Koch, C. and N. Hoiby, *Pathogenesis of cystic fibrosis.* The Lancet, 1993. **341**(8852): p. 1065-1069.
106. Gibson, R.L., J.L. Burns, and B.W. Ramsey, *Pathophysiology and management of pulmonary infections in cystic fibrosis.* American journal of respiratory and critical care medicine, 2003. **168**(8): p. 918-951.
107. Grossman, S. and L.C. Grossman, *Pathophysiology of cystic fibrosis implications for critical care nurses.* Critical care nurse, 2005. **25**(4): p. 46-51.
108. Hodson, M., A. Bush, and D. Geddes, *Cystic Fibrosis, Third Edition*. 2007: Taylor & Francis.
109. Cohen, T.S. and A. Prince, *Cystic fibrosis: a mucosal immunodeficiency syndrome.* Nature medicine, 2012. **18**(4): p. 509-519.
110. Travis, W.D., *Pathology of lung cancer.* Clinics in chest medicine, 2002. **23**(1): p. 65-81.
111. Ettinger, D.S., et al., *Non–small cell lung cancer.* Journal of the national comprehensive cancer network, 2010. **8**(7): p. 740-801.
112. Wanger, J., et al., *Standardisation of the measurement of lung volumes.* European Respiratory Journal, 2005. **26**(3): p. 511-522.
113. Ranu, H., M. Wilde, and B. Madden, *Pulmonary function tests.* The Ulster medical journal, 2011. **80**(2): p. 84.
114. Gustafsson, P., P. Aurora, and A. Lindblad, *Evaluation of ventilation maldistribution as an early indicator of lung disease in children with cystic fibrosis.* European Respiratory Journal, 2003. **22**(6): p. 972-979.
115. Aurora, P., et al., *Multiple-breath washout as a marker of lung disease in preschool children with cystic fibrosis.* American journal of respiratory and critical care medicine, 2005. **171**(3): p. 249-256.
116. Berry, G., *Longitudinal observations. Their usefulness and limitations with special reference to the forced expiratory volume.* Bull Physiopathol Respir (Nancy), 1974. **10**(5): p. 643-656.
117. Hnizdo, E., et al., *Limits of longitudinal decline for the interpretation of annual changes in FEV 1 in individuals.* Occupational and environmental medicine, 2007. **64**(10): p. 701-707.
118. Criée, C., et al., *Body plethysmography–its principles and clinical use.* Respiratory medicine, 2011. **105**(7): p. 959-971.
119. Meneely, G.R. and N.L. Kaltreider, *The volume of the lung determined by helium dilution. Description of the method and comparison with other procedures.* Journal of Clinical Investigation, 1949. **28**(1): p. 129.
120. Horsley, A.R., et al., *Lung clearance index is a sensitive, repeatable and practical measure of airways disease in adults with cystic fibrosis.* Thorax, 2008. **63**(2): p. 135-140.
121. Verbanck, S., et al., *Relationships between the lung clearance index and conductive and acinar ventilation heterogeneity.* Journal of applied physiology, 2012. **112**(5): p. 782-790.
122. Subbarao, P., et al., *Multiple-breath washout as a lung function test in cystic fibrosis. A cystic fibrosis foundation workshop report.* Annals of the American Thoracic Society, 2015. **12**(6): p. 932-939.
123. Verbanck, S., et al., *Ventilation heterogeneity in the acinar and conductive zones of the normal ageing lung.* Thorax, 2012: p. thoraxjnl-2011-201484.
124. Stuart-Andrews, C.R., et al., *Automated detection of the phase III slope during inert gas washout testing.* Journal of applied physiology, 2012. **112**(6): p. 1073-1081.

125. Society, A.T., *Single-breath carbon monoxide diffusing capacity (transfer factor). Recommendations for a standard technique-1995 update.* Am J Respir Crit Care Med, 1995. **152**: p. 2185-2198.

126. Macintyre, N., et al., *Standardisation of the single-breath determination of carbon monoxide uptake in the lung.* European Respiratory Journal, 2005. **26**(4): p. 720-735.

127. Breit, G. and I. Rabi, *Measurement of nuclear spin.* Physical Review, 1931. **38**(11): p. 2082.

128. Rabi, I. and V. Cohen, *Measurement of Nuclear Spin by the Method of Molecular Beams The Nuclear Spin of Sodium.* Physical Review, 1934. **46**(8): p. 707.

129. Purcell, E.M., H. Torrey, and R.V. Pound, *Resonance absorption by nuclear magnetic moments in a solid.* Physical review, 1946. **69**(1-2): p. 37.

130. Bloch, F., *The principle of nuclear induction*. 1953: Kungl. boktryckeriet PA Norstedt & söner.

131. Hahn, E.L., *Spin echoes.* Physical review, 1950. **80**(4): p. 580.

132. Ernst, R. and W. Anderson, *Application of Fourier transform spectroscopy to magnetic resonance.* Review of Scientific Instruments, 1966. **37**(1): p. 93-102.

133. Lauterbur, P.C., *Image formation by induced local interactions: examples employing nuclear magnetic resonance.* Nature, 1973. **242**(5394): p. 190-191.

134. Mansfield, P. and P.K. Grannell, *NMR'diffraction'in solids?* Journal of Physics C: solid state physics, 1973. **6**(22): p. L422.

135. Krane, K.S. and D. Halliday, *Introductory nuclear physics*. Vol. 465. 1988: Wiley New York.

136. Levitt, M.H., *Spin dynamics: basics of nuclear magnetic resonance*. 2001: John Wiley & Sons.

137. Harris, R.K. and B.E. Mann, *NMR and the Periodic Table*. Vol. 342. 1978: Academic Press London.

138. Kauczor, H.U., R. Surkau, and T. Roberts, *MRI using hyperpolarized noble gases.* European radiology, 1998. **8**(5): p. 820-827.

139. Haacke, E.M., et al., *Magnetic resonance imaging: physical principles and sequence design*. Vol. 82. 1999: Wiley-Liss New York:.

140. Möller, H.E., et al., *MRI of the lungs using hyperpolarized noble gases.* Magnetic Resonance in Medicine, 2002. **47**(6): p. 1029-1051.

141. Meier, S., et al., *Hyperpolarized NMR Probes for Biological Assays.* Sensors, 2014. **14**(1): p. 1576-1597.

142. Hatabu, H., et al., *T2* and proton density measurement of normal human lung parenchyma using submillisecond echo time gradient echo magnetic resonance imaging.* European journal of radiology, 1999. **29**(3): p. 245-252.

143. Stock, K.W., et al., *Magnetic resonance T 2* measurements of the normal human lung in vivo with ultra-short echo times.* Magnetic resonance imaging, 1999. **17**(7): p. 997-1000.

144. Naish, J.H., et al., *Modeling of contrast agent kinetics in the lung using T1-weighted dynamic contrast-enhanced MRI.* Magnetic Resonance in Medicine, 2009. **61**(6): p. 1507-1514.

145. Deoni, S.C., B.K. Rutt, and T.M. Peters, *Rapid combined T1 and T2 mapping using gradient recalled acquisition in the steady state.* Magnetic Resonance in Medicine, 2003. **49**(3): p. 515-526.

146. Scheffler, K. and S. Lehnhardt, *Principles and applications of balanced SSFP techniques.* European radiology, 2003. **13**(11): p. 2409-2418.

147. Madani, A., C. Keyzer, and P.-A. Gevenois, *Quantitative computed tomography assessment of lung structure and function in pulmonary emphysema.* European Respiratory Journal, 2001. **18**(4): p. 720-730.

148. Gierada, D.S., et al., *Repeatability of quantitative CT indexes of emphysema in patients evaluated for lung volume reduction surgery.* Radiology, 2001. **220**(2): p. 448-454.
149. Orlandi, I., et al., *Spirometric-gated computed tomography quantitative evaluation of lung emphysema in chronic obstructive pulmonary disease: a comparison of 3 techniques.* Journal of computer assisted tomography, 2004. **28**(4): p. 437-442.
150. Oda, K., et al., *High-resolution CT scoring system-based grading scale predicts the clinical outcomes in patients with idiopathic pulmonary fibrosis.* Respiratory research, 2014. **15**(1): p. 10.
151. de Jong, P.A. and H.A. Tiddens, *Cystic fibrosis–specific computed tomography scoring.* Proceedings of the American Thoracic Society, 2007. **4**(4): p. 338-342.
152. Ruparel, M., et al., *Pulmonary nodules and CT screening: the past, present and future.* Thorax, 2016. **71**(4): p. 367-375.
153. Hsia, C.C., et al., *An official research policy statement of the American Thoracic Society/European Respiratory Society: standards for quantitative assessment of lung structure.* American journal of respiratory and critical care medicine, 2010. **181**(4): p. 394-418.
154. Park, K.J., C.J. Bergin, and J.L. Clausen, *Quantitation of emphysema with three-dimensional CT densitometry: comparison with two-dimensional analysis, visual emphysema scores, and pulmonary function test results.* Radiology, 1999. **211**(2): p. 541-547.
155. Sverzellati, N., et al., *Increased mean lung density: another independent predictor of lung cancer?* European journal of radiology, 2013. **82**(8): p. 1325-1331.
156. Gruden, J.F., *CT in idiopathic pulmonary fibrosis: diagnosis and beyond.* American Journal of Roentgenology, 2016. **206**(3): p. 495-507.
157. Puderbach, M., et al., *Proton MRI appearance of cystic fibrosis: comparison to CT.* European radiology, 2007. **17**(3): p. 716-724.
158. Sundar, K.M. and D.L. Harris, *Initial presentation of idiopathic pulmonary fibrosis as an acute exacerbation.* Respiratory Medicine CME, 2008. **1**(1): p. 43-47.
159. van Beek, E.J. and E.A. Hoffman, *Functional imaging: CT and MRI.* Clinics in chest medicine, 2008. **29**(1): p. 195-216.
160. Zhang, L.J., et al., *Dual-energy CT lung ventilation/perfusion imaging for diagnosing pulmonary embolism.* European radiology, 2013. **23**(10): p. 2666-2675.
161. Mathew, L., et al., *Hyperpolarized 3 He magnetic resonance imaging: comparison with four-dimensional x-ray computed tomography imaging in lung cancer.* Academic radiology, 2012. **19**(12): p. 1546-1553.
162. Bajc, M., et al. *Methodology for ventilation/perfusion SPECT.* in *Seminars in nuclear medicine*. 2010. Elsevier.
163. Thieme, S.F., et al., *Dual-energy CT for the assessment of contrast material distribution in the pulmonary parenchyma.* American Journal of Roentgenology, 2009. **193**(1): p. 144-149.
164. Lu, G.M., et al., *Dual-energy CT of the lung.* American Journal of Roentgenology, 2012. **199**(5_supplement): p. S40-S53.
165. Koike, H., et al., *Quantification of lung perfusion blood volume (lung PBV) by dual-energy CT in patients with chronic thromboembolic pulmonary hypertension (CTEPH) before and after balloon pulmonary angioplasty (BPA): preliminary results.* European journal of radiology, 2016. **85**(9): p. 1607-1612.
166. Tamura, M., et al., *Diagnostic accuracy of lung subtraction iodine mapping CT for the evaluation of pulmonary perfusion in patients with chronic thromboembolic pulmonary hypertension: Correlation with perfusion SPECT/CT.* International Journal of Cardiology, 2017.

167. Imelińska, C., M.S. Downes, and W. Yuan, *Semi-automated color segmentation of anatomical tissue.* Computerized Medical Imaging and Graphics, 2000. **24**(3): p. 173-180.

168. Hatabu, H., et al., *Fast magnetic resonance imaging of the lung.* European journal of radiology, 1999. **29**(2): p. 114-132.

169. Hatabu, H., et al. *Approaches to MR imaging of lung parenchyma utilizing ultrashort TE gradient echo and fast SE sequences*. in *Proceedings, Society of Magnetic Resonance, Second Meeting, San Francisco, CA (August 6–12, 1994)*. 1994.

170. Hennig, J., A. Nauerth, and H. Friedburg, *RARE imaging: a fast imaging method for clinical MR.* Magnetic resonance in medicine, 1986. **3**(6): p. 823-833.

171. Hatabu, H., et al., *MR imaging of pulmonary parenchyma with a half-Fourier single-shot turbo spin-echo (HASTE) sequence.* European journal of radiology, 1999. **29**(2): p. 152-159.

172. Bergin, C., J. Pauly, and A. Macovski, *Lung parenchyma: projection reconstruction MR imaging.* Radiology, 1991. **179**(3): p. 777-781.

173. Johnson, K.M., et al., *Optimized 3D ultrashort echo time pulmonary MRI.* Magnetic resonance in medicine, 2013. **70**(5): p. 1241-1250.

174. Failo, R., et al., *Lung morphology assessment using MRI: A robust ultra-short TR/TE 2D steady state free precession sequence used in cystic fibrosis patients.* Magnetic Resonance in Medicine, 2009. **61**(2): p. 299-306.

175. Ley-Zaporozhan, J., et al., *Visualization of morphological parenchymal changes in emphysema: comparison of different MRI sequences to 3D-HRCT.* European journal of radiology, 2010. **73**(1): p. 43-49.

176. Rajaram, S., et al., *Lung morphology assessment with balanced steady-state free precession MR imaging compared with CT.* Radiology, 2012. **263**(2): p. 569-577.

177. Hochhegger, B., et al., *MRI in lung cancer: a pictorial essay.* 2014.

178. Dournes, G., et al., *Lung morphology assessment of cystic fibrosis using MRI with ultra-short echo time at submillimeter spatial resolution.* European radiology, 2016. **26**(11): p. 3811-3820.

179. Bauman, G., et al., *Non-contrast-enhanced perfusion and ventilation assessment of the human lung by means of fourier decomposition in proton MRI.* Magnetic Resonance in Medicine, 2009. **62**(3): p. 656-664.

180. Bauman, G., et al., *Pulmonary functional imaging: qualitative comparison of Fourier decomposition MR imaging with SPECT/CT in porcine lung.* Radiology, 2011. **260**(2): p. 551-559.

181. Bauman, G., et al., *Validation of Fourier decomposition MRI with dynamic contrast-enhanced MRI using visual and automated scoring of pulmonary perfusion in young cystic fibrosis patients.* European journal of radiology, 2013. **82**(12): p. 2371-2377.

182. Lederlin, M., et al., *Functional MRI using Fourier decomposition of lung signal: reproducibility of ventilation-and perfusion-weighted imaging in healthy volunteers.* European journal of radiology, 2013. **82**(6): p. 1015-1022.

183. Kjørstad, Å., et al., *Quantitative lung perfusion evaluation using Fourier decomposition perfusion MRI.* Magnetic resonance in medicine, 2014. **72**(2): p. 558-562.

184. Kjørstad, Å., et al., *Quantitative lung ventilation using Fourier decomposition MRI; comparison and initial study.* Magnetic Resonance Materials in Physics, Biology and Medicine, 2014. **27**(6): p. 467-476.

185. Bauman, G., O. Pusterla, and O. Bieri, *Ultra-fast Steady-State Free Precession Pulse Sequence for Fourier Decomposition Pulmonary MRI.* Magnetic Resonance in Medicine, 2015.

186. Voskrebenzev, A., et al., *Low-pass imaging of dynamic acquisitions (LIDA) with a group-oriented registration (GOREG) for proton MR imaging of lung ventilation.* Magnetic resonance in medicine, 2017. **78**(4): p. 1496-1505.
187. Voskrebenzev, A., et al., *Feasibility of quantitative regional ventilation and perfusion mapping with phase-resolved functional lung (PREFUL) MRI in healthy volunteers and COPD, CTEPH, and CF patients.* Magnetic Resonance in Medicine, 2017.
188. Henderson, A.C., et al., *Characterizing pulmonary blood flow distribution measured using arterial spin labeling.* NMR in biomedicine, 2009. **22**(10): p. 1025-1035.
189. Hopkins, S.R. and G.K. Prisk, *Lung perfusion measured using magnetic resonance imaging: New tools for physiological insights into the pulmonary circulation.* Journal of Magnetic Resonance Imaging, 2010. **32**(6): p. 1287-1301.
190. Arai, T.J., et al., *Magnetic resonance imaging quantification of pulmonary perfusion using calibrated arterial spin labeling.* Journal of visualized experiments: JoVE, 2011(51).
191. Ley, S. and J. Ley-Zaporozhan, *Pulmonary perfusion imaging using MRI: clinical application.* Insights Imaging, 2012. **3**(1): p. 61-71.
192. Petcharunpaisan, S., J. Ramalho, and M. Castillo, *Arterial spin labeling in neuroimaging.* World journal of radiology, 2010. **2**(10): p. 384.
193. Riley, R. and A. Cournand, *Analysis of factors affecting partial pressures of oxygen and carbon dioxide in gas and blood of lungs: theory.* Journal of applied physiology, 1951. **4**(2): p. 77-101.
194. Jakob, P.M., et al., *Assessment of human pulmonary function using oxygen-enhanced T1 imaging in patients with cystic fibrosis.* Magnetic resonance in medicine, 2004. **51**(5): p. 1009-1016.
195. Naish, J.H., et al., *Improved quantitative dynamic regional oxygen-enhanced pulmonary imaging using image registration.* Magnetic resonance in medicine, 2005. **54**(2): p. 464-469.
196. Molinari, F., et al., *Oxygen-enhanced magnetic resonance imaging: influence of different gas delivery methods on the T1-changes of the lungs.* Investigative radiology, 2008. **43**(6): p. 427-432.
197. Morgan, A.R., et al., *Feasibility assessment of using oxygen-enhanced magnetic resonance imaging for evaluating the effect of pharmacological treatment in COPD.* European journal of radiology, 2014. **83**(11): p. 2093-2101.
198. Jobst, B.J., et al., *Functional lung MRI in chronic obstructive pulmonary disease: comparison of T1 mapping, oxygen-enhanced T1 mapping and dynamic contrast enhanced perfusion.* PloS one, 2015. **10**(3): p. e0121520.
199. Fink, C., et al., *Effect of inspiratory and expiratory breathhold on pulmonary perfusion: assessment by pulmonary perfusion magnetic resonance imaging.* Investigative radiology, 2005. **40**(2): p. 72-79.
200. Ingrisch, M., et al., *Quantitative pulmonary perfusion magnetic resonance imaging: influence of temporal resolution and signal-to-noise ratio.* Investigative radiology, 2010. **45**(1): p. 7-14.
201. Ley-Zaporozhan, J., et al., *Repeatability and reproducibility of quantitative whole-lung perfusion magnetic resonance imaging.* Journal of thoracic imaging, 2011. **26**(3): p. 230-239.
202. Sourbron, S. and D. Buckley, *Tracer kinetic modelling in MRI: estimating perfusion and capillary permeability.* Physics in medicine and biology, 2012. **57**(2): p. R1.
203. Maxien, D., et al., *Quantification of pulmonary perfusion with free-breathing dynamic contrast-enhanced MRI--a pilot study in healthy volunteers.* RoFo: Fortschritte auf dem Gebiete der Rontgenstrahlen und der Nuklearmedizin, 2013. **185**(12): p. 1175-1181.

204. Rajaram, S., et al., *3D contrast-enhanced lung perfusion MRI is an effective screening tool for chronic thromboembolic pulmonary hypertension: results from the ASPIRE Registry.* Thorax, 2013: p. thoraxjnl-2012-203020.
205. Cuenod, C. and D. Balvay, *Perfusion and vascular permeability: basic concepts and measurement in DCE-CT and DCE-MRI.* Diagnostic and interventional imaging, 2013. **94**(12): p. 1187-1204.
206. Ingrisch, M., et al., *Assessment of pulmonary perfusion with breath-hold and free-breathing dynamic contrast-enhanced magnetic resonance imaging: quantification and reproducibility.* Investigative radiology, 2014. **49**(6): p. 382-389.
207. Gordon, Y., et al., *Dynamic contrast-enhanced magnetic resonance imaging: fundamentals and application to the evaluation of the peripheral perfusion.* Cardiovascular diagnosis and therapy, 2014. **4**(2): p. 147.
208. Bell, L.C., et al., *Simultaneous MRI of lung structure and perfusion in a single breathhold.* Journal of Magnetic Resonance Imaging, 2015. **41**(1): p. 52-59.
209. Johns, C.S., et al., *Pulmonary MR angiography and perfusion imaging—A review of methods and applications.* European Journal of Radiology, 2016.
210. Rohrer, M., et al., *Comparison of magnetic properties of MRI contrast media solutions at different magnetic field strengths.* Investigative radiology, 2005. **40**(11): p. 715-724.
211. Keilholz, S.D., et al., *Comparison of first-pass Gd-DOTA and FAIRER MR perfusion imaging in a rabbit model of pulmonary embolism.* Journal of Magnetic Resonance Imaging, 2002. **16**(2): p. 168-171.
212. Jackson, A., D.L. Buckley, and G.J. Parker, *Dynamic contrast-enhanced magnetic resonance imaging in oncology*. 2005: Springer.
213. Nikolaou, K., et al., *Quantification of pulmonary blood flow and volume in healthy volunteers by dynamic contrast-enhanced magnetic resonance imaging using a parallel imaging technique.* Investigative radiology, 2004. **39**(9): p. 537-545.
214. Pruessmann, K.P., et al., *SENSE: sensitivity encoding for fast MRI.* Magnetic resonance in medicine, 1999. **42**(5): p. 952-962.
215. Griswold, M.A., et al., *Generalized autocalibrating partially parallel acquisitions (GRAPPA).* Magnetic Resonance in Medicine, 2002. **47**(6): p. 1202-1210.
216. Korosec, F.R., et al., *Time-resolved contrast-enhanced 3D MR angiography.* Magnetic Resonance in Medicine, 1996. **36**(3): p. 345-351.
217. Delakis, I., O. Hammad, and R.I. Kitney, *Wavelet-based de-noising algorithm for images acquired with parallel magnetic resonance imaging (MRI).* Physics in Medicine and biology, 2007. **52**(13): p. 3741.
218. Khalifa, F., et al., *Models and methods for analyzing DCE-MRI: A review.* Medical physics, 2014. **41**(12).
219. Hansford, B.G., et al., *Dynamic contrast-enhanced MR imaging curve-type analysis: is it helpful in the differentiation of prostate cancer from healthy peripheral zone?* Radiology, 2015. **275**(2): p. 448-457.
220. Wild, J.M., et al., *Comparison between 2D and 3D gradient-echo sequences for MRI of human lung ventilation with hyperpolarized 3He.* Magnetic resonance in medicine, 2004. **52**(3): p. 673-678.
221. Stewart, N.J., et al., *Feasibility of human lung ventilation imaging using highly polarized naturally abundant xenon and optimized three-dimensional steady-state free precession.* Magnetic Resonance in Medicine, 2015.
222. Altes, T.A., et al., *Assessment of lung development using hyperpolarized helium-3 diffusion MR imaging.* Journal of Magnetic Resonance Imaging, 2006. **24**(6): p. 1277-1283.
223. Diaz, S., et al., *Hyperpolarized 3He apparent diffusion coefficient MRI of the lung: reproducibility and volume dependency in healthy volunteers and patients with emphysema.* Journal of Magnetic Resonance Imaging, 2008. **27**(4): p. 763-770.

224. Kaushik, S.S., et al., *Diffusion-weighted hyperpolarized 129Xe MRI in healthy volunteers and subjects with chronic obstructive pulmonary disease.* Magnetic Resonance in Medicine, 2011. **65**(4): p. 1154-1165.
225. Chan, H.F., et al., *Whole lung morphometry with 3D multiple b-value hyperpolarized gas MRI and compressed sensing.* Magnetic resonance in medicine, 2017. **77**(5): p. 1916-1925.
226. Holmes, J.H., et al., *Imaging of lung ventilation and respiratory dynamics in a single ventilation cycle using hyperpolarized He-3 MRI.* Journal of Magnetic Resonance Imaging, 2007. **26**(3): p. 630-636.
227. Holmes, J.H., et al., *Three-dimensional imaging of ventilation dynamics in asthmatics using multiecho projection acquisition with constrained reconstruction.* Magnetic resonance in medicine, 2009. **62**(6): p. 1543-1556.
228. Kyriazis, A., et al., *Dynamic Ventilation 3He MRI for the Quantification of Disease in the Rat Lung.* Ieee Transactions on Biomedical Engineering, 2012. **59**(3): p. 777-786.
229. Fischer, M., et al., *Single-acquisition sequence for the measurement of oxygen partial pressure by hyperpolarized gas MRI.* Magnetic resonance in medicine, 2004. **52**(4): p. 766-773.
230. Yu, J., et al., *Optimization of scan parameters in pulmonary partial pressure oxygen measurement by hyperpolarized 3He MRI.* Magnetic resonance in medicine, 2008. **59**(1): p. 124-131.
231. Yu, J., et al., *Simultaneous measurement of pulmonary partial pressure of oxygen and apparent diffusion coefficient by hyperpolarized 3He MRI.* Magnetic resonance in medicine, 2009. **61**(5): p. 1015-1021.
232. Oros, A.-M. and N.J. Shah, *Hyperpolarized xenon in NMR and MRI.* Physics in medicine and biology, 2004. **49**(20): p. R105.
233. Abdeen, N., et al., *Measurement of xenon diffusing capacity in the rat lung by hyperpolarized 129Xe MRI and dynamic spectroscopy in a single breath-hold.* Magnetic resonance in medicine, 2006. **56**(2): p. 255-264.
234. Driehuys, B., et al., *Imaging alveolar–capillary gas transfer using hyperpolarized 129Xe MRI.* Proceedings of the National Academy of Sciences, 2006. **103**(48): p. 18278-18283.
235. Cleveland, Z.I., et al., *Hyperpolarized 129Xe MR imaging of alveolar gas uptake in humans.* PloS one, 2010. **5**(8): p. e12192.
236. Dregely, I., et al., *Hyperpolarized Xenon-129 gas-exchange imaging of lung microstructure: First case studies in subjects with obstructive lung disease.* Journal of Magnetic Resonance Imaging, 2011. **33**(5): p. 1052-1062.
237. Qing, K., et al., *Assessment of lung function in asthma and COPD using hyperpolarized 129Xe chemical shift saturation recovery spectroscopy and dissolved-phase MRI.* NMR in biomedicine, 2014. **27**(12): p. 1490-1501.
238. Stewart, N.J., et al., *Experimental validation of the hyperpolarized 129Xe chemical shift saturation recovery technique in healthy volunteers and subjects with interstitial lung disease.* Magnetic Resonance in Medicine, 2014.
239. Qing, K., et al., *Regional mapping of gas uptake by blood and tissue in the human lung using hyperpolarized xenon-129 MRI.* Journal of Magnetic Resonance Imaging, 2014. **39**(2): p. 346-359.
240. Meersmann, T. and E. Brunner, *Hyperpolarized xenon-129 magnetic resonance: concepts, production, techniques and applications*. 2015: Royal Society of Chemistry.
241. Stewart, N.J., et al., *Experimental validation of the hyperpolarized 129Xe chemical shift saturation recovery technique in healthy volunteers and subjects with interstitial lung disease.* Magnetic resonance in medicine, 2015. **74**(1): p. 196-207.

242. Norquay, G., et al., *129Xe chemical shift in human blood and pulmonary blood oxygenation measurement in humans using hyperpolarized 129Xe NMR.* Magnetic resonance in medicine, 2017. **77**(4): p. 1399-1408.

243. Appelt, S., et al., *Theory of spin-exchange optical pumping of 3 He and 129 Xe.* Physical Review A, 1998. **58**(2): p. 1412.

244. Walker, T.G. *Fundamentals of spin-exchange optical pumping*. in *Journal of Physics: Conference Series*. 2011. IOP Publishing.

245. Ruppert, K., *Biomedical imaging with hyperpolarized noble gases.* Reports on Progress in Physics, 2014. **77**(11): p. 116701.

246. Norquay G, Stewart NJ, and W. JM. *High 129Xe polarisation (80%) on ahome-built SEOP system*. in *PING14*. 2014. Les Houches, France.

247. Zhao, L., et al., *Gradient-Echo Imaging Considerations for Hyperpolarized 129Xe MR.* Journal of Magnetic Resonance, Series B, 1996. **113**(2): p. 179-183.

248. Wild, J.M., et al., *k-space filtering in 2D gradient-echo breath-hold hyperpolarized 3He MRI: spatial resolution and signal-to-noise ratio considerations.* Magnetic resonance in medicine, 2002. **47**(4): p. 687-695.

249. Maintz, J.B. and M.A. Viergever, *A survey of medical image registration.* Medical image analysis, 1998. **2**(1): p. 1-36.

250. Fischer, B. and J. Modersitzki, *Ill-posed medicine—an introduction to image registration.* Inverse Problems, 2008. **24**(3): p. 034008.

251. Wyawahare, M.V., P.M. Patil, and H.K. Abhyankar, *Image registration techniques: an overview.* International Journal of Signal Processing, Image Processing and Pattern Recognition, 2009. **2**(3): p. 11-28.

252. Oliveira, F.P. and J.M.R. Tavares, *Medical image registration: a review.* Computer methods in biomechanics and biomedical engineering, 2014. **17**(2): p. 73-93.

253. Ireland, R.H., et al., *Feasibility of Image Registration and Intensity-Modulated Radiotherapy Planning With Hyperpolarized Helium-3 Magnetic Resonance Imaging for Non–Small-Cell Lung Cancer.* International Journal of Radiation Oncology* Biology* Physics, 2007. **68**(1): p. 273-281.

254. Ireland, R.H., et al., *An image acquisition and registration strategy for the fusion of hyperpolarized helium-3 MRI and x-ray CT images of the lung.* Physics in medicine and biology, 2008. **53**(21): p. 6055.

255. Ireland, R., et al. *Towards automatic image registration of hyperpolarized 3He MRI and x-ray CT images of the lung*. in *Proc. Int. Soc. Magn. Reson. Med.* 2009.

256. Tahir, B.A., et al., *A method for quantitative analysis of regional lung ventilation using deformable image registration of CT and hybrid hyperpolarized gas/1H MRI.* Physics in medicine and biology, 2014. **59**(23): p. 7267.

257. Hughes, P.J.C., et al. *Ventilation-Perfusion Analysis with Co-Registered Hyperpolarized Gas and CE 1H Perfusion MRI.* in *ISMRM 23rd Annual Meeting.* 2015. Toronto,Ontario,Canada.

258. Sotiras, A., C. Davatzikos, and N. Paragios, *Deformable medical image registration: A survey.* Medical Imaging, IEEE Transactions on, 2013. **32**(7): p. 1153-1190.

259. Tustison, N.J. and B.B. Avants, *Explicit B-spline regularization in diffeomorphic image registration.* Frontiers in neuroinformatics, 2013. **7**.

260. Fitzpatrick, J.M., D.L. Hill, and C.R. Maurer Jr, *Image registration.* Handbook of medical imaging, 2000. **2**: p. 447-513.

261. Hill, D.L., et al., *Medical image registration.* Physics in medicine and biology, 2001. **46**(3): p. R1.

262. Kostelec, P.J. and S. Periaswamy, *Image registration for MRI.* Modern Signal Processing, 2003. **46**: p. 161-184.

263. Maes, F., D. Vandermeulen, and P. Suetens, *Medical image registration using mutual information.* Proceedings of the IEEE, 2003. **91**(10): p. 1699-1722.

264. Glocker, B., et al., *Deformable medical image registration: Setting the state of the art with discrete methods**. Annual review of biomedical engineering, 2011. **13**: p. 219-244.
265. Goshtasby, A.A., *Image registration: Principles, tools and methods*. 2012: Springer Science & Business Media.
266. Avants, B.B., et al., *A reproducible evaluation of ANTs similarity metric performance in brain image registration.* Neuroimage, 2011. **54**(3): p. 2033-2044.
267. Murphy, K., et al., *Evaluation of registration methods on thoracic CT: the EMPIRE10 challenge.* Medical Imaging, IEEE Transactions on, 2011. **30**(11): p. 1901-1920.
268. Ashburner, J., *A fast diffeomorphic image registration algorithm.* Neuroimage, 2007. **38**(1): p. 95-113.
269. Avants, B.B., et al., *Symmetric diffeomorphic image registration with cross-correlation: evaluating automated labeling of elderly and neurodegenerative brain.* Medical image analysis, 2008. **12**(1): p. 26-41.
270. Klein, S., et al., *Elastix: a toolbox for intensity-based medical image registration.* Medical Imaging, IEEE Transactions on, 2010. **29**(1): p. 196-205.
271. Metz, C.T., et al., *Nonrigid registration of dynamic medical imaging data using< i> n</i> D+ t B-splines and a groupwise optimization approach.* Medical image analysis, 2011. **15**(2): p. 238-249.
272. Tang, L., G. Hamarneh, and A. Celler. *Co-registration of bone CT and SPECT images using mutual information*. 2006. IEEE.
273. Auer, M., P. Regitnig, and G.A. Holzapfel, *An automatic nonrigid registration for stained histological sections.* Image Processing, IEEE Transactions on, 2005. **14**(4): p. 475-486.
274. Yoo, T.S., et al., *Engineering and algorithm design for an image processing API: a technical report on ITK-the insight toolkit.* Studies in health technology and informatics, 2002: p. 586-592.
275. Böttger, T., et al., *Implementation and evaluation of a new workflow for registration and segmentation of pulmonary MRI data for regional lung perfusion assessment.* Physics in medicine and biology, 2007. **52**(5): p. 1261.
276. Bhagalia, R., J.A. Fessler, and B. Kim, *Accelerated nonrigid intensity-based image registration using importance sampling.* Medical Imaging, IEEE Transactions on, 2009. **28**(8): p. 1208-1216.
277. Woodhouse, N., et al., *Combined helium-3/proton magnetic resonance imaging measurement of ventilated lung volumes in smokers compared to never-smokers.* J Magn Reson Imaging, 2005. **21**(4): p. 365-9.
278. Ivanovska, T., et al., *Lung Segmentation of MR Images: A Review*, in *Visualization in Medicine and Life Sciences III*. 2016, Springer. p. 3-24.
279. Ray, N., et al., *Merging parametric active contours within homogeneous image regions for MRI-based lung segmentation.* Medical Imaging, IEEE Transactions on, 2003. **22**(2): p. 189-199.
280. Tavares, R.S., et al. *Temporal segmentation of lung region from MRI sequences using multiple active contours*. in *Engineering in Medicine and Biology Society, EMBC, 2011 Annual International Conference of the IEEE*. 2011. IEEE.
281. Tustison, N.J., et al., *Atlas-based estimation of lung and lobar anatomy in proton MRI.* Magnetic resonance in medicine, 2015.
282. Wang, H., et al., *Multi-atlas segmentation with joint label fusion.* Pattern Analysis and Machine Intelligence, IEEE Transactions on, 2013. **35**(3): p. 611-623.
283. Tustison, N.J., et al., *Ventilation-based segmentation of the lungs using hyperpolarized 3He MRI.* Journal of Magnetic Resonance Imaging, 2011. **34**(4): p. 831-841.

284. Guo, F., et al., *Globally optimal co-segmentation of three-dimensional pulmonary 1 H and hyperpolarized 3 He MRI with spatial consistence prior.* Medical image analysis, 2015. **23**(1): p. 43-55.
285. He, M., et al., *Using Hyperpolarized 129 Xe MRI to Quantify the Pulmonary Ventilation Distribution.* Academic Radiology, 2016.
286. Kroonenberg, P.M., *Three-mode principal component analysis: Theory and applications*. Vol. 2 %@ 9066950021. 1983: DSWO press.
287. Horel, J.D., *Complex principal component analysis: Theory and examples.* Journal of climate and Applied Meteorology, 1984. **23**(12): p. 1660-1673.
288. Jolliffe, I., *Principal component analysis*. 2005: Wiley Online Library.
289. Karlsson, A., et al. *Automatic and Quantitative Assessment of Total and Regional Muscle Tissue Volume using Multi-Atlas Segmentation*. in *ISMRM 22nd Annual Meeting & Exhibition, 10-16 May, 2014, Milan, Italy*. 2014.
290. Virgincar, R.S., et al., *Quantitative analysis of hyperpolarized 129Xe ventilation imaging in healthy volunteers and subjects with chronic obstructive pulmonary disease.* NMR in biomedicine, 2013. **26**(4): p. 424-435.
291. He, M., et al., *Extending Semiautomatic Ventilation Defect Analysis for Hyperpolarized 129 Xe Ventilation MRI.* Academic radiology, 2014. **21**(12): p. 1530-1541.
292. Frangi, A.F., et al., *Model-based quantitation of 3-D magnetic resonance angiographic images.* Medical Imaging, IEEE Transactions on, 1999. **18**(10): p. 946-956.
293. Tustison, N.J., et al., *N4ITK: improved N3 bias correction.* IEEE transactions on medical imaging, 2010. **29**(6): p. 1310-1320.
294. Skourikhine, A.N., L. Prasad, and B.R. Schlei. *Neural network for image segmentation*. in *International Symposium on Optical Science and Technology*. 2000. International Society for Optics and Photonics.
295. Indira, S. and A. Ramesh. *Image segmentation using artificial neural network and genetic algorithm: a comparative analysis*. in *Process Automation, Control and Computing (PACC), 2011 International Conference on*. 2011. IEEE.
296. Duraisamy, M. and F. Jane. *cellular neural network based medical image segmentation using artificial bee colony algorithm*. in *Green Computing Communication and Electrical Engineering (ICGCCEE), 2014 International Conference on*. 2014. IEEE.
297. Torbati, N., A. Ayatollahi, and A. Kermani, *An efficient neural network based method for medical image segmentation.* Computers in biology and medicine, 2014. **44**: p. 76-87.
298. Yang, T., *Handbook of CNN image processing: All you need to know about cellular neural networks*. 2002: Yang's Scientific Research Institute.
299. Kanungo, T., et al., *An efficient k-means clustering algorithm: Analysis and implementation.* Pattern Analysis and Machine Intelligence, IEEE Transactions on, 2002. **24**(7): p. 881-892.
300. Kang, D., et al. *An improved method of breast MRI segmentation with Simplified K-means clustered images*. 2011. ACM.
301. Bezdek, J.C., *Pattern recognition with fuzzy objective function algorithms*. 2013: Springer Science & Business Media.
302. Zadeh, L.A., *Fuzzy sets.* Information and control, 1965. **8**(3): p. 338-353.
303. Pham, D.L. and J.L. Prince, *An adaptive fuzzy C-means algorithm for image segmentation in the presence of intensity inhomogeneities.* Pattern recognition letters, 1999. **20**(1): p. 57-68.
304. Wu, K.-L. and M.-S. Yang, *Alternative c-means clustering algorithms.* Pattern recognition, 2002. **35**(10): p. 2267-2278.

305. Chuang, K.-S., et al., *Fuzzy c-means clustering with spatial information for image segmentation.* computerized medical imaging and graphics, 2006. **30**(1): p. 9-15.

306. Haddad, R.A. and A.N. Akansu, *A class of fast Gaussian binomial filters for speech and image processing.* IEEE Transactions on Signal Processing, 1991. **39**(3): p. 723-727.

307. Tomasi, C. and R. Manduchi. *Bilateral filtering for gray and color images*. in *Computer Vision, 1998. Sixth International Conference on*. 1998. IEEE.

308. Paris, S., et al. *A gentle introduction to bilateral filtering and its applications*. in *ACM SIGGRAPH 2007 courses*. 2007. ACM.

309. Bezdek, J.C., R. Ehrlich, and W. Full, *FCM: The fuzzy c-means clustering algorithm.* Computers & Geosciences, 1984. **10**(2): p. 191-203.

310. Lui, J.K., et al., *Semiautomatic Segmentation of Ventilated Airspaces in Healthy and Asthmatic Subjects Using Hyperpolarized MRI.* Computational and mathematical methods in medicine, 2013. **2013**.

311. Hughes, P.J., et al., *Spatial Fuzzy C-Means Thresholding for Semiautomated Calculation of Percentage Lung Ventilated Volume From Hyperpolarized Gas and 1H MRI.* Journal of Magnetic Resonance Imaging, 2017.

312. Dice, L.R., *Measures of the amount of ecologic association between species.* Ecology, 1945. **26**(3): p. 297-302.

313. Norquay, G., et al., *A polariser for on demand production of hyperpolarised 129Xe for human lung MRI.* European Respiratory Journal, 2013. **42**(Suppl 57): p. P2271.

314. Frangi, A.F., et al. *Multiscale vessel enhancement filtering*. in *International Conference on Medical Image Computing and Computer-Assisted Intervention*. 1998. Springer.

315. Altes, T.A., et al., *Hyperpolarized 3He MR lung ventilation imaging in asthmatics: preliminary findings.* Journal of Magnetic Resonance Imaging, 2001. **13**(3): p. 378-384.

316. de Lange, E.E., et al., *The variability of regional airflow obstruction within the lungs of patients with asthma: assessment with hyperpolarized helium-3 magnetic resonance imaging.* Journal of Allergy and Clinical Immunology, 2007. **119**(5): p. 1072-1078.

317. Fain, S.B., et al., *Functional lung imaging using hyperpolarized gas MRI.* Journal of Magnetic Resonance Imaging, 2007. **25**(5): p. 910-923.

318. Mata, J., et al., *Hyperpolarized 3 He MR imaging of the lung: effect of subject immobilization on the occurrence of ventilation defects.* Academic radiology, 2008. **15**(2): p. 260-264.

319. Ruset, I., et al., *A system for open-access 3He human lung imaging at very low field.* Concepts in Magnetic Resonance Part B: Magnetic Resonance Engineering, 2006. **29**(4): p. 210-221.

320. De Zanche, N., et al., *NMR probes for measuring magnetic fields and field dynamics in MR systems.* Magnetic Resonance in Medicine, 2008. **60**(1): p. 176-186.

321. Wild, J.M., et al., *Synchronous acquisition of hyperpolarised 3He and 1H MR images of the lungs - maximising mutual anatomical and functional information.* NMR Biomed, 2011. **24**(2): p. 130-4.

322. Tustison, N.J., et al., *Feature analysis of hyperpolarized helium-3 pulmonary MRI: A study of asthmatics versus nonasthmatics.* Magnetic Resonance in Medicine, 2010. **63**(6): p. 1448-1455.

323. Miller, G., et al., *Hyperpolarized 3 He lung ventilation imaging with B 1-inhomogeneity correction in a single breath-hold scan.* Magnetic Resonance Materials in Physics, Biology and Medicine, 2004. **16**(5): p. 218-226.

324. Sled, J.G., A.P. Zijdenbos, and A.C. Evans, *A nonparametric method for automatic correction of intensity nonuniformity in MRI data.* IEEE transactions on medical imaging, 1998. **17**(1): p. 87-97.

325. Everitt, B.S., *The Cambridge dictionary of statistics*. 2006: Cambridge University Press.
326. Tzeng, Y.-S., K. Lutchen, and M. Albert, *The difference in ventilation heterogeneity between asthmatic and healthy subjects quantified using hyperpolarized 3He MRI.* Journal of Applied Physiology, 2009. **106**(3): p. 813-822.
327. Hamedani, H., et al., *Regional fractional ventilation by using multibreath wash-in 3He MR imaging.* Radiology, 2016. **279**(3): p. 917-924.
328. Halaweish, A.F., et al., *Perfluoropropane gas as a magnetic resonance lung imaging contrast agent in humans.* CHEST Journal, 2013. **144**(4): p. 1300-1310.
329. Couch, M.J., et al., *Pulmonary ultrashort echo time 19F MR imaging with inhaled fluorinated gas mixtures in healthy volunteers: feasibility.* Radiology, 2013. **269**(3): p. 903-909.
330. Ouriadov, A.V., et al., *In vivo regional ventilation mapping using fluorinated gas MRI with an x-centric FGRE method.* Magnetic resonance in medicine, 2015. **74**(2): p. 550-557.
331. Gutberlet, M., et al. *Real-time dynamic fluorinated gas MRI in free breathing for mapping of regional lung ventilation in patients with COPD and healthy volunteers using a 16 channel receive coil at 1.5T.* in *24th annual meeting and exhibition of the International Society for Magnetic Resonance in Medicine*. 2016.
332. Gutberlet, M. and J. Vogel-Claussen, *Fluorinated-Gas MRI.* 2017.
333. Sá, R.C., et al., *Validating the distribution of specific ventilation in healthy humans measured using proton MR imaging.* Journal of Applied Physiology, 2014. **116**(8): p. 1048-1056.
334. Walsh, C.E., et al., *Ventilation heterogeneity measured by single photon emission computed tomography/computed tomography (SPECT/CT) and multiple breath nitrogen washout (MBNW) in asthma.* 2008.
335. Farrow, C.E., et al., *Heterogeneous Bronchoconstriction Measured By Ventilation Single Photon Emission Computed Tomography/Computed Tomography (VSPECT/CT) Is Reduced After Treatment In Asthma*, in *C29. ADVANCES IN PULMONARY IMAGING TO STUDY LUNG STRUCTURE AND FUNCTION.* 2017, Am Thoracic Soc. p. A5151-A5151.
336. Weibel, E.R., *Morphometry of the Human Lung*. 1963: Springer Berlin Heidelberg.
337. Schreider, J.P. and O.G. Raabe, *Structure of the human respiratory acinus.* American Journal of Anatomy, 1981. **162**(3): p. 221-232.
338. Haefeli-Bleuer, B. and E.R. Weibel, *Morphometry of the human pulmonary acinus.* The Anatomical Record, 1988. **220**(4): p. 401-414.
339. Norberg, P., et al., *Quantitative lung SPECT applied on simulated early COPD and humans with advanced COPD.* EJNMMI research, 2013. **3**(1): p. 28.
340. Stewart, N., et al., *Comparison of 3He and 129Xe MRI for evaluation of lung microstructure and ventilation at 1.5 T.* 2016, Eur Respiratory Soc.
341. Rosenthal, M., et al., *Lung function in white children aged 4 to 19 years: II--Single breath analysis and plethysmography.* Thorax, 1993. **48**(8): p. 803-808.
342. McNulty, W. and O.S. Usmani, *Techniques of assessing small airways dysfunction.* European clinical respiratory journal, 2014. **1**(1): p. 25898.
343. Deppe, M.H., et al., *Susceptibility effects in hyperpolarized 3He lung MRI at 1.5 T and 3T.* Journal of Magnetic Resonance Imaging, 2009. **30**(2): p. 418-423.
344. Moratal, D., et al., *k-Space tutorial: an MRI educational tool for a better understanding of k-space.* Biomedical imaging and intervention journal, 2008. **4**(1).
345. Norberg, P., et al., *Does quantitative lung SPECT detect lung abnormalities earlier than lung function tests? Results of a pilot study.* EJNMMI research, 2014. **4**(1): p. 39.
346. Moore, V., *Spirometry: step by step.* Breathe, 2012. **8**(3): p. 232-240.

347. Kalender, W.A., et al., *Measurement of pulmonary parenchymal attenuation: use of spirometric gating with quantitative CT.* Radiology, 1990. **175**(1): p. 265-268.

348. Kauczor, H., et al., *Value of spirometry-gated high resolution computerized tomography of the lung during inspiration and expiration.* RoFo: Fortschritte auf dem Gebiete der Rontgenstrahlen und der Nuklearmedizin, 1998. **169**(6): p. 658-661.

349. Lamers, R., et al., *Reproducibility of spirometrically controlled CT lung densitometry in a clinical setting.* European Respiratory Journal, 1998. **11**(4): p. 942-945.

350. Moroni, C., et al., *Comparison of Spirometric-Gated and-Ungated HRCT in COPD.* Journal of computer assisted tomography, 2003. **27**(3): p. 375-379.

351. D'souza, W.D., et al., *Gated CT imaging using a free-breathing respiration signal from flow-volume spirometry.* Medical physics, 2005. **32**(12): p. 3641-3649.

352. Camiciottoli, G., et al., *Spirometrically gated high-resolution CT findings in COPD: lung attenuation vs lung function and dyspnea severity.* CHEST Journal, 2006. **129**(3): p. 558-564.

353. Matsushita, S., et al., *Quantitative computed tomography assessment of air trapping in relapsing polychondritis: correlations with spirometric values.* Journal of computer assisted tomography, 2014. **38**(6): p. 968-971.

354. Bommart, S., et al., *Relationship between CT air trapping criteria and lung function in small airway impairment quantification.* BMC pulmonary medicine, 2014. **14**(1): p. 29.

355. Wei Zha, et al. *An Adaptive K-means Approach for Assessment of Ventilation Defects in Asthma and Cystic Fibrosis Using Hyperpolarized Helium-3 MRI.* in *ISMRM 23rd annual meeting*. 2015. Toronto.

356. Wild, J.M., et al., *Dynamic radial projection MRI of inhaled hyperpolarized 3He gas.* Magnetic resonance in medicine, 2003. **49**(6): p. 991-997.

357. Salerno, M., et al., *Dynamic spiral MRI of pulmonary gas flow using hyperpolarized 3He: preliminary studies in healthy and diseased lungs.* Magnetic resonance in medicine, 2001. **46**(4): p. 667-677.

358. Koumellis, P., et al., *Quantitative analysis of regional airways obstruction using dynamic hyperpolarized 3He MRI—preliminary results in children with cystic fibrosis.* Journal of Magnetic Resonance Imaging, 2005. **22**(3): p. 420-426.

359. Holmes, J.H., et al., *3D hyperpolarized He-3 MRI of ventilation using a multi-echo projection acquisition.* Magnetic resonance in medicine, 2008. **59**(5): p. 1062-1071.

360. Marshall, H., et al., *Imaging The Effect Of Airway Opening In Asthma Due To Inflation State With 3He MRI*, in *B109. TECHNOLOGIC ADVANCES IN IMAGING FOR PHENOTYPING LUNG DISEASE*. 2013, Am Thoracic Soc. p. A3744-A3744.

361. Lazaar, A., *Bronchial vascular remodeling in asthma and COPD*. 2006: CRC Press.

362. Venegas, J., *Linking ventilation heterogeneity and airway hyperresponsiveness in asthma*. 2007, BMJ Publishing Group Ltd.

363. Muradyan, I., et al., *Inhalation heterogeneity from subresidual volumes in elite divers.* Journal of Applied Physiology, 2010. **109**(6): p. 1969-1973.

364. de Lange, E.E., et al., *Evaluation of asthma with hyperpolarized helium-3 MRI: correlation with clinical severity and spirometry.* CHEST Journal, 2006. **130**(4): p. 1055-1062.

365. Wild, J., et al., *Hyperpolarised gas MR lung imaging–Breaks through to clinical practice*. 2015, Eur Respiratory Soc.

366. Weir, J.P., *Quantifying test-retest reliability using the intraclass correlation coefficient and the SEM.* The Journal of Strength & Conditioning Research, 2005. **19**(1): p. 231-240.

367. Altman, D.G. and J.M. Bland, *Measurement in medicine: the analysis of method comparison studies.* The statistician, 1983: p. 307-317.

368. Ibanez, J. and J. Raurich, *Normal values of functional residual capacity in the sitting and supine positions.* Intensive care medicine, 1982. **8**(4): p. 173-177.
369. Jenkins, S.C., S.A. Soutar, and J. Moxham, *The effects of posture on lung volumes in normal subjects and in patients pre-and post-coronary artery surgery.* Physiotherapy, 1988. **74**(10): p. 492-496.
370. Freydag, A., et al., *Lung volume and ventilation distribution changes by positioning and application of positive airway pressure in healthy subjects.* Applied Cardiopulmonary Pathophysiology, 2013. **17**: p. 267-274.
371. Hopkins, S.R., et al., *Vertical gradients in regional lung density and perfusion in the supine human lung: the Slinky effect.* Journal of Applied Physiology, 2007. **103**(1): p. 240-248.
372. Ruggier, R., *Physiology of ventilation.* Current Anaesthesia & Critical Care, 1996. **7**(5): p. 221-227.
373. Moreno, F. and H.A. Lyons, *Effect of body posture on lung volumes.* Journal of Applied physiology, 1961. **16**(1): p. 27-29.
374. Shahab, L., et al., *Prevalence, diagnosis and relation to tobacco dependence of chronic obstructive pulmonary disease in a nationally representative population sample.* Thorax, 2006. **61**(12): p. 1043-7.
375. Pennati, F., et al., *Assessment of Regional Lung Function with Multivolume 1H MR Imaging in Health and Obstructive Lung Disease: Comparison with 3He MR Imaging.* Radiology, 2014. **273**(2): p. 580-590.
376. Levitzky, M.G., *Pulmonary physiology*. 2003: McGraw-Hill Medical Publishing.
377. Harkness, L.M., et al., *Pulmonary vascular changes in asthma and COPD.* Pulmonary pharmacology & therapeutics, 2014. **29**(2): p. 144-155.
378. Bakakos, P., G. Patentalakis, and A. Papi, *Vascular biomarkers in asthma and COPD.* Current topics in medicinal chemistry, 2016. **16**(14): p. 1599-1609.
379. Kelly, V.J., et al., *Hypoxic pulmonary vasoconstriction does not explain all regional perfusion redistribution in asthma.* American Journal of Respiratory and Critical Care Medicine, 2017(ja).
380. Bauman, G. and M. Eichinger, *Ventilation and perfusion magnetic resonance imaging of the lung.* Polish Journal of Radiology, 2012. **77**(1): p. 37.
381. Kołodziej, M., et al., *Lung function imaging methods in Cystic Fibrosis pulmonary disease.* Respiratory research, 2017. **18**(1): p. 96.
382. Musch, G. and J.G. Venegas, *Positron emission tomography imaging of regional pulmonary perfusion and ventilation.* Proceedings of the American Thoracic Society, 2005. **2**(6): p. 522-527.
383. Melo, M.F.V., et al., *Topographic basis of bimodal ventilation–perfusion distributions during bronchoconstriction in sheep.* American journal of respiratory and critical care medicine, 2005. **171**(7): p. 714-721.
384. Harris, R.S., et al., *Regional pulmonary perfusion, inflation, and ventilation defects in bronchoconstricted patients with asthma.* American journal of respiratory and critical care medicine, 2006. **174**(3): p. 245-253.
385. Wagner, P.D., H. Saltzman, and J. West, *Measurement of continuous distributions of ventilation-perfusion ratios: theory.* Journal of Applied Physiology, 1974. **36**(5): p. 588-599.
386. Johns, C.S., et al., *Lung perfusion: MRI vs. SPECT for screening in suspected chronic thromboembolic pulmonary hypertension.* Journal of Magnetic Resonance Imaging, 2017.
387. Kang, M.-J., et al., *Dual-energy CT: clinical applications in various pulmonary diseases.* Radiographics, 2010. **30**(3): p. 685-698.
388. Cremillieux, Y., et al., *A combined 1H perfusion/3He ventilation NMR study in rat lungs.* Magnetic resonance in medicine, 1999. **41**(4): p. 645-648.

389. Altes, T.A., et al., *Pulmonary embolism: comprehensive evaluation with MR ventilation and perfusion scanning with hyperpolarized helium-3, arterial spin tagging, and contrast-enhanced MRA.* Journal of vascular and interventional radiology, 2005. **16**(7): p. 999-1005.
390. Wagner, P.D., P.F. Naumann, and R.B. Laravuso, *Simultaneous measurement of eight foreign gases in blood by gas chromatography.* Journal of Applied Physiology, 1974. **36**(5): p. 600-605.
391. Kety, S.S., *The theory and applications of the exchange of inert gas at the lungs and tissues.* Pharmacological reviews, 1951. **3**(1): p. 1-41.
392. Farhi, L., *Elimination of inert gas by the lung.* Respiration physiology, 1967. **3**(1): p. 1-11.
393. Yokoyama, T. and L. Farhi, *Study of ventilation-perfusion ratio distribution in the anesthetized dog by multiple inert gas washout.* Respiration physiology, 1967. **3**(2): p. 166-176.
394. Bajc, M., et al., *Grading obstructive lung disease using tomographic pulmonary scintigraphy in patients with chronic obstructive pulmonary disease (COPD) and long-term smokers.* Annals of nuclear medicine, 2015. **29**(1): p. 91-99.
395. Treppo, S., S.M. Mijailovich, and J.G. Venegas, *Contributions of pulmonary perfusion and ventilation to heterogeneity in* $\dot{V}\ a/\dot{Q}$ *measured by PET.* Journal of Applied Physiology, 1997. **82**(4): p. 1163-1176.
396. Kelmenson, D.A., et al., *The effect of omalizumab on ventilation and perfusion in adults with allergic asthma.* American journal of nuclear medicine and molecular imaging, 2013. **3**(4): p. 350.
397. Nagle, S.K., et al., *Magnetic Resonance Imaging of the Lung: Cystic Fibrosis.* 2017.
398. Brenner, D.J. and E.J. Hall, *Computed tomography—an increasing source of radiation exposure.* New England Journal of Medicine, 2007. **357**(22): p. 2277-2284.
399. Cronin, P., J.G. Weg, and E.A. Kazerooni. *The role of multidetector computed tomography angiography for the diagnosis of pulmonary embolism*. in *Seminars in nuclear medicine*. 2008. Elsevier.
400. Henderson, A.C., et al., *Steep head-down tilt has persisting effects on the distribution of pulmonary blood flow.* Journal of Applied Physiology, 2006. **101**(2): p. 583-589.
401. Edelman, R.R., et al., *Noninvasive assessment of regional ventilation in the human lung using oxygen–enhanced magnetic resonance imaging.* Nature medicine, 1996. **2**(11): p. 1236-1239.
402. Chen, Q., et al., *Oxygen enhanced MR ventilation imaging of the lung.* Magnetic Resonance Materials in Physics, Biology and Medicine, 1998. **7**(3): p. 153-161.
403. Mai, V.M. and S.S. Berr, *MR perfusion imaging of pulmonary parenchyma using pulsed arterial spin labeling techniques: FAIRER and FAIR.* Journal of Magnetic Resonance Imaging, 1999. **9**(3): p. 483-487.
404. Bolar, D., et al., *Quantification of regional pulmonary blood flow using ASL-FAIRER.* Magnetic resonance in medicine, 2006. **55**(6): p. 1308-1317.
405. Theilmann, R.J., et al., *Quantitative MRI measurement of lung density must account for the change in T 2* with lung inflation.* Journal of Magnetic Resonance Imaging, 2009. **30**(3): p. 527-534.
406. Burrowes, K.S., R.B. Buxton, and G.K. Prisk, *Assessing potential errors of MRI-based measurements of pulmonary blood flow using a detailed network flow model.* Journal of Applied Physiology, 2012. **113**(1): p. 130-141.
407. Sá, R.C., et al., *MEASUREMENT OF THE DISTRIBUTION OF VENTILATION-PERFUSION RATIOS IN THE HUMAN LUNG WITH PROTON MRI: COMPARISON WITH THE MULTIPLE INERT GAS ELIMINATION TECHNIQUE.* Journal of Applied Physiology, 2017: p. jap. 00804.2016.

408. Capaldi, D.P., et al., *Free-breathing pulmonary 1 H and hyperpolarized 3 He MRI: comparison in COPD and bronchiectasis.* Academic radiology, 2015. **22**(3): p. 320-329.

409. Wild, J.M., et al., *3D volume-localized pO2 measurement in the human lung with 3He MRI.* Magnetic resonance in medicine, 2005. **53**(5): p. 1055-1064.

410. Saam, B., W. Happer, and H. Middleton, *Nuclear relaxation of He 3 in the presence of O 2.* Physical Review A, 1995. **52**(1): p. 862.

411. Wagner, P.D., et al., *Continuous distributions of ventilation-perfusion ratios in normal subjects breathing air and 100% O2.* Journal of Clinical Investigation, 1974. **54**(1): p. 54.

412. West, J.B., *Ventilation-Perfusion Relationships 1, 2.* American review of respiratory disease, 1977. **116**(5): p. 919-943.

413. Miller, G.W., et al., *A short-breath-hold technique for lung pO2 mapping with 3He MRI.* Magnetic Resonance in Medicine, 2010. **63**(1): p. 127-136.

414. Rizi, R.R., et al., *Operating characteristics of hyperpolarized 3 He and arterial spin tagging in MR imaging of ventilation and perfusion in healthy subjects.* Academic radiology, 2003. **10**(5): p. 502-508.

415. Marshall, H., et al., *Mutli-Nuclear MR Imaging Of VQ Distribution Response To Bronchodilator In Asthma*, in *D19. MR. AND MRS.: IMAGING REGIONAL LUNG FUNCTION.* 2014, American Thoracic Society. p. A5416-A5416.

416. Tofts, P.S., *Modeling tracer kinetics in dynamic Gd-DTPA MR imaging.* Journal of Magnetic Resonance Imaging, 1997. **7**(1): p. 91-101.

417. Koh, T.S., et al., *Fundamentals of tracer kinetics for dynamic contrast-enhanced MRI.* Journal of Magnetic Resonance Imaging, 2011. **34**(6): p. 1262-1276.

418. Ingrisch, M. and S. Sourbron, *Tracer-kinetic modeling of dynamic contrast-enhanced MRI and CT: a primer.* Journal of pharmacokinetics and pharmacodynamics, 2013. **40**(3): p. 281-300.

419. Bell, L.C., et al., *Comparison of Models and Contrast Agents for Improved Signal and Signal Linearity in Dynamic Contrast-Enhanced Pulmonary MRI.* Investigative radiology, 2015. **50**(3): p. 174.

420. Cheng, H.L.M. and G.A. Wright, *Rapid high-resolution T1 mapping by variable flip angles: Accurate and precise measurements in the presence of radiofrequency field inhomogeneity.* Magnetic resonance in medicine, 2006. **55**(3): p. 566-574.

421. Crawley, A.P. and R.M. Henkelman, *A comparison of one-shot and recovery methods in T1 imaging.* Magnetic resonance in medicine, 1988. **7**(1): p. 23-34.

422. Brix, G., et al., *Fast and precise T1 imaging using a TOMROP sequence.* Magnetic resonance imaging, 1990. **8**(4): p. 351-356.

423. Henderson, E., et al., *A fast 3D Look-Locker method for volumetric T 1 mapping.* Magnetic resonance imaging, 1999. **17**(8): p. 1163-1171.

424. Bauman, G., et al., *Pulmonary relaxometry with inversion recovery ultra-fast steady-state free precession at 1.5 T.* Magnetic resonance in medicine, 2017. **77**(1): p. 74-82.

425. Liberman, G., Y. Louzoun, and D. Ben Bashat, *T1 mapping using variable flip angle SPGR data with flip angle correction.* Journal of Magnetic Resonance Imaging, 2014. **40**(1): p. 171-180.

426. Risse, F., et al., *Dual-bolus approach to quantitative measurement of pulmonary perfusion by contrast-enhanced MRI.* Journal of Magnetic Resonance Imaging, 2006. **24**(6): p. 1284-1290.

427. Walker-Samuel, S., M.O. Leach, and D.J. Collins, *Reference tissue quantification of DCE-MRI data without a contrast agent calibration.* Physics in Medicine & Biology, 2007. **52**(3): p. 589.

428. Schabel, M.C. and D.L. Parker, *Uncertainty and bias in contrast concentration measurements using spoiled gradient echo pulse sequences.* Physics in Medicine & Biology, 2008. **53**(9): p. 2345.
429. Wang, P., et al., *Effects of flip angle uncertainty and noise on the accuracy of DCE-MRI metrics: comparison between standard concentration-based and signal difference methods.* Magnetic resonance imaging, 2015. **33**(1): p. 166-173.
430. Li, K.L., et al., *Improved 3D quantitative mapping of blood volume and endothelial permeability in brain tumors.* Journal of Magnetic Resonance Imaging, 2000. **12**(2): p. 347-357.
431. Meier, P. and K.L. Zierler, *On the theory of the indicator-dilution method for measurement of blood flow and volume.* Journal of applied physiology, 1954. **6**(12): p. 731-744.
432. Barbier, E.L., L. Lamalle, and M. Décorps, *Methodology of brain perfusion imaging.* Journal of Magnetic Resonance Imaging, 2001. **13**(4): p. 496-520.
433. Murase, K., M. Shinohara, and Y. Yamazaki, *Accuracy of deconvolution analysis based on singular value decomposition for quantification of cerebral blood flow using dynamic susceptibility contrast-enhanced magnetic resonance imaging.* Physics in medicine and biology, 2001. **46**(12): p. 3147.
434. Koh, T., et al., *Assessment of perfusion by dynamic contrast-enhanced imaging using a deconvolution approach based on regression and singular value decomposition.* IEEE transactions on medical imaging, 2004. **23**(12): p. 1532-1542.
435. Smith, M., et al., *Removing the effect of SVD algorithmic artifacts present in quantitative MR perfusion studies.* Magnetic resonance in medicine, 2004. **51**(3): p. 631-634.
436. Press, W.H., et al., *Numerical recipes in C.* Vol. 2. 1996: Cambridge university press Cambridge.
437. Mehndiratta, A., et al., *A control point interpolation method for the non-parametric quantification of cerebral haemodynamics from dynamic susceptibility contrast MRI.* Neuroimage, 2013. **64**: p. 560-570.
438. Ley-Zaporozhan, J., et al., *Assessment of the relationship between lung parenchymal destruction and impaired pulmonary perfusion on a lobar level in patients with emphysema.* European journal of radiology, 2007. **63**(1): p. 76-83.
439. Ley, S., et al., *Quantitative 3D pulmonary MR-perfusion in patients with pulmonary arterial hypertension: correlation with invasive pressure measurements.* European journal of radiology, 2007. **61**(2): p. 251-255.
440. Rijpkema, M., et al., *Method for quantitative mapping of dynamic MRI contrast agent uptake in human tumors.* Journal of Magnetic Resonance Imaging, 2001. **14**(4): p. 457-463.
441. Bell, L.C., *Assessment of pulmonary perfusion using T1-weighted dynamic contrast enhanced MRI.* 2015, The University of Wisconsin-Madison.
442. Neeb, D., et al., *Quantification of pulmonary blood flow (PBF): validation of perfusion MRI and nonlinear contrast agent (CA) dose correction with H 215O positron emission tomography (PET).* Magnetic resonance in medicine, 2009. **62**(2): p. 476-487.
443. Masoli, M., et al., *The global burden of asthma: executive summary of the GINA Dissemination Committee report.* Allergy, 2004. **59**(5): p. 469-478.
444. Hatabu, H., et al., *Quantitative assessment of pulmonary perfusion with dynamic contrast-enhanced MRI.* Magnetic resonance in medicine, 1999. **42**(6): p. 1033-1038.
445. Van Dyk, J., T. Keane, and W. Rider, *Lung density as measured by computerized tomography: implications for radiotherapy.* International Journal of Radiation Oncology* Biology* Physics, 1982. **8**(8): p. 1363-1372.

446. Dehnert, C., et al., *Magnetic resonance imaging of uneven pulmonary perfusion in hypoxia in humans.* American journal of respiratory and critical care medicine, 2006. **174**(10): p. 1132-1138.
447. Aaronson, P.I., et al., *Hypoxic pulmonary vasoconstriction: mechanisms and controversies.* The Journal of physiology, 2006. **570**(1): p. 53-58.
448. Mistry, N.N., et al., *Ventilation/perfusion imaging in a rat model of airway obstruction.* Magnetic resonance in medicine, 2010. **63**(3): p. 728-735.
449. Hueper, K., et al., *Quantitative and Semi-quantitative Measures of Regional Pulmonary Parenchymal Perfusion by Magnetic Resonance Imaging and their Relationships to Global Lung Perfusion and Lung Diffusing Capacity–The MESA COPD Study.* Investigative radiology, 2013. **48**(4): p. 223.
450. Snyder, E.M., et al., *Effects of an Inhaled β2-Agonist on Cardiovascular Function and Sympathetic Activity in Healthy Subjects.* Pharmacotherapy: The Journal of Human Pharmacology and Drug Therapy, 2011. **31**(8): p. 748-756.
451. Nathan, P., et al., *Phase I trial of combretastatin A4 phosphate (CA4P) in combination with bevacizumab in patients with advanced cancer.* Clinical cancer research, 2012. **18**(12): p. 3428-3439.
452. Messiou, C., et al., *Advanced solid tumors treated with cediranib: comparison of dynamic contrast-enhanced MR imaging and CT as markers of vascular activity.* Radiology, 2012. **265**(2): p. 426-436.
453. Miyazaki, K., et al., *Demonstration of the reproducibility of free-breathing diffusion-weighted MRI and dynamic contrast enhanced MRI in children with solid tumours: a pilot study.* European radiology, 2015. **25**(9): p. 2641-2650.